Analysis of Turbulent Characteristics in Flow Past Bluff Bodies

Thesis Submitted by

ANJAN SAMANTA

Index No.: D-7/ISLM/102/21

Doctor of Philosophy

School of Water Resources Engineering
Faculty of Interdisciplinary Studies, Law and Management
Jadavpur University
Kolkata, India

2025

Dedicated to

My Parents

Suchitra Samanta

&

Bhola Nath Samanta

JADAVPUR UNIVERSITY
KOLKATA – 700 032, INDIA

INDEX NO. **D-7/ISLM/102/21**

Title of Thesis

Analysis of turbulent characteristics in flow past bluff bodies

Name, Designation & Institution of the Supervisors

Dr. Rajib Das
Assistant Professor
School of Water Resources Engineering
Jadavpur University
Kolkata, 700 032

Dr. Sankar Sarkar
Assistant Professor
Physics and Applied Mathematics Unit
Indian Statistical Institute
Kolkata, 700016

List of Journal Publications:

Sarkar, M., Samanta, A., Sarkar, D., Das, R., & Sarkar, S. (2023). Turbulence in a wall wake flow downstream of two horizontal cylinders. Marine Georesources & Geotechnology, 42(7), 878-897. DOI: https://doi.org/10.1080/1064119X.2023.2234361

Samanta, A., Sarkar, M., Mondal, H., Das, R., & Sarkar, S. (2023). Turbulence anisotropy in a wall-wake flow downstream of two horizontal cylinders. Flow Measurement and Instrumentation, 94, 102456. DOI: https://doi.org/10.1016/j.flowmeasinst.2023.102456

Samanta, A., Sarkar, S., Das, R., & Mondal, H. (2024). Machine learning algorithms on predicting the turbulent mixed convection flow in a driven-cavity with two horizontal cylinders. *International Communications in Heat and Mass Transfer*, *159*, 108064. DOI: https://doi.org/10.1016/j.icheatmasstransfer.2024.108064

List of Presentation in National/International/Conferences/ Workshops:

Samanta, A., Sarkar, D., Das, R., Sarkar, S. Turbulence Features in a Wall-Wake Flow Downstream of Two Horizontal Cylinders – A Numerical Approach. 2024 2nd International Conference on Nonlinear Dynamics and Applications (ICNDA 2024) organized by Sikkim Manipal Institute of Technology (SMIT). Vol. 2, Chap. 46, October 2024. DOI: https://doi.org/10.1007/978-3-031-69134-8_46

Samanta, A., Das, R., Sarkar, S. Prediction of turbulence anisotropy with Artificial Neural Network in a wall-wake flow downstream of two horizontal cylinders. 1st National conference on Modelling, Analysis and Simulation (MAS 2024). Organized by Department of Mathematics and Computing, Indian Institute of Technology (IIT-ISM), Dhanbad.

"Statement of Originality"

I, **Anjan Samanta**, registered on **21/01/2022,** do hereby declare that this thesis entitled "**Analysis of turbulent characteristics in flow past bluff bodies**" contains literature survey and original research work done by the undersigned candidate as part of Doctoral studies.

All information in this thesis have been obtained and presented in accordance with existing academic rules and ethical conduct. I declare that, as required by these rules and conduct, I have fully cited and referred all materials and results that are not original to this work.

I also declare that I have checked this thesis as per the "Policy on Anti Plagiarism, Jadavpur University, 2019", and the level of similarity as checked by iThenticate software is **9%**.

Signature of Candidate: Anjan Samanta

Date : 27-01-2025

Certified by Supervisors: (Signature with date, seal)

1. Rajib Das 27/01/2025

Dr. RAJIB DAS
Assistant Professor
School of Water Resources Engineering
Jadavpur University
Kolkata-700 032

2. 27.01.2025

Assistant Professor
Physics and Applied Mathematics Unit
Indian Statistical Institute
203, Barrackpore Trunk Road
Kolkata - 700 108

CERTIFICATE FROM THE SUPERVISORS

This is to certify that the thesis entitled "**Analysis of turbulent characteristics in flow past bluff bodies**" submitted by **Mr. Anjan Samanta**, who got his name registered on **21th January, 2022** for the award of the Ph.D. degree of Jadavpur University is absolutely based upon his own work under the supervisions of **Dr. Rajib Das**, Assistant Professor of School of Water Resources Engineering, Jadavpur University and **Dr. Sankar Sarkar**, Assistant Professor of Physics and Applied Mathematics Unit, Indian Statistical Institute, Kolkata and that neither his thesis nor any part of the thesis has been submitted for any degree or any other academic award anywhere before.

1. Rajib Das 27/01/2025

THESIS ADVISOR

Dr. Rajib Das
Assistant Professor
School of Water Resources Engineering
Jadavpur University

Dr. RAJIB DAS
Assistant Professor
School of Water Resources Engineering
Jadavpur University
Kolkata-700 032

2. _____

THESIS ADVISOR

Dr. Sankar Sarkar
Assistant Professor
Physics and Applied Mathematics Unit
Indian Statistical Institute, Kolkata

Assistant Professor
Physics and Applied Mathematics Unit
Indian Statistical Institute
203, Barrackpore Trunk Road
Kolkata - 700 108

ACKNOWLEDGEMENTS

I take this opportunity to express my deep sense of heartfelt gratitude and indebtedness to my supervisors Dr. Rajib Das, School of water resources engineering, Jadavpur University and Dr. Sankar Sarkar, Physics and applied mathematics unit, Indian Statistical Institute, Kolkata for their inspiration, incredible and scholarly guidance at all the stages of my investigation. This work would not have been possible without their boundless help, guidance and encouragement. I am especially grateful to Dr. Sankar Sarkar for providing me with access to the experimental setup of fluvial lab, ISI Kolkata and countless hours of encouragement throughout the journey. I am also grateful to Mr. Mosedul Sarkar, Senior research fellow, ISI Kolkata for his support in my initial days.

I was fortunate to get in touch with many world-famous researchers to participate in many collaborative efforts throughout my doctoral studies and I express my gratefulness to them for their valuable suggestions to enrich my knowledge. I wish to thank Prof. Asis Mazumdar, Director, School of water resources engineering and other members of my Doctoral Scrutiny Committee for their various constructive suggestions throughout the course of this study.

I am forever indebted to Dr. Hiranmoy Mondal, HoD, Department of Applied Mathematics, MAKAUT, WB for harnessing my mathematical capabilities which ultimately helped me to publish articles in several reputed journals. Last but not least, I would like to mention my parents, Mr. Bhola Nath Samanta and Mrs. Suchitra Samanta whose years of sacrifice have made me what I am today. I pray to Almighty for their lifelong good health and happiness.

Date: 27.01.2025
Place: SWRE, Jadavpur University

Anjan Samanta

ANJAN SAMANTA
Ph.D. Scholar
School of Water Resources Engineering
Jadavpur University

List of Symbols

A_f = area occupied by fluid at an elevation z ($M^0L^2T^0$);

A_0 = total area of integration ($M^0L^2T^0$);

b_{ik} = Reynolds stress anisotropy tensor [$= \overline{u_i' u_k'}/(2q) - (\delta_{ik}/3)$] ($M^0L^0T^0$);

C_D = drag coefficient ($M^0L^0T^0$);

C_f = skin friction coefficient ($M^0L^0T^0$);

C_1, C_2 = coefficients ($M^0L^0T^0$);

D = diameter of the sphere (M^0LT^0);

D_1 = height of the sphere above virtual bed level (M^0LT^0);

d = representative sediment diameter (M^0LT^0);

d_{16} = 16 % finer sediment size (M^0LT^0);

d_{50} = median diameter of gravel (M^0LT^0);

d_{84} = 84 % finer sediment size (M^0LT^0);

E_D = normalized turbulent dissipation [$= \varepsilon h/ u_*^3$] ($M^0L^0T^0$);

$\langle E_D \rangle$ = normalized spatially-averaged turbulent dissipation ($M^0L^0T^0$);

F = invariant function [$= (1 + 9II + 27III)$] ($M^0L^0T^0$);

F = flow Froude number [$= \bar{U}/(gh)^{0.5}$] ($M^0L^0T^0$);

F_{ku} = normalized streamwise flux of turbulent kinetic energy, f_{ku}/u_*^3 ($M^0L^0T^0$);

F_{kw} = normalized vertical flux of turbulent kinetic energy, f_{kw}/u_*^3 ($M^0L^0T^0$);

f_E = normalized mean frequency of ejections ($M^0L^0T^0$);

f_{ku} = streamwise flux of turbulent kinetic energy, $0.5(\overline{u'u'u'} + \overline{u'v'v'} + \overline{u'w'w'})$ ($M^0L^3T^{-3}$);

f_{kw} = vertical flux of turbulent kinetic energy, $0.5(\overline{u'u'w'} + \overline{v'v'w'} + \overline{w'w'w'})$ ($M^0L^3T^{-3}$);

f_S = normalized mean frequency of sweeps ($M^0L^0T^0$);

$\langle F_{ku} \rangle$ = $\langle f_{ku} \rangle / u_*^3$) ($M^0L^0T^0$);

$\langle F_{kw} \rangle$ = $\langle f_{kw} \rangle / u_*^3$) ($M^0L^0T^0$);

$\langle f_E \rangle$ = spatially-averaged f_E ($M^0L^0T^0$);

$\langle f_S \rangle$ = spatially-averaged f_S ($M^0L^0T^0$);

g = acceleration due to gravity (M^0LT^{-2});

H = hole-size parameter ($M^0L^0T^0$);

h = flow depth (M^0LT^0);

i = quadrant number ($M^0L^0T^0$);

i_E = mean interval between ejections (M^0L^0T);

i_S = mean interval between sweeps (M^0L^0T);

k = turbulent kinetic energy [$= 0.5(\overline{u'u'} + \overline{v'v'} + \overline{w'w'})$] ($M^0L^2T^{-2}$);

k_s = equivalent roughness height (M^0LT^0);

K_1, K_2 = coefficients ($M^0L^0T^0$);

M_{jk} = third-order moments or skewness [$= \overline{\tilde{u}^j \tilde{w}^k}$] ($M^0L^0T^0$);

M_{03} = skewness of w' [$= \overline{w'w'w'} / [(\overline{w'w'})^{0.5\times3}]$] ($M^0L^0T^0$);

M_{12} = [$\overline{u'w'w'} / [(\overline{u'u'})^{0.5} \times (\overline{w'w'})]$] ($M^0L^0T^0$);

M_{21} = [$\overline{u'u'w'} / [(\overline{u'u'}) \times (\overline{w'w'})^{0.5}]$] ($M^0L^0T^0$);

M_{30} = skewness of u' [$= \overline{u'u'u'} / [(\overline{u'u'})^{0.5\times3}]$] ($M^0L^0T^0$);

n = number of bed particles per unit area ($M^0L^0T^0$);

m = an exponent ($M^0L^0T^0$);

P_D = normalized pressure energy diffusion, [$= p_D h / u_*^3$] ($M^0L^0T^0$);

p = time-averaged hydrostatic pressure ($ML^{-1}T^{-2}$);

p' = pressure fluctuations ($ML^{-1}T^{-2}$);

p_D = pressure energy diffusion [$= \partial(\overline{p'w'/\rho})/\partial z$] ($M^0L^2T^{-3}$);

$\langle p_D \rangle$ = spatially-averaged pressure energy diffusion ($M^0L^2T^{-3}$);

q = the average turbulent kinetic energy in tensor form [$= \overline{u_i' u_i'} /2$] ($M^0L^{-2}T^{-2}$);

q_s = transport rate of sediment ($ML^{-1}T^{-1}$);

R = flow Reynolds number, [$= 4h\overline{U} / \upsilon$] ($M^0L^0T^0$);

R_D = wake Reynolds number ($M^0L^0T^0$);

R_* = shear-particle Reynolds number, [$= d_{50} u_* / \upsilon$] ($M^0L^0T^0$);

r_{uw} = correlation coefficient, [$= -\overline{u'w'} / (\overline{u'u'} \times \overline{w'w'})^{0.5}$] ($M^0L^0T^0$);

S_h = relative submergence, [$= d_{50}/h$] ($M^0L^0T^0$);

$S_{i,H}$ = Reynolds shear stress fractional contribution ($M^0L^0T^0$);

S_w = wake stability parameter ($M^0L^0T^0$);

$\langle S_{i,H} \rangle$ = spatially-averaged $S_{i,H}$ ($M^0L^0T^0$);

s = relative density of sediments ($M^0L^0T^0$);

T = sampling time (M^0L^0T);

T_D = normalized turbulent energy diffusion, [= $t_D h/ u_*^3$] ($M^0L^0T^0$);

$\langle T_D \rangle$ = normalized spatially-averaged turbulent energy diffusion ($M^0L^0T^0$);

T_E = normalized mean-time duration of ejections ($M^0L^0T^0$);

$\langle T_E \rangle$ = spatially-averaged T_E ($M^0L^0T^0$);

T_P = normalised turbulent production [= $t_P h/ u_*^3$] ($M^0L^0T^0$);

$\langle T_P \rangle$ = normalized spatially-averaged turbulent production ($M^0L^0T^0$);

T_S = normalized mean-time duration of sweeps ($M^0L^0T^0$);

$\langle T_S \rangle$ = spatially-averaged T_S ($M^0L^0T^0$);

t_D = turbulent energy diffusion, [= $\partial f_{kw}/\partial z$] ($M^0L^2T^{-3}$);

t_E = mean-time duration of ejections (M^0L^0T);

t_P = turbulent production, [= $-\overline{u'w'}(\partial u/\partial z)$] ($M^0L^2T^{-3}$);

t_S = mean-time duration of sweeps (M^0L^0T);

$\langle t_D \rangle$ = spatially-averaged turbulent energy diffusion ($M^0\ L^2T^{-3}$);

$\langle t_P \rangle$ = spatially-averaged turbulent production ($M^0L^2T^{-3}$);

$U(z)$ = the time-average approach velocity at an elevation z (M^0LT^{-1});

$U(\zeta)$ = approach streamwise time-averaged velocity in similarity solution for plane wall-wake flows (M^0LT^{-1});

$\overline{U}$ = depth-averaged approach velocity (M^0LT^{-1});

u = streamwise velocity component (M^0LT^{-1});

u' = fluctuations of streamwise velocity (M^0LT^{-1});

$\tilde{u}$ = normalized time-averaged streamwise velocity, [= u/u_*] ($M^0L^0T^0$)

u^+ = [= $(\overline{u'u'})^{0.5}/u_*$] ($M^0L^0T^0$);

uw^+ = normalized Reynolds shear stress [= $-\overline{u'w'}/u_*^2$] ($M^0L^0T^0$);

$\langle \overline{u} \rangle$ = spatially-averaged streamwise velocity (M^0LT^{-1});

$\langle u^+ \rangle$ = spatially-averaged normalized streamwise velocity ($M^0L^0T^0$);

u_0 = local velocity in free wake flow theory (M^0LT^{-1});

u_* = shear velocity (M^0LT^{-1});

u_{*c} = critical shear velocity (M^0LT^{-1});

u_1 = velocity defect in free wake flow theory [$= \overline{U} - u$] (M^0LT^{-1});

u_{*1} = shear velocity determined from the bed slope [$= (ghS)^{0.5}$] (M^0LT^{-1});

u_{*2} = shear velocity obtained from the Reynolds shear stress (M^0LT^{-1});

$\langle \overline{u_i' u_j'} \rangle$ = spatially-averaged Reynolds stress in tensor form ($ML^{-1}T^{-2}$);

$\langle \tilde{u}_i \tilde{u}_j \rangle$ = form-induced stress in tensor form ($ML^{-1}T^{-2}$);

v = transverse velocity component (M^0LT^{-1});

v' = fluctuations of transverse velocity component (M^0LT^{-1});

v_D = viscous diffusion [$= -\upsilon(\partial^2 k/\partial z^2)$] ($M^0L^3T^{-4}$) ;

$\langle v_D \rangle$ = spatially-averaged viscous diffusion ($M^0L^3T^{-4}$);

w = vertical velocity component (M^0LT^{-1});

w^+ = [$= (\overline{w'w'})^{0.5}/u_*$] ($M^0L^0T^0$);

w' = fluctuations of vertical velocity component (M^0LT^{-1});

$\tilde{w}$ = deviation of local vertical velocity from $\langle \overline{w} \rangle$ (M^0LT^{-1});

$\langle \overline{w} \rangle$ = spatially-averaged normalized vertical velocity ($M^0L^0T^0$);

x, y, z = streamwise, vertical and transverse distances, respectively (M^0LT^0);

$\hat{x}$ = nondimensional streamwise distance, [$= x/D$] ($M^0L^0T^0$);

y_1 = transverse distance of 50% of the maximum velocity defect (M^0LT^0);

$\hat{y}_1$ = nondimensional transverse distance, [$= y/(z_1 - 0.5D)$] ($M^0L^0T^0$);

$\hat{y}_2$ = nondimensional transverse distance [$= y/(z_2 - 0.5D)$] ($M^0L^0T^0$);

$\hat{z}$ = z/D_1 ($M^0L^0T^0$);

$\hat{z}_c$ = normalized crest height, [$= z_c/h$] ($M^0L^0T^0$);

$\hat{z}_1$ = z/z_1 ($M^0L^0T^0$);

$\hat{z}_2$ = z/z_2 ($M^0L^0T^0$);

$\tilde{z}_1$ = z_1/D_1 ($M^0L^0T^0$);

$\tilde{z}_2$ = z/D_1 ($M^0L^0T^0$);

z^+ = normalized vertical distance [$= z/d_{50}$] ($M^0L^0T^0$);

z_c = crest level of roughness or top of interfacial sub-layer (M^0LT^0);

z_t = elevation of roughness troughs where roughness geometry function, $\phi = 0$ (impermeable bed) or $d\phi/dz = 0$ (permeable bed) (M^0LT^0);

z_1 = height of the 50% of the maximum velocity defect (M^0LT^0);

z_2 = height of 50% of the peak of Reynolds shear stress defect (M^0LT^0);

I, II, III = independent invariants, ($M^0L^0T^0$);

α = an exponent ($M^0L^0T^0$);

β = nondimensional parameter ($M^0L^0T^0$);

γ = specific weight of water ($ML^{-3}T^0$);

$\Delta\sigma_u$ = defect in streamwsie turbulence intensity ($ML^{-1}T^{-2}$);

$\Delta\sigma_w$ = defect in vertical turbulence intensity ($ML^{-1}T^{-2}$);

$(\Delta\sigma_u)_m$ = peak defect of streamwise turbulence intensity ($ML^{-1}T^{-2}$);

$(\Delta\sigma_w)_m$ = peak defect of vertical turbulence intensity ($ML^{-1}T^{-2}$);

$\Delta S_{i,H}$ = net effect of ejections and sweep events [$= S_{4,H} - S_{2,H}$] ($M^0L^0T^0$);

$\Delta\tau$ = $\tau(z)|_{\text{upstream}} - \tau(z)|_{\text{downstream}}$ ($ML^{-1}T^{-2}$);

$\Delta\tau_m$ = peak defect in Reynolds shear stress ($ML^{-1}T^{-2}$);

$-(\Delta\hat{\tau})_m$ = $(-\Delta\tau_m)/(\rho u_*^2)$ ($M^0L^0T^0$);

Δu = velocity defect ($M^0L^1T^{-1}$);

Δu_m = peak velocity defect ($M^0L^1T^{-1}$);

$(\Delta u^+)_m$ = $\Delta u_m/u_*$ ($M^0L^0T^0$);

δ_{ik} = Kronecker delta function ($M^0L^0T^0$);

ε = turbulence diffusivity ($M^0L^2T^{-1}$);

= turbulent dissipation in turbulent energy budget ($M^0L^2T^{-3}$);

$\langle\varepsilon\rangle$ = spatially-averaged turbulent dissipation ($M^0L^2T^{-3}$);

ζ = radial distance in polar-coordinate system ($M^0L^1T^0$);

η_1 = $\zeta/(D_1 - 0.5D)]$ ($M^0L^0T^0$);

Θ = Shields parameter ($M^0L^0T^0$);

Θ_c = critical Shields parameter ($M^0L^0T^0$);

$\bar{\theta}$ = time-averaged quantity;

$\tilde{\theta}$ = $\bar{\theta} - \langle\bar{\theta}\rangle$;

$\langle\bar{\theta}\rangle$ = spatially-averaged quantity;

κ = von Karman constant ($M^0L^0T^0$);

$\lambda_{i,H}$ = detection function ($M^0L^0T^0$);

μ = Coulomb friction factor ($M^0L^0T^0$);

ρ = mass density of fluid ($ML^{-3}T^0$);

ρ_0 = porosity of sediments ($M^0L^0T^0$);

σ = nondimensional pressure ($M^0L^0T^0$);

σ_g = geometric standard deviation of particle size ($M^0L^0T^0$);

$\hat{\sigma}_u$ = σ_u/u_* ($M^0L^0T^0$);

$\hat{\sigma}_w$ = σ_w/u_* ($M^0L^0T^0$);

τ_0 = bed shear stress ($ML^{-1}T^{-2}$);

$\hat{\tau}$ = nondimensional Reynolds shear stress [$= -\tau/(\rho u_*^2)$] ($M^0L^0T^0$);

τ_c = critical bed shear stress ($ML^{-1}T^{-2}$);

τ_d = shear stress due to form drag [$= 0.5C_D a\langle\bar{u}\rangle^2$] ($ML^{-1}T^{-2}$);

τ_f = bed shear stress of fluid ($ML^{-1}T^{-2}$);

τ_s = bed shear stress of sediment particle ($ML^{-1}T^{-2}$);

τ_t = total shear stress ($ML^{-1}T^{-2}$);

τ_{uw} = Reynolds shear stress ($ML^{-1}T^{-2}$);

τ_{vis} = viscous shear stress ($ML^{-1}T^{-2}$);

$\langle\tau_f\rangle$ = form-induced shear stress [$= -\langle\rho\tilde{u}\tilde{w}\rangle$] ($ML^{-1}T^{-2}$);

$\langle\tau_t\rangle$ = spatially-averaged total shear stress ($ML^{-1}T^{-2}$);

$\langle\tau_{uw}\rangle$ = spatially-averaged Reynolds shear stress ($ML^{-1}T^{-2}$);

$\langle\tau_{\mathrm{vis}}\rangle$ = viscous shear stress [$= -\rho\upsilon\langle\partial\bar{u}/\partial z\rangle$] ($ML^{-1}T^{-2}$);

$\langle\hat{\tau}_d\rangle$ = $\langle\tau_d\rangle/u_*^2$ ($M^0L^0T^0$);

$\langle\hat{\tau}_f\rangle$ = $-\langle\tilde{u}\tilde{w}\rangle/(u_*^2)]$ ($M^0L^1T^0$);

$\langle\hat{\tau}_t\rangle$ = $\langle\tau_t\rangle/(\rho u_*^2)$ (ML^0T^0);

$\langle\hat{\tau}_{uw}\rangle$ = $-\langle\overline{u'w'}\rangle/u_*^2)$ ($M^0L^0T^0$);

$\langle \hat{\tau}_{vis} \rangle$ = $-\upsilon\langle\partial\bar{u}/\partial z\rangle/u_*^2$ ($M^0L^0T^0$);

υ = kinematic viscosity of fluid ($M^0L^2T^{-1}$);

ϕ = nondimensional velocity [= u_1/u_0] ($M^0L^0T^0$);

ψ = nondimensional Reynolds stress ($M^0L^0T^0$);

Abbreviations

LDA	Laser Doppler anemometry
LDV	Laser Doppler velocimetry
LRE	Large roughness elements
PSD	Power Spectral Density
TKE	Turbulent kinetic energy
DNS	Direct Numerical Simulation
ML	Machine Learning
CFD	Computational Fluid Dynamics
RANS	Reynolds Averaged Navier-Stokes

Abstract

This study presents experimental and numerical findings of turbulent flow past two (one above other) horizontal cylinders, one cubical and one cylindrical bluff body, followed by predictive determination of turbulence characteristics as well as heat transfer rate using several machine and deep learning methods.

The experimental data captured over a rough-bed with double cylinders having three different diameters, were used for the analysis. To determine one of the most prime behaviors of turbulence characteristics, namely TKE dissipation rate more accurately, the concept of structure function has been employed. Primarily velocity gradient method elucidates TKE dissipation rate, then it has been verified by Kolmogorov's two-thirds law using second order structure function and Kolmogorov's –5/3 law using the method of power spectra.

Some advanced analysis such as correlation coefficient, stress anisotropy, and dissipation anisotropy have been presented and compared location-wise. To demonstrate anisotropy, stress, dissipation tensors along with anisotropic invariant map and function are plotted and thoroughly analyzed. From Reynolds stress tensor, the eigenvalues have been computed to elucidate a newly developed graphical plot of turbulent anisotropy based on barycentric coordinates.

The bursting events and associated time and frequency were first computed from the experimental data and then higher-order moments were evaluated to validate the experimental findings. From the stress ratio of Reynolds Shear Stress (RSS) plots, it is seen that sweep was the main contributing event that attains the maximum value up to 600% to the development of RSS in the near-wake flow region in the vicinity of the wall, causing a rush of accelerating fluid streaks. The average duration and interval of the bursting events suggest that in the near-wake flow region, the bursting events are generally shorter in duration compared to the time between their occurrences. Furthermore, third order moments have been evaluated and utilized to validate bursting events by comparing with the residual shear stress.

A Galerkin based finite element technique is used to numerically investigate the turbulent mixed convection flow as well as heat transport properties in a square cavity with two horizontal cylinders aligned vertically. To predict the thermal distribution within the cavity due to the hot cylinders, both Artificial Neural Network (ANN) as well as Gaussian Process Regression (GPR) models are developed. The results show that both models have been trained effectively for this purpose.

Keywords: Turbulence in open channel, Bluff body hydrodynamics, Turbulence anisotropy and bursting, Mixed convection, Machine learning prediction.

Contents

Chapter 1

Introduction

1.1 General

Turbulent flow in open channels is a subject of considerable interest in hydraulic engineering as most flows occur in practical applications are turbulent. Although many experimental and theoretical research have been made so far, still there remain many problems awaiting proper understanding. Bluff body hydrodynamics is a field within fluid mechanics that focuses on the study of the flow of fluids around objects with blunt shapes, such as cylinders, spheres, cubes, or other geometric forms. These objects are called "bluff bodies" because they create turbulent wakes and separated flow regions behind them due to their shape, as opposed to streamlined bodies that have smooth, streamlined shapes. Understanding bluff body hydrodynamics is important for several engineering applications, which include aerodynamics (such as the design of buildings, bridges, and vehicles), marine engineering (such as ship and offshore platform design), and environmental engineering (including the spread of contaminants in the atmosphere and water bodies). Researchers in this field analyze the flow patterns, pressure distributions, and forces acting on bluff bodies to optimize their design for specific purposes, such as reducing drag, improving stability, or enhancing efficiency. Wind tunnel experiments, Computational fluid dynamics (CFD) simulations, and theoretical models are commonly used tools in studying bluff body hydrodynamics.

Wake flow downstream of two horizontal cylinders is a representative example of the flow around two bluff-bodies. The study of wake flow downstream of one or more bluff-bodies is a matter of considerable interest due to its significance in many practical situations. In shallow flows, the wake flows downstream of a bluff-body are essential for studying a variety of both geophysical and environmental fluid flow scenarios, including pebble clusters, short submerged horizontal cylinders, and fish habitat structures. A wake is the area of disturbed flow downstream a solid object traversing through a fluid, produced by the fluid flowing around the body, or downstream of a solid object submerged in a stream. It is a narrow elongated region,

consists of small and large eddies, which interact with each other in their unruly motion. Wakes are maintained downstream of the body for a certain distance, and as the downstream distance increases, the uninterrupted boundary layer gradually recovers. This depends on the shape, size and flow dynamics of the bluff-body. The presence of a turbulent wake involving recirculation, which significantly affects the body's drag and lift, is the primary feature of wake flows. Flow around bluff-bodies is also an important aspect of aerodynamics. Nevertheless, just a few investigations into the properties of flow past a protruding particle in an open channel have been conducted so far. Examples of projecting particles that are often utilized in numerous scientific investigations include spheres, cylinders, and hemispherical objects. Understanding the laws of hydrodynamics and turbulent mixing mechanisms over gravel beds requires a proper characterization of such flows.

In most of the investigations of turbulence in open channels researchers have used the traditional time-averaged hydrodynamic equations which are also identified as the Reynolds averaged Navier-Stokes (RANS) equations. Some recent studies showed that the RANS holds good only for flows over hydraulically smooth bed. But, for flows over hydraulically rough bed, in particular, near the bed, the time-averaged equations are not sufficient to give satisfactory solution. The irregular bed topography, which is composed of distinct particles with varying orientations and forms, actually causes the flow to be extremely spatially heterogeneous close to the rough bed, which frequently makes utilizing the RANS inconvenient. Hence RANS equations have been tried to solve numerically using Galerkin Finite element method subject to the appropriate boundary conditions. The numerical data obtained were therefore trained via several machine learning algorithms, to be discussed in the subsequent chapters.

1.2 Scope of the Present Work

Time-averaged turbulent flow characteristics, spectral analysis, anisotropy, turbulent kinetic energy, energy budget and bursting analysis are performed in presence of two horizontal cylinders one above the other on uniform gravel bed.

The flow profiles of time-averaged streamwise velocity, Reynolds shear stress and turbulence intensities are investigated at the downstream of a wall-wake. A detailed study on turbulent kinetic energy, indicator, energy budget, anisotropy, higher order moments, contributions of various bursting events towards Reynolds shear stress are analyzed.

Furthermore, the problem of flow past two horizontal cylinders has been studied numerically and then streamlines and isotherms have been studied in order to analyze turbulent mixed convection flow.

1.3 Objectives of the Present Investigation

- To employ both computational and experimental methods to examine the turbulent wake flows behind two horizontal cylinders set on a uniform gravel bed.

- To predict the turbulent flow characteristics as well as heat transfer rate using several machine learning algorithms.

1.4. Structure of the Thesis

The thesis is separated into eight chapters. An introduction to the response of near-bed turbulence characteristics in a wall-wake flow behind two cylinders placed on a uniform gravel bed along with the objectives of the investigations are outlined in Chapter 1. Reviews of relevant literature are given in Chapter 2. In Chapter 3, experimental set-up and procedures for different experiments are described. Basic experimental results and discussions along with energy budget on the response of near-bed turbulence behaviour in a wall-wake flow behind two horizontal cylinders are presented in Chapter 4. The details of stress anisotropy and dissipation anisotropy with quadrant analysis of the conditional statistics of the same are

analyzed in Chapter 5. Turbulence bursting and its correlation with higher order moments in a wake flow behind two horizontal cylinders are explained in Chapter 6. In Chapter 7, a numerical investigation of turbulent mixed convective flow in a driven square cavity comprised of two horizontal cylinders is presented. The conclusions from the present investigation are outlined in Chapter 8.

Chapter 2

Review of Literature

2.1 General

This chapter outlines an in-depth analysis of existing research on three key areas: the features of turbulent wall-wake flows occurring after a bluff body, anisotropy and bursting events in turbulent flow past bluff body, and the implementation of machine learning techniques in hydrodynamic and thermal predictions.

2.2 Fluid Dynamics in the Wake of Bluff bodies

The study of fluid flow around bluff bodies has obtained significant attention because of its numerous practical applications in hydraulic and aerodynamic fields. The key characteristic of these flows is the development of a turbulent wake with recirculation, which substantially impacts the object's drag and lift forces. For instance, airfoils are designed with streamlined shapes to enhance lift relative to drag. In bridge engineering, comprehending the fluid dynamics around surface-penetrating cylinders in open channels is crucial.

The flow pattern downstream of a cylinder serves as a typical example of bluff bodies fluid dynamics. several experimental and computational studies have been performed to investigate the flow properties surrounding bluff bodies.

2.2.1 Basic turbulent characteristics

In the distant wake region of a plane turbulent wake, Schlichting (1968) proposed an equation for velocity distribution similarity. According to him, the similarity equation is

$$\frac{U_1}{U_{1m}} = \frac{U_\infty - u}{\left(U_\infty - u\right)_m} = \left(1 - 0.293\lambda^{3/2}\right)^2 \qquad (2.1)$$

Where $\lambda = y/b_1$, $b_1 = y$, $U_1/U_1m = 0.5$, and b_1 are taken into consideration as the velocity and length scale for the plane wake, and $U_1 = U_\infty - u$ is the velocity defect, U_∞ = undisturbed ambient velocity, and U_{1m} = maximum value of the velocity defect.

Schlichting (1968) calculated the rates at which the velocity defect grows (represented by the transverse length scale b_1) and decays in a plane turbulent wake. These rates were expressed as power functions of the downstream distance (x), derived from the continuity and Navier-Stokes equations for two-dimensional flow under a condition of zero pressure gradient:

$$\frac{U_1}{U_\infty} = C_1 \left(\frac{x}{C_D} \right)^{-0.5} \tag{2.2}$$

$$\frac{b_1}{DC_D} = C_2 \left(\frac{x}{C_D D} \right)^{0.5} \tag{2.3}$$

where C_D = drag coefficient, D = cylinder diameter, Schilchting found the values of $C_1 = 1$ and $C_2 = 0.25$.

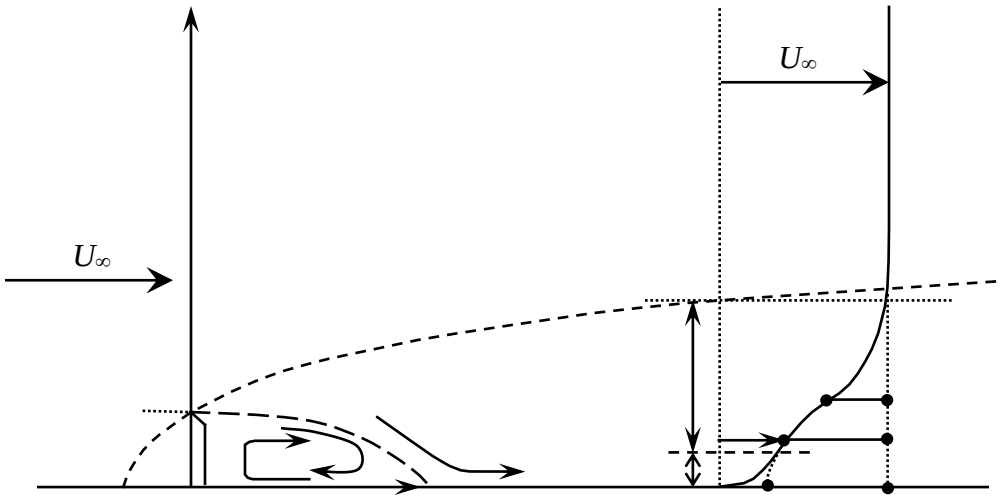

Figure 2.1: An illustration of a plane wall wake.

Sadeque et al. (2008, 2009) used both smooth and rough beds to study the flow dynamics in the shallow near-wake zones behind wall-mounted cylinders in an open channel. The experiment involved cylinders of identical diameter and height, including a surface-piercing cylinder resembling a bridge pier, tested under four different submersion levels and similar flow conditions. For cylinders that were moderately to deeply submerged, the surrounding flows exhibited a closed recirculating wake. Near the cylinders' shoulders, a gradual increment in

bed-shear stress was reflected across all flow regimes, with the rough bed showing a ratio to the approach bed-shear stress twice that of the smooth bed. Flow visualization experiments revealed that horseshoe-shaped vortices were bigger on the rough bed in comparison to the smooth bed. The study found that Perry and Joubert's model could accurately predict velocity deflection around cylinders for both smooth and uneven bed flows.

Tachie and Balachandar (2001) studied shallow wakes behind a sharp-edged two-dimensional flat plate placed normal to the flow on smooth and rough surfaces. They found that the velocity defects for both the smooth and rough beds collapse on a single band at any axial location by using a proper choice of the length and velocity scales. The study revealed that the roughness of the surface has a substantial influence on turbulence parameters.

In order to forecast how deep and shallow wakes will spread behind a surface-piercing item, Balachandar (1999) constructed theoretical models. At low flow depths, the Karman vortex street is destroyed, according to visual observations. Whereas a shallow wake width takes on an asymptotic value if the non-dimensional bed friction number S_f (= C_f / h, where h = entire flow depth and C_f being the skin friction coefficient) reaches a threshold value of $S_f = S_{fc}$ when the total obliteration of Karman vortex street occurs, a deep wake can continue to expand indefinitely, according to the models.

Under varying submergence conditions, Shamloo et al. (2001) investigated shallow wakes behind a hemispherical body on smooth, uneven, and erodible materials. A wall wake in the vertical plane and a plane turbulence wake in the horizontal plane were taken into consideration in order to simplify the 3D wakes created by submerged objects. The downstream of the hemisphere was discovered to have a plane wake after a recirculating flow zone that was around 2D long. Using the idea of inner and outer layer wall wakes, the flow structure in this planar wake zone was examined. In the plane of symmetry, the law of wall was used to study the inner layer and Schlichting's (1930) plane wake equations were used to evaluate the outer layer. The similar idea was also used to assess the longitudinal velocity fluctuation in the transverse direction. An empirical correlation was also put up by Shamloo et al. (2001) to examine the velocity defect downstream of the body.

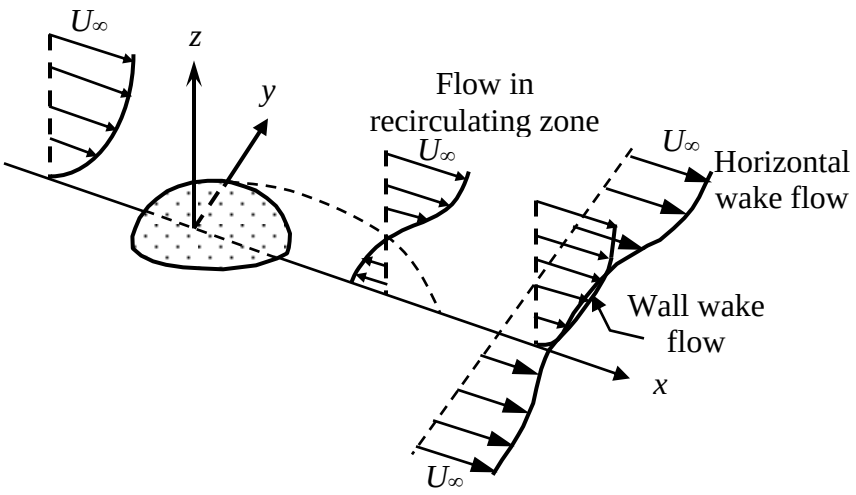

Figure 2.2: Wall-wake flows behind a hemispherical object by Shamloo et al. (2001)

The time-averaged features of turbulent wake flows produced when a sphere is put on a rough wall were investigated by Dey et al. (2011). They found that the Reynolds shear stress, turbulence intensity, and streamwise velocity defect profiles were very similar when normalized by their respective peak defect values. The vertical length scale of the velocity defect profiles was determined by the elevation where the half-peak velocity defect occurred. The vertical lengths for the Reynolds shear stress and turbulence intensity defect profiles were modified according to the height at which the half-peak Reynolds shear stress defect was detected. As one moved further away from the sphere, the values of the peak flaws for each amount dropped, indicating that their original profiles had been restored. Additionally, the velocity defect profiles' theoretical solution of similarity was obtained. A discernible rise in turbulence production within the wall-wake flows was indicated by the negative maximum in pressure energy diffusion and the positive maximum in turbulent production. The quadrant analysis confirmed that sweeps, driven by the influx of fluid streaks, served as the dominant mechanism regulating the wall-wake flows. Although the bursting episodes were more frequent than those in the upstream, they last less time.

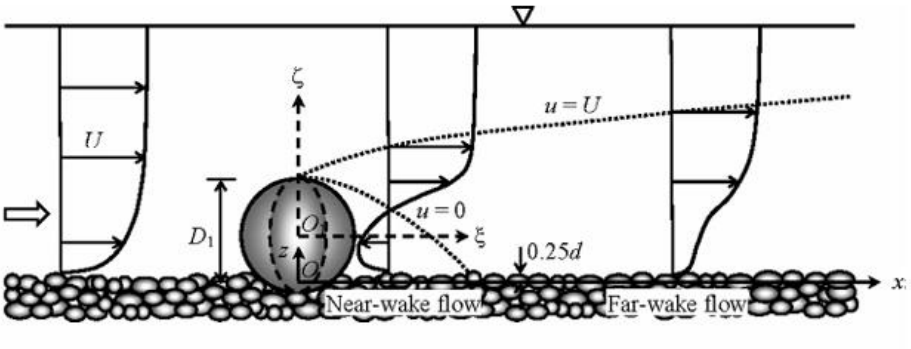

Figure 2.3: Wall-wake flows behind a sphere by Dey et al. (2011)

The turbulence properties of wall-wake flows behind cylinders positioned on or close to the wall were investigated by Dey et al. (2018). They observed that the profiles of Reynolds shear stress, turbulence intensities, and streamwise velocity defect exhibited self-similar behaviour when normalized by their corresponding peak defect values. By using the half-width of the peak defect velocity, the vertical distances of the velocity defect profiles were scaled. Their third-order correlation analysis showed that for the wall-mounted cylinder, sweeps were linked to streamwise acceleration and a downward flux of streamwise Reynolds normal stress (SRNS) in the wall-wake's inner layer, while ejections were linked to streamwise deceleration and an upward flux of SRNS in the outer layer. Similar outer-layer behaviour was seen for the near-wall cylinder; however, inward interaction events emerged from streamwise deceleration in conjunction with a downward flux of SRNS in both the gap flow and the inner-layer wall-wake flow. In the wake flow, there was a notable negative peak in pressure energy diffusion along with strong turbulence kinetic energy (TKE) dissipation and diffusion. The TKE budget in the gap flow, on the other hand, showed a little negative peak in TKE diffusion and a moderate positive peak in pressure energy diffusion.

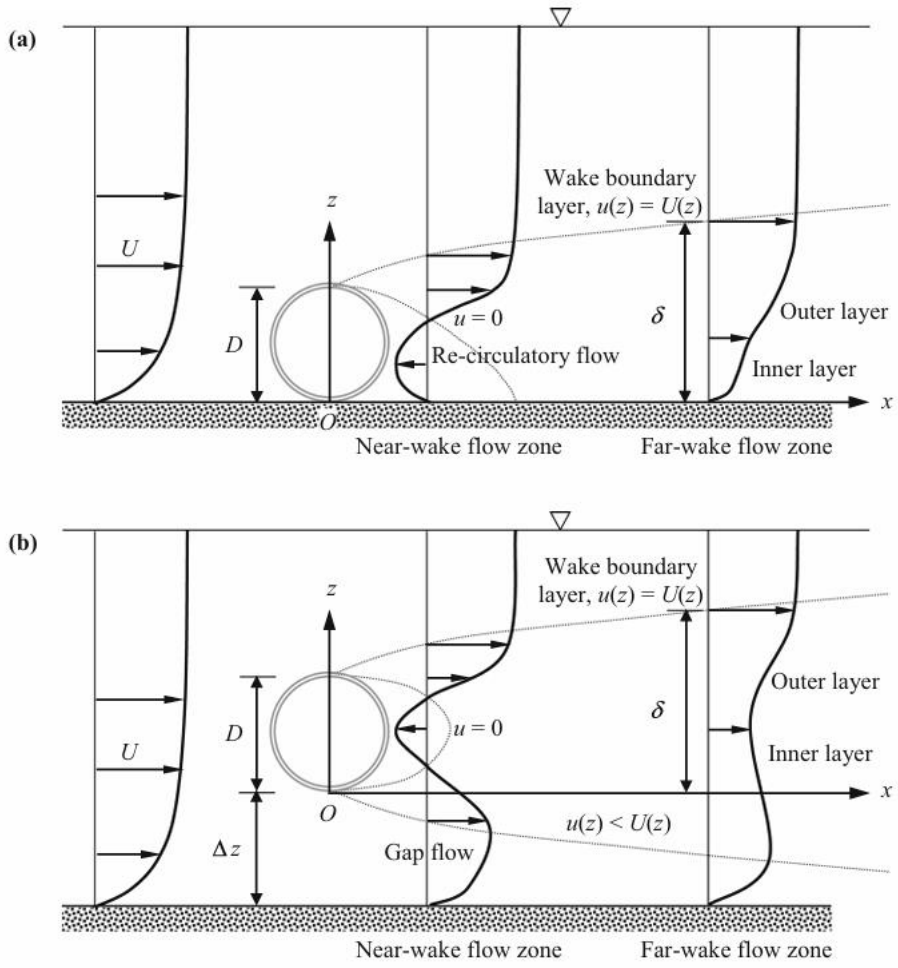

Figure 2.4: Wall-wake flows behind a near-wall and wall-mounted cylinder by Dey et al. (2018)

2.3 Turbulence stress and dissipation anisotropy

Due to tremendous number of fluctuations occurring in a turbulent flow, it is assumed that the flow is having an isotropic turbulence to reduce the modelling complexity. Isotropic turbulence is an idealized turbulent state in which the turbulent fluctuations are considered to be statistically equivalent in all directions. Therefore, the velocity fluctuations are unrestricted with the axis being taken or unchanged with respect to translation and rotation of coordinate system; which concludes the Reynolds normal stresses are equivalent i.e., mathematically, $\overline{u'u'} = \overline{v'v'} = \overline{w'w'}$; where u', v' and w' represent its usual meaning. But in experimental point of view, every turbulence is anisotropic in nature i.e., the fluctuations of the velocity components show directional preference, which also means the Reynolds normal stresses are

unequal. Hence, there is a window of opportunity to analyse the behaviour of turbulence anisotropy in open channel and how far or close the anisotropy stands in comparison with the isotropic turbulence. There are several ways of describing anisotropy in turbulence.

Reynolds shear stress anisotropy tensor is the best tool to examine the degree and nature of turbulence anisotropy introduced by Antonia et al. (1994). The primary gain of the anisotropy tensor analysis is that there is no requirement of any additional component to make non-dimensional and at the same time it enlightens with a complete illustration of the turbulent flow characteristics. Depending on the directions obtained from tensor coordinate systems, the Reynolds shear stress anisotropy tensor a_{ik} can be evaluated based on Rotta (1951) as $a_{ik} = \overline{u_i' u_k'} - \frac{2}{3} q\delta_{ik}$, where q denotes the average TKE (Turbulent Kinetic Energy) ($\overline{u_i' u_i'}/2$) and δ_{ik} denotes the Kronecker delta function, defined as $\delta_{ik} = 0$ if $i \neq k$, or 1 if $i = k$. Furthermore, the stress tensors are normalized by the TKE q as: $b_{ik} = \frac{a_{ik}}{2q} = \overline{u_i' u_k'}/(2q) - (\delta_{ik}/3)$. The b_{ik} is characterized as traceless (i.e., $\Sigma b_{ii} = 0$) and symmetric tensor having values in between $-1/3 \leq b_{ik} \leq 2/3$ and $b_{ik} = 0$ in case of isotropic turbulence. The sign of each diagonal element in b_{ik} represents the effect of the Reynolds shear stress in comparison to the TKE.

On a similar note, dissipation anisotropy tensor can also be implemented regarding the analysis of turbulent anisotropy. The tensor is being defined as follows: $d_{ik} = \varepsilon_{ik}/(2\varepsilon) - (\delta_{ik}/3)$; where $\varepsilon_{ik} = 2\nu\overline{u_{i,j} u_{k,j}}$ ($u_{i,j}$ being the differentiation of u_i with respect to x_k) is the dissipation rate of shear stress and $\varepsilon = \frac{1}{2}(\varepsilon_{11} + \varepsilon_{22} + \varepsilon_{33})$. For isotropic turbulence, all stress and dissipation tensor terms are reduced to zero.

The overall anisotropy of turbulence can be predicted accurately with the help of a cross-plot of two primary independent invariants *II* ($= -b_{ik}b_{ik}/2$ or $-d_{ik}d_{ik}/2$) and *III* ($= b_{ij}b_{jk}b_{ki}/3$ or $d_{ij}d_{jk}d_{ki}/3$); while the first invariant is considered to be zero ($I = b_{ii}$ or $d_{ii} = 0$). The plot of $-II$ versus *III* is defined as Anisotropic invariant map (AIM), in which $-II$ (positive or zero) signifies the scale of anisotropy and *III* signifies the nature of anisotropy. The following curve equations illustrate the potential turbulence states that predominate within the left- and right-curved borders in terms of *II* and *III* : $III = \pm 2(-II/3)^{3/2}$, arising from the bottom cusp i.e., origin ($-II = III = 0$), which is called the Lumley triangle. Following an axisymmetric contraction, the energy ellipsoid of homogeneous turbulence causes a pancake-shaped turbulence, which is explained

by the left-curved boundary. An axisymmetric contraction creates a rod-like form by extending the turbulence eddies axially. However, after undergoing axisymmetric expansion, the energy ellipsoid of turbulence results in a cigar-shaped turbulence structure, which is reflected in the right-curved boundary since one component of the turbulence kinetic energy (TKE) is prominent over the remaining two.

Whereas the 2D isotropic condition at the left vertex of the Lumley triangle is called two-component 2D turbulence, the 1D state of turbulence at the right vertex is called one-component 2D turbulence. In order to move from homogeneous anisotropic turbulence to 3D isotropic turbulence, the ordinate along the direction of the bottom cusp is used ($-II = III = 0$).

Lumley and Newman (1977) were the first researchers to structuralize turbulence anisotropy with the stress tensor terms and anisotropy invariant maps. They pointed out that the one way to address the return to isotropy of homogeneous turbulence in the deficiency of average velocity gradients is to treat changes as being slowly related to turbulence time scales. The problem might be reformulated as determining the shape of three invariant functions based on this one solitary assumption. The thorough examination of limiting behaviour for both small Reynolds number and arbitrary anisotropy and huge Reynolds number and small anisotropy limits the shape of the functions. Requiring non-negative energy, realizability criteria reduce the problem to two functions that are further restricted. It is demonstrated that predictions made using this interpolation form for the functions have great agreement with all available data and that it is a convenient form that satisfies all the requirements.

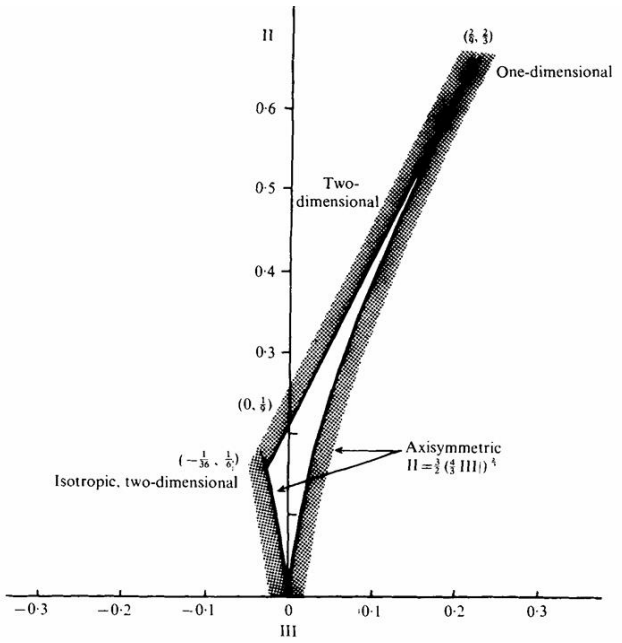

Figure 2.5: Plot of Anisotropic Invariant Map (AIM) for turbulence according to Lumley and Newman (1977)

Anisotropy-invariant maps are introduced in the literature to define a domain where all realizable Reynolds stress invariants must lie. As the anisotropy invariants (*II*, *III*) are nonlinear responses to stressors, it has been shown that the Lumley and Newman framework has limitations. The anisotropy invariants were proposed to have a linear form in terms of eigenvalues by Banerjee et al. (2007). An illustration of anisotropy in turbulent quantities that is visually undistorted is called a barycentric map. It offers a more lucid understanding of anisotropy in turbulence and is founded entirely on the convex combination of the eigenvalues of scalar metrics.

This barycentric map may be utilized to illustrate the normalized Reynolds stress and the anisotropic stress tensor. Additionally, the weighting of every point within the barycentric map may be specified in terms of the one-, two-, or three-component limiting states. They use the spectrum decomposition theorem for second-order tensors to construct the theoretical foundation of the barycentric map. This shows analytically that all turbulence occurs inside or near the boundaries of the barycentric map. It is demonstrated that the barycentric map and the

anisotropy invariant map are exclusively one-to-one dependant in terms of (*II*, *III*), fulfilling the relatability requirements.

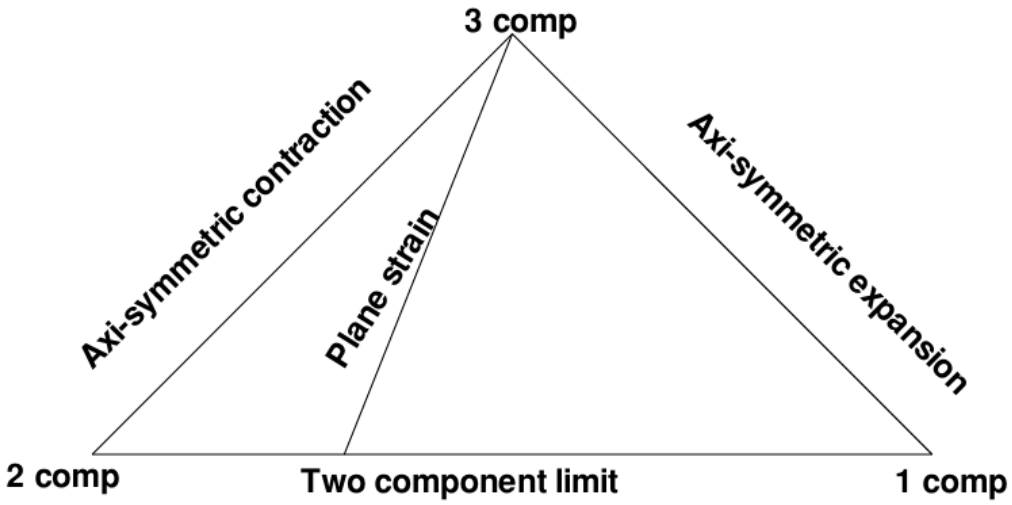

Figure 2.6: A barycentric map, derived from convex combinations, describing nature of turbulence by Banerjee et al. 2007

The characteristics of flow turbulence anisotropy study on two-dimensional stiff dunes are examined by Dey et al. (2020). When looking at the ellipsoid stress form, anisotropy in Reynolds stress is anticipated. The study investigates the spatial changes in various factors, including the eccentricities of the stress ellipsoid, the eigenvalues of the normalized Reynolds stress tensor, the anisotropic invariant map (AIM), and the anisotropic invariant function, across different streamwise positions along the vertical direction. The findings show that oblate spheroid axisymmetric turbulence predominates at the top of the crest, but prolate spheroid axisymmetric turbulence occurs more frequently close to the free surface. As the vertical distance from the crest grows, the contraction to an oblate spheroid axisymmetric condition at the foot of the dune becomes weaker. Up to the edge of the boundary layer, the turbulence anisotropy exhibits a looping pattern, as seen by the AIMs. Additionally, when the streamwise distance grows, anisotropy of turbulence at the boundary layer's edge hits the plane-strain limit up to two-thirds of the stoss-side. Beyond the crest's peak, it crosses this limit and moves towards the direction of oblate spheroid axisymmetric turbulence.

Longo et al. (2017) have examined the dissipation tensors and the Reynolds stress anisotropy using a distinct dataset of wave-breaking measurements. The invariants quantify the anisotropy, which is quite high throughout all phases and especially pronounced for the strongest breakers. During slight energy breakdowns, the dissipation tensor's anisotropy is less noticeable than that of the Reynolds stress tensor. In high-energy breakers, although the dissipation tensor retains some level of isotropy, the Reynolds stress tensor becomes more skewed towards anisotropy. For low energy breakers, the two tensors' primary components have a straightforward proportionality relationship. This implies that some of the traditional turbulence models remain relevant. The link appears to be significantly more complicated for high energy breakers, and no straightforward model can be proposed. These experimental data are not widely available, so a thorough analysis using the similar methodology with DNS obtained data has been made possible. It is anticipated that the dissipation tensor would be impacted by the data's restricted spatial resolution, and that the limited time resolution will have an impact on both tensors. Therefore, it is important to consider these constraints when assessing the reported results.

2.4 Bursting Events and Coherent Structure

2.4.1 Bursting Process

Research conducted in the 1960s and 1970s by Kline et al. (1967), Corino and Brodkey (1969), and Grass (1971) showed that the flow in a turbulent boundary layer near the wall is recurrent and takes the shape of a quasi-cyclic process known as the bursting cycle. The flow alternates between low-speed and high-speed sections close to the bed. They are also known as high- and low-speed streaks, even though there may not be much of a velocity difference between them. Both the high- and low-speed streaks originate locally and momentarily. A limited and transient unfavorable pressure gradient can cause a low-speed fluid streak to separate, much like a boundary layer that is negatively impacted by a pressure gradient. This results in the coherent, low-speed fluid entering the flow's main body. We refer to this as the ejection event. In a procedure known as the sweep, high-speed fluid approaches the bed and brushes away the expelled fluid that remains due to retardation. The descending flow creates a thin, extremely turbulent shear layer with several small-scale vortex during sweep. A quadrant analysis can be used to explain the bursting process. The bursting period is the amount of time between the

production of one low-speed streak and the formation of the subsequent one. An identical sequence of events takes place following the production of this new low-speed streak, and the process repeats itself.

It is possible to determine the mean occurrence periods for sweep events and ejection events by counting how often they happened within a specific time frame. One can determine the frequency of ejection or sweep events in a recorded sample by fixing a hole-size H and counting the number of times the sequence of (u', w') changes in the relevant quadrant. The frequency of sweep and ejection is given by the reciprocal of the time period.

2.4.2 Quadrant Analysis

The quadrant analysis developed by Willmarth and Lu (1972) is an insightful method for characterizing turbulent events that take place in the boundary layer. Depending on the sign convention of the streamwise and vertical velocity variations u' and w', the local flow behaviour is separated into quadrants in the quadrant analysis. Four quadrants are characterized as:

(i) Q_1, first-quadrant $(u'w')_1$, where $u'>0$ and $w'>0$, indicating a situation when a rapid fluid approaches the fluid flow field's center;

(ii) Q_2, second-quadrant $(u'w')_2$, where $u'<0$ and $w'>0$, signifying a situation when a low-speed streak of fluid travels away from the bed and into the center of the fluid field (ejection);

(iii) Q_3, second-quadrant $(u'w')_3$, where $u'<0$ and $w'<0$, signifying a situation when a low-speed fluid approaches the bed; and

(iv) Q_4, second-quadrant $(u'w')_4$, where $u'>0$ and $w'<0$, signifying a situation when a low-speed streak of fluid flows towards the bed (sweep).

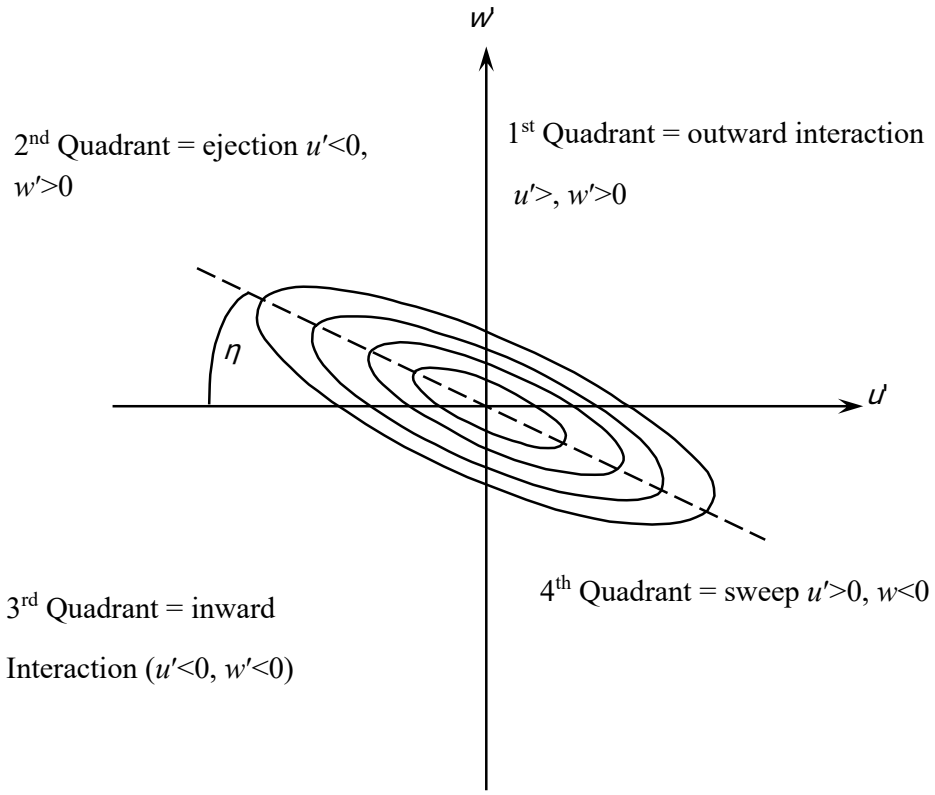

Figure 2.6: Joint probability function of the location of the velocity fluctuation vector in the (u', w') plane.

In an open channel flow, the most important events are obtained from the second and fourth quadrant. Sweep is the most important mechanism event near the wall, whereas ejection dominates at a distance from the wall. The primary causes of Reynolds stress are ejection and sweep events, which are also an expression of the dynamic processes of turbulent structure growth.

Kline et al. (1967) were among the first to examine the turbulent boundary layer's flow structure. Through the use of the hydrogen bubble imaging approach, they demonstrated that the flow arranges itself in alternating unstable arrays of high and low-speed zones, and that the near-bed zone of the flow has an incredibly intricate structure. According to the mean streamwise velocity, the fluid really moves laterally from regions of instantaneous high speed ($+u'$) to regions of low speed ($-u'$). Through a slow sequence of outflow, lift up, abrupt oscillation, and disintegration, the boundary layer's streaky structure interacts with the outer layer of the turbulent flow.

The structural properties of turbulent flow across uneven and smooth beds were investigated by Grass (1971). He discovered two distinct intermittent characteristics of the flow structure at the boundary, known as sweep and ejection, for both smooth and rough beds. Additionally, conditional averaging showed that ejection and sweep both correlate with a very high Reynolds stress contribution, which generates the most turbulence near the boundary.

Lu and Willmarth (1973) deduced from the experimental data that a burst happens when the streamwise velocity at the viscous sub-layer's edge reduces to a low level. Conversely, sweep happens when streamwise velocity increases significantly. The turbulent boundary layer's total Reynolds shear stress production is mostly caused by ejection, with sweep coming in second. Additionally, they determined the typical mean time intervals for sweep and ejection. For the majority of the flow, the mean duration of the two occurrences was about equal and consistent.

Raupach (1981) investigated turbulent formations with a zero pressure gradient across both smooth and rough surfaces. The quadrant analysis's findings indicate that sweep is mostly accountable for the stress close to rough surfaces, and that both surface roughness and closeness to the surface increase its relative size. Regarding surface roughness, the flow in the residue section of the inner and outer layer complies well with the well-known similarity laws. The third-order moments of the normal and streamwise velocity changes are consistently correlated with the distinction between sweep and ejection.

The impact of surface roughness on higher-order velocity moments in wall-wake flow with significant bottom roughness was investigated by Balachandar and Bhuiyan (2007). The flow over two different kinds of rough beds was investigated, and the outcomes were contrasted with those over an open, smooth channel. Higher-order moments of velocity variations, quadrant-based conditional statistics, and TKE generation were also analyzed. It was discovered that the wall condition had a considerable impact on third-order moments over the flow depth. The comparison between rough and smooth beds demonstrated that the influence of bed roughness was not confined solely in the region next to the bed. It is also suggested from the researchers that higher moments could provide an accurate comprehension of the coherent structures of the flow.

The conditional turbulence and dispersion characteristics in the flow across a sequence of dunes were investigated by Dey et al. (2020) using a spatial averaging technique. This was done by analyzing data from various locations at different vertical levels. By superimposing vorticity contours on the velocity vector map, the flow characteristics—such as boundary layer diffusion, wake interference, flow separation, and reattachment—were made visible. The study focused on spatially averaged (SA) streamwise velocity, Reynolds stresses, TKE fluxes, and dispersive kinetic energy (DKE) fluxes, with attention to their vertical profiles. The analysis showed that above the dune crest, temporal ejection events were more associated with dominant SA Reynolds stresses and TKE fluxes, whereas temporal sweep events were linked to the governing mechanism below the crest. Dispersive normal stresses and DKE fluxes revealed that dispersive outward interaction events prevailed near the dune trough, while ejection events were the primary dispersal mechanism in the upper part of the roughness sublayer. Furthermore, in comparison with temporal sweep events, temporal ejection events were shown to be less common but more resilient. The results also suggested that flow below the crest was more turbulent, as indicated by the higher frequency of temporal bursting events compared to above the crest.

2.5 Machine learning predictions in hydrodynamics and thermal science

Machine learning (ML), a branch of artificial intelligence (AI), is based on developing statistical models and methods that enable computers to perform tasks without needing direct programming. The key principle behind ML is allowing computers can acquire information from data and produce predictions or assessments based on this acquired knowledge. ML techniques have shown great potential in various fields, including hydrology and thermal science. Some common applications of ML in these domains are outlined below:

- Flow Rate Prediction: ML models can be trained to predict the flow rate of water in an open channel given inputs such as channel geometry, upstream flow conditions, and other relevant parameters. Regression algorithms like linear regression, decision trees, random forests, and neural networks can be employed for this purpose.
- Flood Prediction: ML algorithms can analyze historical data on rainfall, river discharge, soil moisture, topography, and other factors to predict the likelihood and severity of

flooding events in open channels. Classification algorithms like decision trees, random forests, and support vector machines can be utilized for flood prediction.

- Sediment Transport Prediction: ML models can be trained to predict sediment transport rates in open channels, which is crucial for understanding erosion and sedimentation processes. Features such as flow velocity, sediment size distribution, and channel characteristics can be used as inputs to these models.
- Channel Morphology Prediction: Machine learning can assist in predicting changes in channel morphology over time due to factors such as erosion, sedimentation, and human activities. Models can be trained using historical data on channel geometry, flow characteristics, sediment transport rates, and environmental variables.
- Water Quality Prediction: ML techniques can be applied to predict water quality parameters such as pollutant concentrations, dissolved oxygen levels, and nutrient concentrations in open channels. Models can be trained using water quality monitoring data along with meteorological and hydrological data.
- Designing Heat Exchangers Using Machine Learning: By forecasting temperature distributions, pressure dips, and heat transfer coefficients, machine learning improves heat exchanger performance. Complex, nonlinear interactions between design factors and performance measures are captured by models developed on simulation or experimental data. Rapid design iterations are made possible by surrogate models, which take the place of expensive CFD simulations. By reducing pressure drops, multi-objective optimization with machine learning strikes a compromise between energy consumption and heat transfer efficiency.
- Machine Learning for Thermal Management: By anticipating patterns of heat loss and dynamically controlling cooling, ML improves thermal management in electronics, batteries, and cooling systems. In order to predict overheating hazards and make real-time adjustments to cooling systems, models analyze sensor data, such as temperature, voltage, and workload. ML keeps batteries from experiencing thermal runaway during cycles of charging and discharging, and it keeps devices operating steadily under a range of loads. Predictive algorithms and reinforcement learning optimize cooling

system settings, increasing operational dependability and energy efficiency, particularly in industrial systems.

The research by Cheng et al. (2008) aimed to explore the use of artificial neural networks (ANNs) for simulating turbulence intensity profiles and mean velocity in open channel flows over a smooth boundary. To evaluate turbulent flow conditions, the study utilized a fiber-optic laser Doppler velocimeter (FLDV) in a laboratory flume. Across several locations with differing slopes and aspect ratios, 1,644 data sets in total were gathered. These datasets were split into validation and training sets at random. The simulation model was built using the training data and the multi-layer functional link network (MFLN). The MFLN models developed for this study were able to accurately simulate both the turbulence intensity and velocity profiles, with nearly perfect results. The root mean square error (RMSE) and coefficient of determination (r) values for the models were close to one in all cases, indicating excellent performance. The outcomes show that, in comparison to the log law as well as Reynolds stress model (RSM), which are less successful in simulating velocity profiles along the side wall, the MFLN can accurately recreate the velocity profiles. Whereas the obtained normal turbulence intensities produced by the stress model were inconsistent with the experimental findings, the spanwise turbulence intensities produced by the MFLN were likewise reasonably in agreement with the data.

Reynolds-averaged Navier-Stokes (RANS) equations are in present one of the most widely utilized turbulence simulation models. Anisotropic Reynolds stress tensor modeling is necessary for building RANS simulation, however conventional Reynolds stress closure models only produce somewhat trustworthy predictions. Data-based models of turbulence that utilize advanced machine learning techniques for predicting the Reynolds anisotropy tensor have gained noteworthy attention and developed rapidly in recent years. In their study, Fang et al. (2020) propose three modifications to a conventional neural network to address the Reynolds number dependency, spatial non-locality, and the no-slip boundary condition of the anisotropy tensor. These modifications are specifically aimed at improving the simulation of the Reynolds stress closure for turbulent channel flow. The results demonstrate that the enhanced models provide better prediction accuracy in comparison to the traditional neural network during training and testing on experimental data at various Reynolds numbers. The

most effective model integrates the enforcement of boundary conditions with the injection of Reynolds numbers, yielding superior performance over the Tensor Basis Neutral Network (TBNN) on the turbulent channel flow dataset.

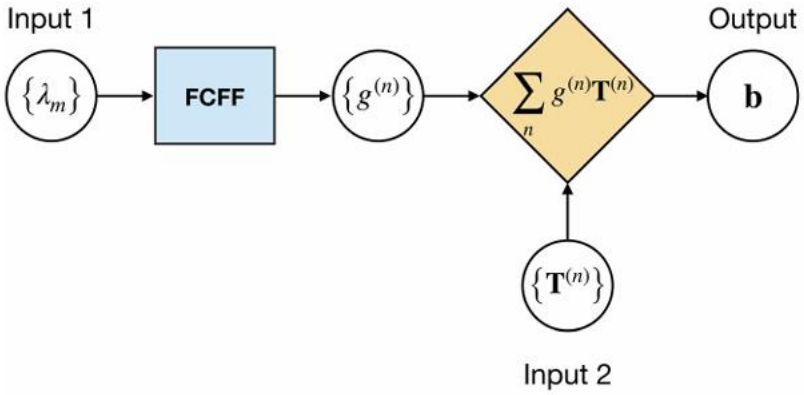

Figure 2.7: Schematic diagram of the TBNN from Fang et al. (2020)

In their study, Morita et al. (2022) address several CFD problems using Bayesian optimization (BO), which leverages Gaussian process regression (GPR), offering practical benefits for a range of applications. The first three problems tackled include structure refinement of a channel flow wall, structure refinement of a lid-driven cavity aimed at optimizing energy dissipation, and the process of refining a spoiler-ice model's regulating parameters in order to get the intended distribution of pressure gradients throughout the turbulent boundary layer that forms on the opposite wall. The adaptability, effectiveness and adaptability of the BO-GPR technique in CFD simulations are highlighted by its broad applicability to various optimization problems, independence from adjoint information, simplicity of including many CFD solvers into the refinement process, and, notably, the comparatively lesser number of essential flow simulations. It is demonstrated that fewer than ninety-nine CFD solver runs are required to guarantee the discovery of the global optimum of the design specifications for sizes up to eight. Moreover, it is noted that the number of design parameters has no discernible effect on the number of flow simulations. For many optimization instances with practical importance, the related computational cost of these simulations can be reasonable.

The phenomena of mixed convective flow over radiantly cooled planes with displacement ventilation in residential settings is gaining popularity because of energy economy and airborne viruses. One machine learning technique that is frequently assessed as an engineering tool is artificial neural networks. A machine learning technique was used in the work by Acikgoz et al. (2022) to forecast the heat transport rates for a wall cooling feature combined with forced and mixed convective flow. This method should be regarded as the first experimental study that examines mixed convection systems in actual live settings in conjunction with an analysis of artificial neural networks in open sources. A multi-layer perceptron network topology for feed forward back propagation has been developed using experimentally observed heat transfer coefficients. Two distinct neural network architectures were developed with varying input parameters, including temperature, velocity, and heat transfer rates, to assess how these input components affect the model's prediction performance. Radiation, convection, and total heat transfer coefficients were estimated using multi-layer perceptron (MLP) neural network methods, leveraging an experimentally obtained dataset for training and validation, which includes 35 data points from the forced and mixed convection circumstances. 70%, 15%, and 15% of the dataset are included in the training, validation, and test data groups, respectively. A Levenberg-Marquardt method was used to compute the training algorithm. The results of the computational solution have been assessed based on the comparison with the target data for all heat transfer coefficients within the ±5% deviation zone. The estimate precision of the numerical models has been carefully investigated, and the performance factors have been calculated.

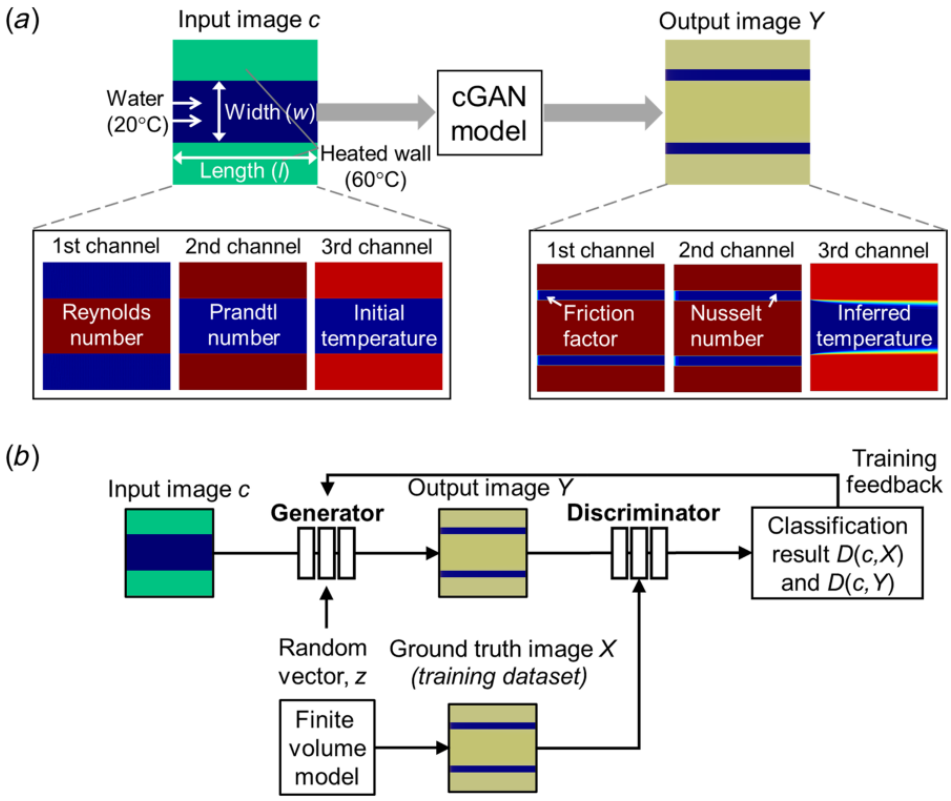

Figure 2.8: (a) Workflow of input-output images and (b) conditional generative adversarial networks architecture by Kang et al. (2022)

Kang et al. (2022) introduced a deep learning framework in case of forced convection heat transfer in internal flows. The model uses graphical inputs representing the geometry of the flow channel and initial flow conditions to train conditional generative adversarial networks (cGANs) to estimate the solution. With this trained cGAN, Nusselt number (*Nu*), flow temperature, and friction factor (*f*) in a heated channel can be quickly predicted throughout an assortment of Reynolds numbers, from 100 to 27,750, without solving the physical governing equations directly. The authors optimized parameters such as size of dataset, number of epochs trained, and a hyperparameter (λ) to improve training efficiency. The cGAN model achieved up to 97.6% accuracy in estimating local *Nu* and *f* distributions. Furthermore, they showed that if

the training dataset was expanded appropriately, the model could also predict solutions for previously unseen flow channel configurations, including constricted, expanded, and rotated channels. A simple data augmentation method enhanced the model's accuracy by 70%. This research highlights how deep learning methods can be utilized to produce accurate and efficient thermofluidic process predictions.

Chapter 3

Experimental Setup and Procedure

3.1 General

All the experiments were carried out at the Fluvial Mechanics Laboratory of the Indian Statistical Institute, Kolkata, India. This chapter presents the details of the experimental setup, the experimental scheme, the procedure followed, and the methods used for measurements.

3.2 Experimental Setup

Experiments were performed in a rectangular-shaped flume at the Fluvial Mechanics Laboratory. A schematic diagram of the flume is shown in figure 3.1.

The length, width and height of the flume were 20m, 0.5m and 0.5m respectively. An Electromagnetic gadget was used to measure the flow discharge, which was provided by a centrifugal pump. For a length of 8 m, the flume's experimental walls were formed of transparent plastic windows, providing an unobstructed view of sediment motions. Outside the main body of the flume there were two non-clogging centrifugal pumps that supply the flow. By controlling the valves in the outlet and bypass pipes, the flow may be changed to any preferred speed, up to 1.30 m/s for a water depth of 35 cm, attributable to the bypass pipes and valves included in both outlet pipes. The flume bed was fabricated by pasting uniform gravels of size d = 2.49 mm to maintain the streamwise slope 3×10^{-4}. Two cylinders, each of diameter D = 0.038 m, were placed horizontally one above another keeping a uniform distance of 0.038 m i.e., gap between two cylinders measured equal with the diameter of single cylinder. They were placed 7m apart from the flume inlet, where the lower cylinder was mounted on the flume bed as shown in figure 3.1. The incoming flow depth h and depth-averaged incoming flow velocity U_0 were approximately maintained as h = 0.25m and U_0 = 0.44 ms^{-1}. In terms of cylinder diameters, the distance between the free surface and the higher cylinder's top is around 3.58D. A Vernier point gauge was implemented to estimate the flow depth and free surface profile with a precision of

±1 mm. Diameter of the cylinder D was required to make some parameters non-dimensional. The diameter-based Reynolds number Re_D yields the value 16720 upon calculation, assuming kinematic viscosity of water to be 10e-6 m^2/s.

The height-based Reynolds number ($Re = 4U_0h/v$) was taken to be quite high, approximately 440000, and the Froude number ($Fr = U_0/\sqrt{gh}$) was 0.28 demonstrating that the experimental circumstances are subcritical along with the turbulent flow. Two similar experiments have been performed maintaining the same environment as mentioned above with the presence of two cylinders, both of them having diameter D = 0.032 and 0.046 m respectively to generate more experimental evidence.

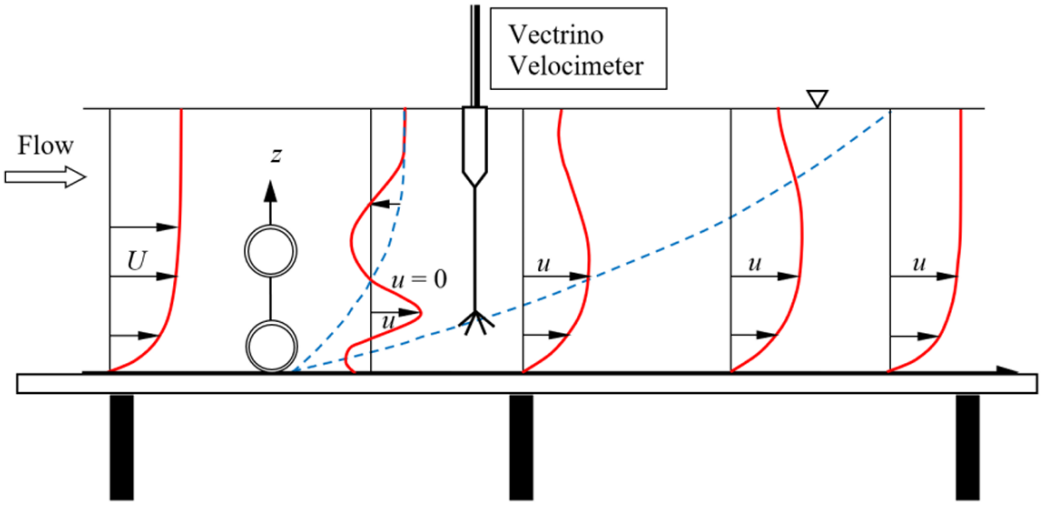

Figure 3.1: Schematic illustration of the experimental configuration.

3.3 Additional Attachments

The instruments were positioned over the flume using an instrument carriage, which was made up of a primary unit and an auxiliary unit. The main carriage unit could move longitudinally along two parallel tracks that crossed the flume. It was possible to place the auxiliary unit across the flume, carrying equipment like the Vectrino and point gauge. This setup facilitated capturing readings from the Vectrino in both vertical and transverse directions at various streamwise distances.

3.4 Method of Measurement

3.4.1 Discharge

Calibrated V-notch weirs at the inflow tank were used to measure the discharges in the flume. A valve installed at the intersection of the input tank and the constant head reservoir controlled the discharge in the flume. The water level was measured with the incorporation of Vernier point gauge having an accuracy of ± 0.1 mm, placed at the inlet tank. The expression for the discharge Q of the flume was

$$Q = 1.139H^{2.346} \tag{3.1a}$$

The height H represents the distance from the sill level of the V-notch to the water surface.

The expression for the discharge Q in flume was

$$Q = 0.9174H^{2.159} \tag{3.1b}$$

In the equations (3.1a) and (3.1b), Q is expressed in m^3/s and H is expressed in m. A secondary method for measuring discharge involved integrating the velocity distribution profiles measured along various vertical lines across the flume, serving as a cross-check.

3.4.2 Bed and Water Surface Levels

A Vernier point gauge, which possessed a precision of ± 0.1 mm, was incorporated to estimate the water's surface and bed levels. The instrument carriage to which the point gauge was mounted was capable of both transverse and streamwise movement.

3.4.3 Measurement techniques and uncertainty estimation

At different streamwise distances, the instantaneous streamwise (u), spanwise (v), and vertical (w) velocity components along the flume centerline were measured using a Nortek Vectrino Plus, a 5-cm down-looking four-beam acoustic Doppler velocimeter. The Vectrino system operated with a 10 MHz acoustic frequency and a 100 Hz sampling rate, offering an adaptable sampling volume of 6 mm in diameter and 1 to 4 mm in height. The data collection has been started just 3mm above the gravel bed to ensure the sampling volume is not affected by the bottom-wall; after this we have slowly increased the sampling height by 2 mm. To get a time-invariant time-average velocity profile, the data have been collected at each point for a duration of 240s. The data collection is being executed in the rectangular section of the flume; hence, our analysis does not include curvature effects.

Before starting the experimental runs, the Vectrino was tested for the uncertainty estimation. To this end, the Vectrino was placed above the rough bed at a streamwise location of x = 10 m from the entrance of the flume. Three-dimensional velocity was captured at a vertical distance of z = 5 cm. Data were collected with 100-Hz sampling frequency at the same location and vertical distance 5 times each of 10 minutes duration. During the data capturing for uncertainty estimation, no changes in the bed or data capturing configurations were changed. The captured data were then analyzed for the uncertainty estimation which showed that the velocity components and rms values of velocity in streamwise, vertical and lateral directions maintained standard deviations below 0.5 cm/s and average maximum percentage error was below 5. However, the Reynolds shear stress parameter showed standard deviations of slightly above 0.5 cm^2/s^2, whereas the average maximum percentage error was just below 5.

Uncertainty Estimation for Vectrino measurements:

U (cm/s)	v (cm/s)	w (cm/s)	$\left(\overline{u'u'}\right)^{0.5}$ (cm/s)	$\left(\overline{v'v'}\right)^{0.5}$ (cm/s)	$\left(\overline{w'w'}\right)^{0.5}$ (cm/s)	$\overline{u'w'}$ (cm^2/s^2)
0.298* (±2.92†)	0.356 (±3.18)	0.231 (±3.26)	0.275 (±2.32)	0.305 (±3.25)	0.211 (±2.18)	0.589 (±4.99)

*Standard deviation.

†Average of maximum (negative and positive) percentage error.

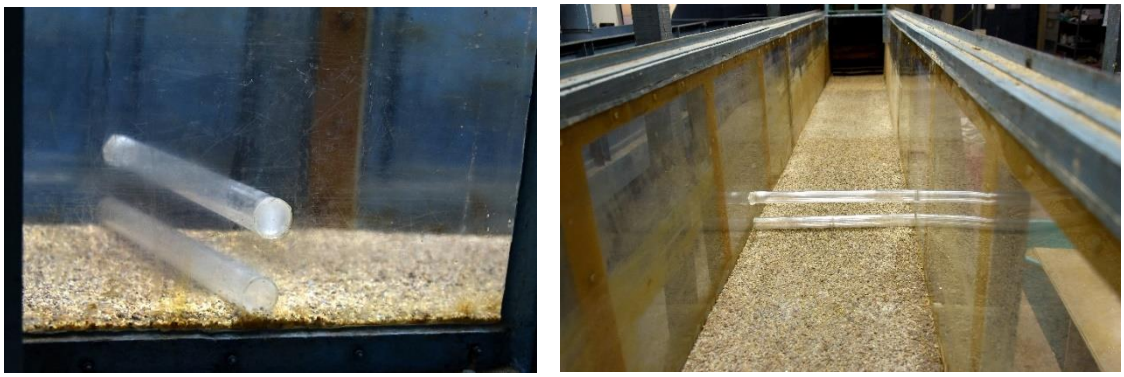

Figure 3.2: Photographs of the experimental setup. Flow direction is from left to right.

Chapter 4

Turbulence in a wall-wake flow downstream of two horizontal cylinders

4.1 Introduction

Wall-wake flow past different shaped bluff bodies is an area of considerable interest because of its numerous possibilities in real-life and industrial applications. Due to the presence of the bluff body in a fluid flow, flow separation occurs, and a disturbed region is observed behind the bluff body, known as wake region. Further, this wake region can be viewed as near-wake and far-wake zones, whose lengths entirely depend on the flow parameters like Reynolds numbers, Froude numbers, etc. and size or shape of the bluff bodies provided. Beyond the far-wake zone, the disturbance occurring by presence of bluff bodies gradually resolves and the initial turbulence characteristics are restored. According to the literature, several works have been performed to observe the turbulence characteristics downstream of a single cylinder mounted on a wall and data were analyzed to study the turbulent characteristics like velocity profile, shear stresses, turbulent kinetic energy (TKE) flux and budget, bursting at the near-wake and far-wake zone. In our experiment we have tried to extend it by taking two horizontal cylinders, one above the other. Both the cylinders have been taken simultaneously in a single experiment which has engineering applications involving a set of tubes in heat exchangers, fuel rods in cylindrical piers, nuclear reactors, and bridge pilings, suspension bridges and gas-oil pipelines. (Zhao et al. (2005), Tong et al. (2015)).

In past decades, numerous experimental investigations have been done regarding flow past the cylinder under certain conditions. Considering a circular cylinder, Angrilli et al. (1982) showed the bottom wall effects on the vortex shedding. When the gap between bottom-wall and cylinder Δz decreased, the velocity characteristic in the downstream region of the cylinder became asymmetric. Miyata et al. (1990) executed an experiment with a cylinder positioned near the free surface and compared it with the numerical results. They observed a drastic decrement in drag coefficient and sudden increase in Strouhal number ($St = FD/U$, F= frequency of vortex shredding, U= flow velocity). However, there was no discussion present for turbulent characteristics which

behave unpredictably in near wake. Fujisawa et al. (2001) carried out an experiment regarding vortex shedding for flow downstream a circular cylinder at Reynolds number Re_D ($=DU/v$, $v=$ kinematic viscosity) = 6700 and 20000. In their study, mean and fluctuating velocities (both streamwise and spanwise), correlation and power spectrum had been analyzed to comprehend the flow field behaviour; some of which have also been presented in our current study. Norberg (2003) experimentally analysed and reviewed the fluctuating lift working on a single cylinder in channel flow. Regarding the evaluation of lift via several methods, 2D as well as 3D simulations were utilized; providing an insight of using simulation in bluff-body hydrodynamics. Reichl et al. (2003) numerically analysed the unsteady behaviour of wake past a circular cylinder at the vicinity of free surface. They used Fluent to analyse numerically the changes in vortex shedding properties and Strouhal number for different gap ratio between the free surface and cylinder. However, there should be a discussion regarding the authenticity and convergence of the numerical method used in the article, namely *volume-of-fluid* (VOF) as the methodology is highly sensitive with the mesh size of domain. In the paper by Kumar et al. (2009), a thorough experimental study was presented regarding the wake development of two side by side circular cylinders downstream with heat release. They basically studied the effects of heat release from one of the cylinders in near wake zone and elaborated unpredictable vortex structures downstream of cylinders, which motivated into studying turbulent phenomena in aforementioned experimental setup. Zhou et al. (2002) analyzed the turbulent wake behaviour past two side-by-side circular cylinder via a closed-circuit wind tunnel experimentation. Their study covered firstly time-averaged streamwise velocity and temperature; followed by phase averaged similar turbulent characteristics and furthermore detailed discussion on vortex patterns in near wake zone. Our discussion only focuses on time-averaged analysis and the result shows a similar trend with their experimental outcomes; motivating to carry out research further into advanced turbulent phenomena.

Xu and Chen (2013) analysed the PIV generated data to estimate turbulence dissipation rate accurately. Firstly, the direct methods involving velocity gradients were used to estimate dissipation rate; furthermore, these were being compared with indirect estimations of TKE dissipation rate from structure functions and energy spectra. The current study also incorporates these methodologies to determine TKE dissipation rate in several locations and compare it with the dissipation rate obtained from numerical modelling.

The flow around two or three circular cylinders with similar diameters placed side by side in shallow water was experimentally studied by Akilli et al. (2004). For different transverse gap ratios, they examined the flow employing the particle image velocimetry (PIV) approach. A Reynolds number of 5000, determined by the diameter of cylinder, was used for the trials, which were conducted in a closed-loop water channel. The study provided flow visualization findings in alongside the PIV measurements. Vorticity, Reynolds stress contours, and instantaneous and time-averaged velocity trends were all produced using the PIV approach. The flow dynamics around two and three circular cylinders of identical diameter *D* placed side by side in a steady crossflow was examined by Sumner et al. (1999). The researchers used visualizations of flows and particle image velocimetry (PIV) to examine center-to-center pitch ratios ranging from 1 to 6 and Reynolds numbers between 500 and 3000. They determined that the two-cylinder structure had three main flow regimes: symmetric flow with synchronized vortex shedding at higher pitch ratios, biased flow combined with synchronized vortex shedding at moderate pitch ratios, and single bluff-body vortex shedding at lower pitch ratios. While the flow visualization via contour plots were the strong findings, the major drawback of the aforesaid article was not focusing on energy cascade or TKE budget which would behave unpredictably due to the variable gap ratio between cylinders. Dey et al. (2018) analysed turbulent characteristics past a wall-mounted and near-wall circular cylinder. They demonstrated velocity, stress behaviour; analyzed third order correlations and TKE budget behind both of the cylinders consecutively; the results of which indicated entirely non-identical profiles (in near wake) in comparison with the outcomes obtained from the vertical-cylinder experimentation. There comes the motivation of working on an experiment in presence of both the horizontal cylinders one above another to explore capricious turbulent behaviour in wall-wake flow as well as utilize it towards validating computational model used to simulate such flow-alike conditions. This investigation aims to deepen the understanding of the intricate interactions between the wall-bounded shear layer and the wake dynamics of one above another cylinders. The experimental results will provide valuable insights into the unsteady flow features and turbulence structures that emerge in such configurations. Furthermore, these findings will serve as a robust benchmark for validating and refining computational models designed to simulate similar flow conditions.

The above literature survey suggests that a lot of experiments have been performed regarding flow past single cylinder, and they have mainly focused on time-averaged velocity and vortex shedding in wake zones. But with two horizontal cylinders there are very limited experimental investigations done by researchers; although there are some numerical simulations available in the literature on similar topics, mostly covering drag and lift coefficients. However, the present problem has also a great significance in understanding different properties of turbulent scaling and energy budget using the structure-functions methodology. For instance, Coscarella et al. (2017) experimented on a tilted flume with an extremely rough bed to investigate the TKE dissipation rate. They basically implemented one of the most insightful theorems available in the turbulence theory, namely Kolmogorov's 4/5th-law to validate the homogeneous properties of turbulence and hence to evaluate TKE dissipation rate ε. Hence, there is a bright scope to understand how flows are being affected in presence of two cylinders i.e., start with basic turbulent characteristics like RSS, intensities to reach up to advanced characteristics like TKE dissipation rate and budget. Thus, the current investigation centers on the experimental perspective on the turbulent wall-wake features downstream of two side by side horizontal cylinders. To provide strong experimental evidence, three different experiments have been performed in the presence of horizontal cylinders having three different diameters. A Vectrino plus probe (ADV) was used along vertical lines to measure instantaneous velocity of the flow. The downstream profiles of velocity, intensity, Reynolds Shear Stress (RSS) are analyzed. Furthermore, several methods have been discussed to evaluate the TKE dissipation rate ε, especially using the concepts of structure functions and spectral analysis. The aforesaid analysis is restricted to time-averaged outcomes.

4.2 Description of the Experiment

An experiment was conducted in a rectangular flume at the Fluvial Mechanics Laboratory of the Indian Statistical Institute in Kolkata, India. The flume had a total length of 20 meters, with a width and height of 0.5 meters each. An Electromagnetic gadget was used to measure the flow discharge, which was provided by a centrifugal pump. The flume bed was fabricated by pasting uniform gravels of size d = 2.49 mm to maintain the streamwise slope $S = 3 \times 10^{-4}$. The incoming flow depth h together with depth-averaged incoming flow velocity U_0 were roughly maintained as h = 0.25m and U_0 = 0.44 ms^{-1} respectively. In terms of cylinder diameters, the distance between the

free surface and the higher cylinder's top is around 3.58*D*. The diameter-based Reynolds number Re_D yields the value 16720 upon calculation, assuming kinematic viscosity of water to be 10e-6 m^2/s. The height-based Reynolds number ($Re = 4U_0h/\nu$) was taken to be quite high, approximately 440000, and the Froude number ($Fr = U_0/\sqrt{gh}$) was 0.28 demonstrating that the experimental circumstances are subcritical along with the turbulent flow. Two similar experiments have been performed maintaining same environment as mentioned above with the presence of two cylinders, both of them having diameter D = 0.032 and 0.046m respectively to generate more experimental evidence.

The velocity power spectral density function $F_{ii}(f)$ are determined with the help of discrete fast Fourier transforms (FFT) (f is the frequency). For reference, the $F_{ii}(f)$ at a vertical distance of z = D and a streamwise distance of $x = 4D$ after the spike removal is illustrated in figure 4.2. The $F_{ii}(f)$-profiles of signals obtained by despiking illustrate a reasonable agreement with the '–5/3 scaling-law' within the inertial subrange for frequency f > 1 Hz. These features show the appropriacy of the Vectrino probe sampling in turbulent open channel flows.

To verify the fully developed flow over the gravel bed, the equation of time-averaged streamwise velocities was used, known as logarithmic law which is given as follows (Dey (2014)):

$$\frac{u}{u_*} = \frac{1}{\kappa}\ln\left(\frac{z}{z_0}\right) \qquad (1)$$

Where u_* denotes the shear velocity, calculated by $u_* = \sqrt{ghS}$ = 0.027 ms^{-1} according to Grams et al. (2006) and $z_0 = k_s/30$ for R_* ($=u_*k_s/\nu$) ≥ 70; k_s being Nikuradse's equivalent roughness valued 0.00249 m. Moreover, κ is the von kármán constant = 0.41. In figure 4.4, nondimensional time-averaged streamwise velocity distribution at x/D = -2 with respect to nondimensional vertical distance (in logarithmic scale) have been plotted and compared with the theoretical result obtained from equation (1), found mostly overlapping.

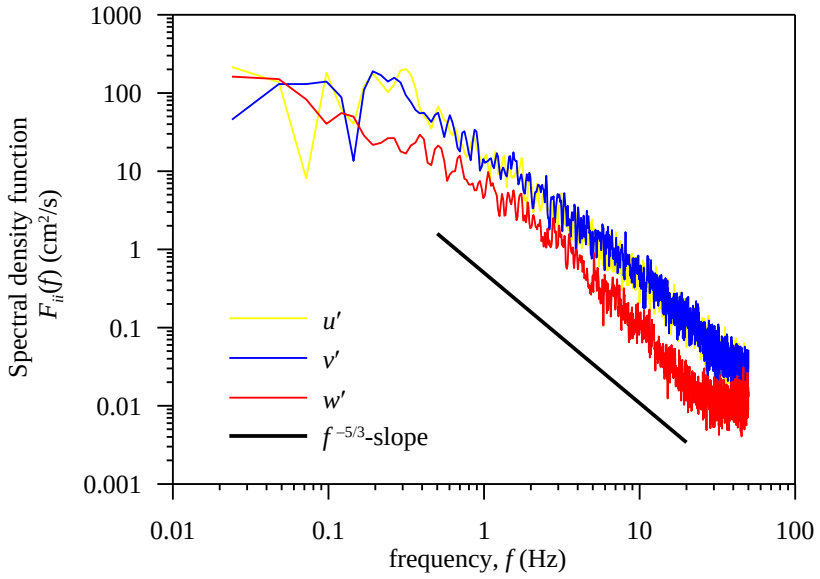

Figure 4.2: Velocity power spectra density function $F_{ii}(f)$ at a vertical distance of $z = D$ and a streamwise distance of $x = 4D$ after the spike removal

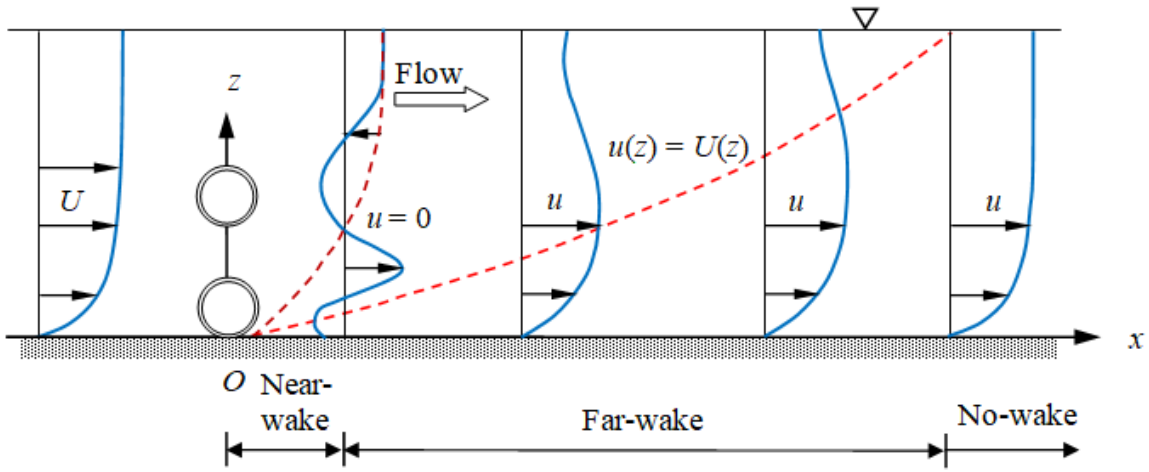

Figure 4.3: Definition sketch for flow past a pair of cylindrical bluff bodies

4.3 Time-averaged Velocity profile

The defining sketch of the wake flow past two adjacent horizontal cylinders is schematically displayed in figure 4.3. The cylinder's walls are separating the incoming flow as it traverses the horizontal cylinders in the immediate downstream, creating a recirculatory bubble with the streamwise velocity in the opposite direction. The term "near-wake flow" describes this flow. Far-wake flow is the term used to describe the flow far behind the cylinders. In this flow zone, the effects of the cylinders on flow get weak and as a result the reversed flow starts disappearing. As the downstream distance increases more, the disturbed flow starts recovering its initial velocity profile. The near-wake zone is defined by a reversed flow velocity that is lower than the incoming velocity at a particular vertical distance because the effects of the reversed flow caused by near-wall cylinders dominate those of viscous diffusion. However, in the far-wake flow, the impacted flow and the development of a near-wall shear layer work together to progressively transform the flow into an approaching, unbroken flow as the downstream distance from both cylinders increases.

Figures 4.5(a-c) show the streamwise velocity distributions at different x/D positions downstream of two cylinders placed one above other with a gap of diameter of a cylinder, both of them having diameter D = 0.038, 0.032 and 0.046 m respectively. Here D represents the diameter of the cylinders, as well as the space between two cylinders. Unfortunately, Vectrino probe is not capable of capturing the reversed flow in near-wake zone, because of its physical limitations. Broken lines are the measured vertical profiles in these figures. Due to recirculation effects occurring downstream of two cylinders, one can observe two sudden dumps in u profiles up to $x/D < 3$. As downstream distance x increases, u distribution slowly recovers its undisturbed initial velocity profile in far-wake region. There is a hint of flow recovery in the graphs; at x/D = 8, u-profile seems to be similar with the initial approach velocity profile, although a full recovery can be seen at a far downstream distance. Due to the occurrence of two severe concavities in u-distribution, four points of inflection ($d^2u/dz^2 = 0$) can be seen in the below figures.

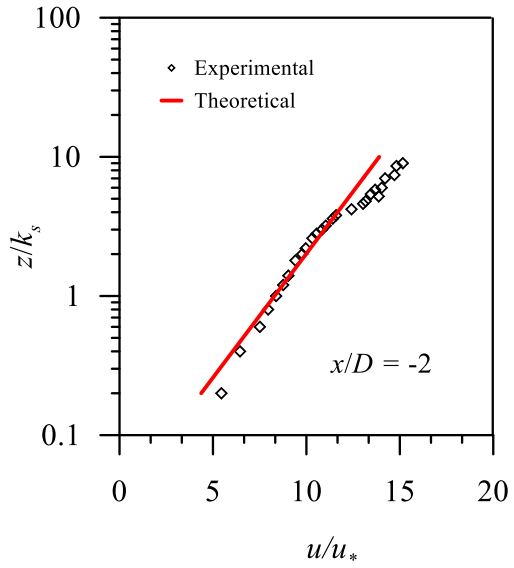

Figure 4.4: Data plot of time-averaged streamwise velocity distributions at x/D = -2 and overlapping on theoretical curve obtained from equation (1).

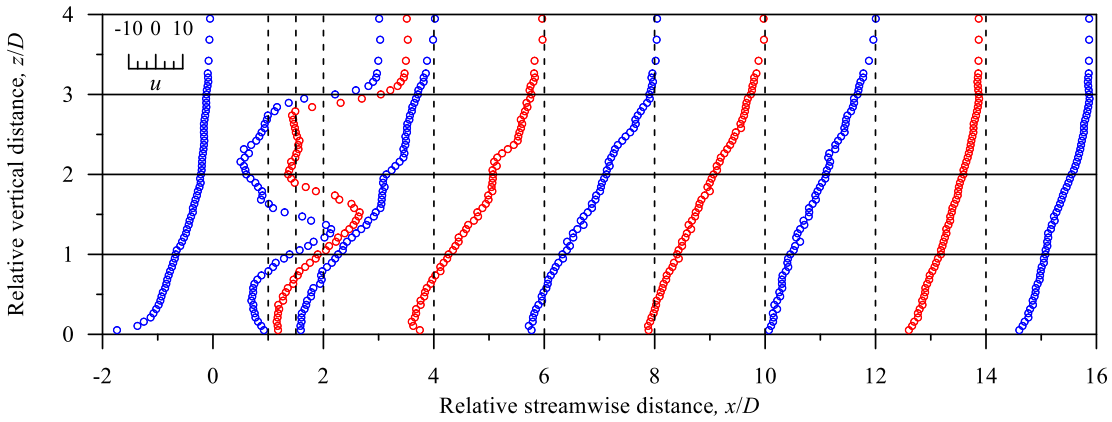

Figure 4.5(a): Streamwise velocity distributions for flow past a pair of cylindrical bluff bodies having diameter D = 0.038 m

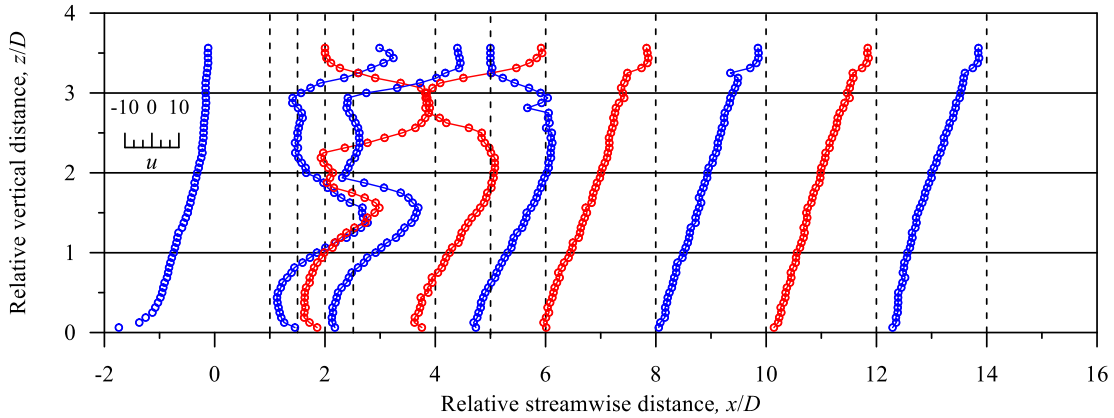

Figure 4.5(b): Streamwise velocity distributions for flow past a pair of cylindrical bluff bodies having diameter D = 0.032 m

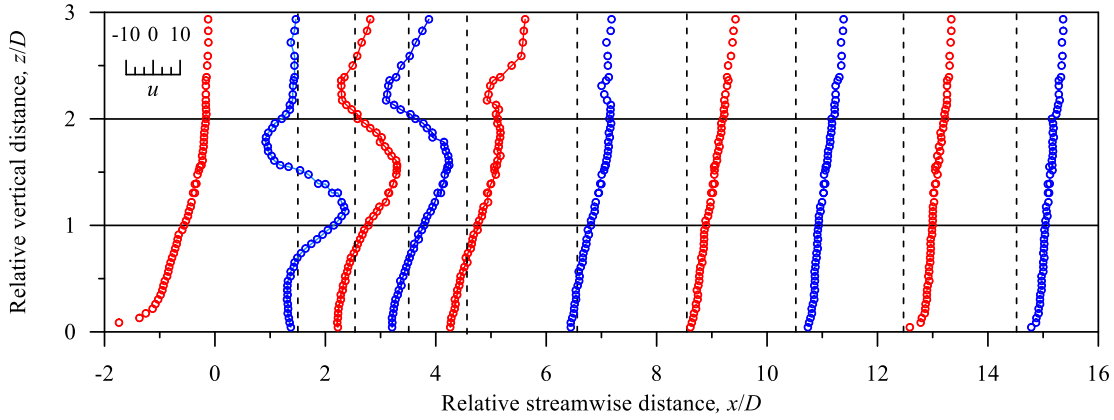

Figure 4.5(c): Streamwise velocity distributions for flow past a pair of cylindrical bluff bodies having diameter D = 0.046 m

4.4 Reynolds Shear Stress

Figures 4.6(a-c) explicate the vertical profiles of Reynolds Shear Stress (RSS) τ for different x/D values, in presence of cylinders with different diameters. Here τ represents RSS relative to density of fluid (ρ) and is defined by $-\overline{u'w'}$; where u' and w' respectively denote the streamlined and vertical variations of velocity components with respect to their time-averaged values (Dey et al.

(2018), Dey (2014)). The following discussion will explain the behavior of τ profile at different vertical and downstream distances irrespective of the diameter of cylinders.

One interesting observation is that RSS varies linearly with vertical distance z in the undisturbed flow region. Conversely, in the downstream proximity of both cylinders, τ begins with a positive value close to the bottom wall and progressively rises as z increases, until it achieves its local maximum at $z/D \approx 1$. At this point the distribution is having a change in its nature; hence, it is a point of inflection for given profile. After that, τ reduces with the increment of z until the curve changes its sign at $z/D \approx 1.6$. Then profile is having a decrement followed by an increment and subsequently a sign change at $z/D \approx 2.2$. Finally in the positive quadrant, it attains its peak value and again faces a point of inflection near $z/D \approx 3$. From then onwards τ-profile decreases with z. One interesting fact is that due to the presence of two horizontal cylinders, we can observe three points of inflection in τ-profile. Also, it can be observed from the profiles that the individual magnitude (absolute value) gradually reduces with an increase in streamwise distance x/D, which directly implies turbulent shear stress influenced by the disturbance in wall-wake flow downstream of both cylinders lessens bit by bit with x. As a result, three peaks (one negative, two positive) start disappearing gradually and at near $x/D = 14$ the τ-profile is having almost linear distribution with respect to z which is nothing but τ-characteristic in the undisturbed flow zone.

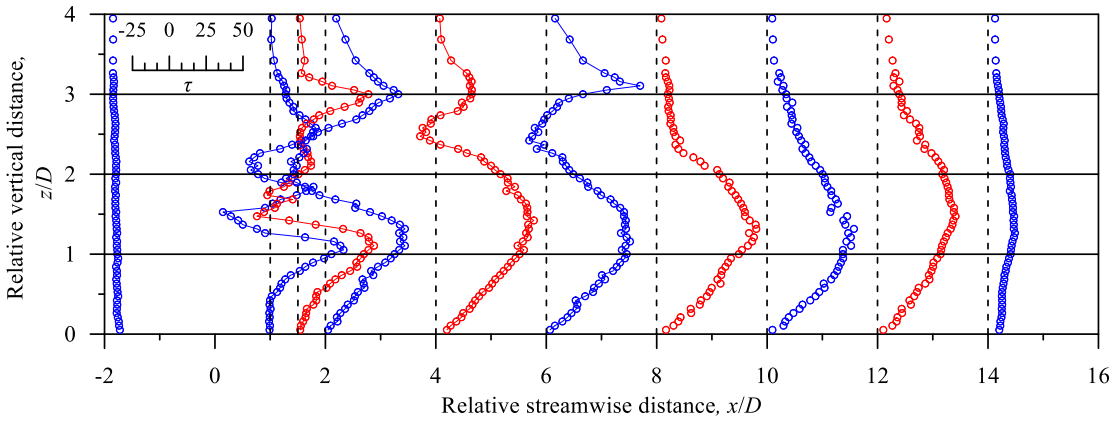

Figure 4.6(a): Reynolds shear stress (RSS) for flow past a pair of cylindrical bluff bodies having diameter $D = 0.038$ m

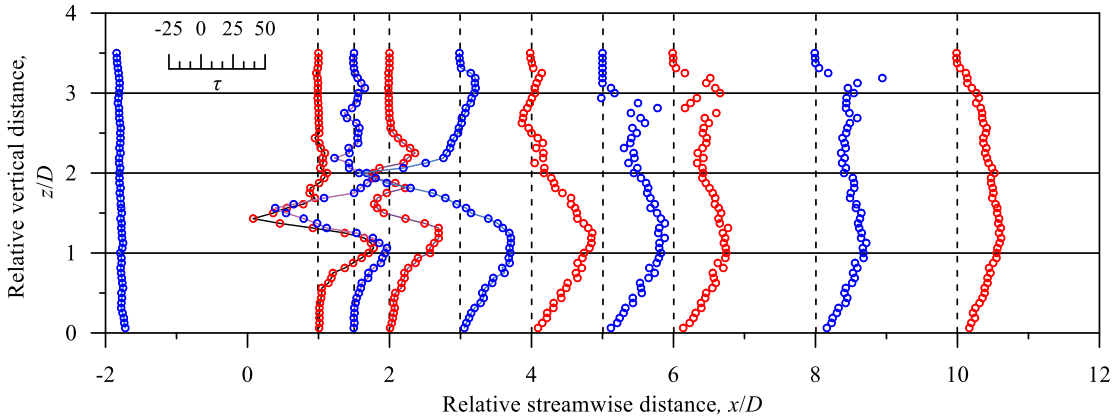

Figure 4.6(b): Reynolds shear stress (RSS) for flow past a pair of cylindrical bluff bodies having diameter D = 0.032 m

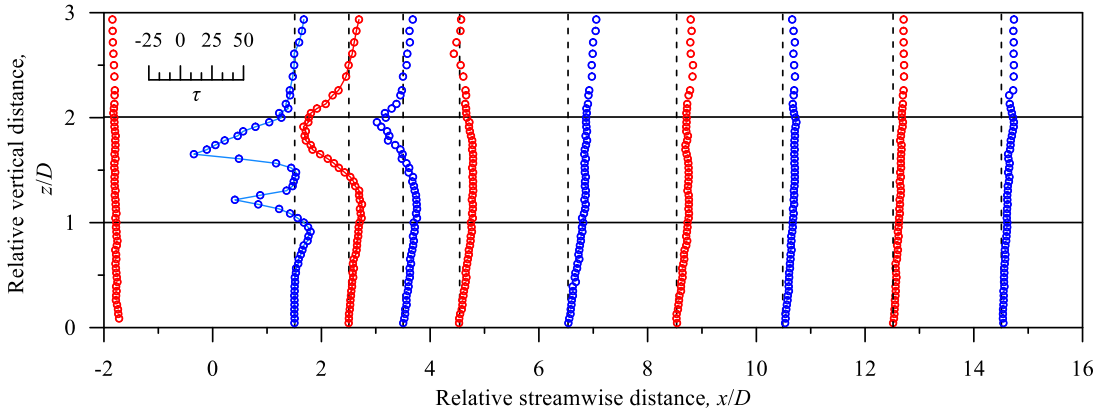

Figure 4.6(c): Reynolds shear stress (RSS) for flow past a pair of cylindrical bluff bodies having diameter D = 0.046 m

4.5 Turbulence Intensities

Turbulence intensity is used to represent the amount of dispersion or scattering of some velocity data sample over a sufficiently long time period. Figures 4.7(a-c) explain the vertical profile of streamwise and turbulent intensities σ_u and σ_w, which are given by the expressions $\sqrt{\overline{u'u'}}$ and $\sqrt{\overline{w'w'}}$, respectively (Dey et al. (2018), Dey (2014)) for cylinders with different diameter. The

following discussion will explain the behavior of intensity profiles at different vertical and downstream distances irrespective of the diameter of cylinders.

From the analysis provided in Dey et al. (2018), it is certain to get a decreasing profile for σ_u and σ_w in the undisturbed upstream region. Moreover, in behind of both the cylinders, the σ_u and σ_w profiles tend to increase with an increase in z till it attains its first peak at about $z/D \approx 1.5$, same as shear stress profiles. Because of having a point of inflection ($d^2u/dz^2 = 0$) at peak, the curve is now diminishing with increase in z. Due to the presence of another cylinder, we now have another point of inflection and profile again starts rising until it reaches to its maximum value at $z/D \approx 2.5$. Afterwards, we observe the usual deteriorating profile. The origination of these profile peaks is caused by the increment in absolute values of turbulence intensities due to the flow mixing process in near-wake zone. Hence, these peaks start to disappear after a drastic increase in x and at about $x/D = 8$, the intensity profiles nearly resemble with uninterrupted upstream distribution. Hence, we can observe a fair amount of similarity between RSS and intensity profiles in both near-wake and far-wake domain, only noticeable difference is due to the fact that intensity is nothing but rms of velocity fluctuations, it always lies on positive quadrant.

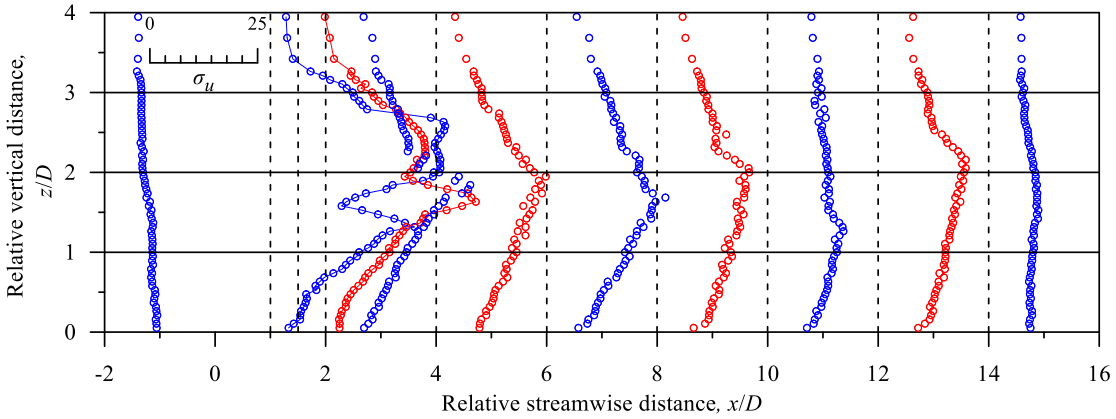

Figure 4.7(a)(i): Streamwise turbulence intensity for flow past a pair of cylindrical bluff bodies having diameter $D = 0.038$ m

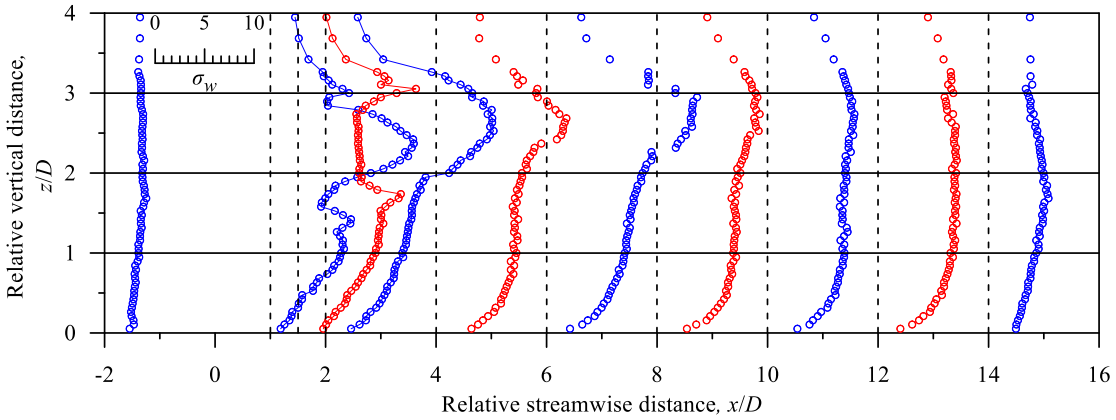

Figure 4.7(a)(ii): Vertical turbulence intensity for flow past a pair of cylindrical bluff bodies having diameter D = 0.038 m

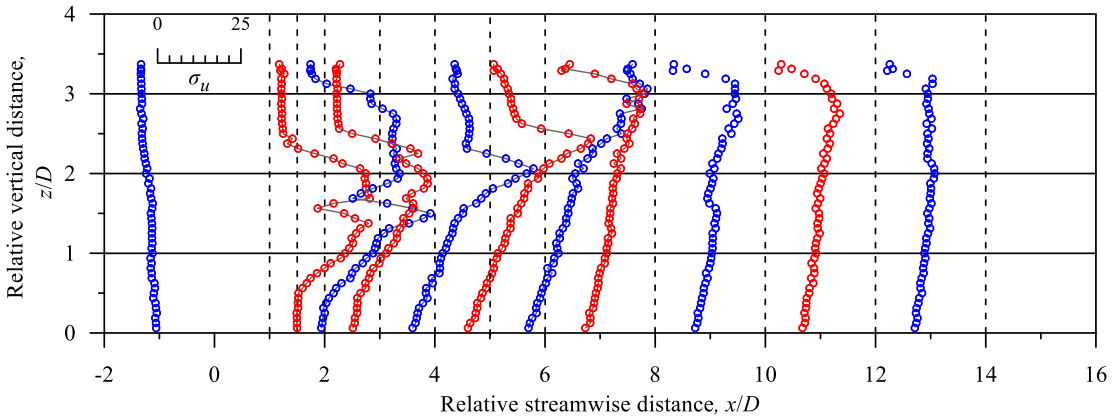

Figure 4.7(b)(i): Streamwise turbulence intensity for flow past a pair of cylindrical bluff bodies having diameter D = 0.032 m

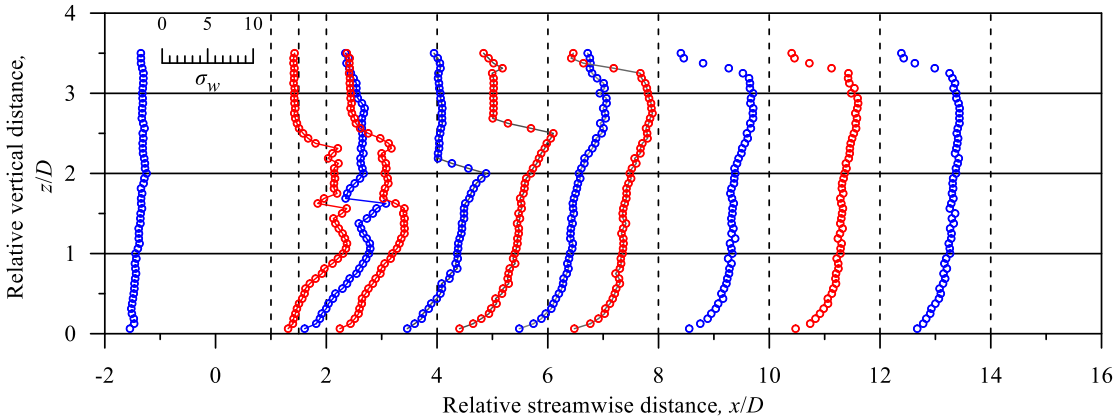

Figure 4.7(b)(ii): Vertical turbulence intensity for flow past a pair of cylindrical bluff bodies having diameter D = 0.032 m

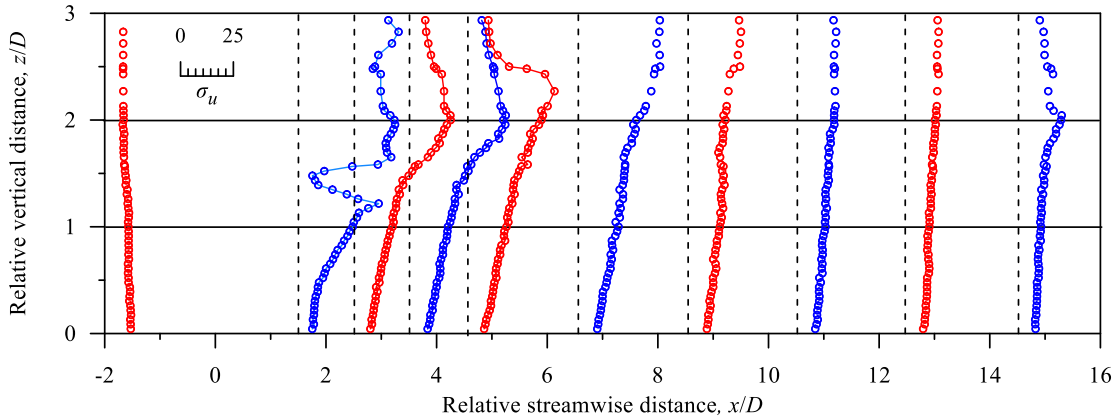

Figure 4.7(c)(i): Streamwise turbulence intensity for flow past a pair of cylindrical bluff bodies having diameter D = 0.046 m

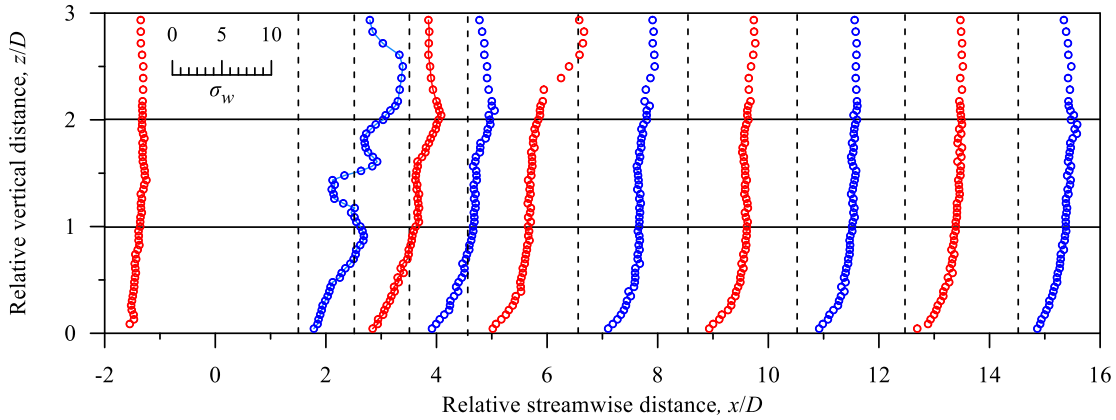

Figure 4.7(c)(ii): Vertical turbulence intensity for flow past a pair of cylindrical bluff bodies having diameter D = 0.046 m

4.6 Turbulent Kinetic Energy dissipation rate and various ways of determination

TKE dissipation rate ε is the rate of energy loss due to the turbulent flow from one position to another. Basically, TKE is being converted into thermal energy. Calculating TKE dissipation rate ε is an essential quantity as it is used as a parameter in many expressions like length scales, budget etc. In subsequent discussion we will try to elaborate some methods to evaluate ε. Afterwards, one comparative study regarding the accuracy of the methods will be presented.

(i) The TKE dissipation rate may be estimated using a variety of techniques, according to the literature.

For example, according to Irwin (1973), Krogstad PA, Antonia RA. (1999), Sarkar and Mazumder (2018), the ε could be estimated from the below equation:

$$\varepsilon = (15\upsilon/u^2)\overline{(\partial u'/\partial t)^2} \qquad (2)$$

where u' is the velocity fluctuation in the streamwise direction and v is the kinematic viscosity of water.

(ii) The ε can also be calculated from the velocity power spectra with the help of Kolmogorov's −5/3 power law formulated on the following mathematical representation:

$$E(k_w) = C_1 \varepsilon^{2/3} k_w^{-5/3} \qquad (3)$$

where $E(k_w)$ denotes one-dimensional energy spectrum, C_1 and k_w respectively indicate the Kolmogorov constant and wave number of the eddies ($2\pi/l$, l = size of the eddies) (Wan et al. (2010), Zhu et al. (2001), Dey et al. (2018), Han et al. (2000), etc.). The numerical value of ε derived from −5/3 power law is influenced by the value of Kolmogorov universal constant C_1 which ranges from 1.5 to 2.

(iii) One of the most accurate methods of determining the value of ε is the utility of structure functions (Sarkar et al. (2021), Sarkar et al. (2022)).

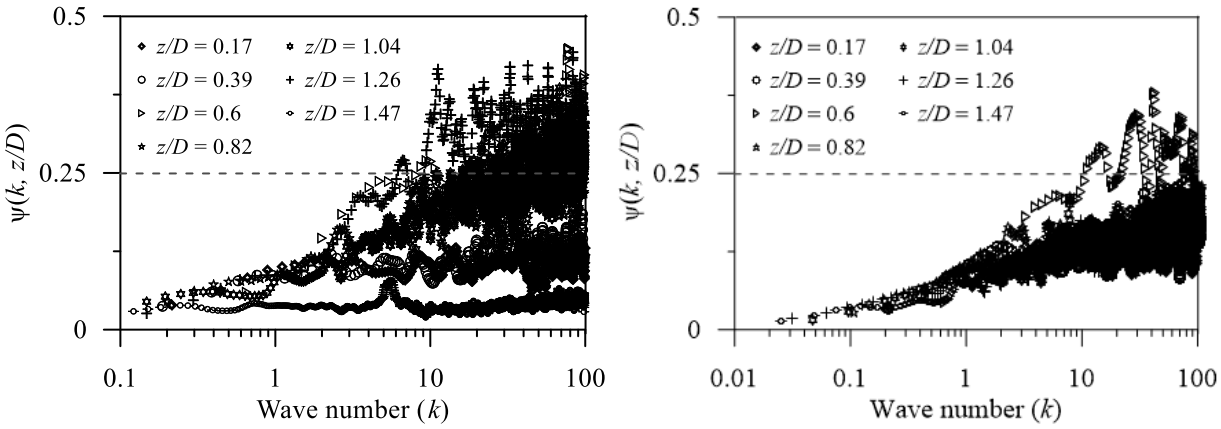

Figure 4.8: Taylor coefficient $\psi(k, z/D)$ as a function of k at normalized vertical distance at $z/D = 0.17, 0.39, 0.6, 0.82, 1.04, 1.26, 1.47$ downstream distances 1.5D and 2.5D respectively.

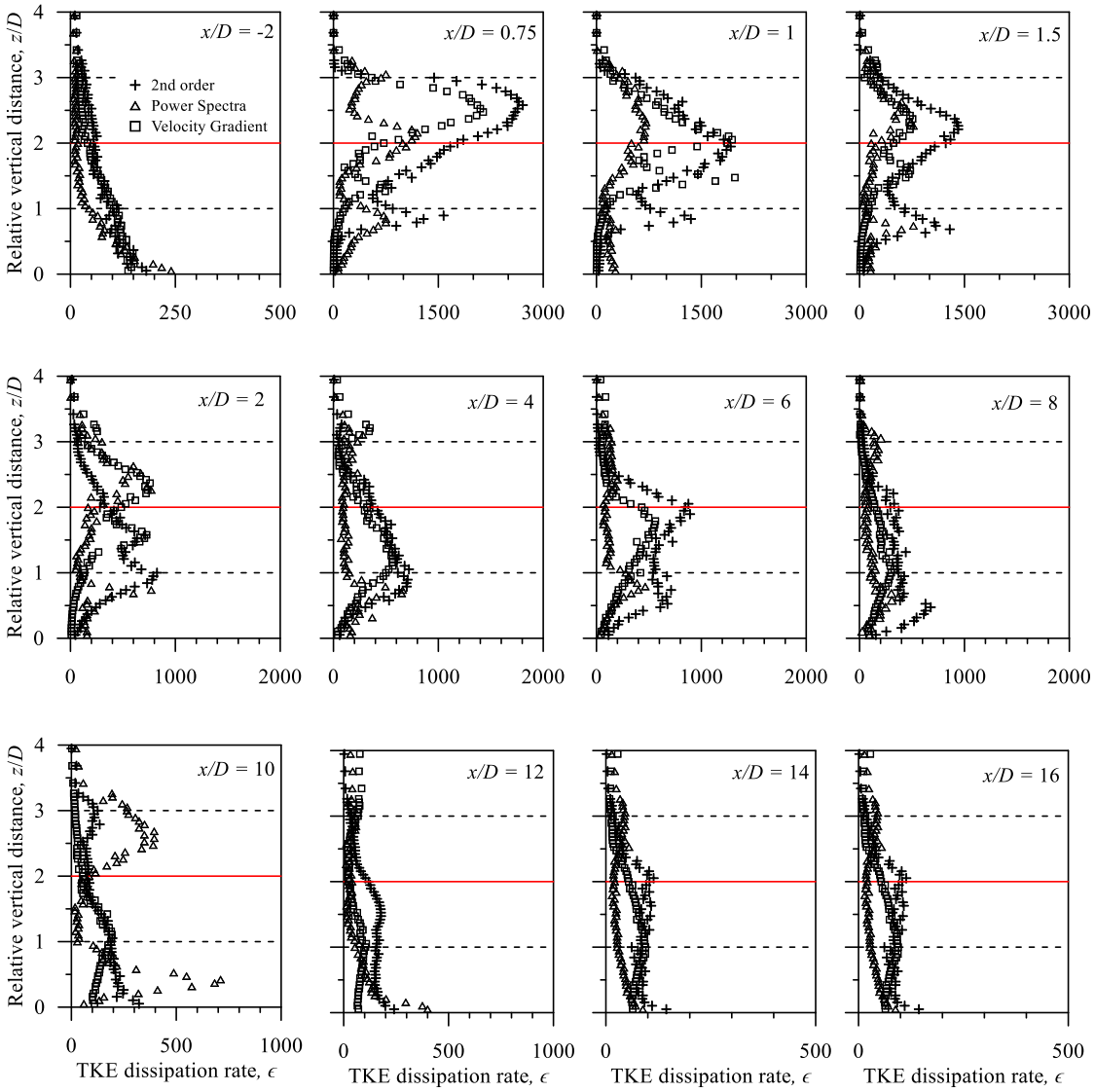

Figure 4.9(a): TKE dissipation rates estimated from the three-aforementioned procedure for flow past a pair of cylindrical bluff bodies having diameter D = 0.038 m

A n^{th}-order structure function is defined as the statistical moment of the flow velocity increments. Structure functions of any order can be expressed in the following generic form: (Ting et al. (1996)):

$$S_p(\mathbf{r}) = \langle (u(\mathbf{x} + \mathbf{r}) - u(\mathbf{x}))^n \rangle \qquad (4)$$

for any $n > 0$, where **x**, **x** + **r** are points in a turbulent flow regime, $u(r)$ indicates the flow velocity increment in the turbulent velocity field, r is the length $|\mathbf{r}|$ of **r**, and the angle brackets represent an average. While experimentation, Instantaneous velocity data are being collected using Vectrino probe at different time intervals. Hence, in order to apply the 4/5th law, it is required to convert the time lags τ (i.e., Δt, $2\Delta t$, $3\Delta t \ldots$, $\Delta t = 0.01$ s) into spatial distance r by using Taylor hypothesis, being described as $r(x,z) = \overline{u}(x,z)\Delta t$; where $\overline{u}(x,z)$ is time-averaged velocity component in streamwise direction.

In order to validate the Taylor hypothesis, Taylor coefficient $\psi(k, z) = 2\pi\sqrt{kE(k,z)}/\bar{u}(z)$ has been utilized as proposed by Ferraro et al. (2016) and Sarkar et al. (2021); where k indicates the wave number. In figure 4.8 Taylor coefficient $\psi(k, z/D)$ has been plotted with respect to k at normalized vertical distance $z/D = 0.17, 0.39, 0.6, 0.82, 1.04, 1.26, 1.47$ at downstream distances $1.5D$ and $2.5D$ respectively; which is within its acceptable limit ($\ll 1$). In the vicinity of the bed, the points are not verified for Taylor hypothesis due to the fact that it exhibits violation near the pebble bed as well as $\bar{u}(z)$ attains very small values.

It is worth noting that since Kolmogorov's breakthrough work, numerous researchers, including Kolmogorov himself, have contributed to its refinement. In particular, Kolmogorov (1995) and Padhi et al. (2019) proposed that the structure function of second order can be more effective in approximating the dissipation rate (ε). This approach aligns with Kolmogorov's two-thirds law, where ε is determined using the structure function of second order, which adheres to the 2/3 scaling law within the inertial subrange. However, our prior experience indicates that the higher-order (above $n = 2$) structure functions are very much fluctuating in nature and hence inconsistent to determine the ε-values especially downstream of a bluff body. Therefore, we only take help of the structure functions of second order to estimate the ε taking account of the following expression (Penna et al. (2020)):

$$\langle\varepsilon\rangle = (1/r)\,(\langle\Delta u\rangle^2/C_2)^{3/2}, \qquad (5)$$

where C_2 is a universal constant, valued as 2.12.

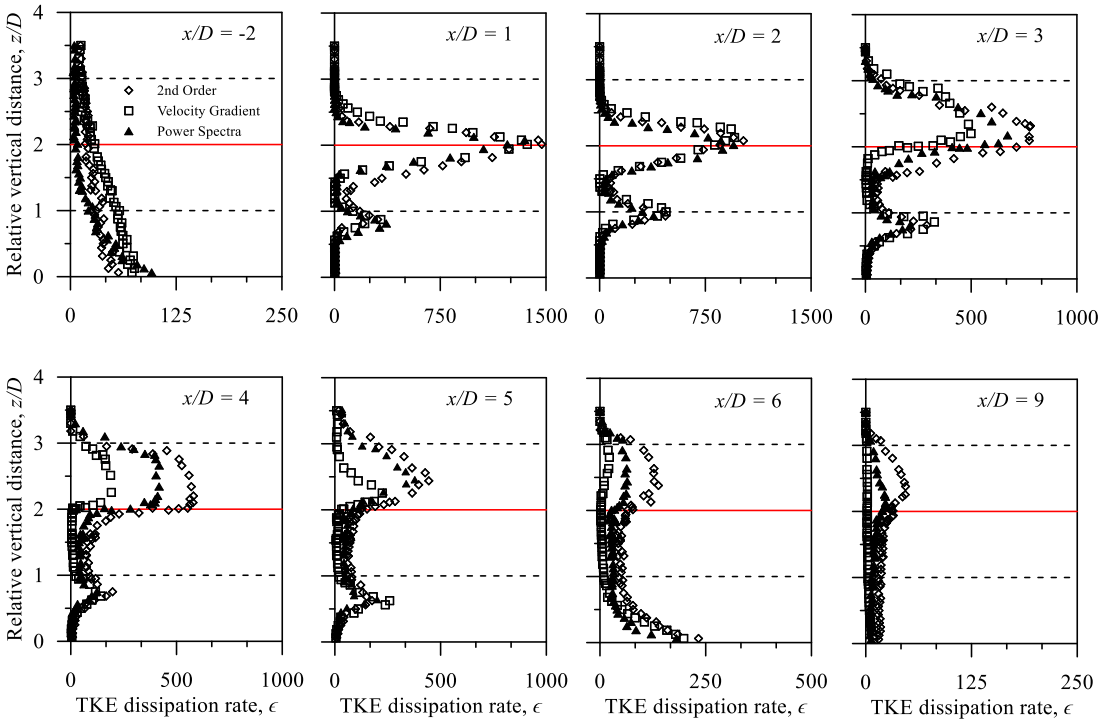

Figure 4.9(b): TKE dissipation rates estimated from the three-aforementioned procedure for flow past a pair of cylindrical bluff bodies having diameter D = 0.032 m

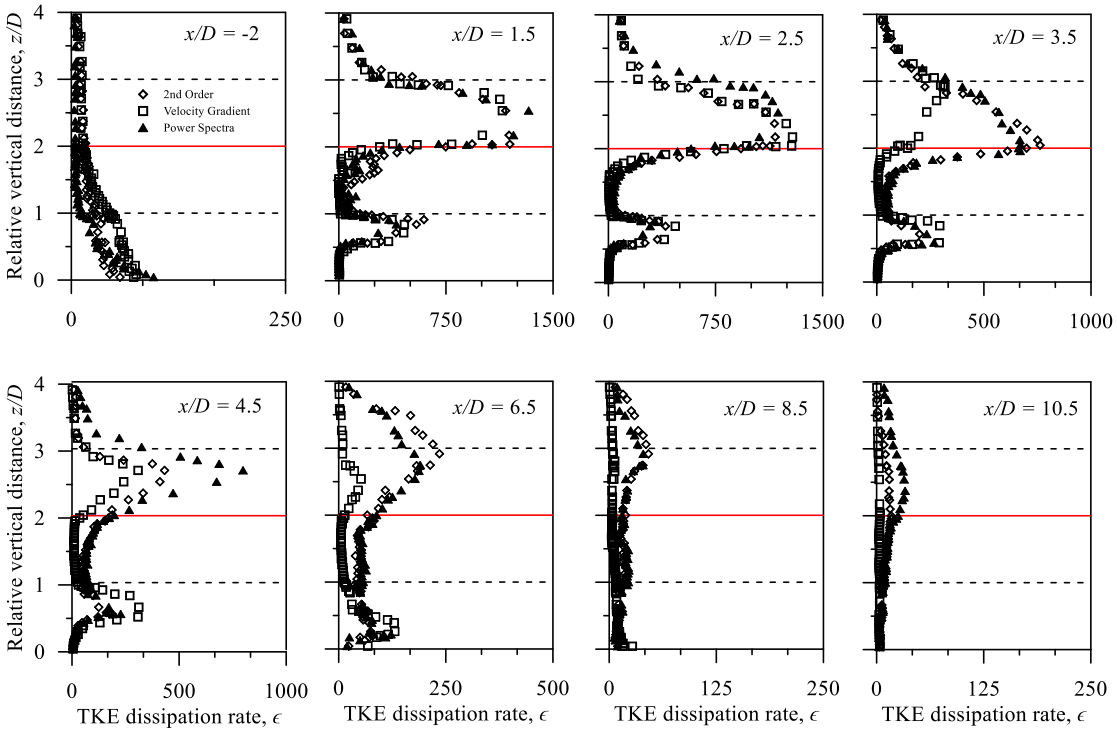

Figure 4.9(c): TKE dissipation rates estimated from the three-aforementioned procedure for flow past a pair of cylindrical bluff bodies having diameter D = 0.046 m

The vertical distributions of the TKE dissipation rates estimated from the three aforementioned procedures are shown in figure 4.9(a-c) at several streamwise distances, upstream and downstream of the cylinders having different diameters. Although there is a slight difference in their values estimated from different techniques, the agreement of overall vertical distributions of the dissipation rate is good. Because to the roughness of the bed at upstream and far-wake flow, the dissipation rate starts with a large value and decreases with vertical distances. In contrast, in the wake flow behind the two horizontal cylinders one above another with a gap of diameter of one cylinder, the influence is clearly visible. Dissipation rate increases with vertical distances, and attains peak value at z/D = 1 (i.e., near above the wall mounted cylinder), then immediately starts decreasing and attains low value peak at z/D = 1.5 i.e., just behind the upper horizontal cylinder; again, starts increasing and reaches maximum peak at z/D = 2, immediately above the upper horizontal cylinder. Then it tends to zero with vertical distance close to the free surface flow. The

impact of two bluff-bodies on the data plot is firmly visible in the wake flow till $x/D = 4$, afterwards diminishes with downward distances in far-wake flow.

4.7 Turbulent Length Scales

In bluff body hydrodynamics, eddies are known as whirling and reversed flow of fluid caused by some obstacles. Due to the chaotic nature of flow, the eddies can differ by a very small length-scale to a larger one. Hence it would be absurd to ask about individual size and traversing length of eddies in different flow range. But it is possible to look out for definitions of length-scales that explain the traversing length and size of eddies consistent with their characteristic properties. This traversing length can also be interpreted as mixing length, being defined as the average distance covered by eddies before getting degenerated. We are concerned about the size of eddies as they are responsible for momentum and energy transfer especially in the downstream vicinity. Large-scale eddies are having considerable amount of TKE in their possession and are very unstable. They soon break down to smaller-scale eddies leading to transportation of TKE. This phenomenon is identified by energy cascading. For identification of large eddies, the dimension of physical setup is enough. But for small-eddies, the length-scales can be evaluated from fluid viscosity which are widely known as Taylor micro scale and Kolmogorov length scale.

4.7.1 Taylor microscale

In the inertial subrange, the dimension of eddies is known as the Taylor microscale and it is defined as follows (Dey et al. (2018), Dey (2014)):

$$\lambda = \sqrt{\frac{15\upsilon\overline{u'^2}}{\varepsilon}} \qquad (6)$$

Where $\overline{u'^2}$ is the streamwise turbulence intensity and ε denotes the TKE dissipation rate.

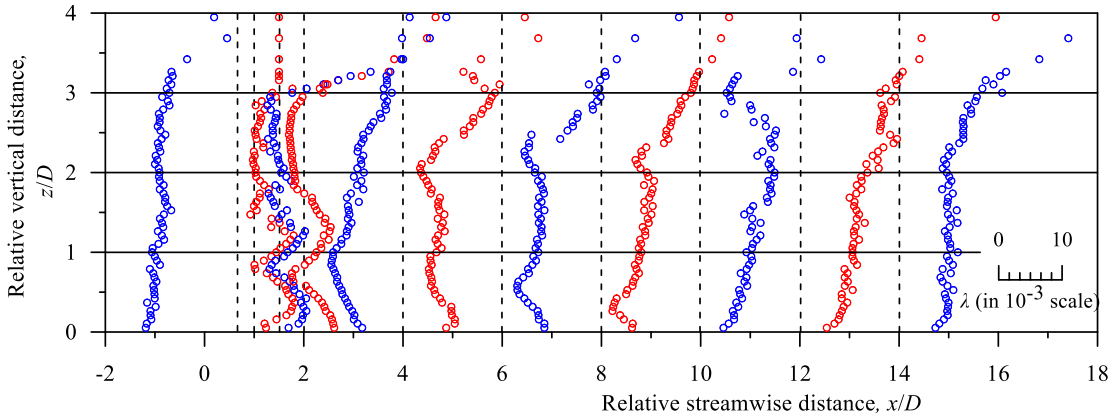

Figure 4.10(a): Taylor microscale profiles for flow past a pair of cylindrical bluff bodies having diameter D = 0.038 m

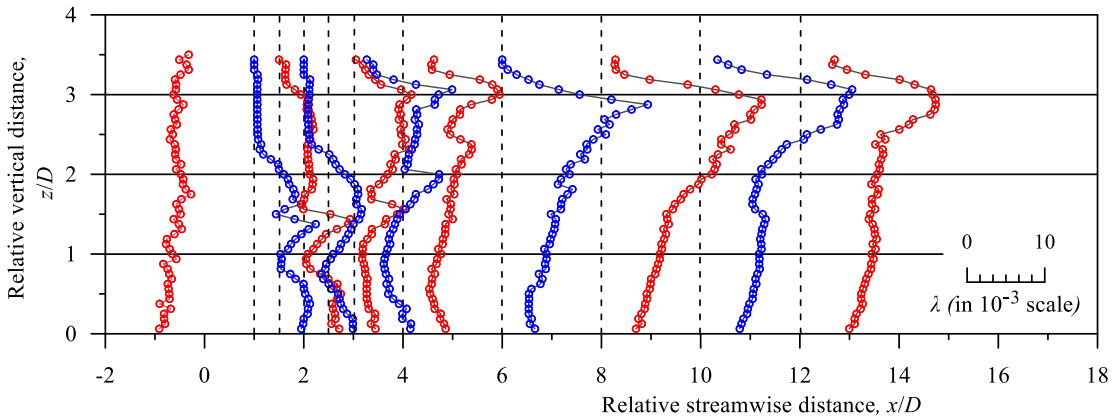

Figure 4.10(b): Taylor microscale profiles for flow past a pair of cylindrical bluff bodies having diameter D = 0.032 m

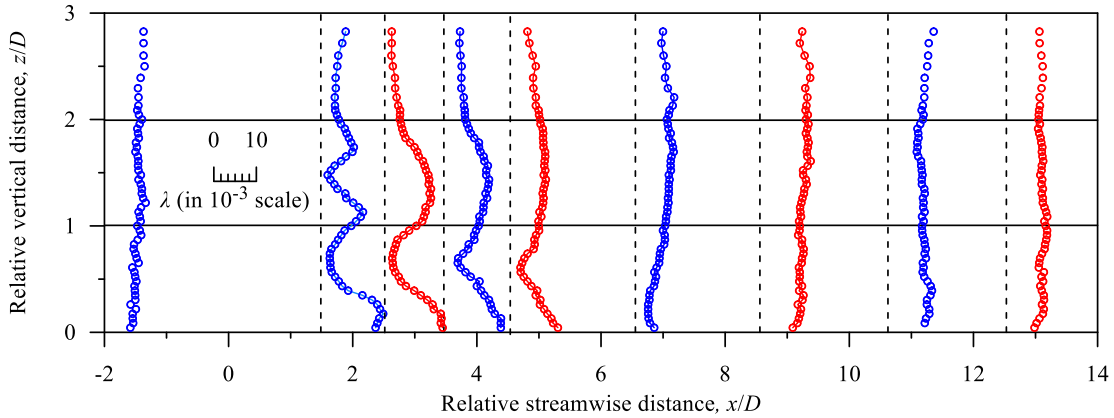

Figure 4.10(c): Taylor microscale profiles for flow past a pair of cylindrical bluff bodies having diameter D = 0.046 m

Figures 4.10(a-c) elucidate vertical data plots for Taylor microscale λ at different streamwise positions for cylinders with different diameters. Regardless of the cylinder diameter it is observed that initially with the increment of the vertical distance z, λ is having a diminishing profile until $z/D \approx 1$. Afterwards, we can observe a sudden elevation in the length-scale profile which lasts up to $z/D \approx 1.5$, after which length-scale profile undergoes a drastic decrement. From now onwards λ-profile stays almost invariant or decreases mildly with z until $z/D \approx 3$; followed by a slight increment in profile. One important observation is the values of Taylor length-scale are elevating gradually with the increment of downstream distance x. This is because of the reduction in TKE dissipation rate ε with gradual elevation in distance towards streamwise direction.

4.7.2 Kolmogorov length scale

As downstream distance increases, the disturbance caused by two cylinders gradually reduces and after a certain distance viscosity takes over and TKE starts to disperse into heat. This zone is known as dissipation range. Eddies present in this range have already been through a lot of cascading processes and hence they are on a very small scale.

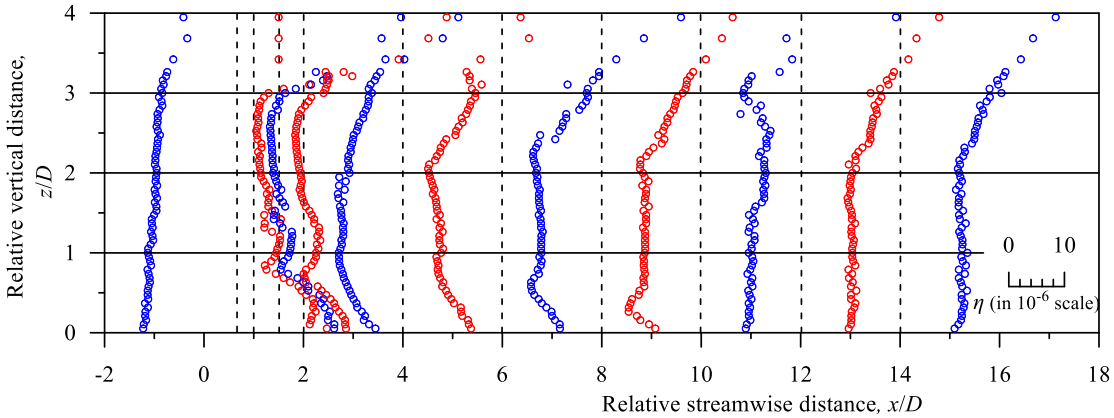

Figure 4.11(a): Kolmogorov length scale profiles for flow past a pair of cylindrical bluff bodies having diameter D = 0.038 m

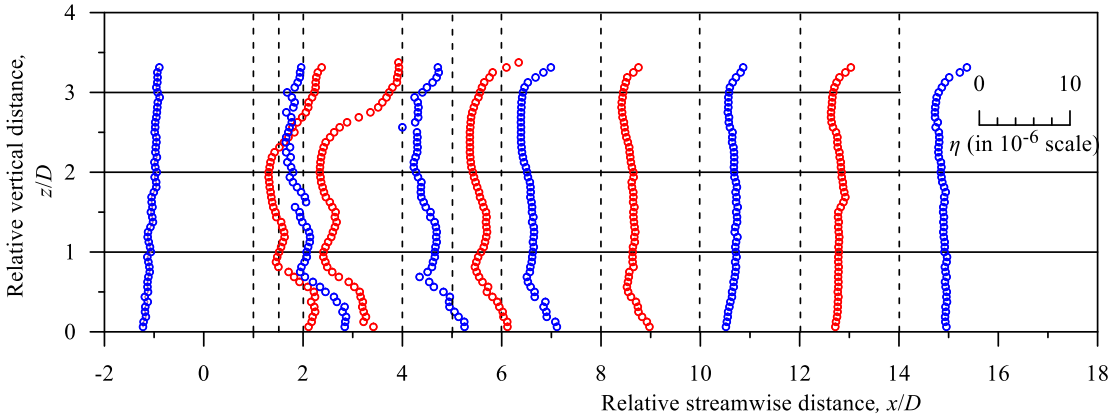

Figure 4.11(b): Kolmogorov length scale profiles for flow past a pair of cylindrical bluff bodies having diameter D = 0.032 m

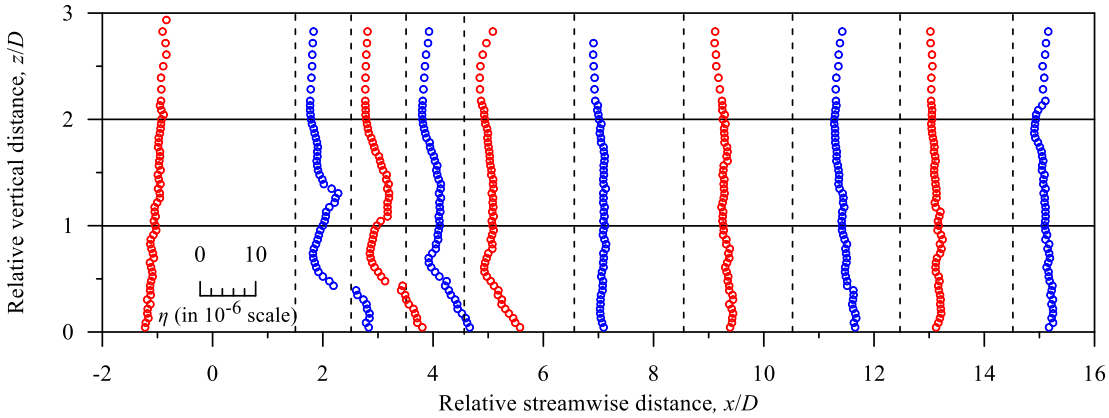

Figure 4.11(c): Kolmogorov length scale profiles for flow past a pair of cylindrical bluff bodies having diameter D = 0.046 m

According to Kolmogorov's first similarity hypothesis, for small-scale motions the statistical features can be fully identified by TKE dissipation rate ε and kinematic viscosity υ. The length-scale for dissipation range is no exception and known as Kolmogorov's length scale η. It is given by (Dey et al. (2018), Dey (2014)):

$$\eta = \left(\frac{\upsilon^3}{\varepsilon}\right)^{1/4} \qquad (7)$$

Figures 4.11(a-c) elucidate the vertical profile for Kolmogorov length scale at different x for cylinders having distinct diameters. It can be observed that Kolmogorov length scale profiles have almost same characteristics as of Taylor micro scales; only noticeable difference is much greater magnitude in case of Taylor length scale. Kolmogorov length scale is having escalating distributions as we move further downstream from cylinders.

4.8 Turbulent Kinetic energy fluxes

Figures 4.12 and 4.13 present the vertical distributions of the streamwise and normal TKE fluxes, f_{ku} and f_{kw} , respectively. These TKE fluxes are obtained using velocity fluctuations' third-order moments. The streamwise TKE flux, f_{ku} is calculated using the equation:

$$f_{ku} = 0.5\left(\overline{u'^3} + \overline{u'}\,\overline{v'^2} + \overline{u'}\,\overline{w'^2}\right) \qquad (8)$$

and the vertical TKE flux, f_{kw} is calculated by the equation (Dey et al. (2018), Dey (2014)):

$$f_{kw} = 0.5\left(\overline{u'^2}\,\overline{w'} + \overline{v'^2}\,\overline{w'} + \overline{w'^3}\right) \qquad (9)$$

The equations for f_{ku} and f_{kw} clearly indicate that positive f_{ku} values represent the transport of streamwise TKE flux downstream, while negative f_{ku} values correspond to upstream transport. Similarly, positive f_{kw} values signify upward vertical TKE flux, whereas negative f_{kw} values denote downward flux. Notably, these TKE fluxes reflect the prevalence of turbulent bursting events, as highlighted by their sign conventions.

Figures 4.12 and 4.13 explain the profiles for streamwise and vertical TKE fluxes at different lengthwise distances x/D for cylinders with different diameters. The following discussion will explain the behavior of flux profiles at different vertical and downstream distances irrespective of the diameter of cylinders. One important thing to mention is that the TKE Production rate (t_P) mostly shows higher values than TKE dissipation rate except for energy deficient flow region. Hence to maintain a kinematic equilibrium, TKE flux transfers from energy opulent zone to energy deficient zone. Hence in this analysis, we have gone through detailed explanation about transportation of fluxes. In near wake zone, streamwise and normal fluxes f_{ku} and f_{kw} are having positive and negative values respectively at near-wall zone. It indicates that f_{ku} and f_{kw} are having streamwise and downward transfer of TKE fluxes respectively in near wall vicinity; which composes an accelerating effect in motion of fluid particles. Afterwards, f_{ku} increases gradually to reach its maximum value at $z/D \approx 1$and immediately changes it sign. For the rest of the values of z, flux profile remains in negative side. Up until $z/D \approx 3$ profiles are having a slight increment followed by a gradual decrement.

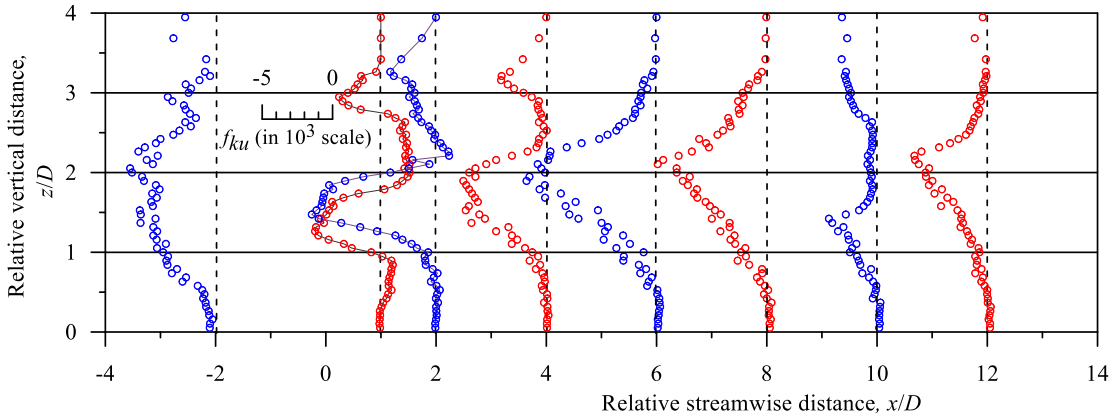

Figure 4.12(a): Streamwise TKE flux profiles for flow past a pair of cylindrical bluff bodies having diameter D = 0.038 m

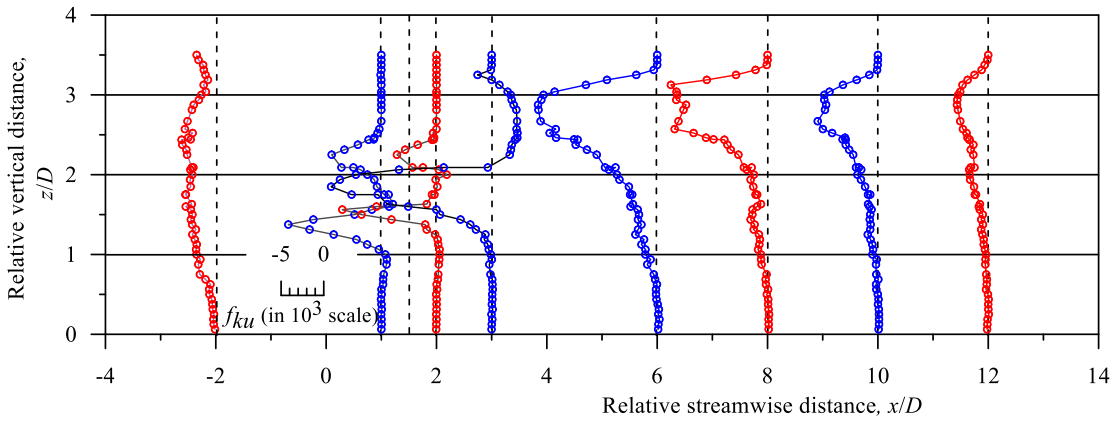

Figure 4.12(b): Streamwise TKE flux profiles for flow past a pair of cylindrical bluff bodies having diameter D = 0.032 m

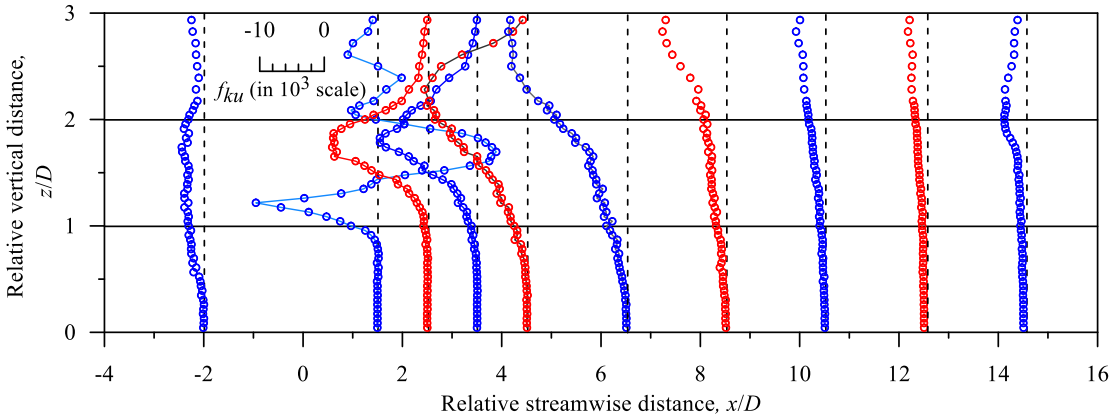

Figure 4.12(c): Streamwise TKE flux profiles for flow past a pair of cylindrical bluff bodies having diameter D = 0.046 m

In far wake, at x/D = 8, we can observe a similar profile of f_{ku} with the undisturbed upstream flow. For the case of f_{kw}, it is having its maximum negative value at $z/D \approx 1.8$. Afterwards it escalates rapidly and goes to positive side at about z/D = 2.5; reaches to its positive maximum at $z/D \approx 3$ and reduces slightly for the rest. In the far wake at x/D = 8 the f_{kw} profile is quite similar like that of in the upstream zone; where the entire vertical flux is in the upward direction. One significant observation is that in away-bed region when $z/D \geq 3.5$, f_{ku} and f_{kw} are having negative and positive profiles respectively. It indicates that in upper layer f_{ku} flux transfers against the streamwise direction meanwhile f_{kw} is having an upward transport; hence both of them compose retarding process whilst fluid particles arrive slowly. At the downstream flow, $0 < x/D \leq 6$ it can be observed that the flux profiles are having disagreements in sign over the flow depth maintaining the following fact that abs(f_{ku}) > abs(f_{kw}). The far wake flow is identified by the transfer of TKE fluxes against the streamwise direction and towards upward direction, which involves a retardation process that keeps up with the downstream distance of both cylinders.

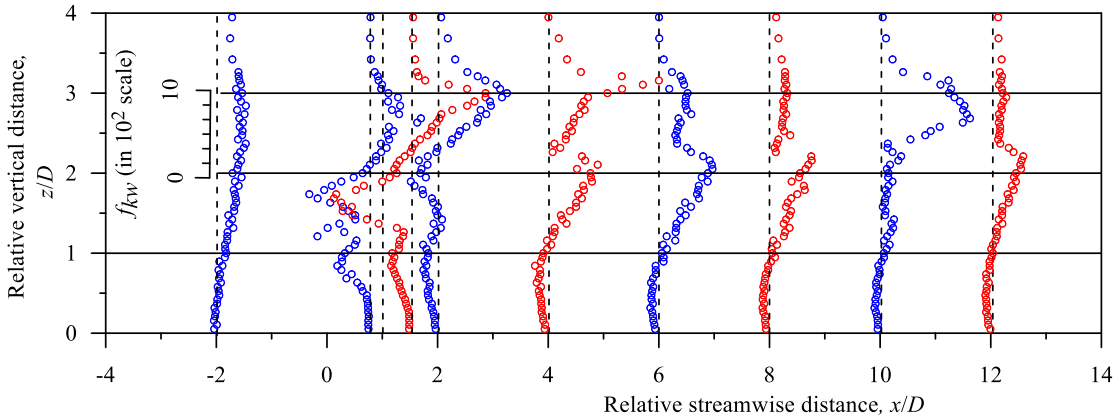

Figure 4.13(a): Vertical TKE flux profiles for flow past a pair of cylindrical bluff bodies having diameter D = 0.038 m

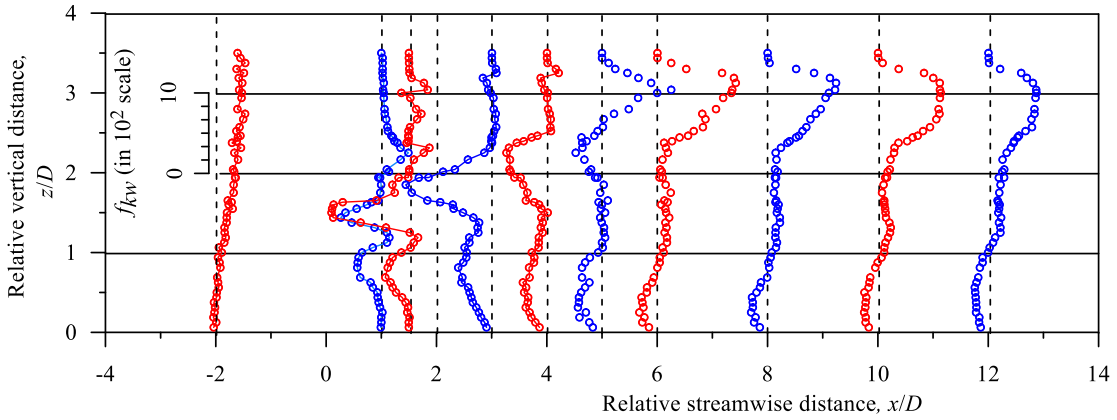

Figure 4.13(b): Vertical TKE flux profiles for flow past a pair of cylindrical bluff bodies having diameter D = 0.032 m

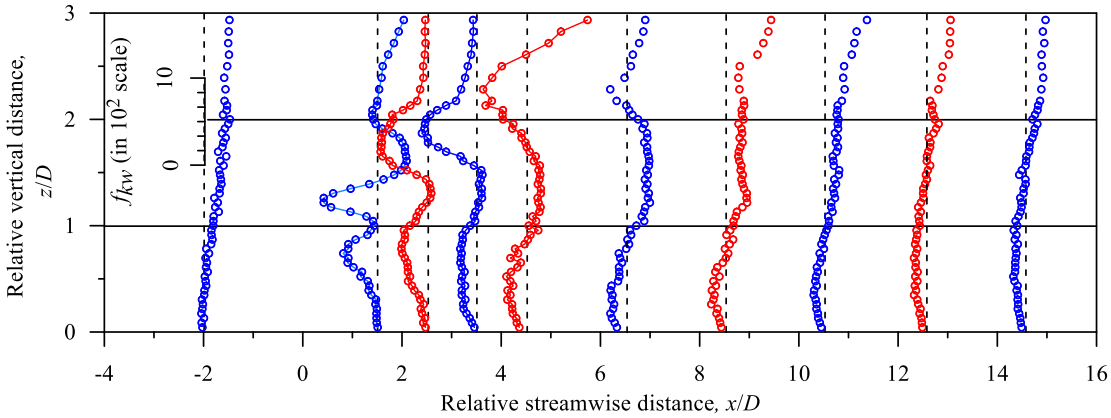

Figure 4.13(c): Vertical TKE flux profiles for flow past a pair of cylindrical bluff bodies having diameter D = 0.046 m

4.9 Turbulent Kinetic Energy (TKE) Budget

Stabilizing the velocity variations that transfer kinetic energy is necessary to comprehend the physical processes taking place in turbulent flow. Our goal is to stabilize this amount, which is represented by the TKE (k). The TKE budget quantifies the impacts of several turbulent processes, including viscous diffusion rate (ν_D), pressure energy diffusion rate (p_D), TKE production rate (t_P), TKE dissipation rate (ε), and TKE diffusion rate (t_D), in order to preserve dynamic stability in turbulent flow. For a uniform free surface flow, the TKE Budget is given as follows (Dey et al. (2018), Dey (2014)).

$$t_p = \varepsilon + t_{\mathrm{D}} + p_{\mathrm{D}} - \nu_D \qquad (10)$$

Where, $t_p = \overline{u'w'}\frac{\partial u}{\partial z}; t_D = \frac{\partial f_{kw}}{\partial z}; p_D = \left(\frac{1}{\rho}\right)\left(\frac{\partial \overline{p'w'}}{\partial z}\right); \nu_D = \upsilon(\partial^2 k/\partial z^2); p'$ is the fluctuations of hydrostatic pressure with respect to the fluid densityρ. The viscous diffusion rate ν_D is negligible in this fully developed turbulent flow because of high Reynolds number. It is worth mentioning that this is not true at the straight wall and at the cylinder walls, where the viscous diffusion term balances the turbulence dissipation rate. Formally, there should also be a convective term in the TKE equation, because due to the cylinders the vertical mean velocity is not zero near the cylinders, although it is comparatively small (Vreman et al. (2018)). For determining the

production rate t_P, the gradient of u profiles with respect to flow depth z and RSS- profiles have been utilized. For estimation of dissipation rate ε, Kolmogorov's four-fifth law about structure function of third-order can be used as described in Taylor length-scale. Pressure energy diffusion rate (p_D) was computed using the relation that the sum of all terms equated to zero and the assumption that the viscous diffusion term is negligible.

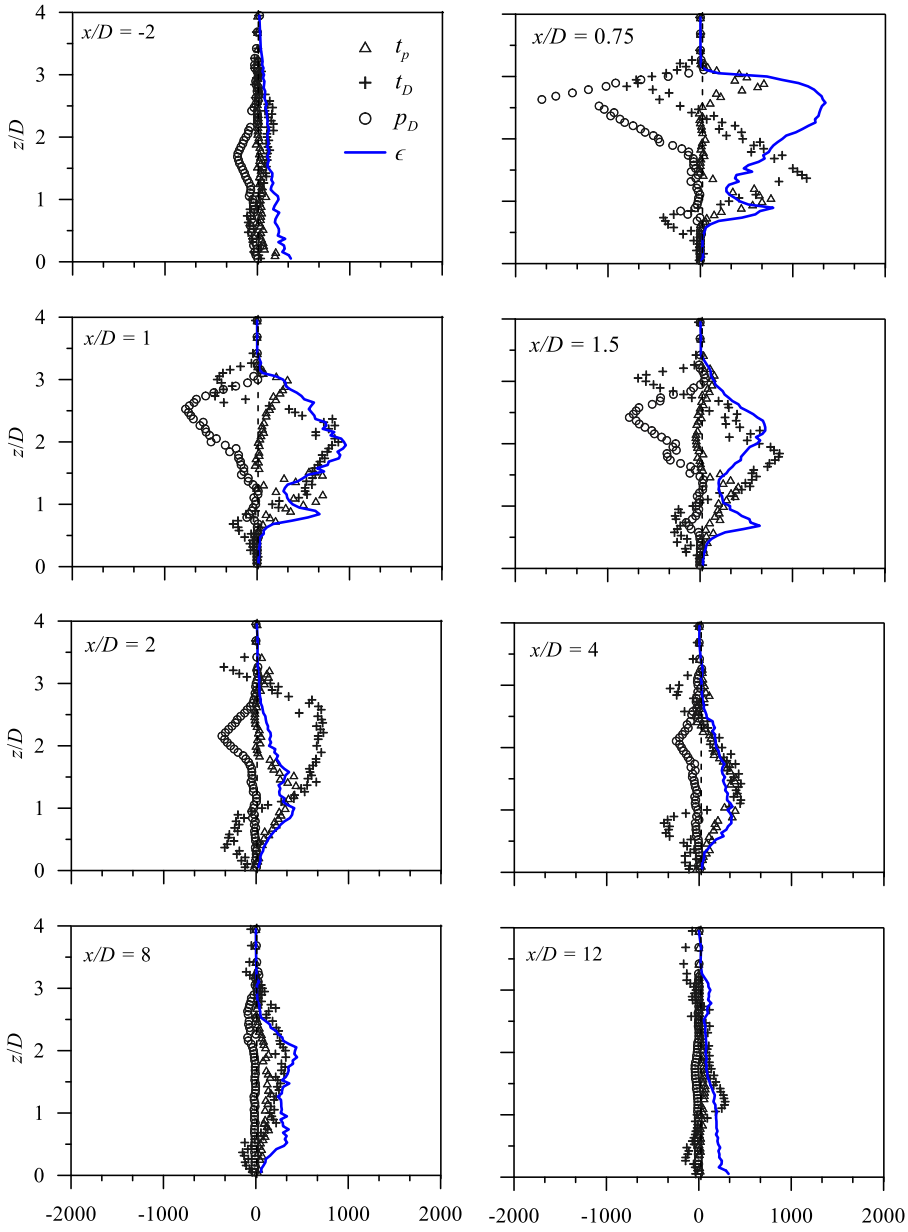

Figure 4.14(a): TKE budget components, t_P, t_D, p_D with respect to different heights z/D at different x/D for flow past a pair of cylinders having diameter D = 0.038 m

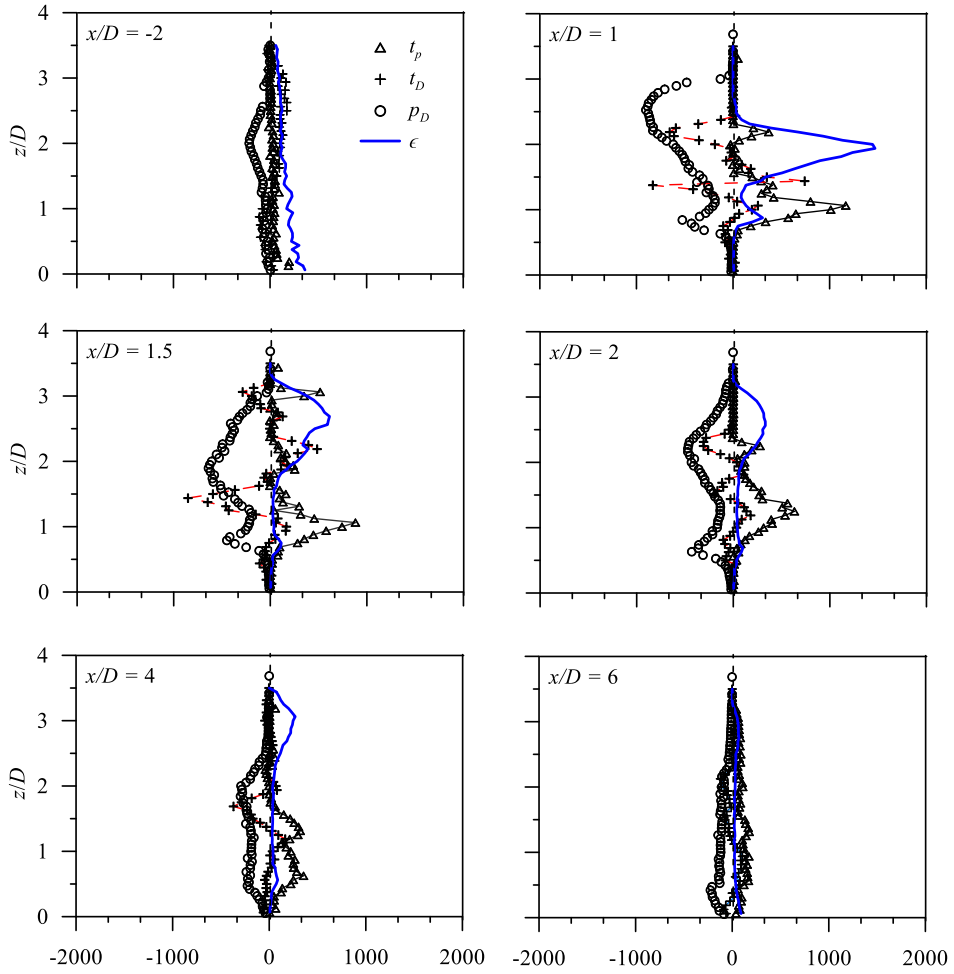

Figure 4.14(b): TKE budget components, t_P, t_D, p_D with respect to different heights z/D at different x/D for flow past a pair of cylindrical bluff bodies having diameter D = 0.032 m

Figures 4.14(a), 4.14(b) elucidate the TKE Budget elucidating the behaviour of components t_P, t_D and p_D with vertical distance z/D at different downstream distances x/D for cylinders having different diameters. Regardless of the cylinder diameter, it is seen that in the uninterrupted upstream flow, the components are all having positive values near the wall with $t_P > t_D > p_D$ and diminish with increment of z/D. In the downstream of cylinders, a dynamic steadiness is maintained above both the cylinders ($z/D > 3$). The t_P is having a small positive value in near-wall zone which is increasing until reaching its maximum at z/D = 1.5; thereafter decreases with the increment of z and after $z/D > 3.5$ it becomes almost invariant of z/D. Also peaks in t_P profiles tell us about a strong mixing happening in wake; occurring huge amount of TKE production near the

top vicinity of cylinders. Not much later we can observe large energy dissipation; but afterwards there is a huge drop in both production and dissipation above cylinders, as mentioned earlier. About the rest of the two budget components t_D and p_D, two contrasting profiles can be seen; for instance, when t_D attains positive maximum in its profile, p_D possesses a negative maximum at that location. Although some negative values can be seen near the wall for t_D profiles at $4 \geq x/D > 0$. This is because it has been discussed that in downstream vicinity of cylinders, TKE produces very rapidly; resulting the diffusion components p_D and t_D to be negative. As the nondimensional distance in downstream direction x/D increases, there is a decrement in peaks of t_D-, p_D- and t_P-profiles. Subsequently the profiles of all Budget components start looking identical with the uninterrupted upstream profiles. We end the discussion by leaving the following conclusion: wall-wake flow is being identified by highly negative pressure energy diffusion rate together with a sufficient TKE production rate, stabilized by the amplified TKE diffusion and dissipation rates.

4.13 Conclusion

This article presents the experimental outcomes of turbulent flow past two cylinders: one wall-mounted, another suspended. Experimental data have been analyzed to elucidate streamwise velocity, RSS, turbulence intensity, length scales and budget. For evaluation of TKE dissipation rate, different methodologies have been implemented including several order structure functions. Due to the presence of two cylinders, recirculatory flow is observed in the near wake zone whereas no significant change is observed in the far wake zone. Stress and intensity profiles indicate that values increase significantly close downstream of both cylinders and then decline with downstream position and vertical height. TKE dissipation rate profiles indicate higher amount of dissipation behind the suspended cylinder compared to wall-mounted cylinder in near-wake zone; but as we go far downstream it is observed that decaying of dissipation rate is more behind suspended cylinder. Length scale profiles show higher values in near bed; which indicates comparatively larger eddies' existence behind wall mounted cylinders within inertial subrange and dissipation range respectively. In near bed zone, positive streamwise flux and negative vertical flux are being observed, which directs streamwise and downward transportation of TKE fluxes respectively, whereas for the rest of the bed zones negative streamwise, positive vertical fluxes are visible suggesting an upward transport and retardation process with slow fluid motion. The

duration of the TKE budget suggests that the wake flow is characterized by a significant negative pressure energy diffusion rate in conjunction with high TKE diffusion and dissipation rates, while the flow in gap is characterized by a small negative TKE diffusion rate maximal and a very small positive pressure energy diffusion rate maximal. To support these outcomes, three different experimental outcomes have been presented for each of the aforementioned characteristics, which show consistency of the graphs upon comparing at different downstream positions.

Chapter 5

Turbulence anisotropy in a wall-wake flow downstream of two horizontal cylinders

5.1 Introduction

Turbulent flow in presence of one or more bluff bodies in shallow flows has been a topic of considerable interest in hydraulics due to its importance in several real-life hydraulic engineering problems in connection with environmental and geophysical flow systems. In bluff-body hydrodynamics sphere, plate, cylinder and many more alike symmetrical two-dimensional (2D) objects have been taken account of largely. One crucial phenomenon rises behind bluff-body due to its presence in flow, known as wake region. The uninterrupted upstream flow characteristics are recovered far downstream of the bluff body. Dey et al. (2018) experimentally studied turbulent flow past a wall-mounted and then a near-wall horizontal cylinder; furthermore, compared the turbulent characteristics obtained location wise. The environment being used in our work is slightly different than this; in a single experiment, both cylinders were taken at once which has engineering applications such as fuel rods in nuclear reactors, cylindrical piers, bridges and piggybacking pipelines.

In past decades, numerous bluff body experimentations have been performed. In bluff-body hydrodynamics, A basic notion of self-similarity in the velocity deficit profiles behind a circular cylinder operating under an incoming free-stream turbulent flow was developed by Schlichting (1961). However, because there are two cylinders, the flow characteristics shown in this study are far more complex than those in Schlichting (1961), and as a result, the wake zone exhibits unexpected behavior. Balachandar et al. (2004) studied wake flow behind a wall-mounted vertical cylinder which provided a clear understanding about vortex shredding in wake. Turbulent flow features near a short wall-mounted cylinder were analyzed by Smith and Foster (2007). They used LES (large Eddy simulation), a mathematical modelling for turbulent flows to analyze submerged pipeline flow under rivers. Verma and Govardhan (2011) studied flow behind two side by side cylinders in numerical aspect using a modelling software Ansys fluent. They basically discussed

the effects of cylinders in lift and drag coefficients. Using PIV techniques, Wang and Tan (2008) experimentally analyzed the turbulent features in wake zone behind a circular cylinder. They concluded that when $\Delta z/D$ (Δz = thickness of the space between the cylinder and the wall, cylinder diameter is D) varies over 0.1 to 0.4, significant diminution in the lengths of wake recirculation is formed because of the detachment in shear layer. Ozgoren (2006) analyzed the formation of vortex structures and flow features behind a circular cylinder under uniform inlet for different Reynolds number ($Re = 4U_0h/v$, U_0=incoming flow velocity, h = flow depth, v = kinematic viscosity). They concluded that when Re increases, an elevation in length of vortex formation can be observed. Sadeque et al. (2007) analysed the features of superficial turbulent behaviour behind a wall-mounted vertical cylinder over rough and smooth walls. Lin et al. (2001) analyzed the turbulent quantities downstream of a near-wall circular cylinder for $1.15 \times 10^4 \geq Re \geq 780$and $4 \geq \Delta z/D \geq 0$. They pointed out that time-averaged velocity profiles have some sort of resemblance. Using PIV method, Kahraman et al. (2012) analysed the vortical structures of wake flow behind a cylinder in superficial flow depth. They analyzed both instantaneous and averaged velocity profiles in wake zone. Lacey and Roy (2007) investigated the flow features downstream of a submerged pebble cluster. Ozdil and Akilli (2015) analyzed the flow quantities downstream a circular cylinder for several values of $\Delta z/D$ and $Re = 5 \times 10^3$ in superficial depth with the help of PIV method. The time-averaged flow features divulge that towards the rotation of vortices, there are certain disagreements between the primary as well as developing circulation bubbles which are frequent. Zdravkovich et al. (1977) reviewed the flow interaction between two cylinders in several positions. They reached in a conclusion that in presence of two cylinders the turbulent characteristics may be completely different from the single cylinder case scenario, especially in the near wake zone. Under certain equilibrium conditions, Sarkar et al. (2022) investigated the turbulence characteristics and evaluation of the TKE budget for flow over a bimodal deteriorated bed. The structural functions data corroborated the agreement with the Kolmogorov's 2/3-, 4/5-, and Monin-Yaglom's 4/3-laws by indicating the presence of inertial subrange inside smaller time-lag ranges. Yet, there are considerable disparities between the TKE dissipation rates predicted by the 4/5 and 4/3 laws of turbulence.

In order to characterize the turbulent flow, it is crucial to identify how much the flow is being dispersed from isotropic circumstances, known as turbulence anisotropy. In this regard, first

breakthrough about characterizing anisotropy with the help of certain turbulence zones within a triangle had been made by Lumley and Newman (1977); later improved by Choi and Lumley (2001). Several flume experiments were performed in the past decade to analyze Reynolds stress anisotropy behavior. Roussinova et al. (2009) analyzed stress anisotropy tensor in a smooth and rough shallow open-channel flow. They concluded that stress anisotropy tended to become isotropic in nature in near-wall zone, where the roughness density effects were predominant; whereas in smooth bed turbulence would be less isotropic at the vicinity of free surface due to higher values of the correlation coefficient. Coscarella et al. (2020) explored the significance of roughness of bed on turbulence anisotropy within two distinct regions of open-channel turbulent flow. Using anisotropy angles in conjunction with second-order structure functions, they analyzed the characteristics of turbulence anisotropy. Similarly, utilising a mix of Lumley and barycentric maps as well as the more recent spheroid and color maps, Ali et al. (2018) investigated a thermally segregated wind turbine array boundary layer. Their findings revealed that negative buoyancy in stably stratified flows suppressed turbulent fluctuations, influencing the development of Reynolds stress and leading to increased flow anisotropy. Sarkar et al. (2015) compared anisotropy in turbulence in flows over noncohesive sediment beds at the entrainment threshold with those over stationary beds. Their results indicated that, for immobile beds, the turbulence tended toward one-component isotropy with increasing vertical distance, whereas for mobile beds, the turbulence transitioned to three-dimensional isotropy at mid-flow depth. Dey et al. (2020) examined the features of length scales and anisotropy in various parts of a submerged turbulent plane offset jet. The anisotropic invariant maps obtained from their Reynolds stress anisotropy analysis showed that the anisotropy tended to decrease towards the three-dimensional isotropy in the preattachment region, beginning from the wall and continuing through the left curvy boundary of the Lumley triangle until the half of the recirculatory bubble zone's depth. In the nonuniform sediment beds, Sharma et al. (2021) analysed the Reynolds stress anisotropy in the absence of seepage and with downward seepage flow. They came to the conclusion that invariant function data sets demonstrated a clearly defined two-component isotropy in the flow's near wall zone and a roughly three-component isotropy in the flow's outside area when comparing seepage flows to no seepage flow. The experimental findings of turbulent flow measurements made in a bimodal deteriorated channel bed composed of a sand-gravel combination were presented by Sarkar et al. (2021). By establishing the validity of turbulence laws at various sites over the bed and giving a clear grasp

of the Reynolds stress anisotropy along with TKE budget, their research significantly improved the concept of turbulent flow over a degraded bed. Mahananda et al. (2021) examined how aspect ratio affected the TKE budget, Reynolds stress anisotropy, conditional statistics, TKE fluxes, and other higher-order statistics of fluctuating velocity components in hydraulically demanding narrow open channel flows. In low aspect ratio flows, rod-like axisymmetric turbulence was limited to the intermediate layer, according to their study of the Reynolds stress anisotropy invariant map (AIM). Higher aspect ratio flows, on the other hand, showed axisymmetric turbulence that was rod-like throughout the flow depth. Anisotropy of Reynolds stress in the fluid movement surrounding the bridge pier for both downhill and no seepage was investigated experimentally by Chavan et al. (2022). Anisotropic invariant map profiles showed a trend toward one-component isotropy as the flowing depth increased at the scour hole's edge, but a tendency toward three-component isotropy at the open surface.

There are some bluff body experiments present in literature mentioning anisotropy. For instance, anisotropy behaviour in turbulent flow over rigid dunes were analysed by Dey et al. (2020). At different streamwise distances along the vertical, the spatial developments of the AIM, as well as function, Reynolds stress tensor eigenvalues, and stress ellipsoid eccentricities were examined. Sarkar et al. (2015) studied turbulent length scales as well as anisotropy of flow past a wall-mounted sphere and showed the looping trend in AIM in near-wake. Anisotropy behaviour in wave flume was further investigated by Longo et al. (2017) who presented several ways of representing turbulence anisotropy. They introduced stress anisotropy first in terms of Lumley triangle and later by barycentric map; furthermore, they analyzed dissipation anisotropy to understand anisotropic behaviour of Turbulence Kinetic Energy (TKE) dissipation rate (ε).

The above literature study indicates that there are several works being done by researchers regarding flow past bluff body especially cylinder, but no experimental study is present having bluff bodies as two one above another horizontal cylinders. Due to the presence of two closely placed cylinders, it is expected that the amount of anisotropy in turbulence would be much higher than that of a single cylinder in near wake zone. Hence, in the subsequent discussion we will be presenting basic turbulence characteristics such as velocity, stress and indicator; then stress anisotropy tensor and its representation in terms of Lumley triangle together with description of

dissipation anisotropy; finally, barycentric map visualization and one-one correspondence with AIM.

5.2 Description of the Experiment

An experiment had been performed in a rectangular-shaped flume at the Fluvial Mechanics Laboratory of Indian Statistical Institute, Kolkata, India. The flume was 20 metres in total length, 0.5 metres in width, and 0.5 metres in height. The in-depth discussion of the experimental set up with uncertainty estimation for Vectrino measurements has been thoroughly described for this experimental environment in chapter 3.

To validate the accuracy of the data being gathered by the Vectrino, discrete fast Fourier transforms (FFT) were used to analyse the velocity power spectral density function $F_{ii}(f)$. Figure 5.1 depicts the $F_{ii}(f)$ after despiking in several vertical positions at streamwise distance $x = 1D$ ($D = 0.032$m). Inside the inertial subrange in case of frequency $f > 1$ Hz, the $F_{ii}(f)$-profiles of signals derived by spike reduction demonstrate adequate consistency with the "−5/3 scaling-law" except at $z/D = 1.75$, suggesting presence of high recirculation in intermediate zone of the cylinders. Moreover, it has been observed from figure 5.1 of power spectra that the spectral density functions of u, v and w are satisfying the following relation: $F_{uu} > F_{vv} > F_{ww}$, at immediate downstream of the cylinders indicating high anisotropy. Gradually, at $z/D = 2.25$ and above, spectral density values tend to merge together i.e., $F_{uu} \approx F_{vv} \approx F_{ww}$, which suggests a tendency of converging towards three-dimensional isotropy above the horizontal cylinders. More elaborative discussion will be presented to the readers in the subsequent discussions, with the incorporation of anisotropy invariant maps and functions.

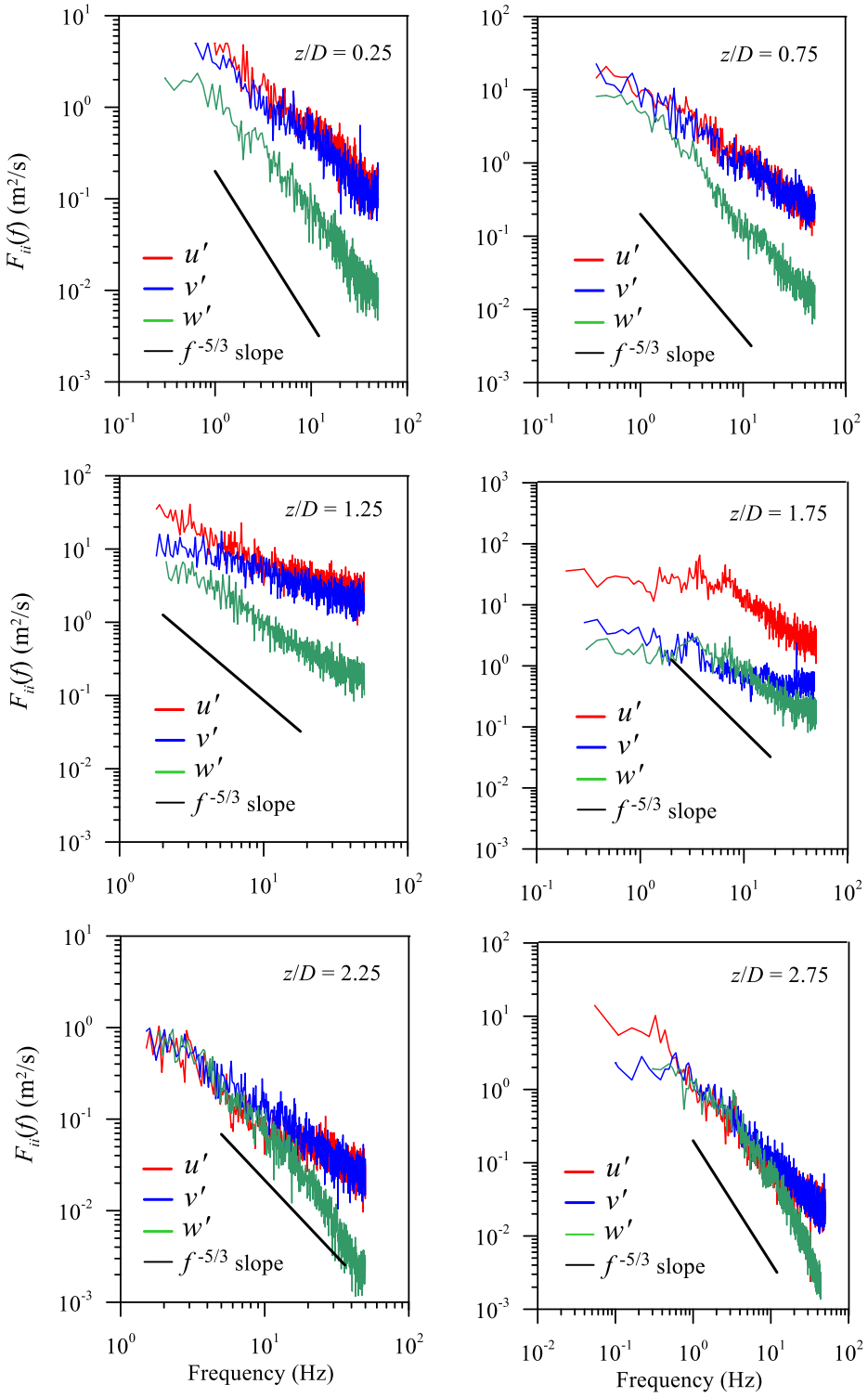

Figure 5.1. Velocity power spectra density function $F_{ii}(f)$ in several vertical positions at streamwise distance $x = 1D$ after despiking

5.3 Time-averaged Velocity profile

Figures 5.2(a-c) display the vector plot of velocity distributions in streamwise direction at various x/D points in the downstream direction of two cylinders stacked one above another with a cylinder-diameter-sized space (D = 0.038, 0.032 and 0.046 m respectively) between them. Due to vortex shedding downstream of the cylinders, two abrupt drops are seen in streamwise profiles up to x = 1.5D. u-distribution gradually regains its unaltered upstream velocity profile in far wake zone with the increment in downstream distances. Another illustration of flow recovery is shown in below figures, where the u-profile appears to be nearly equivalent to the upstream distribution at $x = 8D$. In the u-distribution, there are two significant concavities that result in four points of inflection (where $d^2u/dz^2 = 0$) that are discernible at the coordinates $z/D \approx 0.5$ and 2, respectively.

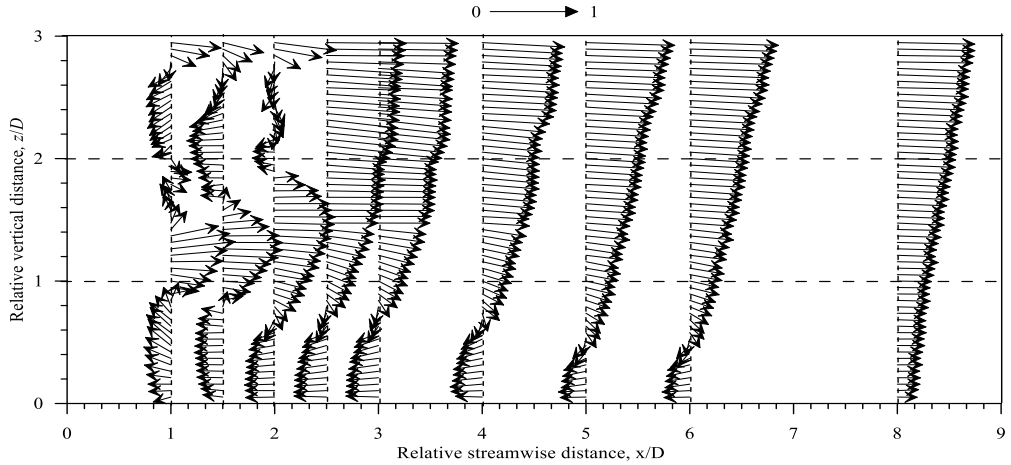

(a)

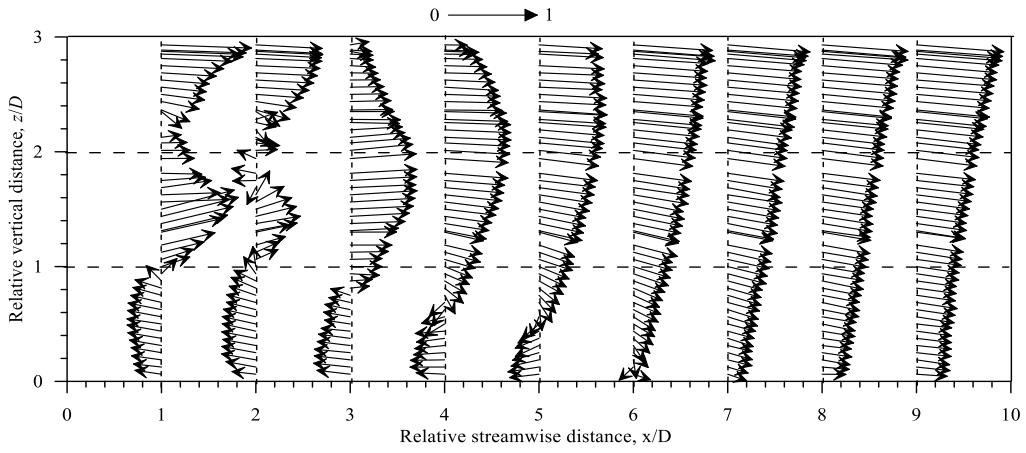

(b)

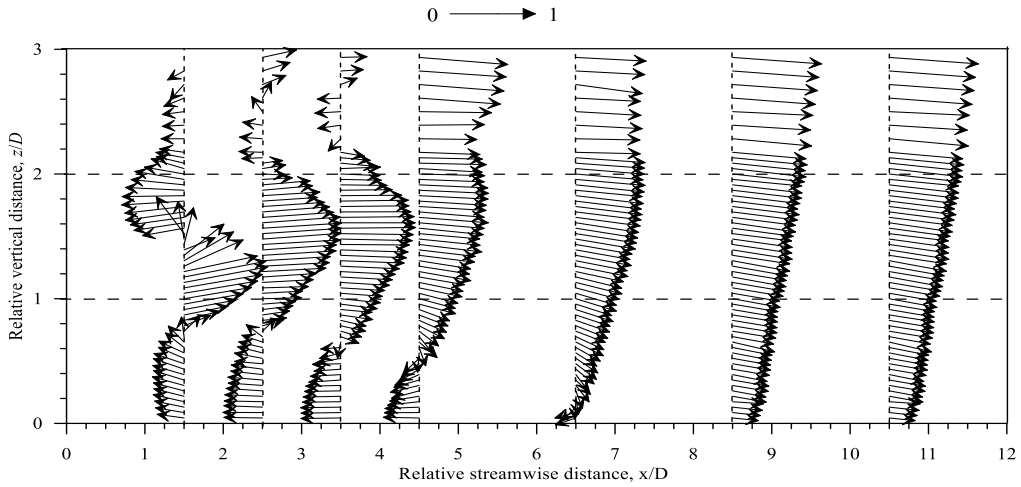

(c)

Figure 5.2. Vector plot of velocity distributions in streamwise direction at various *x*/*D* points in the downstream direction of two cylinders stacked one above another

5.4 Turbulent Kinetic Energy and Indicator

The time-averaged kinetic energy per fluid mass associated with the eddies is known as the turbulent kinetic energy (TKE) of a turbulent flow. The TKE is calculated using the variations of the components associated with fluctuating velocity as follows: $\boldsymbol{k = 0.5\left(\overline{u'^2} + \overline{v'^2} + \overline{w'^2}\right)}$; where u', v', and w' represent, respectively, the variations of the streamwise, spanwise, and vertical velocity components compared to their time-averaged quantities u, v, and w. Figure 5.3 depicts the vertical trends of TKE for flow past two cylindrical bluff bodies having three different diameters 0.038, 0.032 and 0.046 m respectively. It is seen that immediate downstream of the cylinders, TKE is much greater in comparison with the turbulent outer layer ($z/D > 3$). Moreover, TKE generation is greater in the intermediate zone ($z/D \approx 2$) of the cylinders than the near bed zone ($z/D \approx 1$). The observations are uniform irrespective of the diameter of the cylinders, indicating the validity of the

TKE results obtained. In all three figures, the fluctuations in the TKE value diminished at about $x = 10D$ and henceforth, the profile starts assuming its uninterrupted upstream values.

Depending on the experimental results, the local turbulence level was quantified using the average turbulence intensity I_{av}, referred to as the turbulence indicator. It can be evaluated using the following mathematical expression $I_{av} = \sqrt{2k/3}/\bar{U}$, Where k is TKE defined above, and $\bar{U}$ is the norm of time-averaged velocity components i.e., $\bar{U} = \sqrt{\bar{u}^2 + \bar{v}^2 + \bar{w}^2}$. It is quite useful to indicate high, medium and low turbulence present in an open channel flow due to its nondimensional nature. Dey et al. (2020) has utilized this characteristic in order to estimate the turbulence for flow past an isolated dunal bedform, a problem essentially belongs to bluff-body hydrodynamics. Later, Sarkar et al. (2023) has incorporated this quantification method to analyze structure functions in degraded channel bed. Figure 5.4 illustrates the vertical distributions of Turbulence Indicator for all three experimental environments. It supports the fact that in presence of both cylinders, turbulence generation is much more significant in the intermediate zone of the cylinders. One interesting observation is visible at $x/D \approx 8$, where I_{av} valued much higher at near bed region in case of cylinder with diameter 0.032 m. This could be an indication of turbulence indicator highly correlated with the diameter of the bluff-bodies present in the flow. However, as we go far downstream from $x/D = 10$, the profiles as usual seem identical with the upstream flow.

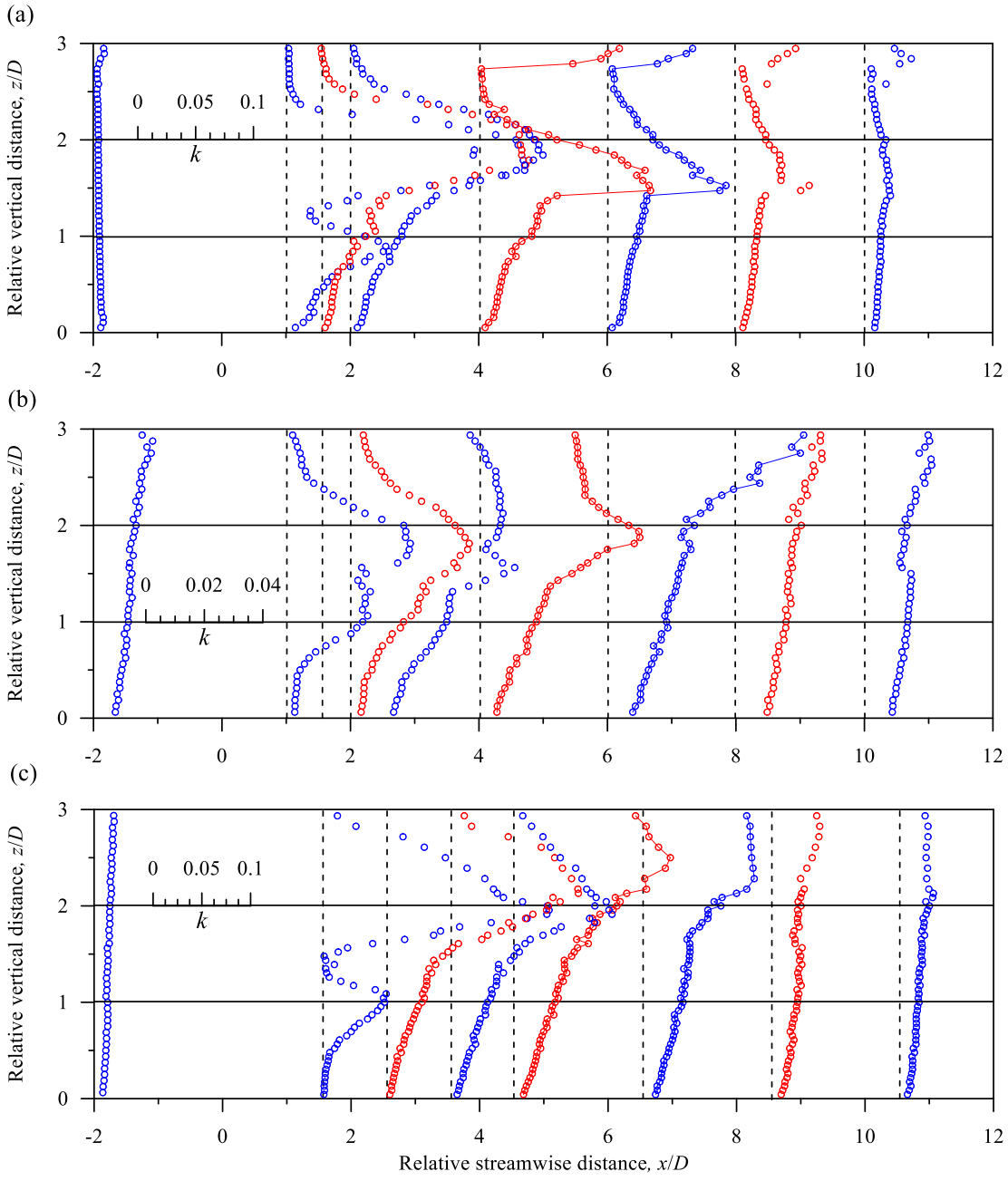

Figure 5.3. The vertical trends of TKE at various *x*/*D* points in the downstream direction of two cylinders stacked one above another with diameter **(a)** *D* = 0.038 m **(b)** *D* = 0.032 m **(c)** *D* = 0.046 m

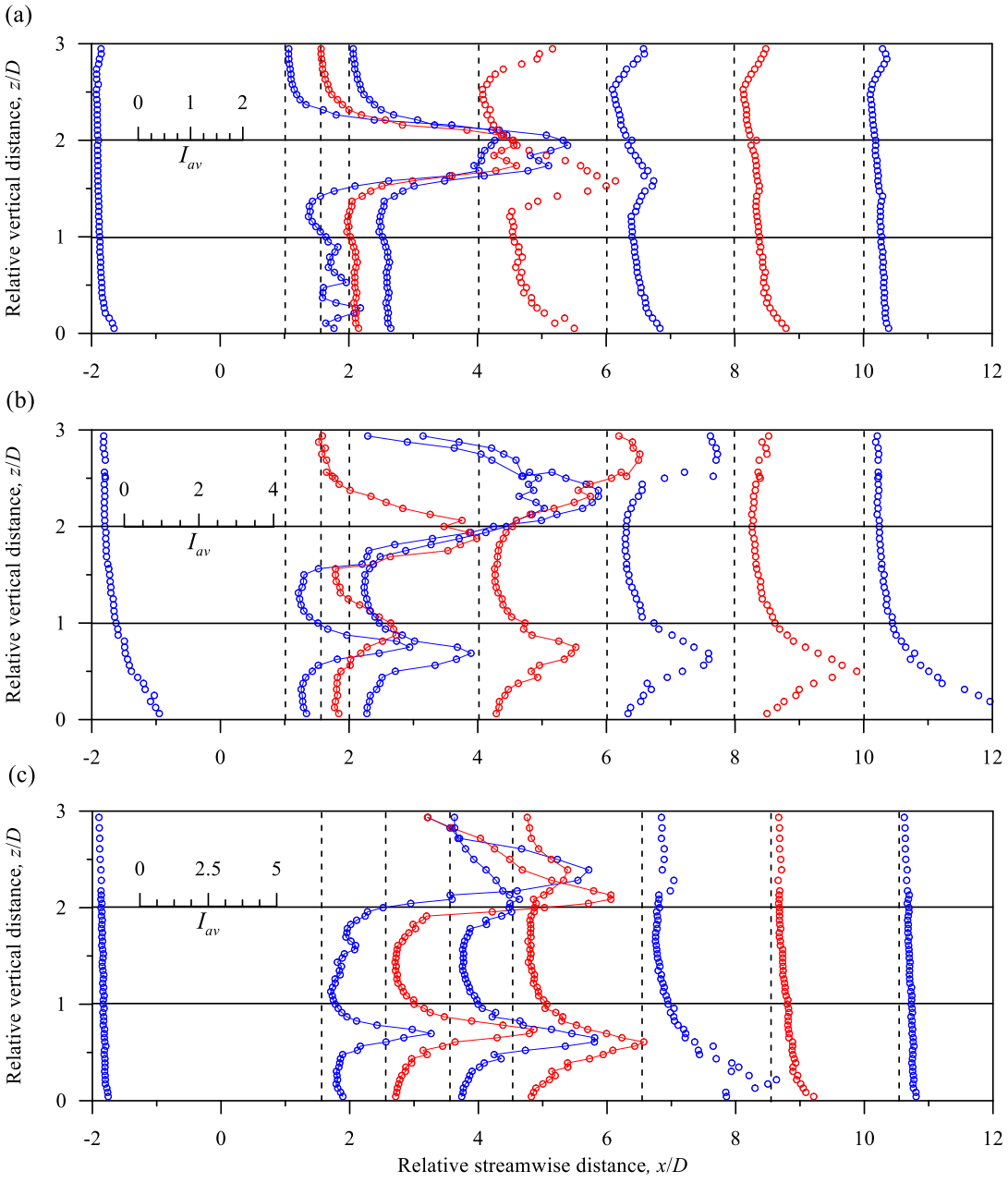

Figure 5.4. The vertical distributions of Turbulence Indicator at various *x*/*D* points in the downstream direction of two cylinders stacked one above another with diameter **(a)** *D* = 0.038 m **(b)** *D* = 0.032 m **(c)** *D* = 0.046 m

5.5 Correlation Coefficient

The vertical illustration of turbulence correlation coefficient are presented in figure 5.5(a-c). The turbulence correlation coefficient (ρ_{uw}) is described as the ratio of Reynolds stress (with respect to ρ) to the product of vertical and streamwise turbulence intensities. Mathematically, it is expressed as ρ_{uw} [$= -\overline{u'w'}/(\overline{u'u'}\times\overline{w'w'})^{0.5}$]. Near the bed, the ρ_{uw} = 0.4 – 0.5 which decreases with increase in depth. The values agree well with Hinze (1987) and Schlichting (1979) who found ρ_{uw} = 0.4 – 0.5 over most of the portion of the boundary layer. On the other hand, Dey and Nath (2010) observed $\rho_{uw} \approx 0.35$ near the bed to $\rho_{uw} \approx 0.2$ at $z^+ = 0.6$ for flow over a gravel bed and Dey and Raikar (2007) reported that the magnitude of ρ_{uw} is mostly invariant at ρ_{uw} = 0.43 for $z^+ < 0.6$ and diminishes in the direction of the free surfaces.

From the graph it is evident for near wake region, up to z/D = 1 the correlation coefficient slowly increases but after hitting its 1st peak value [$\rho_{uw} \approx 0.5$] it decreases gradually up to z/D = 1.5 where it changes its sign. It indicates that streamwise and vertical velocity components are varying linearly where initially they are moving in same direction but from z/D = 1.5 up to z/D = 2.5, their nature is quite opposite to each other. Afterwards, when z/D > 2.5 the correlation coefficient data trends are more or less identical irrespective of their downstream positions indicating the same behaviour of streamwise and vertical velocity throughout near-wake and far-wake. The non-uniformity of correlation coefficient values in near bed zone is suggesting the violation of isotropic turbulence (Sarkar et al. (2016)) i.e., existence of high anisotropy immediate downstream of the cylinders, discussed in detail in the forthcoming section. At about x/D = 12 i.e., far downstream position of the cylinders, a flow recovery of uninterrupted upstream profile is visible.

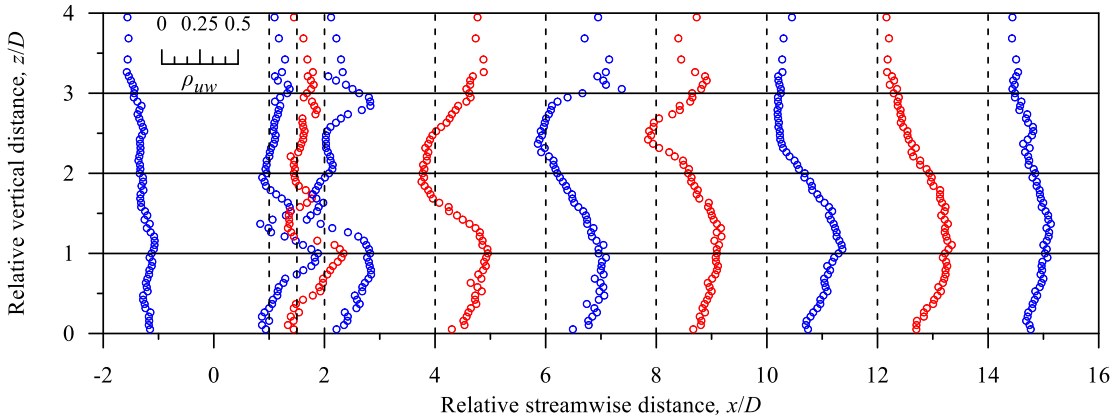

Figure 5.5(a). The vertical distributions of turbulence correlation coefficient at various x/D points in the downstream direction of two cylinders stacked one above another with diameter D = 0.038 m

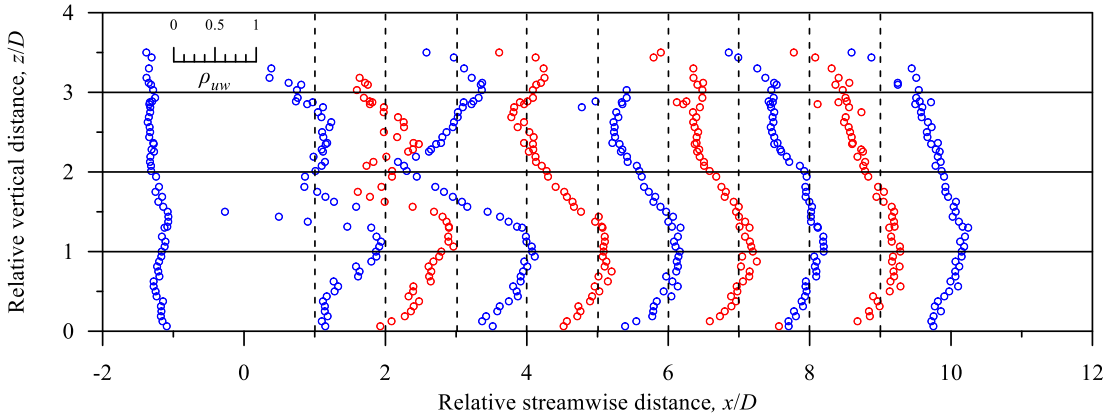

Figure 5.5(b). The vertical distributions of turbulence correlation coefficient at various x/D points in the downstream direction of two cylinders stacked one above another with diameter D = 0.032 m

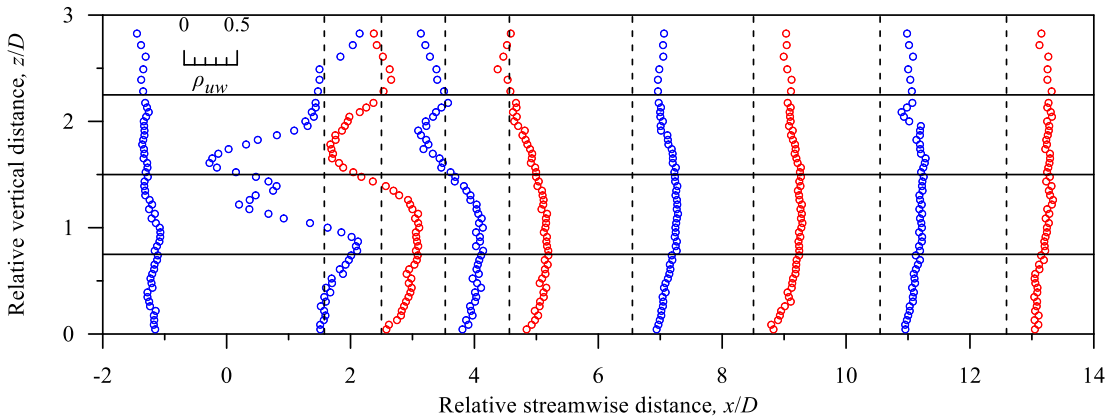

Figure 5.5(c). The vertical distributions of turbulence correlation coefficient at various x/D points in the downstream direction of two cylinders stacked one above another with diameter D = 0.046 m

5.6 Turbulence Anisotropy: stress and dissipation

Due to tremendous number of fluctuations occurring in a turbulent flow, it is assumed that the flow is having an isotropic turbulence to reduce the modelling complexity. Isotropic turbulence is an idealized turbulent state in which the turbulent fluctuations are considered to be statistically equivalent in all directions. Therefore, the velocity fluctuations are unrestricted with the axis being taken or unchanged with respect to translation and rotation of coordinate system; which concludes the Reynolds normal stresses are equivalent i.e., mathematically, $\overline{u'u'} = \overline{v'v'} = \overline{w'w'}$; where u', v' and w' represent its usual meaning. But in experimental point of view, every turbulence is anisotropic in nature i.e., the variations of the velocity components show directional preference, which also means the Reynolds stresses are unequal. Hence, there is a window of opportunity to analyse the behaviour of turbulence anisotropy in open channel and how far or close the anisotropy stands in comparison with the isotropic turbulence. There are several ways of describing turbulence anisotropy as mentioned in Dey & Nath (2010) and Pope (2000).

Reynolds shear stress anisotropy tensor is the best mathematical concept to analyze the nature and degree of turbulence anisotropy introduced by Antonia et al. (2002). The primary gain of the anisotropy tensor analysis is that there is no requirement of any additional component to make non-dimensional and at the same time it enlightens with a full-fledged illustration of the turbulent

flow features. Depending on the orientations obtained from tensor based coordinate systems, the Reynolds shear stress anisotropy tensor a_{ik} may be evaluated based on Rotta (1951) as $a_{ik} = \overline{u_i' u_k'} - \frac{2}{3} q\delta_{ik}$, where q denotes the average TKE ($\overline{u_i' u_i'}/2$) and δ_{ik} denotes the Kronecker delta function, defined as $\delta_{ik} = 0$ if $i \neq k$, or 1 if $i = k$. Furthermore, the stress tensors are normalized by the TKE q as $b_{ik} = \frac{a_{ik}}{2q} = \overline{u_i' u_k'}/(2q) - (\delta_{ik}/3)$. The b_{ik} is characterized as traceless (i.e., $\Sigma b_{i\,i} = 0$) and symmetric tensor having values in between $-1/3 \leq b_{ik} \leq 2/3$ and $b_{ik} = 0$ in case of three-dimensional isotropy. Each diagonal element's sign in b_{ik} indicates the impact of the Reynolds stress in relation to the TKE. (Dey (2014) and Hamilon et al. (2014)).

On a similar note, dissipation anisotropy tensor can also be implemented regarding the analysis of turbulent anisotropy as mentioned in Longo et al. (2017) and Djenidi et al. (2012). The tensor is being defined as follows: $d_{ik} = \varepsilon_{ik}/(2\varepsilon) - (\delta_{ik}/3)$; where $\varepsilon_{ik} = 2\nu\overline{u_{i,j} u_{k,j}}$ ($u_{i,j}$ being the differentiation of u_i with respect to x_k) is the dissipation rate of shear stress and $\varepsilon = \frac{1}{2}(\varepsilon_{11} + \varepsilon_{22} + \varepsilon_{33})$. For isotropic turbulence, all of stress and dissipation tensor terms are reduced to zero.

Figure 5.6(a) elucidates the vertical profiles of RSS anisotropy tensor b_{ik} for turbulent flow past two horizontal cylinders at different streamwise positions. The profiles of RSS tensor elements b_{11} and b_{31} indicate that the wall-wake flow closer to bed produces less turbulent anisotropy in the streamwise direction compared to their upstream distributions, whereas the wall-wake flow's constituent b_{33} remains constant. In contrast, the component b_{22} causes production of greater turbulence anisotropy in the spanwise direction. For every b_{ik} components, it is evident that as we go far downstream of the cylinders, the trend is going to recover gradually and lastly is identical with the uninterrupted upstream flow trend of anisotropy tensor. A nearly identical profile is observed in case of dissipation tensor d_{ik}, being elucidated in figure 5.6(b).

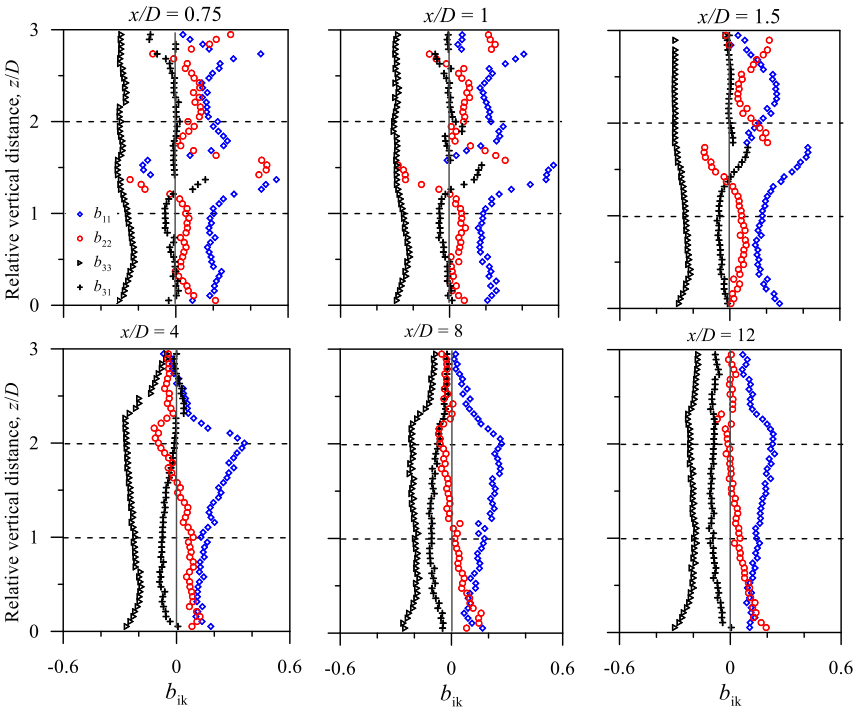

Figure 5.6(a). The vertical profiles of stress anisotropy tensor b_{ik} for turbulent flow past two horizontal cylinders (D = 0.038)

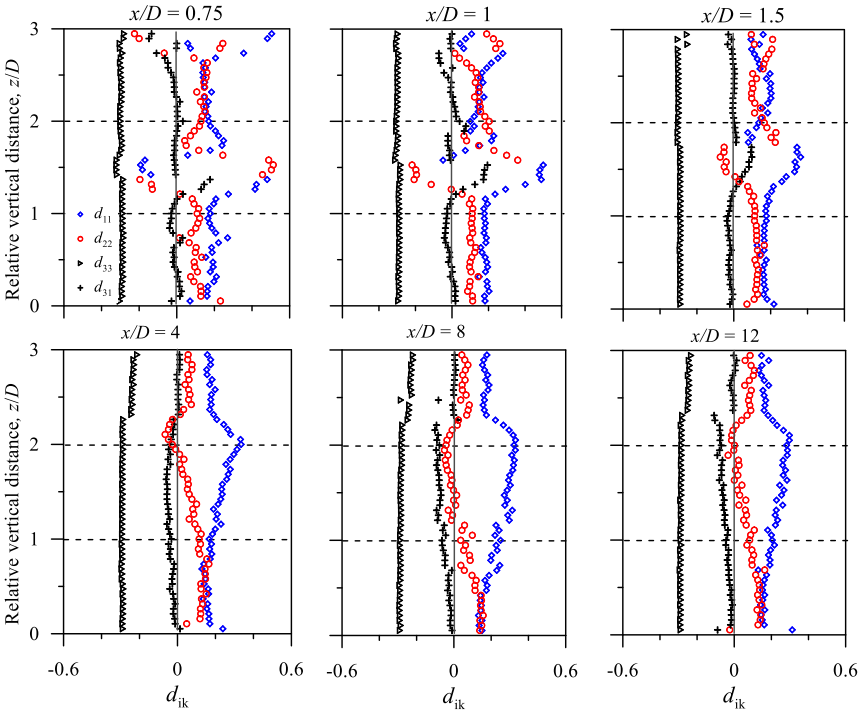

Figure 5.6(b). The vertical profiles of dissipation anisotropy tensor d_{ik} for turbulent flow past two horizontal cylinders (D = 0.038)

The overall anisotropy of turbulence can be predicted accurately with the help of a cross-plot of two primary independent invariants *II* (= $-b_{ik}b_{ik}/2$ or $-d_{ik}d_{ik}/2$) and *III* (= $b_{ij}b_{jk}b_{ki}/3$ or $d_{ij}d_{jk}d_{ki}/3$); whereas it is considered that the first invariant is zero ($I = b_{ii}$ or $d_{ii} = 0$). Anisotropic invariant map (AIM) is the cross-plot of -*II* versus *III*, where *III* signifies the type of anisotropy and -*II* (positive or zero) signifies the degree of anisotropy. The Lumley triangle, which is derived from the equations $–II = III = 0$ (origin) and $III = \pm 2(–II/3)^{3/2}$, represents the potential states of turbulence that might exist inside the left- and right-curved limits in terms of -*II* and *III*. When homogeneous turbulence undergoes axisymmetric contraction, the energy ellipsoid gives birth to pancake-shaped turbulence, as indicated by the left-curved boundary. This situation results in axially stretched turbulence eddies that take on a rod-like shape. In contrast, the right-curved boundary represents cigar-shaped turbulence, which is caused by the axisymmetric expansion of the energy ellipsoid of turbulence, where one component of TKE predominates over the other two.

Two-component 2D turbulence, represented at the left vertex of the Lumley triangle, represents the 2D isotropic condition of turbulence. This is distinct from one-component 2D turbulence, located at the right vertex, which represents a 1D turbulence state. The ordinate of homogeneous turbulence anisotropy trends toward the bottom cusp of the triangle, where $-II = III = 0$, indicating the direction of 3D isotropic turbulence.

AIMs are being plotted in figure 5.7(a) and 5.7(b) where *–II* against *III* are considered in each plot, maintaining their anisotropic bound by Lumley triangle. There is one unique characteristic being observed in the graphs, especially in near-wake zone that due to the presence of two bluff-bodies, huge anisotropy is being produced which results in occupying most spaces in the triangle. In near wake zone, the trend is as follows: the anisotropy seems to be moving from near pancake-shaped turbulence towards right side where 1D turbulence prevails in near-wall i.e., $z/D = 0$ –1.5. Afterwards, data plot moves towards left vertex showing the behaviour of anisotropy to reduce in 2D isotropy. Then the data set elucidates tendency of moving towards the bottom cusp and further staying close to origin with the further increase in *z/D*; which shows the anisotropy leaning towards the 3D isotropy. But as we go far downstream of cylinders the data set will trend from the vicinity of 2D isotropy towards the bottom cusp which indicates the 3D isotropy; hence there is a clear visualization of anisotropy recovery of the undisturbed upstream flow. In other words, the turbulence anisotropy behaves in the wall-wake flow to gradually return to a 1D (one-dimensional)

isotropy below the mid-flow depth zone and to trend in the direction of a 2D (two-dimensional) isotropic state in near-wall zone.

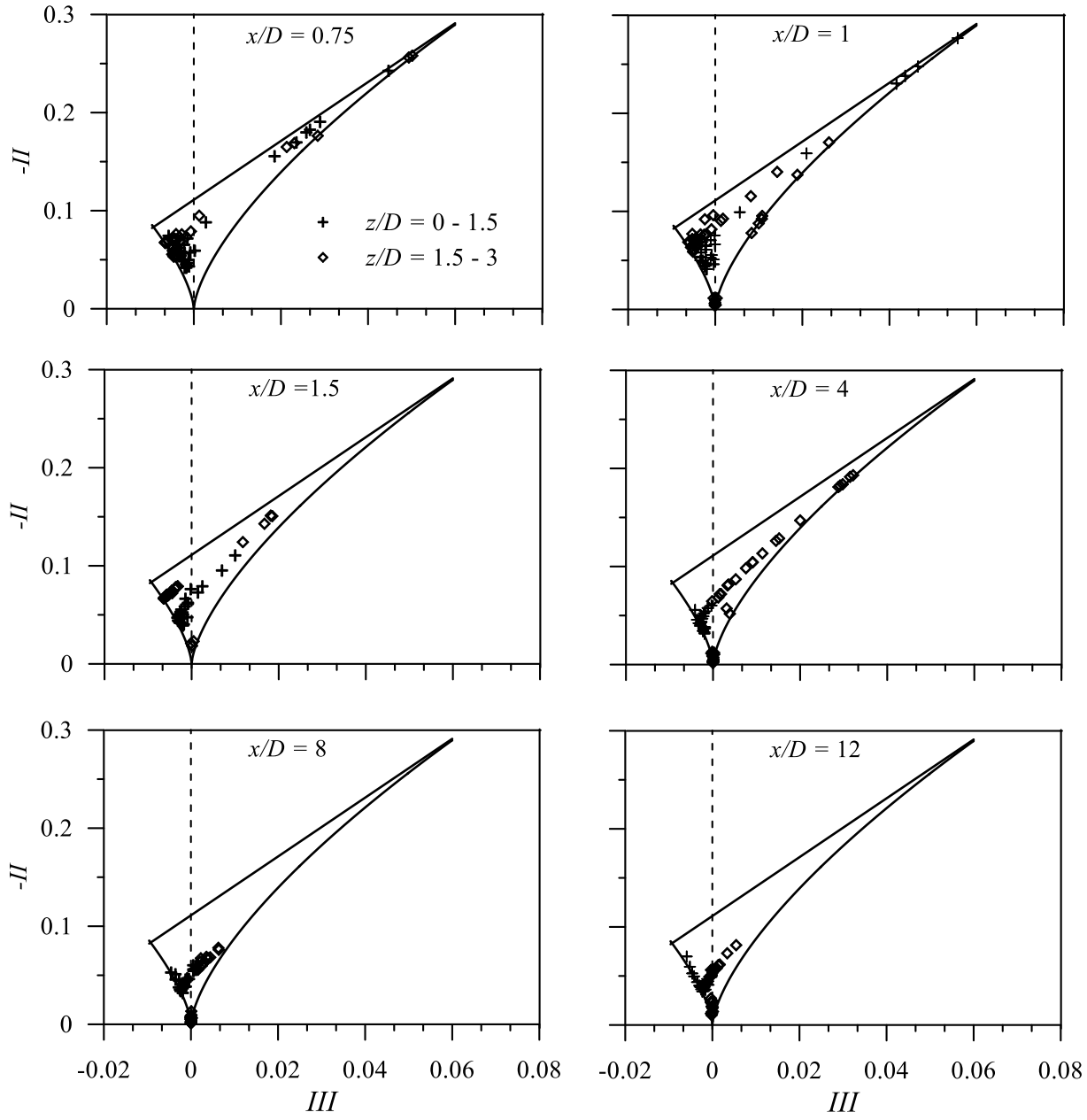

Figure 5.7(a). AIMs for different streamwise positions downstream of cylinders in case of stress anisotropy (D = 0.038)

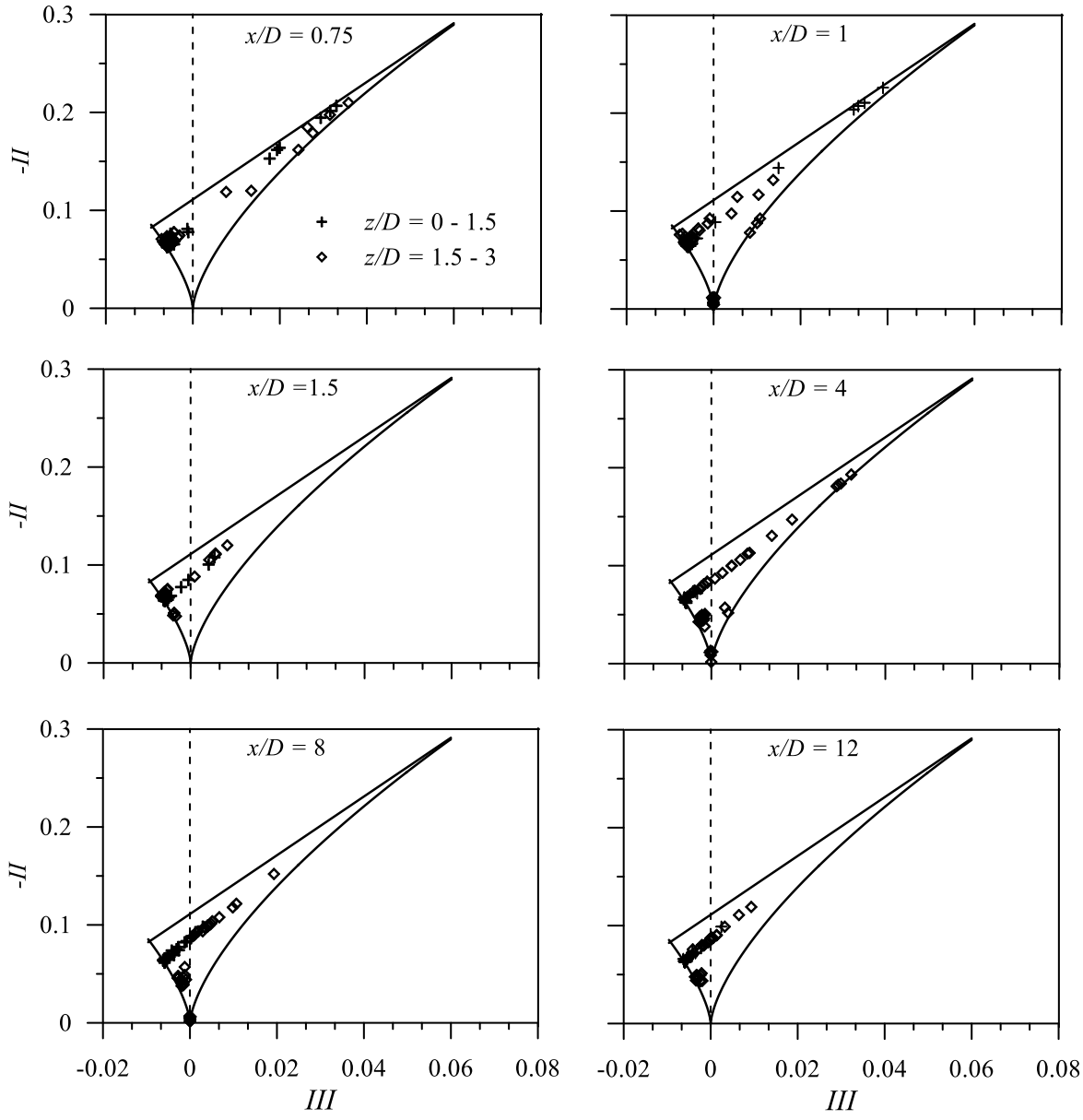

Figure 5.7(b). AIMs for different streamwise positions downstream of cylinders in case of dissipation anisotropy (D = 0.038)

Another simple and effective way to identify whether turbulence is two-dimensional or three-dimensional is by using the invariant function **F**, which is computed as **F** = 1 + 9*II* + 27*III* because of its ease of use. **F** = 0 indicates two-dimensional turbulence, whereas, **F** = 1 denotes an isotropic three-dimensional condition. Figure 5.8(a) elucidates the profiles of **F** with flow depths at several

streamwise distances. It is graphically more intriguing to observe that in near wake flow, data sets have values close to x-axis in mid flow which indicates existence of strong turbulence anisotropy. However, as the streamwise distance increases, the data set is having trend of going towards the **F**-value 1; showing the affinity towards the 3D isotropy. Although overall the graphs are increasing in nature irrespective of the downstream position in near-bed region i.e., $z/D = 0 – 0.6$; indicating moving toward three-dimensional isotropic state in near-wall. As it is expected, the loads of profiles in different x/D position are showing the tendency of recovery of the undisturbed upstream anisotropy profile at about $x = 8D$. In figure 5.8(b), invariant function **F** shows similar trend in case of dissipation anisotropy, but the overall values of **F** are less compared to the aforementioned diagram.

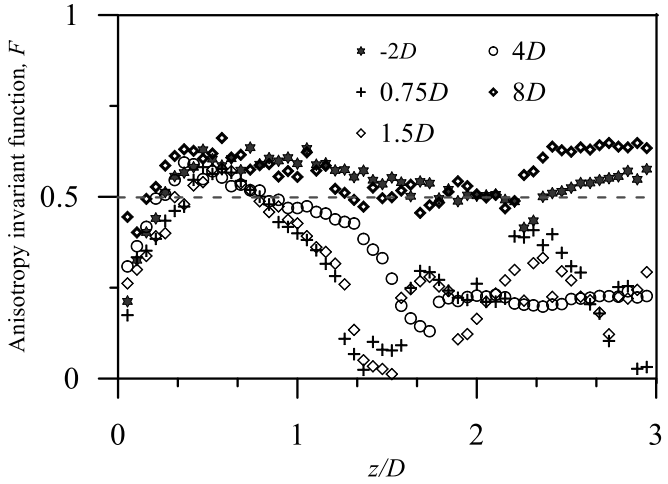

Figure 5.8(a). Vertical distribution of anisotropy invariant function **F** at different x/D positions in case of stress anisotropy ($D = 0.038$)

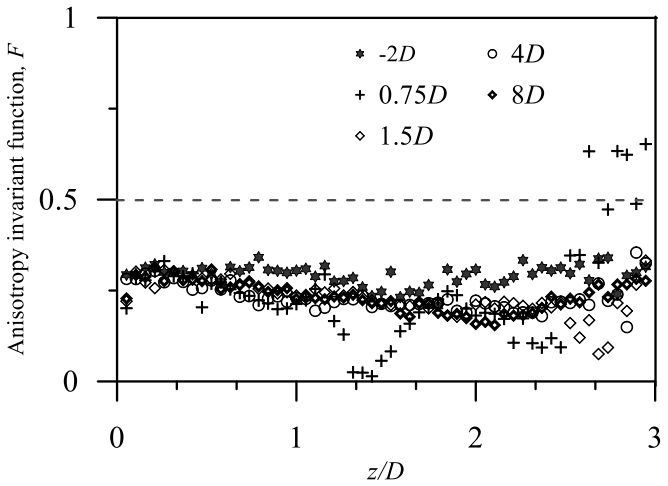

Figure 5.8(b). Vertical distribution of anisotropy invariant function **F** at different *x/D* positions in case of dissipation anisotropy (D = 0.038)

5.7 Barycentric map

The Lumley triangle has the demerit that its nonlinear behaviours distort these data randomly over the map and make analysis less comprehensible. By using a convex combination of the three limiting phases (1C, 2C, and 3C) represented by barycentric coordinates, this flaw was rectified in Banerjee et al. (2007). Firstly, it is required to evaluate these states which are nothing but weights or coefficients based on eigenvalues of the anisotropy tensor. RSS anisotropy tensor b_{ik} is defined as a symmetric and traceless tensor and the eigenvalues of this tensor are defined as follows considering the fact that trace i.e., sum of eigenvalues is zero:

λ_1 = max {eigenvalues of b_{ik}}, λ_3 = min {eigenvalues of b_{ik}}, $\lambda_2 = -\lambda_1 - \lambda_3$

The limiting state anisotropy tensors are defined as follows:

$\hat{a}_{1c} = diag\ (\frac{2}{3}, -\frac{1}{3}, -\frac{1}{3})$ indicating one-component limiting state,

$\hat{a}_{2c} = diag\ \left(\frac{1}{6}, \frac{1}{6}, -\frac{1}{3}\right)$ indicating two-component limiting state,

$\hat{a}_{3c} = diag\ (0, 0, 0)$ indicating three-component limiting state.

The anisotropy tensor $\hat{a}_{ij}$ can be represented with the incorporation of basis tensors as:

$$\hat{a}_{ij} = C_{1c}\hat{a}_{1c} + C_{2c}\hat{a}_{2c} + C_{3c}\hat{a}_{3c};$$

$$C_{1c}, C_{2c}, C_{3c} \geq 0$$

These C_{1c}, C_{2c}, C_{3c} are the coefficients of the basis tensors required to represent anisotropy tensor which satisfies the following: $C_{1c} + C_{2c} + C_{3c} = 1$; means the combination taken account of is convex. These C_{ij} are described in terms of eigenvalues as:

$$C_{1c} = \lambda_1 - \lambda_2$$

$$C_{2c} = 2\,(\lambda_2 - \lambda_3)$$

$$C_{3c} = 3\lambda_3 + 1$$

The barycentric map serves as an effective tool for visualizing the nature of turbulence anisotropy in tensor $\hat{a}_{ij}$ for several type of turbulent flows which in our case is flow past cylinders. To plot the barycentric mapping, we denote the basis matrices $\hat{a}_{1c}$, $\hat{a}_{2c}$, $\hat{a}_{3c}$ of the above equation as the three vertices of the triangle respectively starting from right; which further can be mapped into three points (x_{1c}, y_{1c}), (x_{2c}, y_{2c}) and (x_{3c}, y_{3c}) in the Euclidean space by suitable transformation indicating the three limiting states. For plotting a point, the convex combination of the limiting states used is described as below:

$$x_{new} = C_{1c}\,x_{1c} + C_{2c}x_{2c} + C_{3c}x_{3c}$$

$$y_{new} = C_{1c}y_{1c} + C_{2c}y_{2c} + C_{3c}y_{3c}$$

Another important observation of the barycentric map is that the data points do not leave the triangle due to the convex combination; hence the triangle can be drawn by taking any three arbitrary points (x_{1c}, y_{1c}), (x_{2c}, y_{2c}) and (x_{3c}, y_{3c}) preferably representing equilateral triangle. Due to the fact that all limiting state coefficients range between [0, 1] and that an equilateral triangle does not produce any visual bias toward a particular limiting state, the barycentric map is depicted as an equilateral triangle.

Before jumping into the barycentric maps, it is mandatory to check whether the barycentric coordinates C_{1c}, C_{2c}, C_{3c} provide correct analogy to the turbulence anisotropy. In order to validate this, we use the relation between these coordinates and third principal invariant (*III*) defined as below (Andersson et al. (2021)):

$$III = \frac{2}{9}C_{1c} + \frac{1}{6}C^2_{1c}C_{2c} - C_{1c}C^2_{2c} - \frac{1}{36}C^3_{2c}$$

Figure 5.9 elucidates third principal invariant *III* profile with respect to flow depth at streamwise distance *x/D* = 2 evaluated from stress anisotropy tensor b_{ik} and barycentric coordinates C_{ic} respectively. It is evident from the graphs that they are having identical profile with increment up to z/D ≈ 2.3, followed by a gradual decrement. It ensures the turbulence anisotropy predication of the barycentric map obtained from the translation of stress anisotropy tensor.

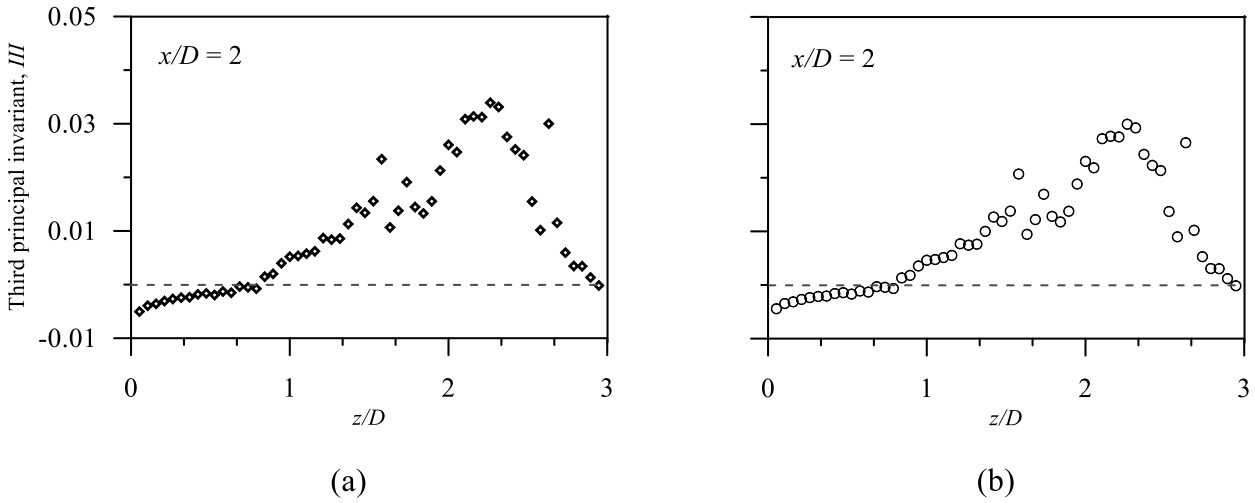

Figure 5.9. Third principal invariant *III* profile with respect to flow depth at streamwise distance *x/D* = 2 evaluated from (a) stress anisotropy tensor b_{ik} and (b) barycentric coordinates C_{ic}

Figure 5.10. represents barycentric maps for stress anisotropy in wall-wake flow past cylinders at several streamwise positions. Each map being convex combinations of three points, has been described via a equilateral triangle having vertex as 1c, 2c and 3c. These are representatives for limiting states which are defined as follows:

One-component turbulence (1c): Anisotropy eigenvalues are given by $\{2/3, -1/3, -1/3\}$, where the turbulence is only effective in a single direction along eigenvector corresponding to a certain nonzero eigenvalue.

Two-component axisymmetric turbulence (2c): Anisotropy eigenvalues are {1⁄6, 1⁄6, −1⁄3}, where a certain direction is ineffective and turbulence only have the scope to act through a 2D plane.

Three-component isotropic turbulence (3c): Anisotropy eigenvalues are {0, 0, 0}. As the eigenvalues indicate, this is the representative of 3D isotropic state where turbulent characteristics have no such directional preferences i.e., fluctuations can act randomly in any direction having the same impact on flow.

In near-wake region, the data set trend is observed to be from left to right towards the vertex 1c; meaning the anisotropy is being shifted from two-component to one-component which indicates strong generation of anisotropy behaviour in near-wall zone. Afterwards, the flowchart of data gradually inclines in the direction of vertex 3c which is nothing but the representative of 3D isotropy. Hence with the increment in flow height, the nature of anisotropy is shifted towards 3D isotropy. One interesting fact is that in the vicinity of cylinders at x/D= 0.75 the barycentric coordinates are forming two loops; small one is near the vertex 2c and the large one is spreading from 2c towards 1c. It is consistent with the fact that the anisotropy invariant function, **F** is having two sudden falls in the same streamwise position [see figure 5.8] which correspond to the loops in barycentric map. In fact, these falls or loops are generated just behind the cylinders as the amount of disturbance in the vicinity of the cylinders is huge. Also, in Lumley triangle the bottom cusp being the indication of 3D isotropy, is similar to the concept of three-component turbulence 3c present in barycentric triangle. In fact, there is a one-one correspondence between AIM (-*II* vs *III*) and barycentric coordinates. As the downstream distances increases, the anisotropy behaviour is becoming more limited between 2c and 3c suggesting pure isotropy dominance and recovery of undisturbed upstream flow characteristics.

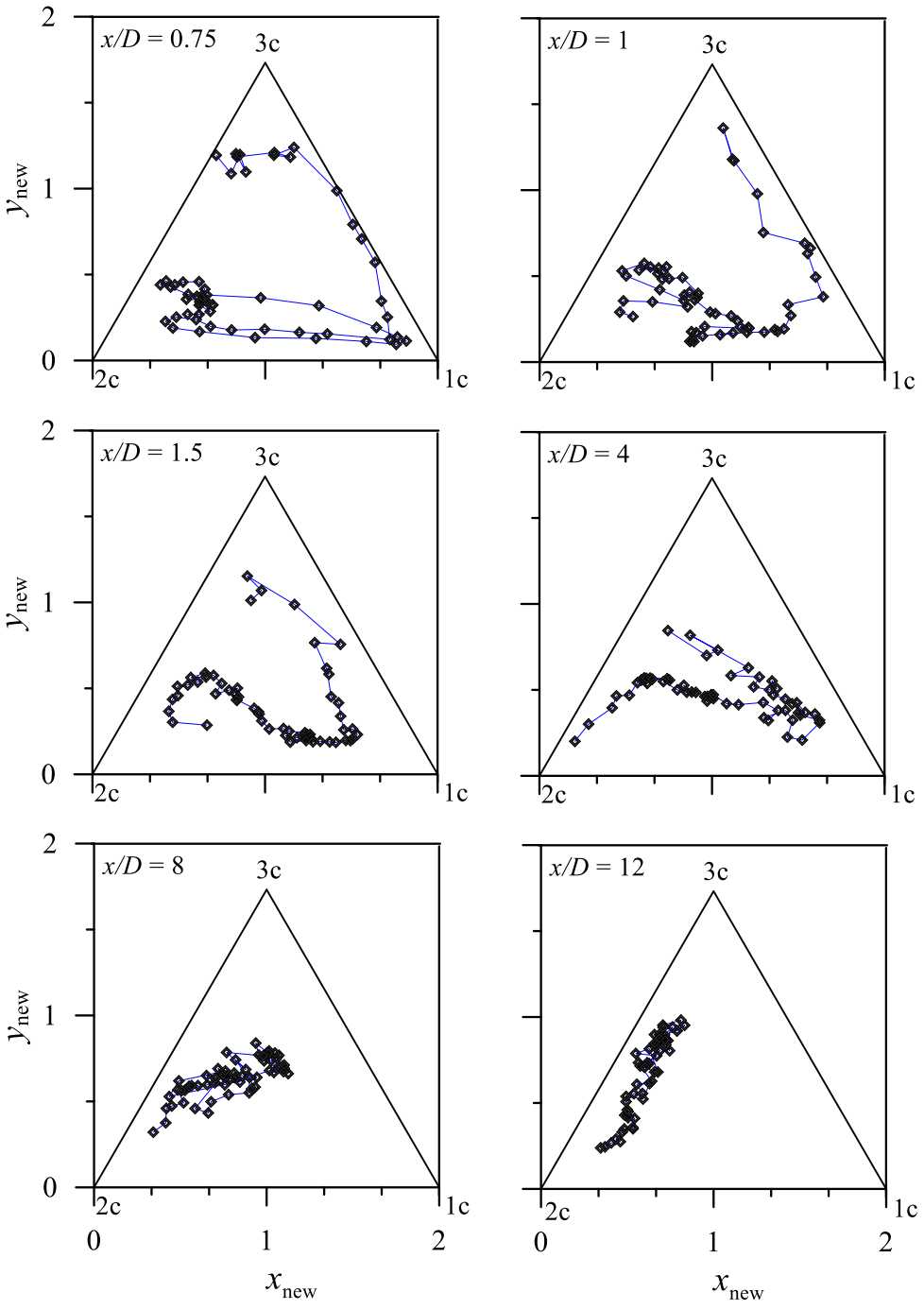

Figure 5.10. Barycentric maps for stress anisotropy in wall-wake flow past cylinders with diameter D = 0.038 m

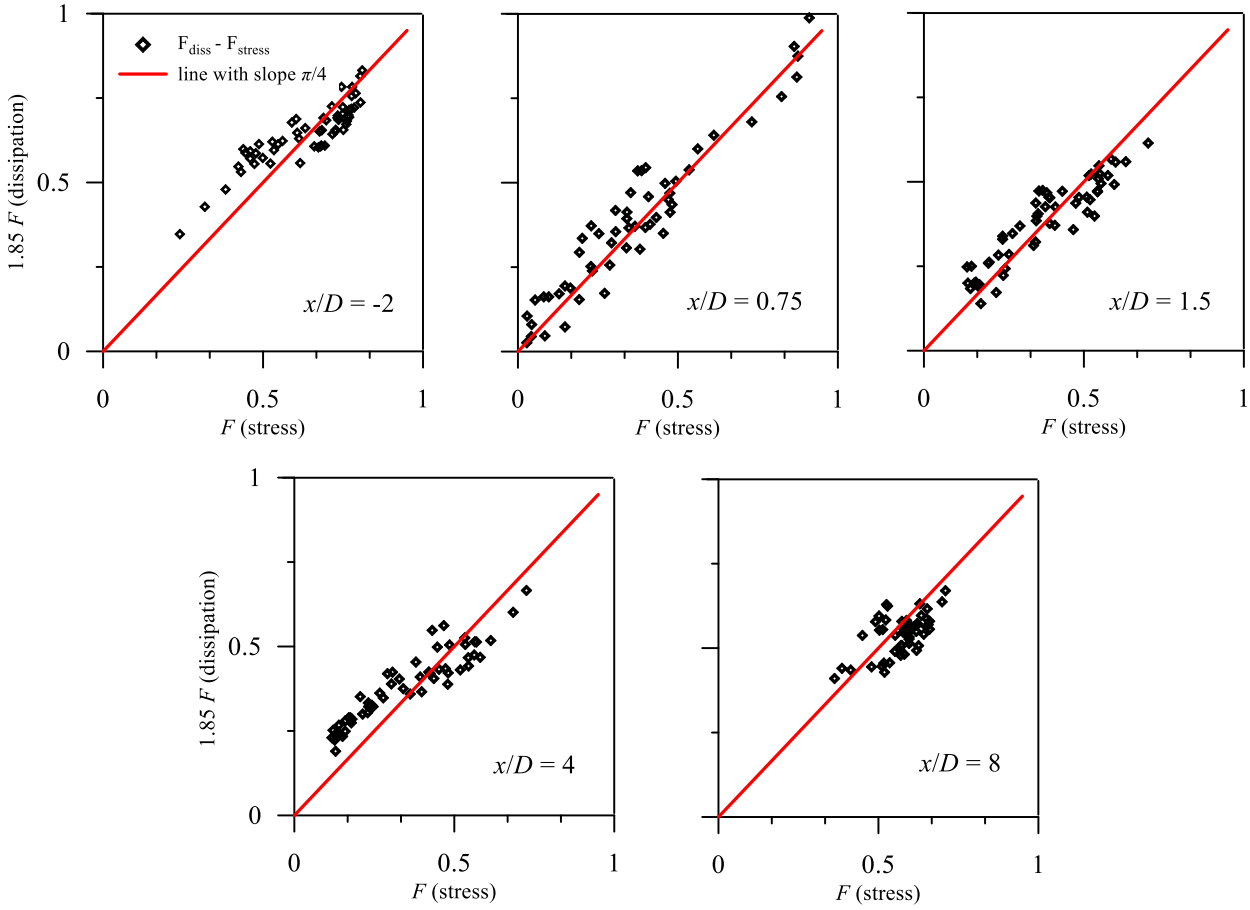

Figure 5.11. Comparison between anisotropic invariant functions for stress and dissipation at different downstream positions, mostly overlapping with the line having slope $\boldsymbol{\pi}/4$

5.8 Conclusion

The experimental results of turbulent flow through two cylinders—one mounted on a wall and the other suspended—are presented in this article. The data obtained from flume experiments have been thoroughly analysed to elucidate streamwise velocity, RSS, turbulent kinetic energy and indicator, correlation; furthermore, RSS anisotropy and dissipation anisotropy have been presented to analyse the nature of turbulence with the help of Anisotropy Invariant Map (AIM) and

barycentric map. In the near wake, recirculatory flow arises because of the interaction between the two cylinders, whereas the far wake region exhibits no significant variation. Distributions of Reynolds shear stress and turbulence indicators reveal a notable increment in values immediately behind both cylinders, with these increases being strongly influenced by the diameters of the bluff bodies in the flow. Correlation values indicate a linear relationship between streamwise and vertical velocities in near bed and near surface zone, but having less negative correlations behind the cylinders suggesting reverse flow due to opposite directions of streamwise and vertical fluctuations. Stress and dissipations tensor have been compared for different downstream positions which shows the near-wall wake flow produces lesser turbulence anisotropy in the streamwise direction in comparison with their upstream distributions. According to AIMs, the turbulence anisotropy in the wall-wake flow exhibits a behaviour that converges towards a 2D (two-dimensional) isotropy close to the wall and gradually returns to a 1D (one-dimensional) isotropy beneath the mid flow depth zone because of the existence of two cylinders. Invariant function **F** indicates in near wake flow, data sets have values near zero in mid flow suggesting existence of strong turbulence anisotropy. Moreover, upon comparison, stress **F** values are quite larger than dissipation **F** values, validating **F** (stress) ≈ 1.85 **F** (dissipation) in figure 5.11, at near wake as well as far wake zone. To visualize anisotropy in a more convenient way, AIMs have been mapped into barycentric coordinates, which provide insights such as correspondence between the sudden falls in **F** with the loops formed inside the equilateral triangle. Three separate experimental results for some of the aforementioned features have been shown to corroborate these findings; these results demonstrate the consistency of the graphs when compared at various downstream points.

The experimental setup faces constraints due to the limitations of Acoustic Doppler Velocimetry (ADV). Specifically, while the sample frequency has minimal impact on the time-averaged velocity measurements, ADV struggles to accurately assess turbulent characteristics beyond a 1 cm sub-region within the 3 cm profiling scope. This necessitates careful consideration when using ADV to study turbulence in open channel flows.

An ideal solution would involve utilizing Particle Image Velocimetry (PIV), which provides spatial and temporal resolution to capture detailed turbulence dynamics. Alternatively, numerical modeling presents a viable option for overcoming these limitations. For instance, Baykal et al. (2015) used 3D numerical models based on the RANS equations with the κ-ω turbulence closure

to study scouring and flow around a vertical circular cylinder, incorporating vortex shedding and sediment transport. In our case, replicating the experimental setup through numerical modeling using commercial software offers a promising avenue. Implementing the RANS equations alongside the κ-ω turbulence model would enable the generation of detailed data for turbulence analysis. Future research will focus on empirically studying additional turbulent properties and integrating numerical modeling into experimental frameworks to validate findings.

Chapter 6

Turbulent bursting and higher-order moments in the wake flow behind two horizontal cylinders

6.1 Introduction

Hydraulicians have continued to be interested in wake flow behind a wall-mounted bluff body due to its applicability in several real-world hydraulic engineering scenarios including environmental and geophysical flow structures. The wall-wake flow, which is the prolonged interrupted flow zone behind a wall-mounted obstruction, is crucial to the erosion of riverbeds caused by hydraulic structures. Obstacles such as water-conveying pipelines, and cables placed on riverbeds interact with the flow in ways similar to bluff body dynamics, leading to flow separation, increased turbulence, and vortex shedding. These flow disruptions can cause localized scouring and sediment deposition, impacting the river's morphology and the stability of the structures. In addition, fish passages and habitat structures are often designed to accommodate the altered flow, ensuring that fish can navigate these obstacles while maintaining suitable habitats. The design of such passages must consider the effects of these obstacles on flow patterns to ensure minimal ecological disruption, preserve water quality, and avoid interference with fish migration routes. Careful placement of these structures helps balance environmental needs with human infrastructure. The wake flow zones namely, near and far wake are the two most critical regions in bluff body hydrodynamics. They continue downstream of a wall-mounted bluff body for a specific distance, based on the body's size and form and the flow conditions and finally return to the undisturbed condition. Assessing the importance of the problem, a large number of researchers of different fields have explored the problem from different directions using different techniques. For instance, Dey (2014) focused primarily on the hydraulics problems that need a thorough understanding of sediment characteristics in turbulent flows, as here is where the majority of current research findings in the area are presented. Schlichting et al. (1979) proposed a classical similarity theory in bluff-body hydrodynamics to describe the velocity defect profiles in free wake flows behind a circular cylinder subjected to an approach free-shear flow. Sadeque et al. (2008) presented experimental

findings on flow over cylindrical structures in an open channel. Their observations, derived from flow visualization studies, were validated through measurements of bed-shear stress and deflected flow velocity over the cylinders. It has been discovered that submerging a cylinder suppresses alternating vortex shedding and strengthens 3D flows in the downstream wake. Dey et al. (2018) investigated the turbulent features of wake flows behind cylinders positioned near the bed and mounted on the wall. When normalized by their respective peak defect values, the streamwise velocity defect, Reynolds shear stress, and intensity distributions exhibited a degree of self-preserving behavior.

Flow around cylinders can significantly interact with aquatic elements like fish, plants, and sediment in various ways. For instance, submerged aquatic plants and sediment in river systems can modify flow patterns, creating complex fluid-structure interactions. These plants often act as natural roughness elements, altering the hydrodynamics and influencing sediment transport and deposition. This can have direct effects on bluff body flows, such as in the case of underwater structures where the presence of vegetation may change the wake dynamics behind the structure, influencing local sedimentation patterns and flow-induced vibrations (Wu et al. (2022); Madsen et al. (2001)). Additionally, fish are affected by these flow alterations, as they need to navigate both the wake structures created by bluff bodies and the modified environments influenced by plants and sediment. The fluid-structure interactions can also impact energy dissipation and nutrient distribution, crucial for aquatic ecosystems (Ben Jebria et al. (2023); Farzadkhoo et al. (2023)). Few of the research works relevant to bluff-body hydrodynamics can be found in (Wang et al. (2022); Ali and Dey (2024); Sarkar and Dey (2020); Dey et al. (2020); Dey et al.(2018)). However, the bluff-body plays an important role in turbulent bursting which is also an important phenomena in open-channel turbulence and therefore in the current chapter, we were keen to explore the turbulent bursting downstream a pair of bluff-bodies. Here, two cylinders of same diameter were taken concurrently one above the other with a gap of the diameter of a cylinder during a single experiment. It is important to note that the turbulent bursting under aforementioned experimental condition was not experimentally explored so far according to the literature survey.

Research on open-channel turbulence from 1960 to 1970, including studies by Kline et al. (1967), Corino and Brodkey (1969), and Grass (1971), demonstrated that the flow patterns near the wall in a turbulent boundary layer exhibit repetitive behavior. This flow follows a quasi-

cyclic process known as the bursting cycle. In principle, the flow alternates between low-speed and high-speed sections close to the bed. They are also known as high- and low-speed streaks, even though there may not be much of a velocity difference between them. A limited and transient unfavorable pressure gradient can cause a low-speed fluid streak to separate, much like it does a boundary layer in presence of an unfavourable pressure gradient. This leads the coherent, low-speed fluid to enter to the flow's main volume. This phenomenon is referred to as the ejection event. In the sweep process, high-speed fluid moving towards the bed displaces the expelled fluid left behind due to retardation. The quadrant analysis categorizes the local flow behavior into four quadrants, depending on the sign convention of the streamwise velocity fluctuation (u') and vertical velocity fluctuation (w'). Four quadrants are categorized as follows: The first quadrant, characterized by $u' > 0$ and $w' > 0$, represents a high-speed fluid event moving toward the fluid flow field's center; the second quadrant, characterized by $u' < 0$ and $w' > 0$, represents a low-speed fluid event moving toward the fluid field's center and away from the wall (ejection); the third quadrant, characterized by $u' < 0$ and $w' < 0$, represents a low-speed streak of fluid moving to the direction of the wall; and the fourth quadrant, where $u' > 0$ and $w' < 0$, represents the inward movement of high-speed streak of fluid from the outer flow to the direction of the wall (sweep). The first researchers to detect bursting occurrences in open-channel flow were Nakagawa et al. (1977). They sought to investigate the contribution of bursting events to the total Reynolds stress by using the conditional probability distribution of Reynolds stress. However, the quadrant analysis introduced by Lu and Willmarth (1973) is one of the most effective and easiest way to understand turbulent bursting in two-dimensional form. Experimental research was done by Mianaei and Keshavarzi (2010) to examine the turbulent bursting occurrences in near-bed over the ripples and the process of sediment transport. The examination of the shear stress ratio across the ripples for each quadrant at the fixed bed experiments revealed that, while it changes as one moves downstream, the shear stress ratios of quadrants (*II*) and (*IV*) were greater than those of quadrants (*I*) and (*III*) upstream of the first ripple. Ikani et al. (2023) analyzed how each bursting event contributed to the formation of RSS to determine the crucial events and turbulence features surrounding the piers. While sweeps were more prevalent downstream, powerful ejection and sweep events had been reported in the uninterrupted near-wake flow. Ghasemi (2016) presented an innovative technique for

Figure 6.1. Photographs of the experimental set up

determining the wave numbers linked to the macroturbulence and bursting. This work had implications for bedload and suspended load sediment transport, as demonstrated by the results of this study, which offered a method to compute the streamwise TKE of bursting and macro-turbulence for a given roughness. The time-averaged characteristics of turbulent flows around a sphere set on a rough wall were investigated by Dey et al. (2011). The quadrant analysis verified that sweeps, which were caused by a surge of fluid streaks, were the regulating mechanism in wall-wake flows. Although the bursting episodes were more frequent than those in the upstream, they last shorter periods of time. In order to better understand wall-wake flow, Bauri et al. (2020) performed experimental research to look into the impact of immersed cylinders on bursting occurrences and sediment transport. Wall-wake flows were governed by sweeps, as their quadrant analysis demonstrated. Similar findings were reported by other research that used quadrant analysis to examine a single circular bridge pier as in Keshavarzi et al. (2014). Dey et al. (2020) conducted experimental research on the turbulence properties in

flow across and inside the interfaces of 2D dunes. Their bursting analysis supported the notion that the flow zone above the crest and the interfacial sublayer are governed by ejections and sweeps, respectively.

Aforementioned discussion suggests that numerous research have been performed on experimental analysis of turbulent bursting in open channel flow to analyse basic turbulent flow characteristics such as velocity, intensity; however, there is no investigation present in literature which demonstrated experimental bursting results in presence of two bluff bodies altogether. In the presence of two cylinders, Sarkar et al. (2023) showed how flows are influenced; that is, from basic turbulent features like Reynolds Shear Stress (RSS) and intensities, up to sophisticated characteristics like TKE dissipation rate and budget. Additionally, in the same experimental environment, Samanta et al. (2023) presented several advanced analyses, including correlation coefficient, stress anisotropy, and dissipation anisotropy. Therefore, to extend our previous work, this manuscript focuses on turbulent bursting events in near-wake and far-wake zone downstream of two horizontal cylinders. Moreover, it is wise to accept that open-channel flow is highly chaotic in nature. Hence in near-wake, especially in presence of two cylinders under or overestimation may happen in few positions.

6.2 Experimental setup

The analysis of the current chapter is solely dependent on the experimental data of Sarkar et al. (2023) and Samanta et al. (2023). Salient features of the experiment, pre- and post-processing of the raw data are thoroughly explained in chapter 3 and 4. The experiment was conducted in the Fluvial Mechanics Laboratory of the Indian Statistical Institute in Kolkata, India in a rectangular-shaped flume (figure 6.1).

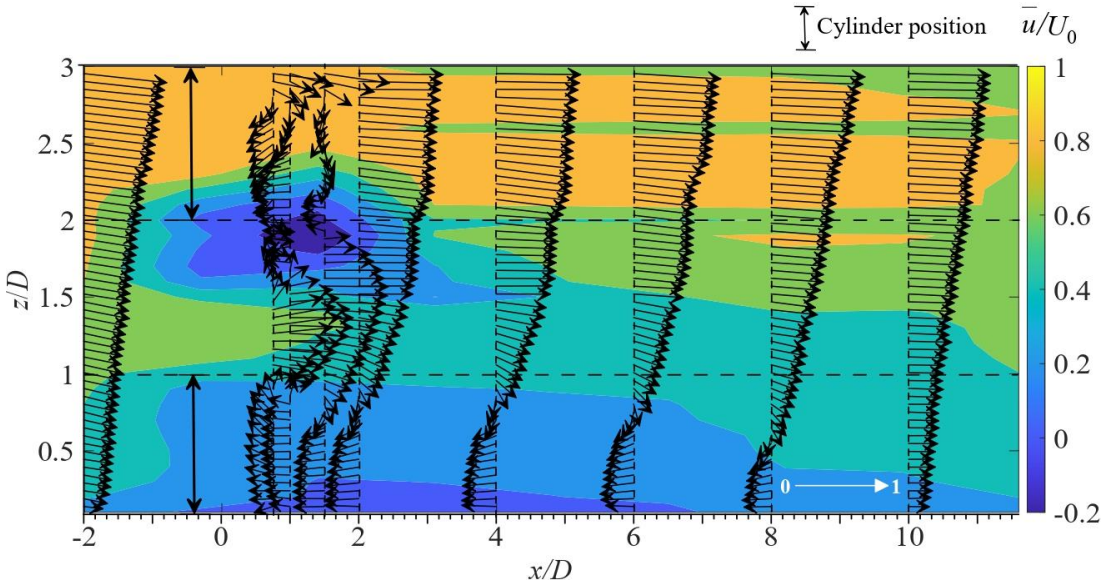

Figure 6.2. Contours of streamwise velocity vector in wall-wake flow past two horizontal cylinders

6.3 Physics of flow

Bluff-body hydrodynamics is one of the most intriguing topics in fluid mechanics and it is pertinent to understand the physics of flow past bluff-bodies. In general, far upstream of the such bodies, no effect is observed. However, the wakes are generated behind the bluff body that sustains up to a fixed distance given the shape of the body and the flow parameters and diminishes as one moves further downstream. In the present research, the experimental configuration of the wall-wake flow past two horizontal cylinders one above another is being considered and shown in figure 6.2. The incoming flow via the horizontal cylinders in just downstream position is being divided by the cylinder walls and generates recirculatory eddies with a reversed streamwise velocity, being depicted with the incorporation of contours and non-dimensional streamwise velocity vectors ($\overline{u}/U_0$) as evident from the figure 6.3. The term "near-wake flow" describes this flow. Reversed flow with a velocity that is lower than the approaching velocity at a particular elevation characterizes the near-wake zone because the effects of the near-wall cylinder-induced reversed flow govern those of viscous diffusion. Far-wake flow is the term for the disrupted flow that continues behind the cylinders. The cylinders' influence on

flow become weaker in this flow zone, which make the reversed flow to gradually diminish. The physical constraints of the Vectrino probe prevent it from recording the reversed flow in the near-wake. Two high deterioration in streamwise velocity up to $x/D < 3$ can be seen as a result of recirculating effects in figure 6.3. In the far-wake zone, the velocity distribution gradually regains its original velocity profile, which was not altered, as the downstream distance x grows. The figures show some indication of flow recovery; at $x/D = 10$, the $\overline{u}/U_0$-profile resembles the velocity profile from the first approach, but a nearly-full recovery is shown at a considerable downstream distance. However, it is well-established from this as well as earlier studies that since the velocity vectors modify significantly due to the placement of the bluff-body, all the parameters change their behavior accordingly. It is pertinent to discuss that based on the present experimental data used in this article, so far the authors have presented their results in terms of turbulent streamwise velocity, Reynolds shear and normal stresses, intensity, anisotropy in the aforementioned experimental conditions can be seen in Samanta et al. (2023). However, to avoid the repetition of the flow physics that were already explored, in the next section onwards the turbulent bursting results based on the quadrant analysis will be discussed.

6.4 Quadrant Analysis

Studying the conditional statistics of the velocity variations (u' and w') on an $u'w'$ -plane is essential to comprehend the features of the bursting events, which are being characterized by four quadrants, namely outward interactions Q_1 ($u', w' > 0$), ejections Q_2 ($u' < 0, w' > 0$) , inward interactions Q_3 ($u', w' < 0$), and sweeps Q_4 ($u' > 0, w' < 0$) . A hole-size threshold H (Dey (2014)) is used to determine which quadrant's stronger contributions to $-\overline{u'w'}$ are; where $-\overline{u'w'}$ represents the Reynolds Shear Stress (RSS). Stronger events, characterized by data plots extending beyond the hole region, can be distinguished from weaker events confined within the hole region, based on the values of *H*. The hole region is determined by the following $u'w'$-curve, $|u'w'| = H \left(\overline{u'^2}\right)^{0.5} \left(\overline{w'^2}\right)^{0.5}$. The following equation can be used to calculate the time-averaged contribution to the overall Reynolds shear stress for a particular quadrant *i* beyond the hole size *H*:

$$\overline{u'w'}^{i,H} = \lim_{T\to\infty} \frac{1}{T}\sum_0^T u'w'\lambda_{i,H}dt$$

When the instantaneous time is *t*, the sampling time is *T*, and the indicator function $\lambda_{i,H}$, being defined as

$\lambda_{i,H}$ = 1, when in quadrant Q_i and $|u'w'| \geq H \left(\overline{u'^2}\right)^{0.5} \left(\overline{w'^2}\right)^{0.5}$ and $\lambda_{i,H} = 0$, otherwise.

The previously described approach, referred to as quadrant analysis, quantifies the fractional contributions made by the bursting events in quadrant *i* beyond the region of hole-size *H* toward the formation of RSS. The proportionate fractional contributions to the formation of RSS are provided by:

$$S_{i,H} = \frac{\overline{u'w'}^{i,H}}{\overline{u'w'}}$$

The data plots of the $S_{i,H}$ with respect to dimensionless vertical distances *z*/*D* for *H* = 0 at various *x*/*D* are displayed in figure 6.3 and 6.4 to help analyze the proportionate contributions towards the RSS from the bursting incidents. To analyse the significance of high-frequency occurrences with minimal values relating to every set of *u*' and *w*' in a wall-wake flow, it is essential to set *H* = 0. The Q_2 and Q_4 events close to the wall contribute almost 90% ($S_{2,0} \approx S_{4,0} \approx 0.9$) to the RSS in the unaffected upstream flow (*x*/*D* = −2), while the Q_1 and Q_3 incidents provide moderate influence, at 40% each ($S_{3,0} \approx S_{1,0} \approx 0.4$). It appears that the emergence of a number of high-speed fluid stripes from the outside flow zone nearly cancels out the production of low-speed fluid streaks from the near-wall flow region, as the magnitudes of the Q_1, Q_3, Q_2 , and Q_4 events are nearly identical. The assumption that the occurrences cancel one another completely in the near-wall area is further supported by the observation that the mean durations of the Q_2 and Q_4 events are the same, as illustrated in the next section. But far away from the wall (*z*/*D* ≈ 3.5), the Q_2 event characterizes the unaltered upstream flow, suggesting that the Q_2 events leads to a dominant, slower moving process. All events show a marked amplification in the inner layer of the wall-wake flows downstream of the cylinders (*x*/*D* > 0). In near-wake flow zone immediately behind the cylinder (*x*/*D* = 0.75-1.5), for 0 < *z*/*D* < 1.5, the contributions of Q_1, Q_3 events are nearly equal and cancel one another out; although, Q_4 event (sweep) dominates over Q_2 (ejection) which is also reflected in the third order moment plots (figure 6.10). One intriguing observation is that in the near-wake zone,

sweep events contribute to the creation of RSS in the order of 600% ($S_{4,0} \approx 6$) at $x/D = 1$ near the wall, resulting in a surge of accelerating fluid streaks. This massive amount of inrush is due to the presence of two cylinders downstream, due to which another surge is observed at about $z/D \approx 2$. The reason behind such dominance of sweep events in near-wake is due to the reduction of stress in overall bursting events after time-averaging, making stress in sweep six times larger than overall bursting period. There are findings from literature (Sarkar (2016); Demare, et al. (1999); Raushan et al. (2018)), where stress ratios are reported to be 4 or 6, contributing 400 or 600 % to the formation of RSS. All the events' contributions, however, diminish as z/D increases further. When the distributions of Q_2 and Q_4 events intersect at $z/D \approx 2$, Q_2 events take precedence over Q_4 events with the increment in z/D. Consequently, because of the surge of fast-moving fluid stripes, sweep events serve as the controlling mechanism in wall-wake flows; while ejection prevails over sweep far away from the bed. The governing effect of the Q_4 events eventually diminishes as the distance x/D grows, allowing the Q_2 events to emerge and restore the flow properties in the unaffected upstream flow. Meanwhile, the Q_1 and Q_3 events' contributions are remained rather minimal, aside from immediate behind the cylinders, where the inward interaction Q_3 mostly dominate over the outward interaction Q_1.

Figure 6.5 and 6.6 illustrate how $|S_{i,H}|$ varies for H at various z/D and $x/D = -2$ (unaffected upstream flow), 0.75, 2 (near-wake flow), 6 (far-wake flow) respectively. To depict the properties of $|S_{i,H}|$ at the regions of near-wall flow and intermediate zone between two cylinders, the heights $z/D = 0.26$, 0.52, and 1.05 were used. As is customary, each event has a relatively high effectiveness for smaller H values, but their contributions decrease as H increases. All the events, regardless of location x or vertical distance z, vanish completely for $H \geq 15$. More specifically, the Q_2 and Q_4 events stay finite, whereas the Q_1 and Q_3 events disappear at a lesser value of H (H = 5-7) due to prolonged effects of ejection and sweep events over larger hole sizes. The detailed explanation is given by the elliptical dispersion of the u' and w' data plots, which have a primary axis that is skewed over the second and fourth quadrants. Two cylinders's presence were prevalent at $x/D = 0.75$, where large values of stress ratio were observed irrespective of the hole size and quadrants.

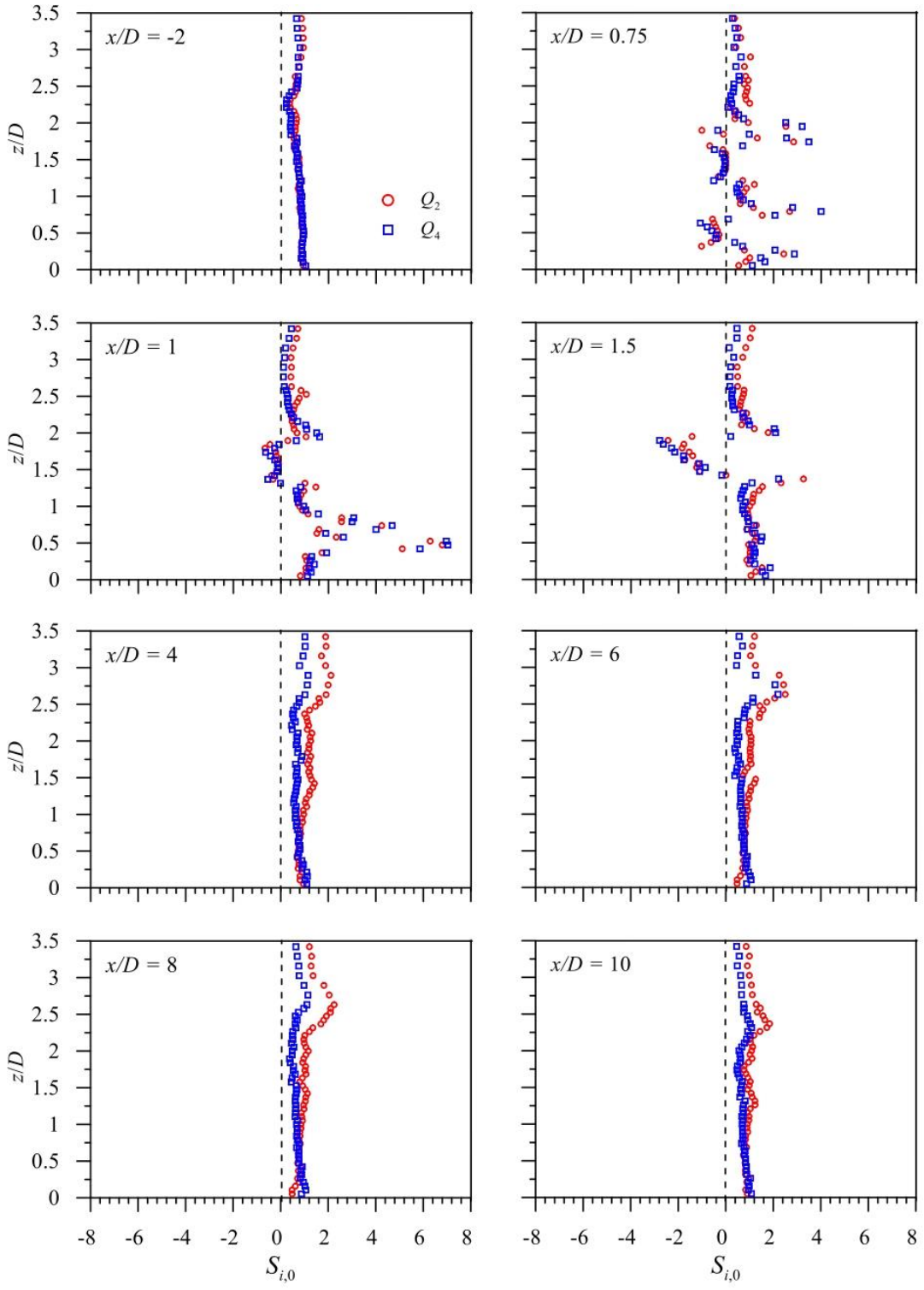

Figure 6.3. The data plots of the $S_{i,H}$ $(i = 2,4)$ with respect to non-dimensional vertical distances z/D for H = 0 at various x/D

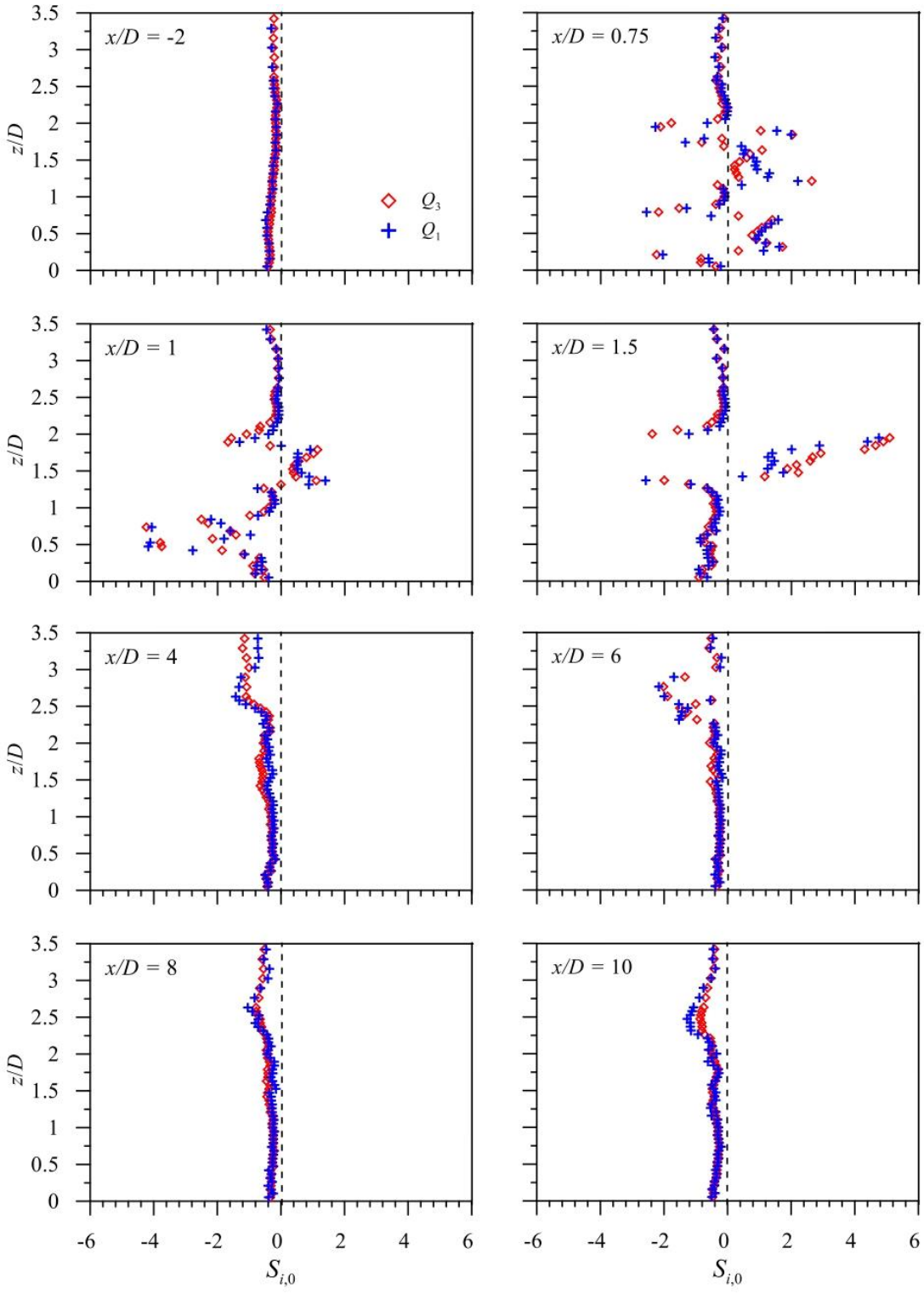

Figure 6.4. The data plots of the $S_{i,H}$ $(i = 1,3)$ with respect to non-dimensional vertical distances z/D for $H = 0$ at various x/D

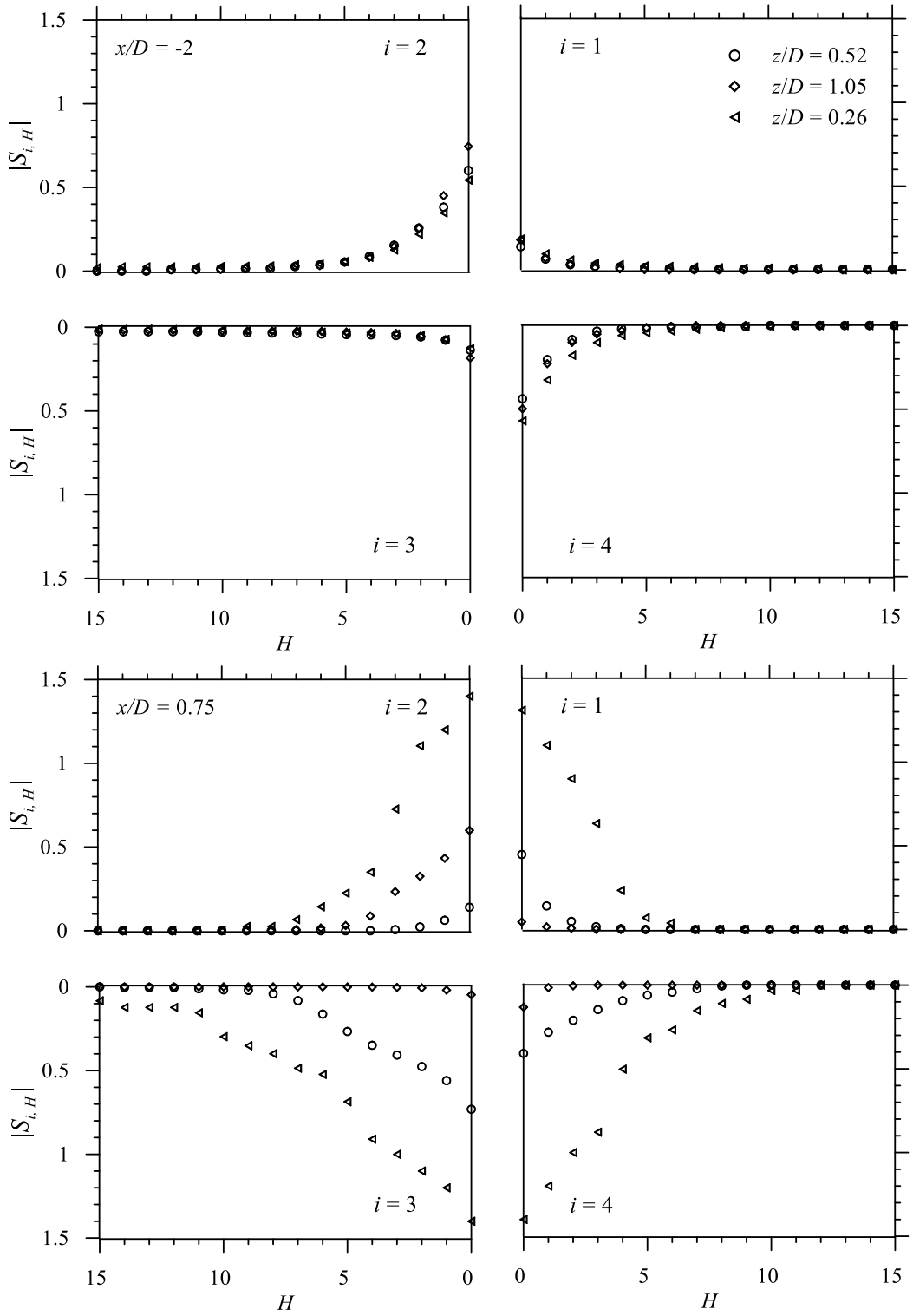

Figure 6.5. Variation of $|S_{i,H}|$ with H at several z/D and $x/D = -2$, 0.75.

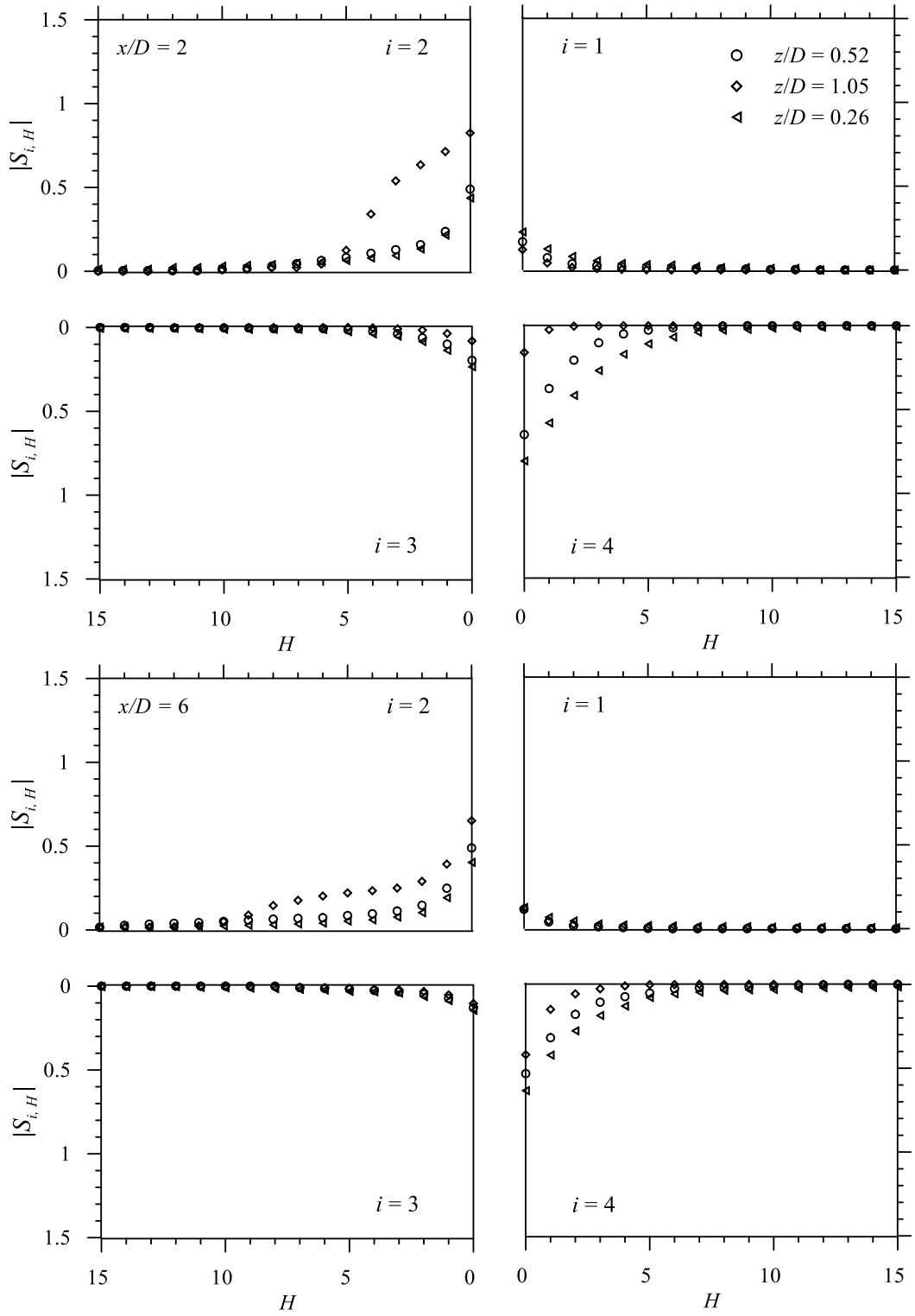

Figure 6.6. Variation of $|S_{i,H}|$ with H at several z/D and x/D = 2, 6.

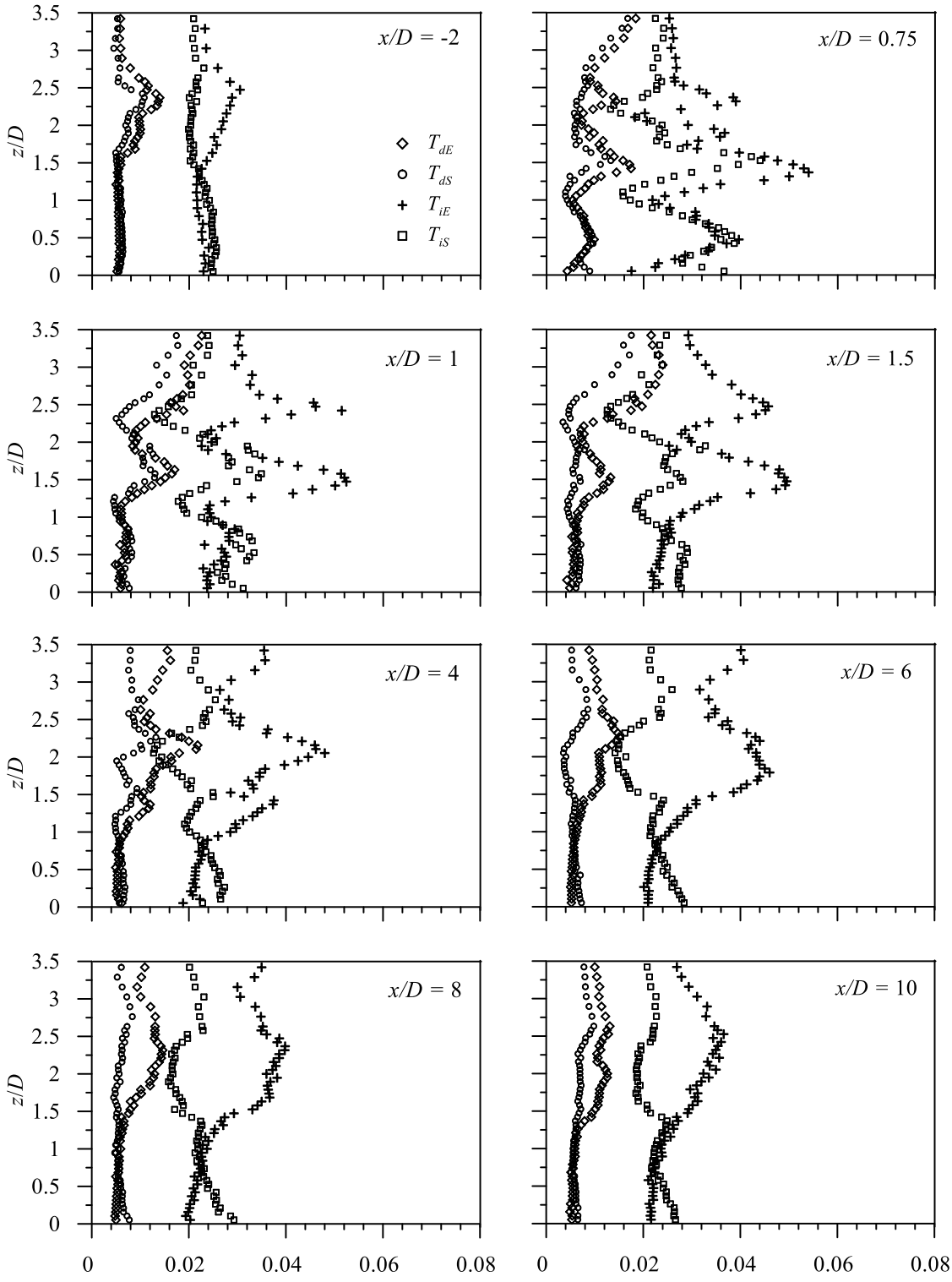

Figure 6.7. The distributions of T_{dE}, T_{dS}, T_{iE}, and T_{iS} with non-dimensional elevation for H = 0 at various x/D.

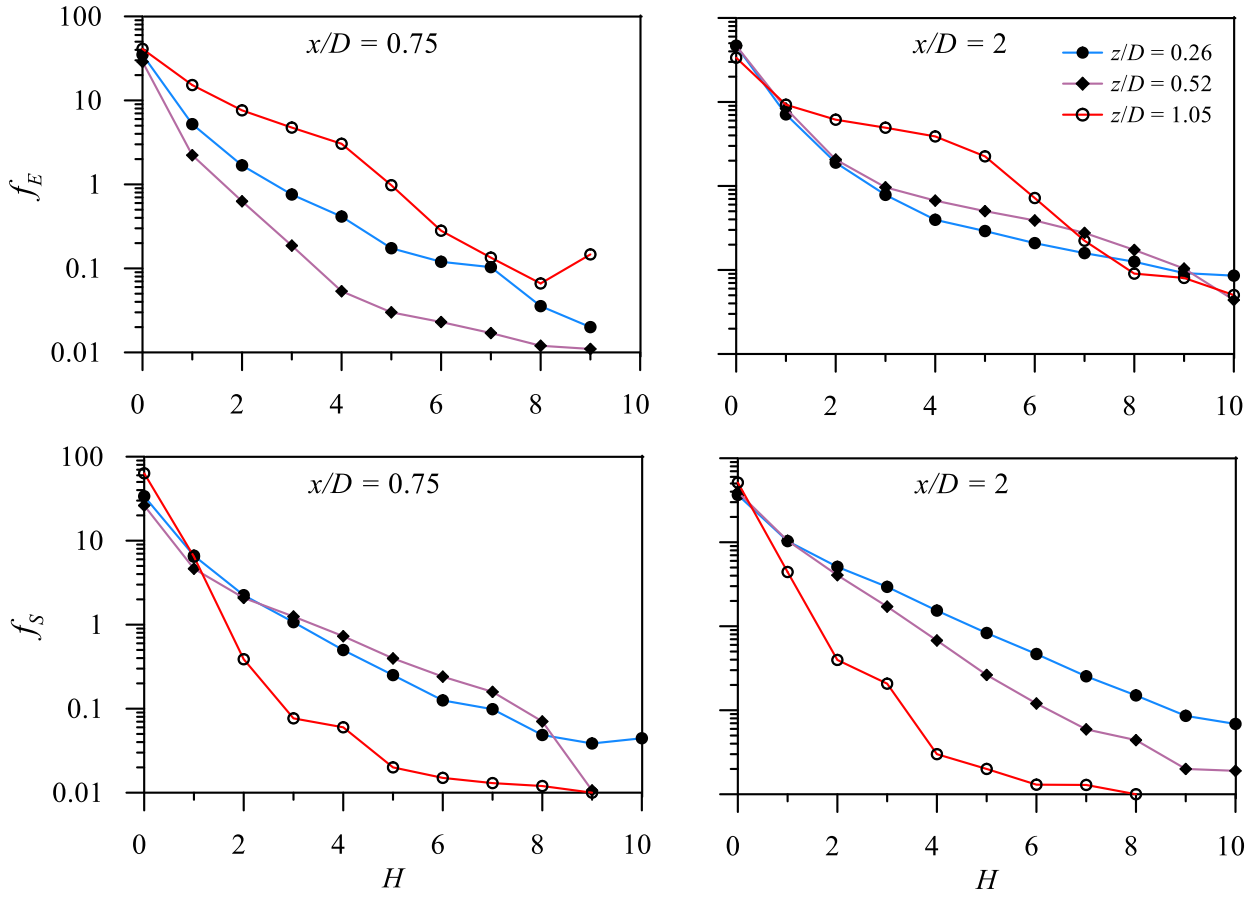

Figure 6.8. The distribution of bursting frequencies f_E and f_S with respect to different hole size H at z/D = 0.26, 0.52, and 1.05 in several downstream distances

6.5 Duration and frequencies of bursting events

For a particular H, the numbers of Q_2 or Q_4 event occurrences in a recorded sample were gathered in order to analyze the durations and frequencies of these events. This allowed for the estimation of the mean time-intervals between ejections (i_E) and sweeps (i_S) as well as the mean duration of ejections (t_E) or sweeps (t_S). The dimensionless mean time-durations of ejection and sweep may be expressed as T_{dE} (= $t_E u_*/D$) and T_{dS} (= $t_S u_*/D$), respectively. Similarly, the dimensionless mean time-intervals for the same are T_{iE} (= $i_E u_*/D$) and T_{iS} (= $i_S u_*/D$), respectively. Subsequently, the dimensionless frequencies from the 2^{nd} and 4^{th} quadrant bursting events are defined to be as follows: $f_E = (i_E{}^{-1}) D/u_*$ and $f_S = (i_S{}^{-1}) D/u_*$; where,

$$i_E = \frac{1}{N}\sum_{i=2}^{N} ts_{Q_2}^{(i)} - ts_{Q_2}^{(i-1)}$$

$$i_S = \frac{1}{N}\sum_{i=2}^{N} ts_{Q_4}^{(i)} - ts_{Q_4}^{(i-1)}$$

N is the total number of observations in ejection/sweep event at a specified location, ts_{Q_k} are the timestamps for ejection or sweep events, being defined as $ts_{Q_k} = l_{k,H}\,\tau$ ($l_{k,H}$ = location of the data points where indicator function $\lambda_{k,H} = 1$, τ = time step = 0.01s).

For H = 0 at various x/D, the distributions of T_{dE}, T_{dS}, T_{iE}, and T_{iS} with non-dimensional elevation are shown in figure 6.7. The T_{dE} and T_{dS} appear to be almost comparable in magnitude over the whole flow depth, however in the majority of the sections, the T_{iE}, and T_{iS} are different and longer than the mean durations. In the unaffected upstream flow, the T_{dE} and T_{dS} remain almost unchanged up until $z/D < 1.5$, followed by a gradual increment then decreases in the outer layer. But in the immediate downstream positions, two sudden humps are visible in each of the time profiles just behind both the cylinders, indicating prolonged bursting events to be taken place. Another interesting observation is that the highest peak is visible in between two cylinders ($z/D \approx 1.5$), which means bursting cycle is longest at the recirculation zone. In summary, the bursting incidents in the wall-wake flow are essentially less lasting than their period of recurrence. Also, the near-wake flow is being described by long duration of ejection and sweeps as well as their interval of occurrence especially in the recirculation zone with ejection dominates over sweep, but the dominance gradually fades away with the increment in downstream distance towards far-wake zone.

Figure 6.8 elucidates the distribution of bursting frequencies f_E and f_S with respect to different hole size H at z/D = 0.26, 0.52 and 1.05, in several downstream distances. It demonstrates how the bursting frequencies drop monotonically as H increases. This indicates that a lower frequency of incidents corresponds with stronger events. Also, it is observed that mean frequencies in case of sweep increases towards the bed, while opposite phenomena are visible in case of ejection. Thus, it may be concluded that the mean length of ejection events with lower rates of occurrence is more sustained than the mean duration of sweep events with relatively greater frequency in near wall flow.

6.6 Higher order moments of velocity fluctuations and its relation with residual conditional shear stress

The third-order moments of velocity fluctuations are crucial for understanding turbulence due to their ability to represent the schematic coherent structures within the flow. That being said, according to their signs, they directly correlate with the temporal bursting occurrences. The generalized equation provided by Raupach (1981) for the moments of third order of velocity fluctuations is as below:

$$M_{ij} = \overline{\hat{u}^i \hat{w}^j}$$

Where $\hat{u} = u'/\sqrt{\overline{u'u'}}$ and $\hat{w} = w'/\sqrt{\overline{w'w'}}$, and i, j being non-negative integers with $i + j = 3$. Based on the obtained values of i, j from this relation, the following third order moments have been evaluated as follows: M_{30}, M_{03}, M_{21} and M_{12}. M_{30} signifies the flux of streamwise mean-sqaured velocity fluctuation and M_{03} indicates the flux of vertical mean-sqaured velocity fluctuation. Whereas, M_{21} and M_{12} denote the diffusion of streamwise and vertical mean-sqaured velocity fluctuations, respectively.

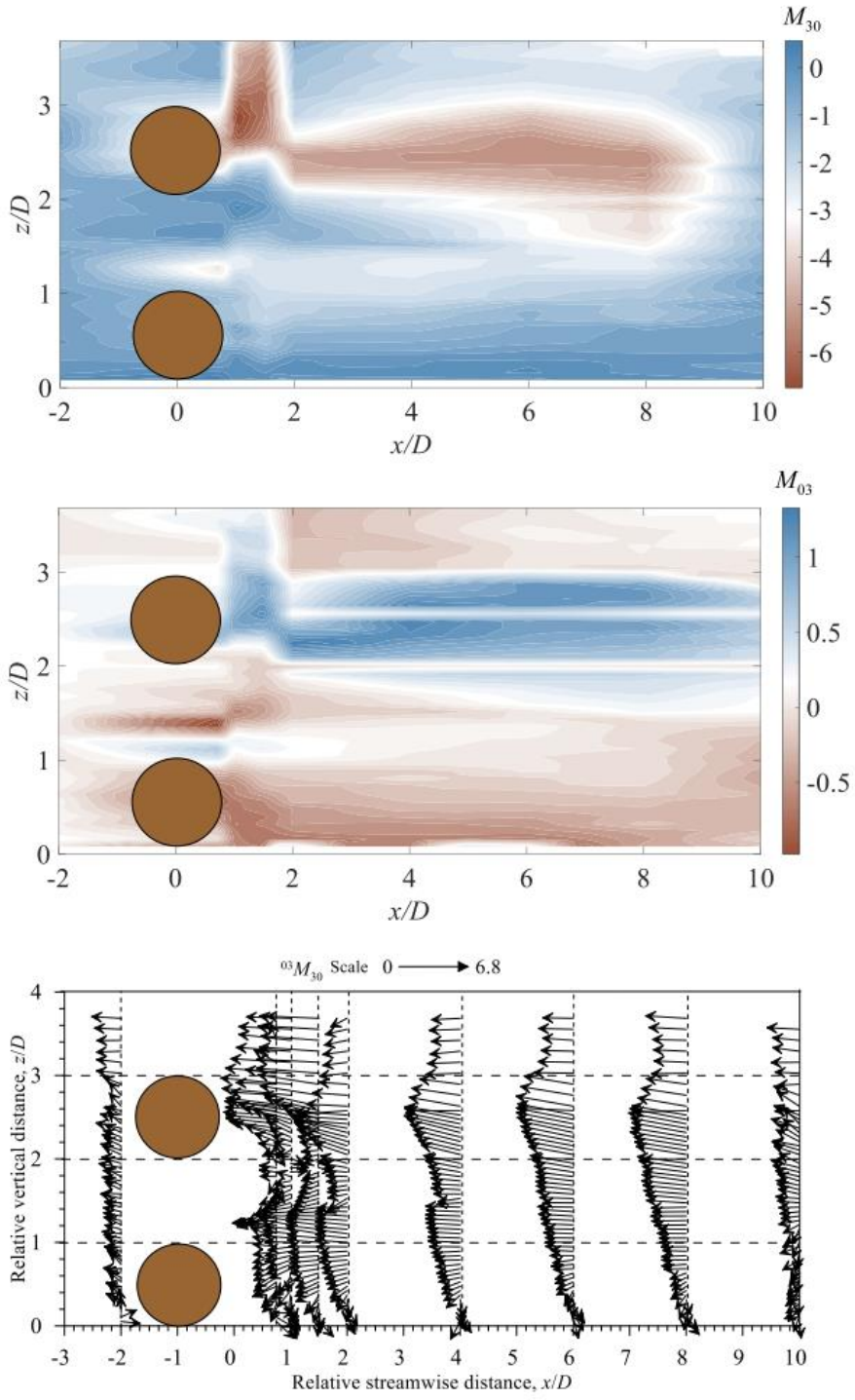

Figure 6.9. Contour and vector plot for third order moments M_{30} and M_{03} respectively in flow past two horizontal cylinders

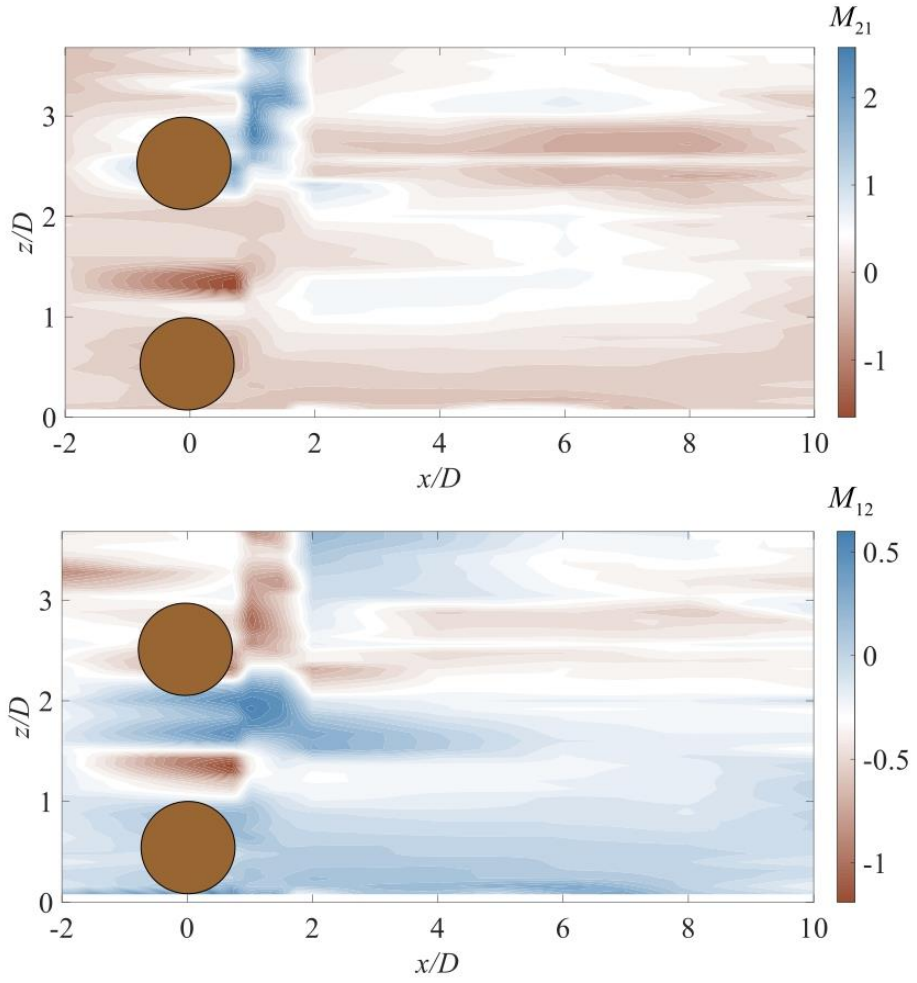

Figure 6.10. Contour plot for third order moments M_{21} and M_{12} respectively in flow past two horizontal cylinders

Figures 6.9 and 6.10 depict the contour plots for third order moments respectively in flow past two horizontal cylinders. The flow zone behind the wall-mounted cylinder ($z/D \approx 0-1$) exhibits incompatible sign variations in flux, positive M_{30} and negative M_{03}, and diffusion, negative M_{12} and positive M_{21}, whereas the flow zone behind the upper cylinder ($z/D \approx 2-3$) throughout the channel appears to be identified by pairings of flux, strong negative M_{30} and positive M_{03} and diffusion, positive M_{12} and negative M_{21}. It should be noted that although the positive and negative M_{03} indicate an upstream and a downstream transport of vertical mean-sqaured velocity fluctuation, respectively, the positive and negative M_{30} represent a downward and an upward transport of streamwise mean-sqaured velocity fluctuation. The positive and

negative M_{12} indicate an upstream and a downstream diffusion of vertical mean-sqaured velocity fluctuation, respectively, whilst the positive and negative M_{21} define a downstream and an upstream diffusion of streamwise mean-sqaured velocity fluctuation. One intriguing finding is that due to the placement of two cylinders, the magnitude of M_{30} moment is much higher compared to the other moments due to strong skewness of streamwise fluctuation behind the cylinders, as observed in figure 6.11. This is indeed visible in the vector plot of flux vector ${}^{03}M_{30}$ with magnitude $\sqrt{M_{30}^2 + M_{03}^2}$ and direction $tan^{-1}\frac{M_{03}}{M_{30}}$, which shows higher magnitude of ${}^{03}M_{30}$ with decelerating kind; suggesting an obstruction to the flow. In brief, the thorough analysis of the third-order moments M_{ij} provides insights about the prevalence of bursting events within distinct flow zones. The sweep events are caused by the preponderance of the combinations of (positive M_{30} and negative M_{03}) and (negative M_{21} and positive M_{12}) in near wall zone; whereas, the ejection events are detected by the prominence of the contrary sign pairings of third-order moments in far-wall zone, also supported by the findings in figure 6.4.

The intermittent nature of turbulence in the flow is illustrated by the fourth-order moment of velocity fluctuations, also known as the "coefficient of kurtosis" of the velocity fluctuations (Dey et al. (2010)). The following definition applies to the dimensionless fourth-order moment of streamwise and vertical velocity fluctuations: $F_u = \overline{u'^4}/(\overline{u'^2})^2$ and $F_w = \overline{w'^4}/(\overline{w'^2})^2$. The standard normal distribution, also known as mesokurtic distribution has the kurtosis value 3. Any distribution with kurtosis value more or less than 3 are known as leptokurtic or platykurtic respectively. Figure 6.11 depicts the contour plots of F_u and F_w respectively which demonstrates a strong presence of F_u throughout the channel compared to F_w, especially behind the upper cylinder. It is indeed supported by the high scale magnitude of M_{30}. As a result, the fourth-order moments shows leptokurtic nature in most of the flow zones, especially behind cylinders where $F_u >> 3$; suggesting strong intermittencies in both the directions for near-wake region.

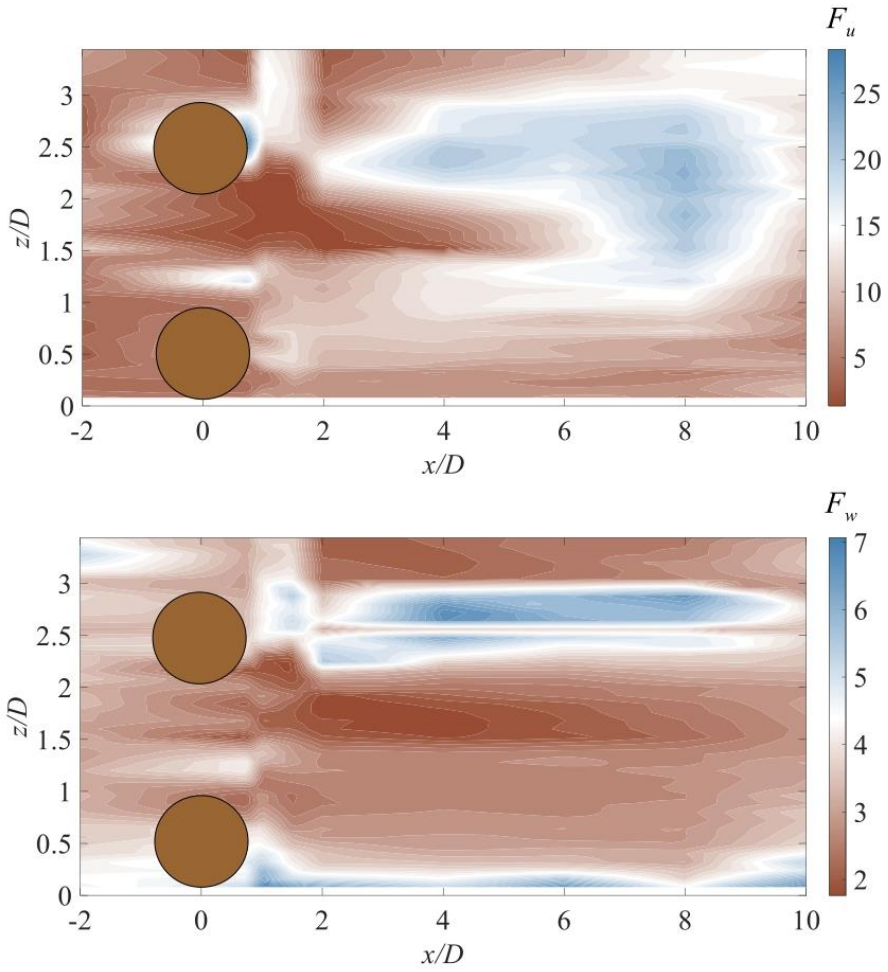

Figure 6.11. Contour plot for fourth order moments F_u and F_w respectively in flow past two horizontal cylinders

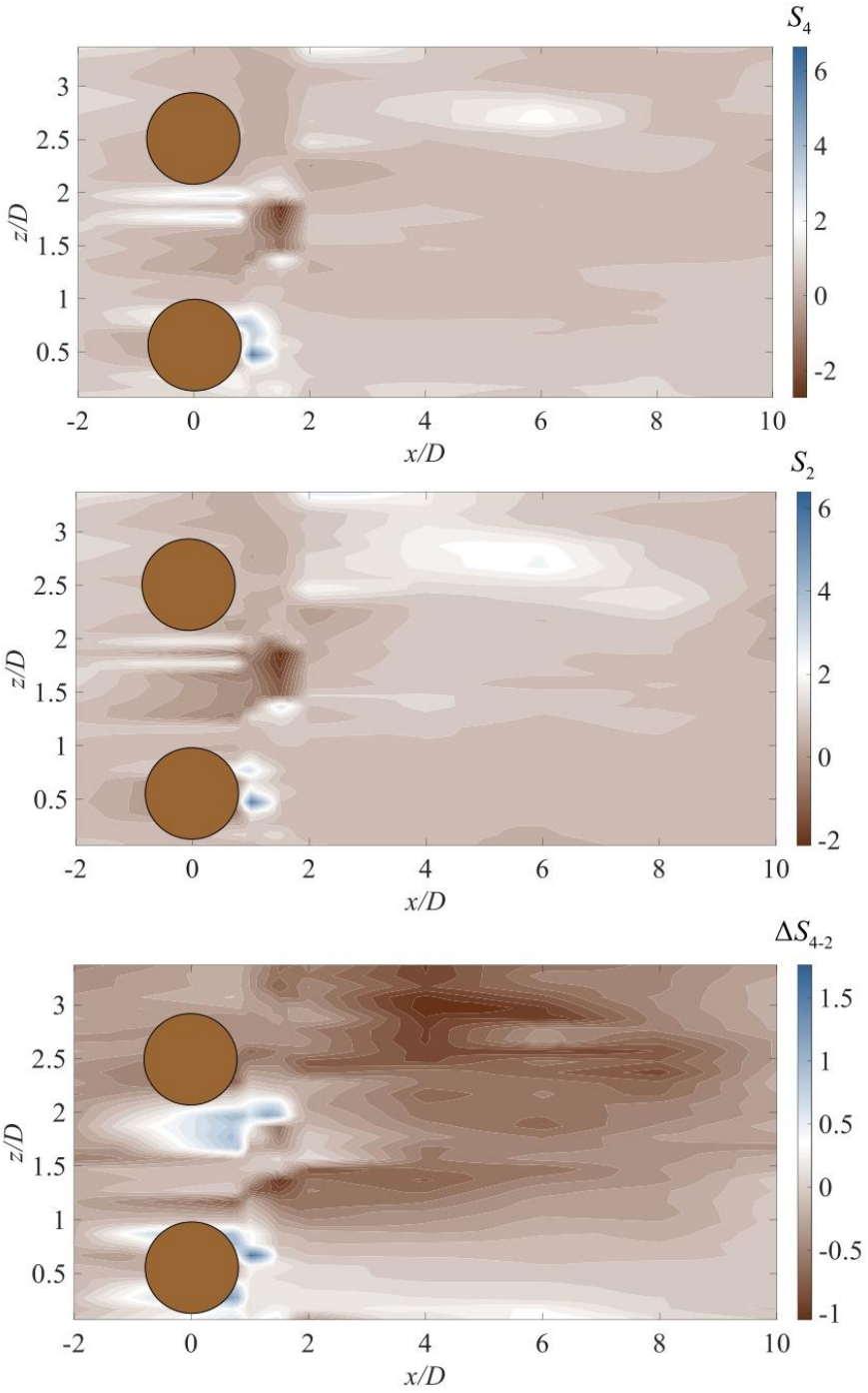

Figure 6.12. Contour plots of sweep $S_{4,0}$ and ejection $S_{2,0}$ events and their residual RSS ΔS_{4-2}

The primary contributions to the overall RSS are sweeps and ejections, therefore it's intriguing to see how important each is in the flow from the residual conditional shear stress. The contours of the residual shear stress $\Delta S_{4-2} = S_{4,0} - S_{2,0}$ together with sweep and ejection events are shown in figure 6.12 to illustrate a further understanding of the dominance of specific bursting events. The recirculation zone, or flow zone between two cylinders, is where the majority of $S_{4,0}$ or sweep events accumulate, according to the contours of residual RSS. Due to the impacts of wake flow vortices at this flow region, the rapidly flowing fluid strips from the form-induced sublayer surge towards the wall-bed. Moreover, According to Raupach (1981) and Mignot et al. (2009), this ΔS_{4-2} exhibits a correlation with 3rd order moment M_{30}. More specifically, there is a simplified linear relationship connecting the turbulent velocity skewness for the streamwise component and the residual shear stress for $H = 0$, in case of gravel bed channel flow:

$$\Delta S_{4-2} = 0.37 M_{30}$$

Figure 6.13 depicts the behaviour of ΔS_{4-2} with M_{30} over different downstream distances x/D. In case of uninterrupted upstream flow, aforementioned relation is being satisfied as most of the data lies within the range of line of agreement, validating the gravel-bed experimental evidences. However, due to large scale sweep and ejection events occurring in near wake zone as reported in previous discussions, ΔS_{4-2} with M_{30} deviates from the line of agreement. Nevertheless, as we move far downstream from cylinder positions, recovery of deviation is visible in the subsequent graphs and at $x/D = 10$, the flow behaviour is identical with the upstream profile as the linear relationship is again prominent in the far-wake zone. Sarkar et al. (2016) have validated the same for turbulent flow with an array of large gravel obstacles with minor overestimation. In our present setup with such complex flow patterns being observed due to the presence of two bluff bodies, it is expected to obtain some under or overestimation to a certain extent in near-wake zone.

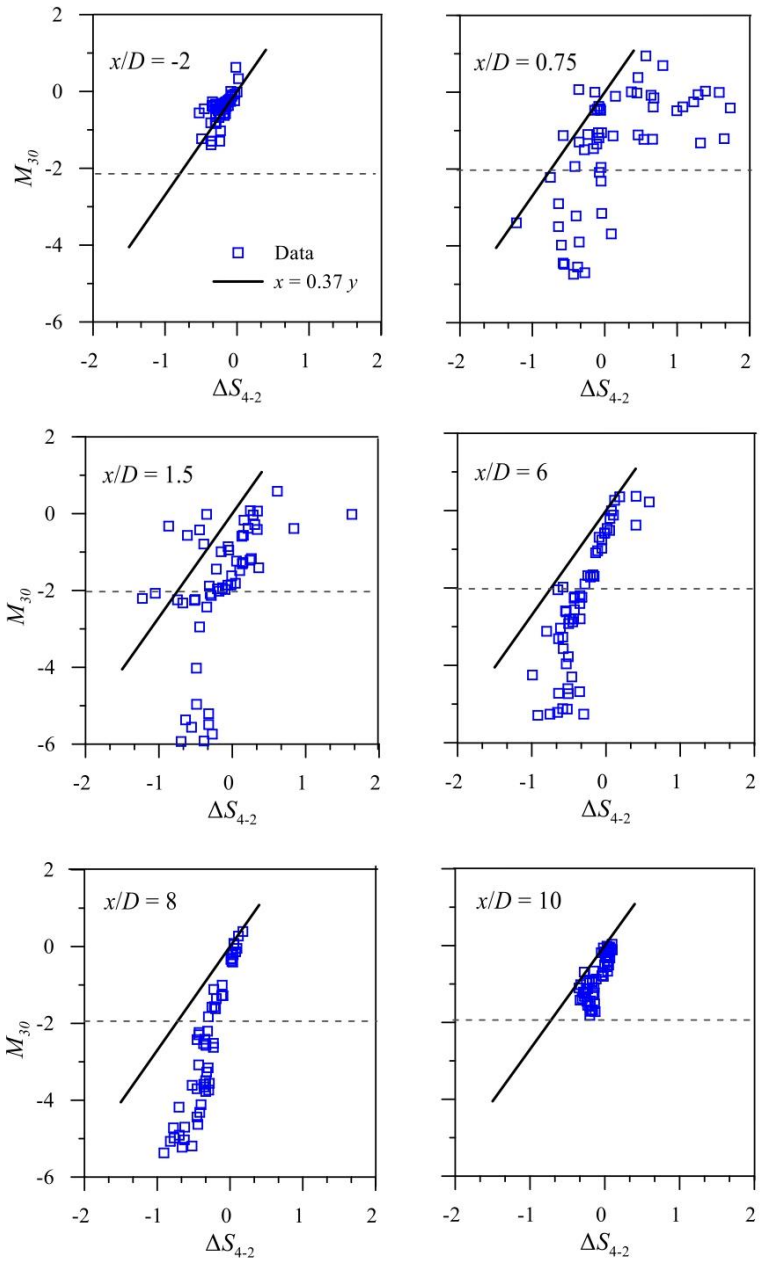

Figure 6.13. M_{30} plotted against ΔS_{4-2} for flow past two horizontal cylinders at different bed locations x/D. The line of agreement represents the law $\Delta S_{4-2} = 0.37 M_{30}$

6.7 Concluding Remarks

This study aims to illustrate a structured approach towards the determination of turbulent bursting in an open channel flow with two horizontal cylinders acting as bluff bodies. From the

stress ratio of RSS plot, sweep events have been found to contribute 600% ($S_{4,0} \approx 6$) to the production of RSS at the near-wake zone at $x/D = 1$ near the wall, causing a rush of accelerating fluid streaks. The Q_2 event describes the unaltered upstream flow far away from the bed ($z/D \approx 3.5$), indicating that it precedes a dominating, slower moving process. However, the contributions of the Q_1 and Q_3 events have remained very small, with the exception of the area just downstream of the cylinders, where the inward interaction Q_3 predominates over the outward interaction Q_1. The average bursting durations and intervals indicate that The bursting events of the wall-wake flow are essentially shorter than their occurrence interval. Additionally, the near-wake region is specified by long-duration ejections and sweeps, as well as the intervals between them, particularly in the recirculation zone of two cylinders, where ejection predominates over sweeps. However, this dominance gradually wanes as downstream distance increases toward the far-wake zone. It is possible to infer from the mean frequency plots that the mean duration of sweep events, which have relatively higher frequencies, is less persistent in near wall flow than the mean duration of ejection events, which have lower frequencies of occurrence. It is seen that while the Q_1 and Q_3 events disappear at a lower value of H (H = 5-7) as a result of the prolonged impacts of ejection and sweep events over bigger hole sizes, the Q_2 and Q_4 events remain finite. The presence of two cylinders were prevalent at $x/D = 0.75$, where high stress ratio values were seen regardless of the hole's size or quadrants. In most flow zones, particularly behind cylinders where $F_u >> 3$, the fourth-order moments have a leptokurtic nature, indicating substantial intermittencies in both directions for the near-wake zone. Subsequently, The amplitude of the M_{30} moment is much bigger than the other moments because of the considerable skewness of the streamwise fluctuation behind the cylinders. In fact, the ejection events are identified by the prominence of the the contrary sign pairings of third-order moments in the far-wall zone, while the sweep events are caused by the majority of the combinations of (positive M_{30} and negative M_{03}) and (negative M_{21} and positive M_{12}) in the near wall zone. The interdependence of M_{30} with bursting is indeed validated by elucidating crossplots with residual shear stress, which shows well agreement when double cylinder disruptions are absent in the flow zone. After many significant research on linear stability by Ali et al. (2021), stability analysis for the current environments of experimentation may also be helpful for future progress in the bluff-body hydrodynamics.

Chapter 7

Machine learning algorithms on predicting the turbulent mixed convection flow in a driven-cavity with two horizontal cylinders

7.1 Introduction

The driven cavity flow, as studied by Shankar et al. (2000), is a commonly investigated phenomenon due to its frequent occurrence in various applications. One of the main challanges in computational fluid dynamics is figuring out the circulating flow within the cavity. Mixed convection in environments with one or more moving boundaries is particularly intriguing, as recirculation and flow mixing are improved by the shear stress produced by the moving surface, which significantly influences the imposed thermal gradient. The ratio of the the Grashof number with the Reynolds number (Gr/Re^2, also known as the Richardson number *Ri*) is the characteristic that characterizes the mixed convection regime. Mixed convection inside lid-driven flows has various applications, including high-performance building insulation, drying technologies, solar power collectors, and the manufacture of float glass, as highlighted in the research by Wong et al. (2021), Ayli et al. (2020), and Ali et al. (2019).

A significant number of research works in the literature is focused on lid-driven cavity flow together with its heat transfer characteristic, utilizing several combinations of cavity shapes, fluids, and incorporated temperature gradients. 3D mixed convection within a pair of lid-driven cubic enclosure at several Reynolds numbers (*Re*) and Richardson numbers (*Ri*) was simulated by Ouertatani et al. (2009). These researchers found that a particular pairing of *Re*=400 and *Ri*=1 enhanced heat transmission by about 76%. Waheed (2009) investigated the heat transport and fluid flow that arise from the combined action of buoyancy and driving lid forces in rectangular enclosures. His study, which was performed at a Reynolds number of 100 with

different Richardson numbers, Prandtl numbers, and aspect ratios, showed that a higher Richardson number improved fluid flow, the enclosures' energy distributions, and the heated wall's heat flux. However, this study could be more interesting if there is one blockage present inside of the rectangular cavity. Sivakumar et al. (2010) inverstigated mixed convective heat transport in lid-driven enclosures with varying heating section lengths at different positions. Their results illustrated that the heat transport rate increased when the heating section was positioned at the top or middle of the cavity's heated wall. An isothermally heated rectangular block was positioned at various points within a cavity by Dagtekin and Oztop (2002) in order to simulate the cooling of electronic equipment. They investigated several bluff body designs after discovering that the body's size had the greatest impact on the mixed convection flow. Cheng (2011) investigated flow and heat transport in a enclosure, where shear force from the upper lid's movement and buoyancy force from the bottom heating drove the flow. A broad range of Re ($10 \leq Re \leq 2200$), Gr ($100 \leq Gr \leq 4.84 \times 10^6$), Pr ($0.01 \leq Pr \leq 50$), and Ri ($0.01 \leq Ri \leq 100$) were covered by the author. Plotting and computation of average Nusselt numbers at the location of heated bottom wall demonstrated how differences in Richardson numbers affect heat transport. In a cavity containing an isothermally heated square obstacle and isothermal cold wall temperatures applied to all cavity walls, Islam et al. (2012) studied mixed convection. They expected that the cavity's upper wall would slide continuously to the right during their investigation. Their results indicated that the eccentricity of the blockage, the blockage ratio, and the Richardson number all had an impact on the average Nusselt number measured along the solid block. While their work had significant impact on mixed-convection flow research, their numerical findings were not compared with prior experimental work. Using a square cavity and a heated cylinder positioned in the middle, Billah et al. (2011) developed a numerical model of mixed convection heat transport. The horizontal walls of the hole were thought to be adiabatic, and the left cold wall was supposed to rise gradually. The temperature of the cavity's right wall was kept chilly. This study showed that the diameter of the cylinder and the ratio of fluid-solid thermal conductivity significantly affected the flow field and temperature distribution. The goal of Rodrigues et al. (2020) was to optimize the design of two rectangular fins positioned in a square cavity that was exposed to stable stratification and unsteady mixed convective flow. They employed constructal design and a thorough search approach to achieve the optimization. The optimum thermal performance was likewise found

for asymmetric fin arrangements with distinct fraction areas for each fin. Ismael et al. (2015) performed a numerical modelling of the fluid flow fields and mixed convection within a trapezoidal cavity. The findings indicated that the Nusselt number behaved differently from the Richardson number according on the orientation of the lid, and that the Nusselt number was significantly influenced by the angle of inclination of the side walls. More significant research works related to mixed convection can be found in Borahel et al. (2022) and Ismael et al. (2020).

In addition to the mixed convection, the cavity flow is assumed to be turbulent in nature, hence turbulence models should be incorporated. The largest percentage of flows analyzed in real-world environments are classified as turbulent, a term that describes motions where the primary stream is overlaid by an irregular fluctuation (Subramanya et al. (2009)). The unpredictable oscillations, referred to as mixing or eddy motion, are responsible for turbine and turbocompressor losses, in addition to the substantial resistance encountered by turbulent flow in pipes. Previously, the primary method used to study turbulent mixed convection, specifically in air was experimentation. For instance, mixed convection in a rectangular convection cell was measured using PIV by Schmeling et al. (2011). In addition, A naturally ventilated chamber with a heated floor and two entrances to a chilly exterior was the subject of a simplified geometry study by Gladstone and Woods (2001). Additionally, geometrically straightforward parallelepiped chambers with no internal impediments and homogenous heat sources heating them from below were investigated by Fitzgerald and Woods (2007). In addition to these experimental studies of mixed convection in generic rooms, there is considerable interest in the physics and engineering of mixed convection past heated barriers, as investigated by Linden et al. (1999) and Bosbach et al. (2006), to enhance understanding of such phenomena. However, the majority of numerical studies on mixed convection have been carried out for either laminar flows, as described in the previous section. There are some instances of turbulent mixed convection flow work where they have considered RANS equations. Significant differences in the RANS predictions of mixed convection were found in a comparison research performed by Costa et al. (1999) and Blay et al. (1992), who tested a few of the turbulence models that were available. They held the turbulence models accountable for these disparities. Thus, accurate predictions of mixed convection in complex domains with exterior and interior barriers require

robust turbulence models. From there comes the motivation for gradually moving towards machine learning algorithms for prediction tasks.

A few examples of the many applications for which heat transfer research is useful include in recovering thermal storage systems for energy, high-temperature heat exchangers, isolated nuclear reactors, and combustion chambers Mehendale et al. (2000) and Walvekar et al. (2016). In this sense, the heat transfer coefficient—more especially, the Nusselt number—made it feasible for a larger heat exchange rate. A number of studies have lately considered the prediction model for this heat transfer parameter since machine learning methods are quite effective at both reducing costs and improving accuracy when estimating heat exchange rate. Bhattacharya et al. (2022) developed a neural network architecture and a multivariate regression method to estimate the Nusselt number and Reynolds number (Re) in thermal convective turbulent flow. While all of the models' predictions were quite near to one another, they found that the machine-learning models produced during this study fitted the experimental and numerical data the best. In order to predict the forced convective heat transport properties of turbulent nanofluid pipe flow, Kocak et al. (2022) presented and examined the predictive powers of various regression approaches, namely artificial neural networks (ANN), and adaptive neuro-fuzzy inference systems (ANFIS). The results using multiple regression, ANN, and ANFIS were examined. The findings demonstrated that ANFIS is a useful tool, with predictions having a R^2 of 0.9987. Sanhueza et al. (2023) investigated the effectiveness of convolutional neural networks (CNNs) in translating a rough surface's height map into its precise local skin friction factors and Nusselt numbers, directly from one image to another. The greatest errors generated by deep learning were just 8.1% for the global skin friction factors and 2.9% for the Nusselt numbers, according to their careful comparison with correlations already found in the literature. Additionally, the deep learning findings showed only a slight sensitivity to changes in the dataset size and demonstrated stability when applied to rough surfaces with sudden changes in their roughness components. Geridonmez et al. (2024) used data from a numerical process to statistically simulate average Nusselt number $\overline{Nu}$. Neural Networks (NN) model was firstly incorporated to predict $\overline{Nu}$, followed by interpolation. NN outputs outperformed curve fitting on test data in terms of goodness of fit as measured by the mean squared error (MSE) metric. Conversely, it was demonstrated that interpolation could serve as

a modeling substitute as well. Apart from neural networks, Gaussian Process Regression (GPR) is another potent algorithm used for prediction task, although there are not much evidences of the utilization of this algorithm in computational fluid dynamics. Duan et al. (2019) elucidated a method to quantify the consistency between CFD simulation and experiment, inspired by Gaussian process regression. For the local agreement, concrete information was provided by the statistically weighted square error. Using the standardized Euclidean distance, the entire agreement was evaluated. The dynamic viscosity ratio of Al_2O_3/H_2O was predicted in the study by Kumar et al. (2021) utilizing ML methods such as Gaussian process regression and multilayer perceptrons. The results showed that the Matern kernel function yielded the best performance, achieving a lower RMSE value of 0.018 and a regression coefficient value of 0.99 for both models. The cost of doing experimental test runs would be decreased by this research project, and the models' predictions were accurate. Several CFD problems were addressed by Morita et al. (2022) using Bayesian optimization (BO), which is based on Gaussian process regression (GPR) and may have practical significance. It was demonstrated that fewer than ninety-nine CFD solver runs were required to guarantee the discovery of the global optimum of the design parameters for sizes up to eight. Moreover, it was noted that the number of design parameters had no discernible effect on the number of flow simulations. A study by Said et al. (2022) examined the thermal efficiency of a small-scale solar technology that used a flat plate solar collector to capture solar heat. GPR and boosted regression trees (BRT), two contemporary ensemble machine learning approaches, were created using experimental data to predict the energy-exergy effectiveness of the technology and the energy efficacy of the solar collector. The GPR-based models exhibited excellent efficacy, with Pearson's coefficient (R) of 0.9999, a coefficient of determination (R^2) ranging from 0.9998 to 0.9999, mean squared error (MSE) between 0.0015 and 0.0524, and RMSE between 0.0124 and 0.0723. However, for determining the hyperparameters for the machine learning models, most of the aforementioned research had used trial-and-error methodology which is inadequate; instead optimization algorithms such as Bayesian optimization, gradient boosting can be used which would efficiently determine hyperparameters by minimizing loss function.

Aforementioned discussion suggests that previous research on mixed convection in lid-driven was focused on square or single cylinder obstruction or a cavity with differential heating. Numerous industrial applications such as mixing tanks, boilers, and chemical reactors, have

obstacles designed by joining of two or more cylinders one above the other Asrari et al. (2021) Sedahmed et al. (1995). It is challenging to assess the heat and mass transport properties of these engineering applications experimentally, although there are some experimental evidences in literature for instance, Sarkar et al. (2023) and Samanta et al. (2023) on open channel flow past two horizontal cylinders. In order to investigate this problem of utmost engineering importance numerically, RANS equations together with appropriate heat transfer equation have been presented subject to proper boundary conditions. Then the aforementioned problem has been evaluated by utilizing Galerkin finite element methodology and several results including streamlines and isotherms have been presented for different Richardson and Reynolds number. Even though a number of theoretical and experimental research on turbulent mixed convection have been developed, there is very little agreement between them, and the process is time-consuming and costly. To overcome this difficulty, two most widely used ML algorithms, ANN and GPR have been incorporated to approximate the thermal behaviour of turbulent flow inside the cavity.

7.2 Mathematical Formulation

The flow under consideration is assumed to be two-dimensional, turbulent, steady, and incompressible. The schematic diagram of the cavity flow has been provided in figure 7.1. Two cylindrical blockages of diameter $D = H/4$ have been incorporated in the cavity, where H is the height of the flow zone and L being the length of the cavity. For simplification in the boundary conditions, it is assumed that $L = H = 1$ i.e., a square cavity of unit length is considered. No slip boundary conditions have been implemented on the bottom and the right wall, as well as on both of the cylinder surfaces. Streamwise velocities have been incorporated on top and the left wall, suggesting a free surface inflow inside the cavity. All cavity walls are subject to an isothermal cold wall temperature of T_c (300 K), while the cylindrical surfaces are subject to an isothermal hot wall temperature of T_h (301 K). Additionally, water ($Pr \approx 7$) is used as the working fluid in the cavity. With the exception of density, which is predicted to change linearly with temperature based on the Boussinesq assumption, all other thermophysical characteristics of the fluid being utilized are assumed to stay constant (Spiegel et al., 1960).

In light of the aforementioned factors, the analysis is made dimensionless by adding the following variables.

$$x = x/H, y = y/H, u = u/u_t, v = v/u_t, \theta = \frac{T-T_c}{T_h-T_c},$$

$$p = \frac{p}{\rho u_t^2}, Re = \frac{u_t H}{\nu}, Gr = \frac{g\beta(T_h-T_c)H^3}{\nu^2}, Pr = \frac{\nu}{\alpha}$$

where P represents the non dimensional pressure term, the Reynolds number is Re, the Grashof number is Gr, and the Prandtl number is Pr. x, y, u, v have been made non dimensional with the division of cavity height H and streamwise velocity at the top surface $u_t = 1$. The following equations indicate normalised Reynolds Averaged Navier Stokes equations (Rodi (1997)) with heat transfer in y-momentum:

$$u\frac{\partial u}{\partial x} + v\frac{\partial u}{\partial y} = -\frac{\partial p}{\partial x} + \frac{1}{Re}\left(\frac{\partial^2 u}{\partial x^2} + \frac{\partial^2 u}{\partial y^2}\right) - \frac{\partial}{\partial x}\left(\overline{u'u'}\right) - \frac{\partial}{\partial y}\left(\overline{u'v'}\right) \quad (1)$$

$$u\frac{\partial v}{\partial x} + v\frac{\partial v}{\partial y} = -\frac{\partial p}{\partial y} + \frac{1}{Re}\left(\frac{\partial^2 v}{\partial x^2} + \frac{\partial^2 v}{\partial y^2}\right) - \frac{\partial}{\partial x}\left(\overline{u'v'}\right) - \frac{\partial}{\partial y}\left(\overline{v'v'}\right) + \frac{Gr}{Re^2}\theta \quad (2)$$

Normalised Reynolds averaged heat transfer equation (Samanta et al . (2023)):

$$u\frac{\partial \theta}{\partial x} + v\frac{\partial \theta}{\partial y} = \frac{1}{RePr}\left(\frac{\partial^2 \theta}{\partial x^2} + \frac{\partial^2 \theta}{\partial y^2}\right) - c_p\frac{\partial}{\partial x}\left(\overline{\theta'u'}\right) - c_p\frac{\partial}{\partial y}\left(\overline{\theta'v'}\right) \quad (3)$$

Continuity equation:

$$\frac{\partial u}{\partial x} + \frac{\partial v}{\partial y} = 0 \quad (4)$$

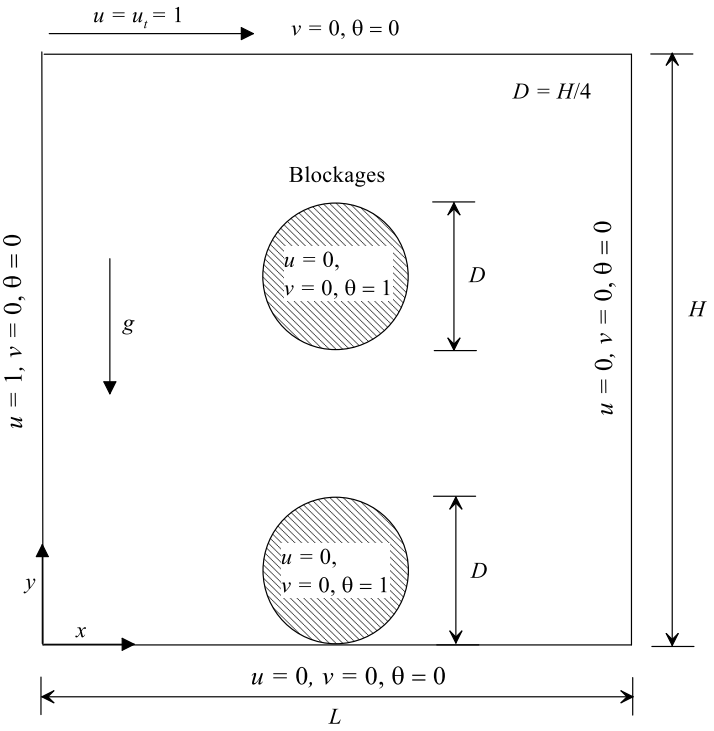

Figure 7.1. Schematic diagram of the model setup

$\frac{-\overline{u\prime v\prime}}{\frac{\partial v}{\partial x}}$ is the ratio of stress with velocity gradient in the streamwise direction, also described as eddy viscosity or ϵ_h, where h in subscript denotes streamwise direction. In a similar manner, $\frac{-\overline{v\prime v\prime}}{\frac{\partial v}{\partial y}}$ is denoted by ϵ_v, where v essentially indicates vertical direction.

Isotropic turbulence refers to a hypothetical state in fluid dynamics where turbulence is uniform in all directions (Antonia et al. (1994)). In such a state, statistical properties of turbulence, such as energy dissipation rates, are the same in all directions; which means $\overline{u'u'} \approx \overline{u'v'} \approx \overline{v'v'}$. Hence, in case of isotropic turbulence, streamwise and nomal velocity fluctuations vary in the same order in both directions. Therefore,

$$\epsilon_h \approx \frac{-\overline{u\prime v\prime}}{\frac{\partial v}{\partial x}} \approx \frac{-\overline{u\prime u\prime}}{\frac{\partial u}{\partial x}} \tag{5}$$

$$\epsilon_v \approx \frac{-\overline{u\prime v\prime}}{\frac{\partial u}{\partial y}} \approx \frac{-\overline{v\prime v\prime}}{\frac{\partial v}{\partial y}} \tag{6}$$

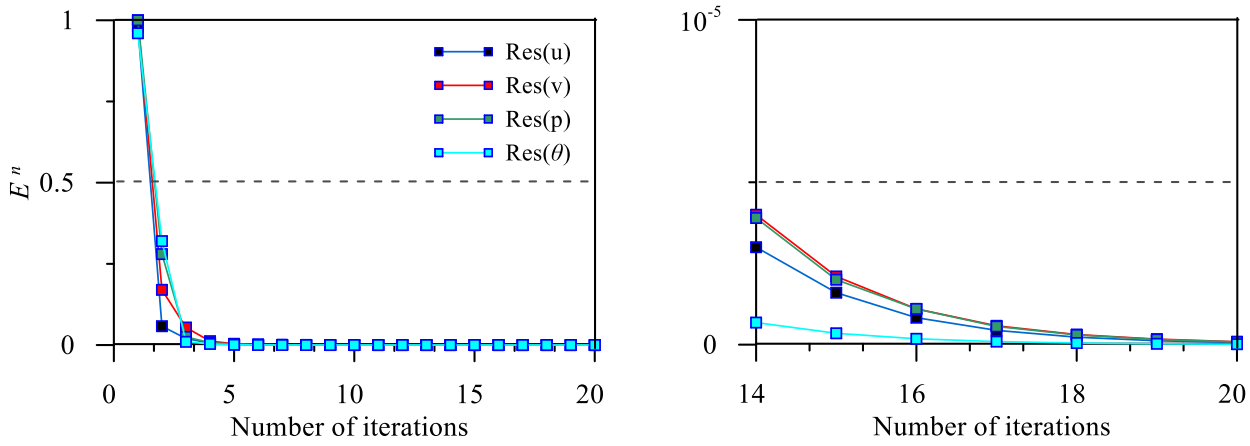

(a) (b)

Figure 7.2. Relative error E^n propagation (a) at each of the iteration (b) in between 14-20 iterations

In a similar manner, we can define the eddy diffusivity of heat as follows:

$$\epsilon_{th} \approx \frac{-\overline{\theta' u'}}{\frac{\partial \theta}{\partial x}} \tag{7}$$

$$\epsilon_{tv} \approx \frac{-\overline{\theta' v'}}{\frac{\partial \theta}{\partial y}} \tag{8}$$

The turbulent Prandtl number Pr_t is described as the ratio $\frac{\epsilon_h}{\epsilon_{th}} \approx \frac{\epsilon_v}{\epsilon_{tv}}$ of the above given values, by similarity with the molecular Prandtl number $Pr = \frac{\mu c_p}{k}$. Thus, given the turbulent Prandtl number Pr_t, the following mathematical equations characterize the stress terms in heat transfer equation (Kafoussias et al. (1999)):

$$-\overline{\theta' u'} = \frac{\epsilon_h}{Pr_t} \frac{\partial \theta}{\partial x} \tag{9}$$

$$-\overline{\theta' v'} = \frac{\epsilon_v}{Pr_t} \frac{\partial \theta}{\partial y} \tag{10}$$

Hence the reformed momentum equations and heat equation are defined as:

$$u\frac{\partial u}{\partial x}+v\frac{\partial u}{\partial y}=-\frac{\partial p}{\partial x}+(\frac{1}{Re}+\epsilon_h)\frac{\partial^2 u}{\partial x^2}+(\frac{1}{Re}+\epsilon_v)\frac{\partial^2 u}{\partial y^2} \quad (11)$$

$$u\frac{\partial v}{\partial x}+v\frac{\partial v}{\partial y}=-\frac{\partial p}{\partial y}+(\frac{1}{Re}+\epsilon_h)\frac{\partial^2 v}{\partial x^2}+(\frac{1}{Re}+\epsilon_v)\frac{\partial^2 v}{\partial y^2}+\frac{Gr}{Re^2}\theta \quad (12)$$

$$u\frac{\partial \theta}{\partial x}+v\frac{\partial \theta}{\partial y}=(\frac{1}{RePr}+\frac{c_p\epsilon_h}{Pr_t})\frac{\partial^2 \theta}{\partial x^2}+(\frac{1}{RePr}+\frac{c_p\epsilon_v}{Pr_t})\frac{\partial^2 \theta}{\partial y^2} \quad (13)$$

with boundary conditions:

$$\text{at}, y=0: u=0, v=0, \theta=0 \qquad \text{at}, y=1: u=1, v=0, \theta=0 \quad (14)$$

$$\text{at}, x=0: u=1, v=0, \theta=0 \qquad \text{at}, x=1: u=0, v=0, \theta=0 \quad (15)$$

$$\text{at both cylinder walls}: u=0, v=0, \theta=1 \quad (16)$$

A T_C is used as a reference temperature to compute the local Nusselt number along the midline between two cylinders and top wall of the cavity as below:

$$Nu_y=(\frac{\partial \theta}{\partial y})_{y=H,3H/8} \quad (17)$$

By integrating, the average Nusselt number is determined as follows:

$$\overline{Nu}=-\int_0^1 Nu_y\,dx=-\int_0^1 \frac{\partial \theta}{\partial y}dx \quad (18)$$

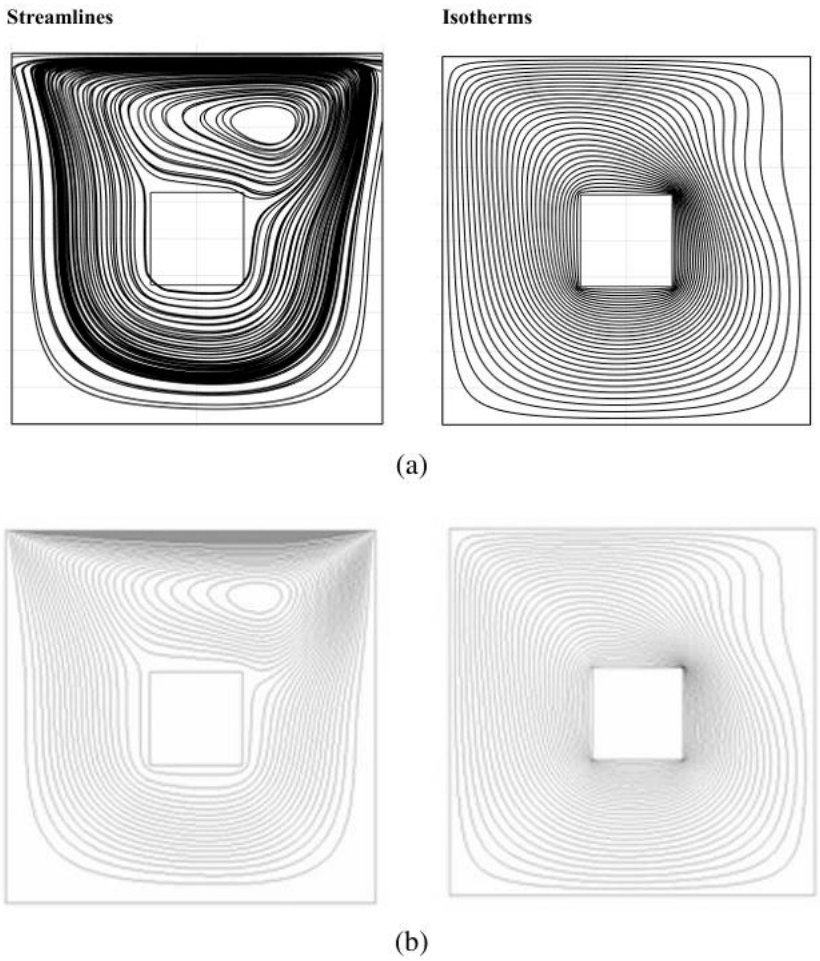

Figure 7.3. Comparison of streamlines and isotherms of (a) present work (b) Islam et al. (2012)

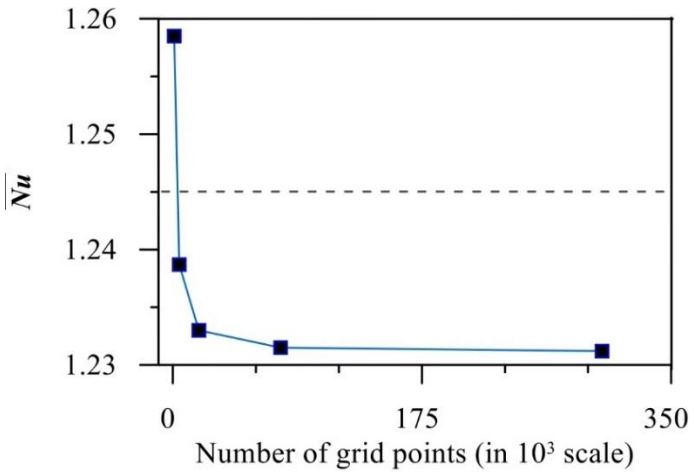

Figure 7.4. Grid independence study: convergence of the average Nusselt number evaluated on the top wall of the present problem, followed by consecutive mesh refinement.

7.3 Solution Methodology

In the current study, a Galerkin based finite element methodology (Fan et al. (1999)) was used to solve the governing equations in a cavity flow heated from two circular cylinders acting as blockage inside and subject to the previously mentioned boundary constraints. The Galerkin approach is used to construct a weak form of the governing equations, which leads to the finite element equations. The virtual quantities of pressure, velocity, and temperature are utilized to weight the continuity, momentum, and energy equations. The following equations are used to estimate the unknown variables $U_x, U_y, P,$ and T inside each of the simply formed, non-overlapping sections that make up the continuum domain:

$$U_x \approx U_x^h = \phi^T[u] \tag{19}$$

$$U_y \approx U_y^h = \phi^T[v] \tag{20}$$

$$P \approx P^h = \psi^T[p] \tag{21}$$

$$T \approx T^h = \Theta^T[\theta] \tag{22}$$

where the interpolation functions for temperature, pressure, and velocity are denoted by the symbols ϕ, ψ and Θ respectively. The values of the relevant variables at the element's nodes constitute the vectors $[u], [v], [p]$ and $[\theta]$. The residual error in each of the governing equations is achieved by replacing these basic functions into the boundary conditions and governing equations:

$$\text{Continuity: } f_1(\phi, U_x, U_y) = E_1 \tag{23}$$

$$\text{Momentum: } f_2(\phi, \psi, \Theta, U_x, U_y, P, T) = E_2 \tag{24}$$

$$\text{Energy: } f_3(\phi, \Theta, U_x, U_y, T) = E_3 \tag{25}$$

where the residuals following the implementation of the finite element approximations are denoted by the letters E_1, E_2, and E_3. By positioning the residuals orthogonal to each element's interpolation function, the Galerkin model of the weighted residuals approach aims to decrease such errors to zero in a weighted sense, as below:

$$\int_A \psi . E_1 \, dA = \int_A \psi . f_1 \, dA = 0 \tag{26}$$

$$\int_A \phi . E_2 \, dA = \int_A \phi . f_2 \, dA = 0 \tag{27}$$

$$\int_A \Theta . E_3 \, dA = \int_A \Theta . f_3 \, dA = 0 \tag{28}$$

Each element produced by this process has a system of equations that can be expressed as

$$K(\Phi).\Phi = F \tag{29}$$

Where K denotes the stiffness matrix, representing the diffusion and convection of energy, and F is the load vector, which includes the boundary conditions., and Φ is the column vector containing the unknown variables. Using the Newton–Raphson method, the fluid region's discretized equations were solved. As seen below, the solution was considered to have converged when the dependent variable's relative change between two iterations was less than 10^{-6}.

$$E^n = \left|\frac{\Lambda^{n+1} - \Lambda^n}{\Lambda^{n+1}}\right| < 10^{-6} \tag{30}$$

where Λ is the representative of either u, v, p or θ and the superscript n denotes the ongoing iteration number of the finite element scheme. Figure 7.2 shows relative error E^n at each of the iteration n, converging towards zero after 5th iteration. It is also evident from 2(b) that after 14th iteration errors have magnitude quite less than 10^{-5}, and at 20th iteration $E^n < 10^{-6}$ being satisfied, it is concluded that the solution has converged.

Ri	Isothermal Cold Cylinder			
	Present	Khanafer et al. (2013)	Nek5000 (2013)	Minimum Relative error
0.01	2.872	2.92	2.91	1.3%
1	3.3883	3.50	3.47	2.5%
5	4.5631	4.69	4.67	2.2%
10	4.842	5.04	4.99	3%

Table 7.1. Average Nusselt number $\overline{Nu}$ comparison for four different Richardson number $Ri = 0.01,1,5,10$ in case of isothermal cold cylinder

7.4 Code Validation

The computational process is verified by comparison with the numerical outcomes of Khanafer et al. (2013) as well as Nek5000, a spectral element method-based open-source CFD solver data, at the lower heated surface of a lid-driven cavity with a single circular cylinder in mid-position. The computations were executed to evaluate average Nusselt number $\overline{Nu}$ for four different Richardson number $Ri = 0.01,1,5,10$ in case of isothermal cold cylinder in table 7.1 with $Re = 100, Pr = 0.7$. An overall agreement between the current computation and Khanafer et al. (2013) is observed to be quite well, with an average error rate of around 3%.

To produce more validation to our said methodology, the streamlines and isotherms derived from present method were compared with Islam et al. (2012) in case of a lid driven cavity in presence of an isothermally heated square blockage with $Re = 100$ and $Ri = 0.1$. The results upon comparison in figure 7.3 showed good agreement with correct indications of vortex zone and isothermal lines. We looked at five distinct non-uniform grid systems with 1148, 4592, 18368, 75781, 301538 nodes each to determine the average Nusselt number along the top wall.

Figure 7.4 demonstrates the grid convergence of $\overline{Nu}$ which reveals that 75781 number of nodes are appropriate to calculate all the aforesaid quantifiers and to report the further results.

To produce thermal validation of the said method experimentally, it has been applied on forced convective turbulent flow past a square bluff body and the findings obtained have been compared with several numerical as well as experimental findings in literature. Table 7.2 shows the average Nusselt number evaluated on the entire surface of the bluff body under consideration with $Re = 22000$ and $Pr = 0.71$. Upon comparison, it is found that the the present numerical model estimated the mean Nusselt number efficiently with average deviations 5.7% and 1.7% in case of experimental findings (Hilpert et al. (1933), Igarashi et al. (1985)) and 2.4% for other numerical method (Feijó et al. (2022)). Moreover, it is feasible to produce experimental validation of the said method with the incorporation of our own data obtained from Fluvial Mechanics Laboratory of the Indian Statistical Institute in Kolkata, India in a rectangular-shaped flume. Based on these experimental data, our research group has already published few articles (Sarkar et al. (2023) and Samanta et al. (2023)) analysing turbulence characteristics in wall-wake flow past two horizontal cylinders. Figure 7.5 depicts the snippet of the experimental setup together with a thorough comparison of streamwise velocity profile at immediate downstream of cylinders, obtained from both methodology. Table 7.3 illustrates few location wise comparison of streamwise velocity values u along with their deviations. It is evident from both figure and table that previously discussed numerical method can efficiently estimate velocity as well as heat transfer rate with acceptable error rates.

	$\overline{Nu}$	Deviation (%)
Hilpert (1933)	115.8	5.7
Igarashi (1985)	107.60	1.7
Feijo et al. (2022)	104.9	2.4
Present work	109.486	–

Table 7.2. Comparison of average Nusselt number $\overline{Nu}$ evaluated on the entire surface of the bluff body in force convective turbulent flow

Streamwise velocity (Experimental)	Streamwise velocity (Numerical)	Deviation (%)
1.89	1.88	1.8
28.04	27.09	3.3
15.35	16.16	5
20.54	20.47	0.3
31.62	31.20	1.3

Table 7.3. Comparison of streamwise velocity u obtained from experiment and present numerical model in case of turbulent flow past two horizontal cylinders

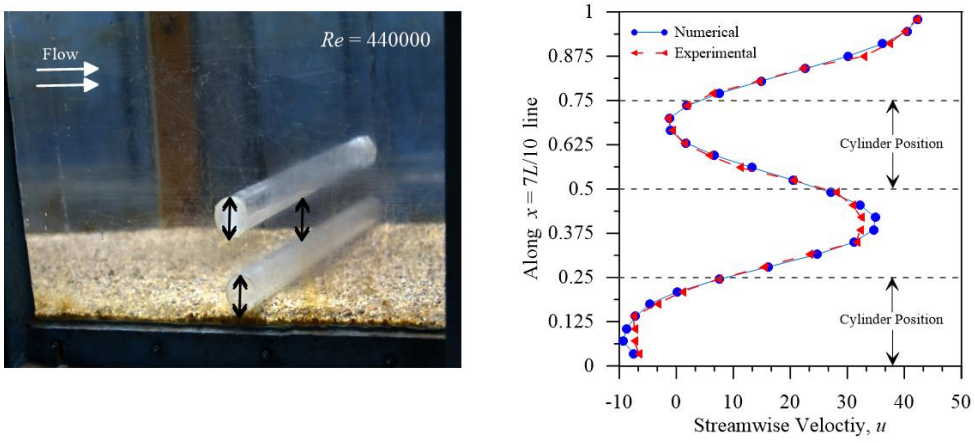

(a) (b)

Figure 7.5. (a) Photograph of the experimental set up (b) comparison of streamwise velocity from present numerical work and experimental data

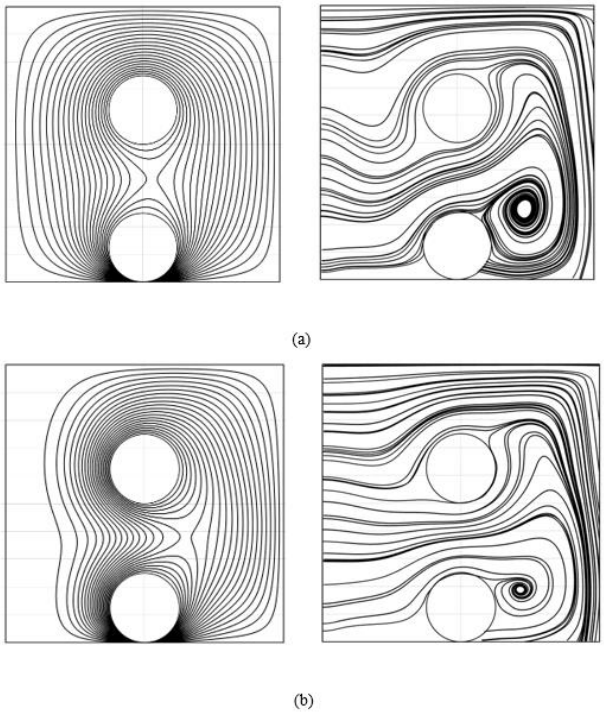

Figure 7.6. Isotherms and Streamlines for cavity flow with two cylinders inside for (a) $Ri = 200, Re = 5$ (b) $Ri = 50, Re = 100$

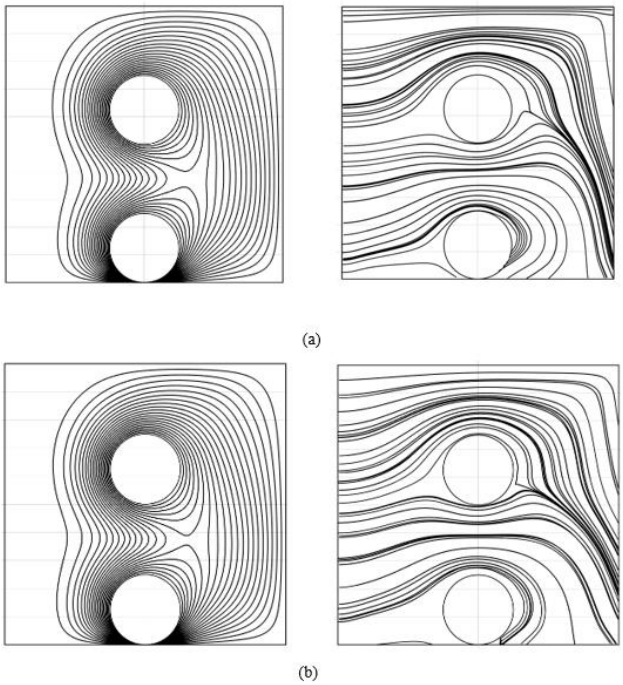

Figure 7.7. Isotherms and Streamlines for cavity flow with two cylinders inside for (a) $Ri = 10, Re = 1000$ (b) $Ri = 1, Re = 5000$

7.5 Results and discussion - for numerical solution

The impact of having two circular cylinders in the cavity is displayed in figure 7.6 by isotherms and streamlines for a range of Reynolds and Richardson values. While the isothermal cylinder walls are kept at $\theta = 1$, the cavity wall temperature is maintained at $\theta = 0$. For these simulations, Pr, ϵ remain fixed at 7 and 0.1 respectively. Heat transmission from the heated obstruction surfaces in the present flow arrangement is influenced by both the natural convection effects brought on by the buoyancy-driven flow and the forced convective effects induced from the lid motion. The creation of a whirling vortex that rotates clockwise with its center somewhat pushed toward the upper right corner is the primary flow behavior for the rightward lid motion alone. But due to the presence of two cylinders and displacement of left wall with constant velocity, the vortex region is being formed downstream of two cylindrical blockages, also known as recirculation region in the literature (Samanta et al. (2023)). This recirculation zone is getting smaller with the increment in Reynolds number Re from 5 to 100. This zone is completely diminished in figure 7.7 as $Re = 1000$ and 5000 respectively indicates transitional and turbulent flows. Furthermore, tiny counterclockwise vortices indicating extremely weak forced convective flow can be visualized in the cavity's lower left corner. The isothermal behavior seen in these graphs aligns with the streamlines and thermal boundary conditions imposed. The isotherms for low Reynolds number and high Richardson values appear to be equally distributed throughout the cavity, but in the subsequent plots, they become more clustered in the direction of the bottom wall and the cylindrical surfaces, suggesting the formation of thin boundary layers with significant normal temperature gradients alongside these areas. For $Ri \leq 50$, this phenomena is more prominent i.e., in presence of strong natural convection.

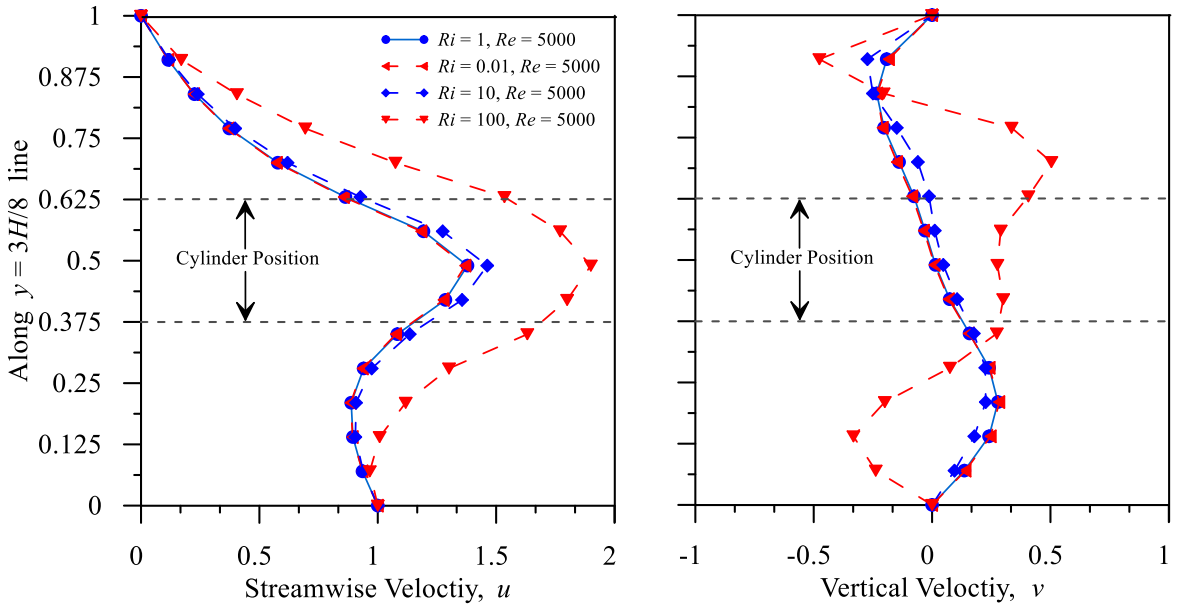

Figure 7.8. Streamwise and vertical velocity profiles along mid-line between cylinders $y = 3H/8$ inside cavity for different Richardson numbers and $Re = 5000$

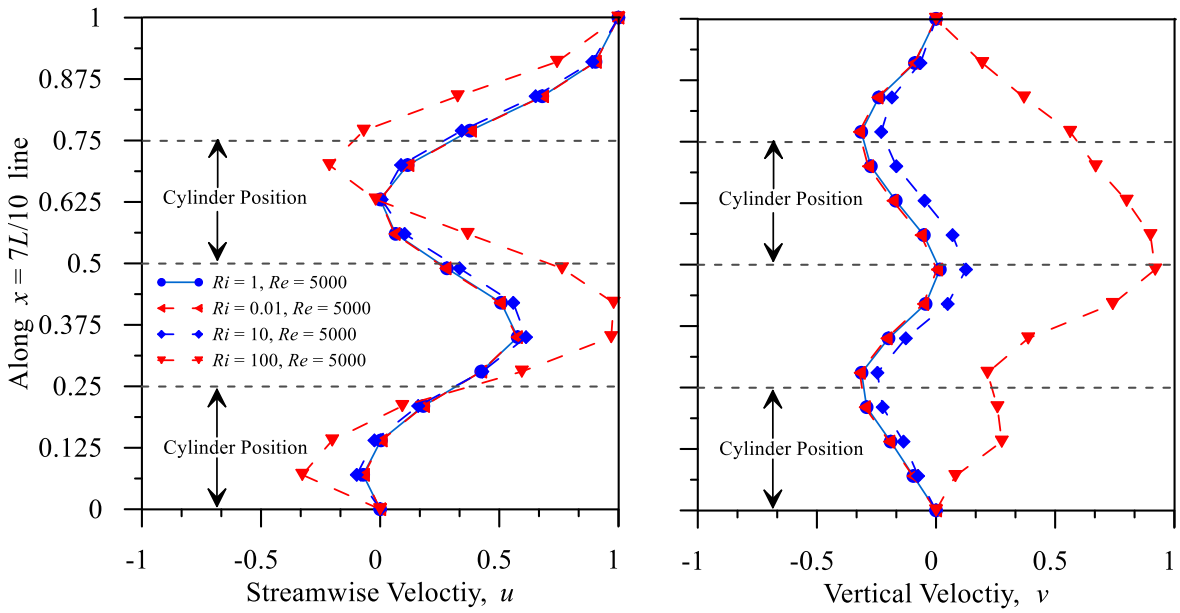

Figure 7.9. Streamwise and vertical velocity profiles along immediate downstream of cylinders $x = 7L/10$ inside cavity for different Richardson numbers and $Re = 5000$

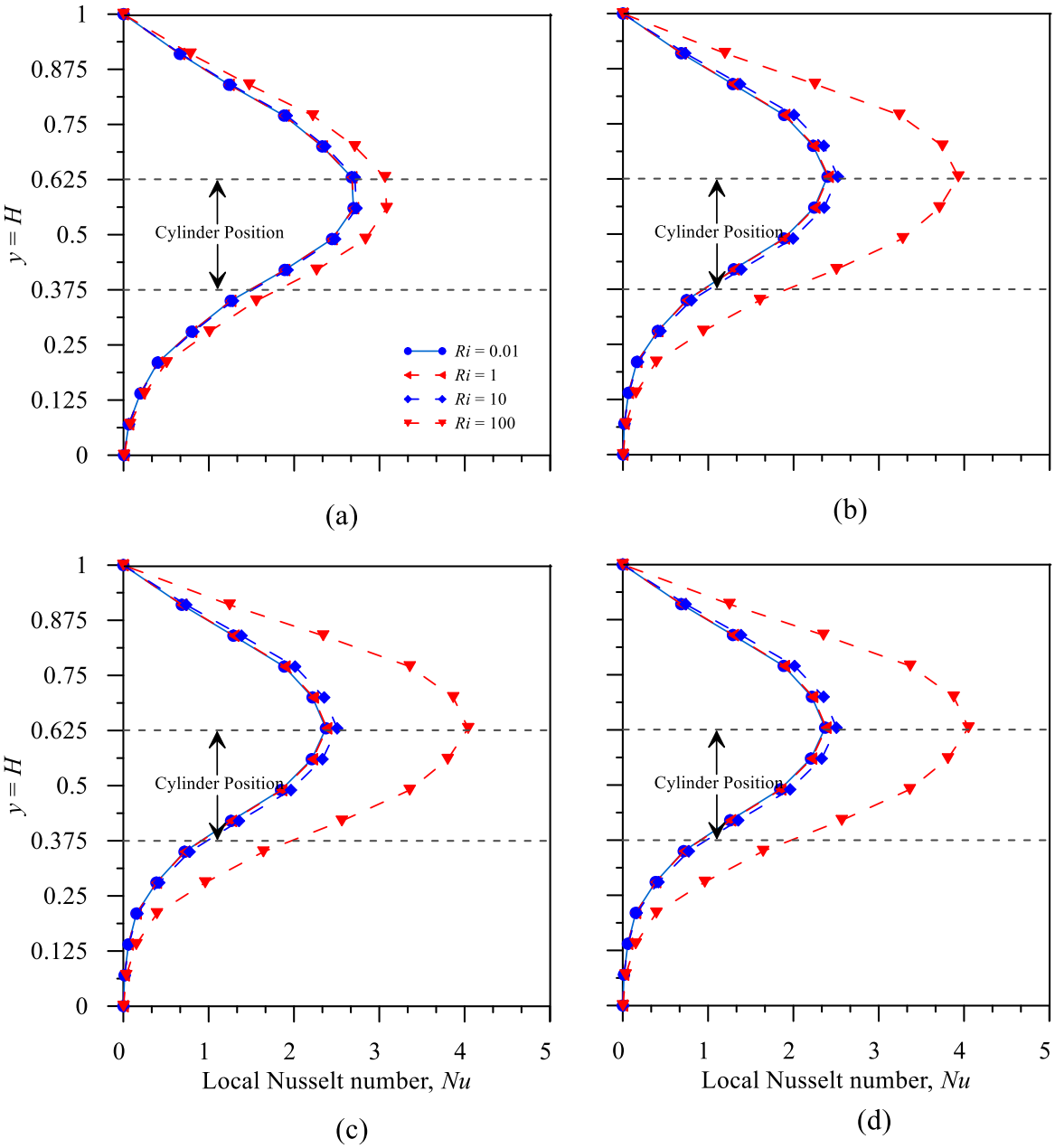

Figure 7.10. Variation of the local Nusselt number Nu on the top wall of the cavity for several Richardson numbers in case of (a) $Re = 5$ (b) $Re = 100$ (c) $Re = 1000$ (d) $Re = 5000$

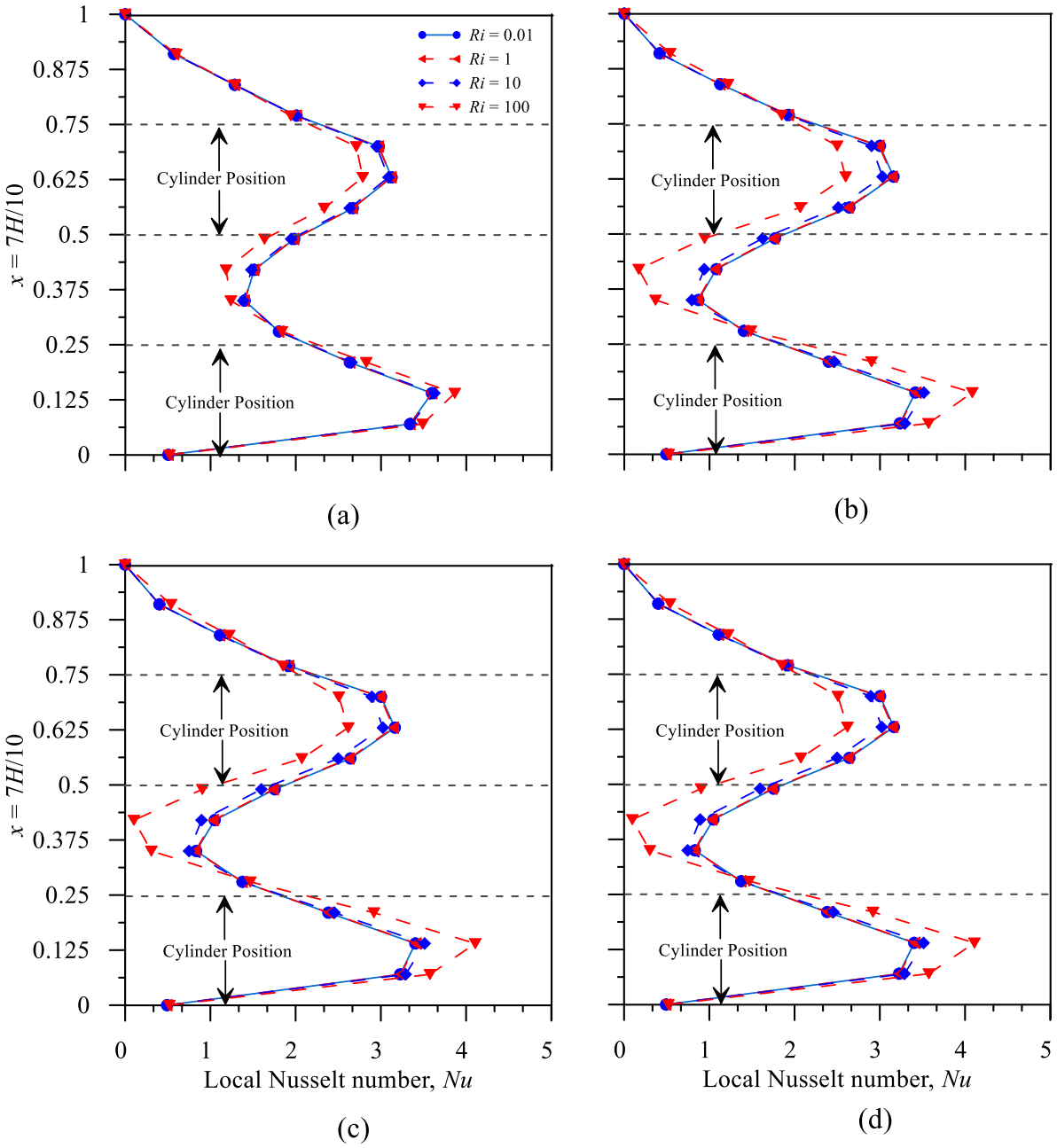

Figure 7.11. Variation of the local Nusselt number Nu at immediate downstream of both cylinders for several Richardson numbers in case of (a) $Re = 5$ (b) $Re = 100$ (c) $Re = 1000$ (d) $Re = 5000$

The streamwise u and vertical v velocity profiles in the horizontal and vertical specified planes, respectively, provide a summary of the hydrological characteristics of the mixed convective flow in figure 7.8 and 7.9. A strong convection together with high turbulent flow is evident at high $Ri = 100$ and $Re = 5000$. Presence of streamwise flow with high magnitude is observed in between two cylinders, as depicted in figure 7.8. In figure 7.9, at immediate downstream position, the u-velocity profiles display flow characteristics that are in accordance with the setup i.e., negative streamwise velocity is observed behind the wall mounted cylinder indicating the flow reversal; although after reaching minima, velocity profile starts increasing and reaches its peak in between both cylinders, followed by another decrement leading to flow reversal although do not reach up to the minima. Henceforth, the profile keeps increasing to reach its maximum value 1, maintaining the boundary conditions. This suggests that there is a recirculation zone behind both of the cylindrical blockages, which is further supported by the streamline plots in figure 7.6. The u-velocities are all zero and negative in the vicinity of the cylindrical blockages, indicating some kind of channel flow feature. This channel flow characteristics are indeed validated from Sarkar et al. (2023) and Samanta et al. (2023), where the authors have presented experimental results of turbulent flow past to horizontal cylinders, one above the other. Upon comparing their velocity profile with ours, it is certain to get the flow reversals and four points of inflection in u-profile at immediate downstream position, also depicted in our findings.

Starting from the upper left corner and moving steadily towards the right, the local Nusselt number, Nu, variation along the cavity's top wall and immediate downstream of the cylinder are displayed in the respective figures 7.10 and 7.11. The intensive grouping of isotherms around the cylindrical obstructions causes a spike in the local Nusselt number at the cylinder sites, indicating a notable temperature differential there. With the growth in Ri from 0.01 to 10, there are no significant change observed in local Nusselt number values, but for $Ri = 100$ a noticeable hike is observed in Nusselt number values due to high temperature gradients. Furthermore, there is a positive correlation being observed between Nusselt number and Reynolds number Re. For laminar flow $Re = 5$, the peaks of the Nusselt number are not high in comparison with the peaks in case of transitional and turbulent flow $Re = 1000, 5000$. Also, there is only one peak for Nu when evaluated along the top wall; on the other hand two gradual

peaks are observed at behind both of the cylinders in figure 7.11, which gradually diminish due to the presence of isothermal hot cylinders. Some of these findings are indeed supported by Morshed et al. (2015) and Islam et al. (2012).

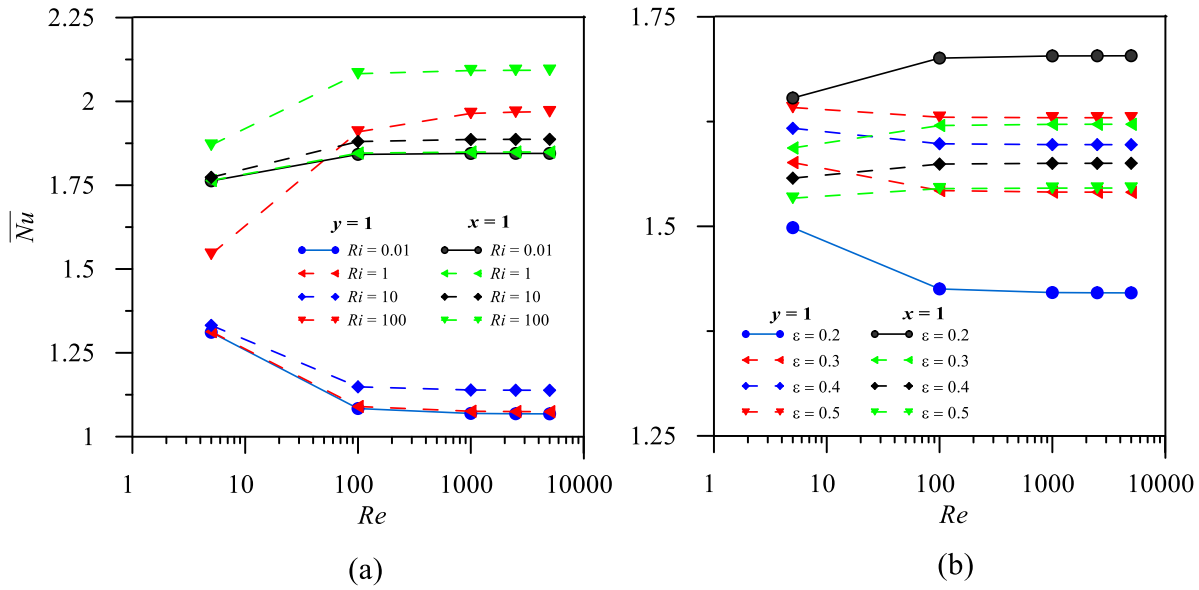

Figure 7.12. Variation of the average Nusselt number $\overline{Nu}$ at top wall and immediate downstream of both cylinders for several (a) Richardson numbers and (b) dissipation rates

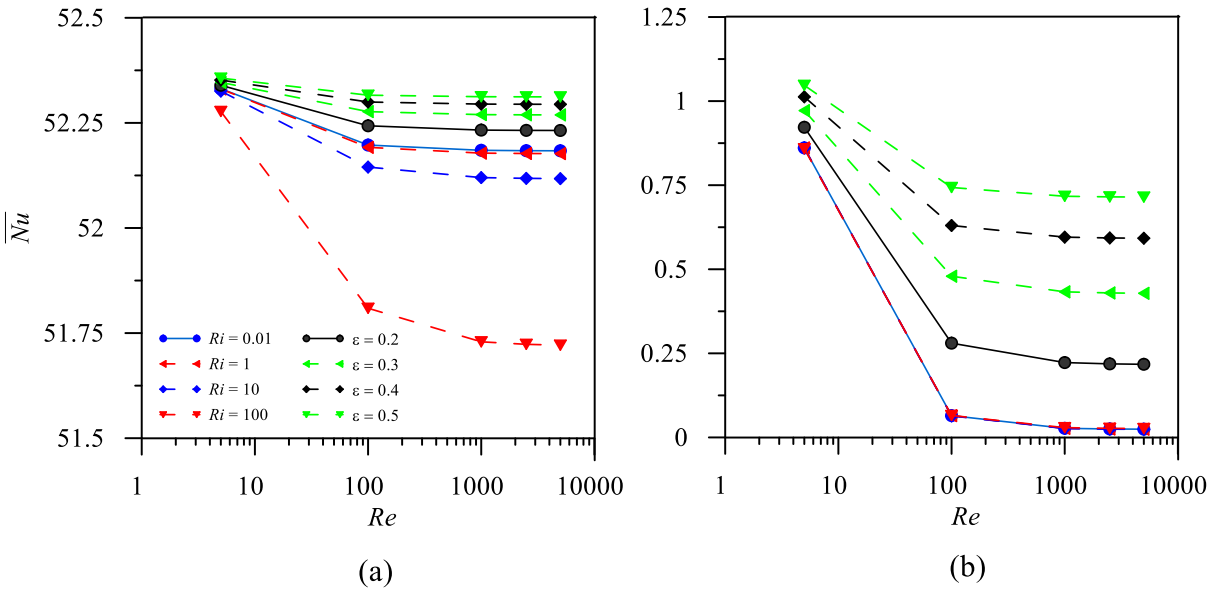

Figure 7.13. Variation of the average Nusselt number $\overline{Nu}$ for several Richardson numbers and dissipation rates at (a) bottom wall and (b) left wall

The average Nusselt number at different cavity plane is the only measure that accurately describes the overall properties of heat transmission for each scenario that is examined here. The average Nu at the cavity's top surface ($y = 1$) and behind the cylinders ($x = 1$) as a function of Re (in logarithmic scale) is depicted in figure 7.12 with increasing Ri and ϵ. While the $\overline{Nu}$ grows monotonically with Re, it tends to an asymptotic value at larger Re values. This asymptotic behaviour is also observed with respect to Ri and ϵ, however the nature of increment or decrement depends upon the position inside the cavity. At the top wall, $\overline{Nu}$ gradually increases with respect to Ri and ϵ due to strong convection, but constant or small fluctuating profiles are observed with respect to Re, indicating that flow being laminar or turbulent has insignificant effect on overall heat transfer. Another interesting observation is found at the immediate downstream of cylinders, where $\overline{Nu}$ decreases with the increment in eddy viscosity. If the eddy viscosity becomes too high, it can disrupt the thermal boundary layer near the surface of the cylinders (Vraciu et al. (2020)). This disruption can reduce the effectiveness of convective heat transfer, leading to a decrement in the values of Nusselt number. To give a comprehensive idea about the overall heat transfer, the average Nu at the cavity's bottom wall ($y = 0$) and left wall ($x = 0$) has been illustrated in figure 7.13. Similar asymptotic behaviour of $\overline{Nu}$ is observed again in these zones with respect to Re. Because of the vicinity of the heated cylinder in the bottom wall, the $\overline{Nu}$ values in that zone is excessively higher in scale rather than the other cold walls.

As was previously mentioned, the aim of our current research is to develop a predictive model that uses the Nusselt number to estimate the thermal distribution of a cavity flow with cylindrical blockages. To do this, the model needs to have certain input variables, or specific parameters in the sense that the target variable should only be somewhat dependent on the inputs. As figure 7.12 suggests, Ri, Re and ϵ will be taken into consideration for input variables in order to set $\overline{Nu}$ as target, for both top wall and immediate downstream positions. Therefore, all of the previously listed factors will be taken into account while discussing the model development and results in the subsequent parts.

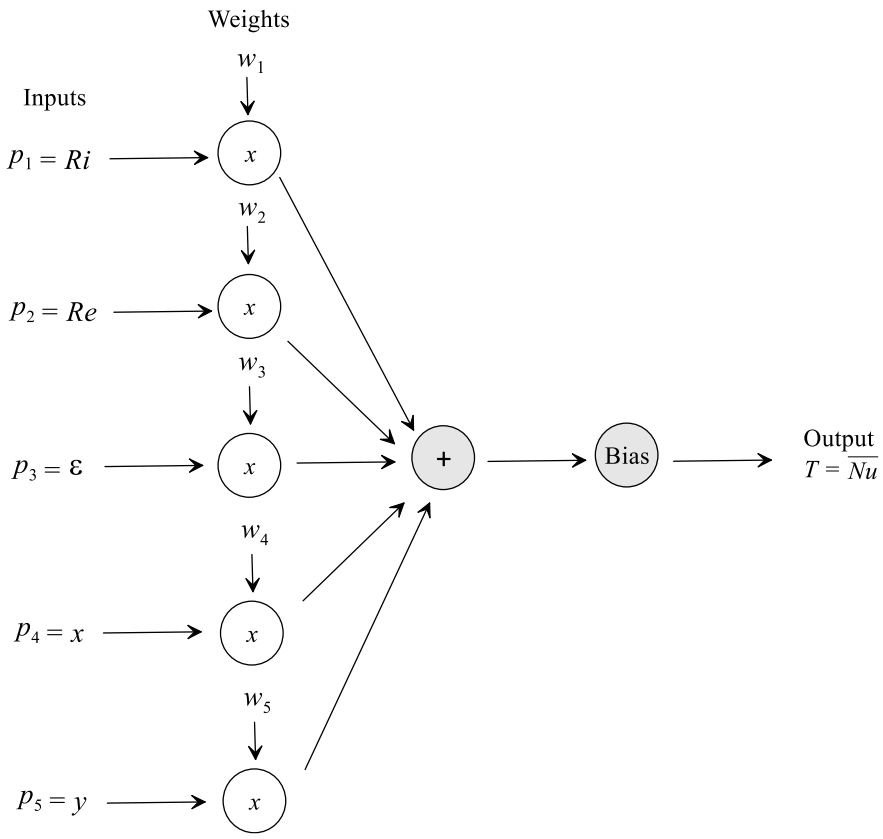

Figure 7.14. Schematic diagram of the ANN model used

7.6 Predictive model 1: Neural Network

An artificial neural network (ANN) basically is a ML model for prediction which, after training on a set of input and output data, can forecast the expected output. Since an artificial neuron serves as the ANN's computing unit, it is often referred to as a "computational neuron". Figure 7.14 depicts a schematic of a computational neuron in an ANN model having five inputs and one output. A neural network (ANN) model's fundamental process is multiplying input characteristics $(p_1, p_2, \dots, p_n)$ by weights $(w_1, w_2, \dots, w_n)$ to get the sum of weighted inputs $(p_1 w_1 + p_2 w_2 + \cdots + p_n w_n)$. An output or target T is produced when the total of the weighted inputs is compared to a predetermined threshold value, sometimes referred to as "bias". An output signal is sent farther in the network if the weighted total of the inputs equals or exceeds the bias; otherwise, it is not.

An artificial neural network (ANN) that uses one or more hidden layers of computation to transfer information forward from an input layer to an output layer is called a feedforward network. The activation function of the many neurons at the hidden layer allows them to respond to the weighted inputs. The output layer consists of one or more output nodes that provide the predicted result y by using an activation function. Logistic-sigmoid activation function is used to transfer the learning process in our case, defined by

$$S(x) = \frac{1}{1+e^{-x}} \tag{31}$$

If the input layer of a feedforward network is directly linked to the output layer, the network is considered single-layer. If one or two hidden layers connect a feedforward network's input layer to the output layer, it is referred to as a two- or three-layer network. To determine the optimal number of connected layers along with the size of each layers, Bayesian optimization technique (Cho et al. (2020)) is used, which is more preferred than mere trial-and-error. Using hyperparameter tuning, the primary goal of Bayesian optimization methods is to minimize an objective function—in this case, the mean square error (MSE). Artificial neural networks (ANNs) will be trained and tested on all available data, if not otherwise specified, into two sub-datasets. When the validation performance of the ANN model does not improve, the training process is terminated; this determination is based on the validation data set.

Re	*Ri*	ε	*x*	*y*	$\overline{Nu}$
5	0.01	0.1	0	1	1.3111
5	0.1	0.1	0	1	1.3113
5	1	0.1	0	1	1.3131
5	10	0.1	0	1	1.332
5	100	0.1	0	1	1.5442
. . .	. . .	. . .	. . .	. . .	. . .
5000	1	0.5	0	1	1.6296
5000	1	0.2	1	0	1.7035
5000	1	0.3	1	0	1.6218
5000	1	0.4	1	0	1.5753
5000	1	0.5	1	0	1.5457

Table 7.4. Brief description of the dataset used for training machine learning models

Variable type	Parameters	Sample size	Mean	Standard devia-tion	Min	Max	Range
Inputs	Re	91	1721	1878.664	5	5000	4995
	Ri	91	12.79	31.14438	0.01	100	99.99
	ε	91	0.211111	0.145683	0.1	0.5	0.4
	x	91	0.5	0.502801	0	1	1
	y	91	0.5	0.502801	0	1	1
Outputs	$\overline{Nu}$	91	1.580821	0.287625	1.0679	2.0929	1.025

Table 7.5. Statistical features of the datasets

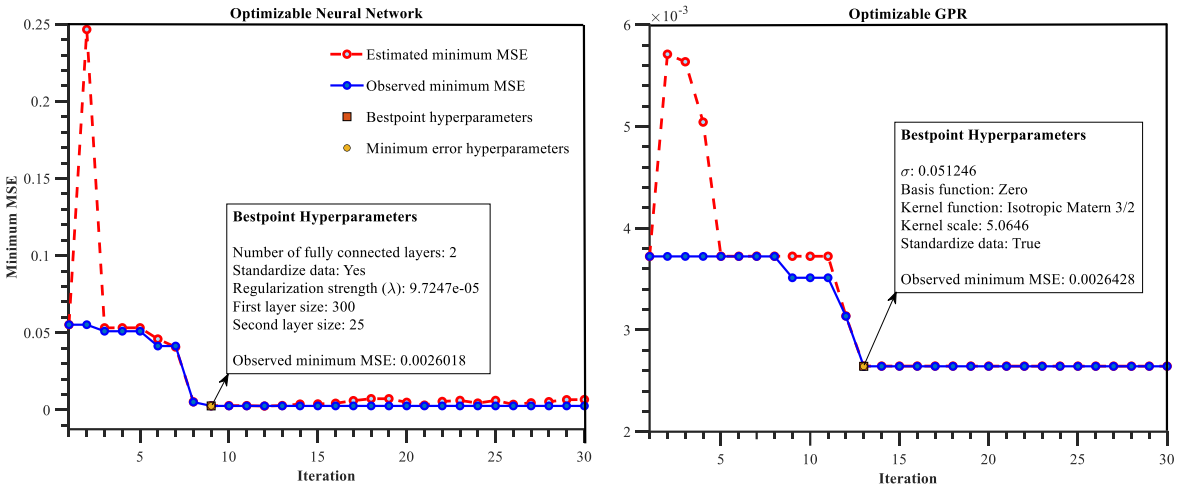

(a) (b)

Figure 7.15. Minimum MSE plots during the training of (a) ANN and (b) GPR models

7.7 Predictive model 2: Gaussian Process Regression (GPR)

A nonparametric probabilistic model dependent on kernels is called Gaussian Process Regression (GPR). Similar to other Bayesian techniques, GPR does not seek to identify models that "best fit" the data by mapping the underlying function $f(x)$ to a particular structure such as linear or quadratic. Rather, given fresh test inputs, they compute posterior predictive distributions. With this kind of method, uncertainty about model estimates may be quantified,

and the reliability of forecasts on subsequent testing points can be enhanced by using the knowledge of the uncertainty (Kopsiaftis et al. (2019)).

The application of Bayesian optimisation (BO) in this study distinguishes it from other response-surface approaches in that it generates a series of samples for the design parameters that converge to the global optimal instead of a predetermined set of samples. It has been shown (Park et al. (2022)) that the BO-GPR locates the global optima in a computationally efficient manner, meaning that the total number of simulations required does not grow exponentially with the design parameter dimension.

Gaussian processes can be thought of as the infinite-sized collections of real-valued variables that multivariate Gaussians are extended to. To be more precise, a Gaussian process is a set of random variables $\{f(\mathbf{x}): \mathbf{x} \in \mathrm{X}\}$ that are defined by a covariance function $k(\mathbf{x}, \mathbf{x}')$ and their mean function $\mu(\mathbf{x})$ in order that

$$\begin{bmatrix} f(\mathbf{x}_1) \\ \vdots \\ f(\mathbf{x}_n) \end{bmatrix} \sim \mathcal{N}\left(\begin{bmatrix} \mu(\mathbf{x}_1) \\ \vdots \\ \mu(\mathbf{x}_n) \end{bmatrix} \begin{bmatrix} k(\mathbf{x}_1, \mathbf{x}_1) & \dots & k(\mathbf{x}_1, \mathbf{x}_n) \\ \vdots & \ddots & \vdots \\ k(\mathbf{x}_n, \mathbf{x}_1) & \dots & k(\mathbf{x}_n, \mathbf{x}_n) \end{bmatrix}\right). \tag{32}$$

The above equation can be rephrased as follows::

$$f(\cdot) \sim \mathcal{GP}(\mu(\cdot), k(\cdot, \cdot)) \tag{33}$$

in which each Gaussian dimension is associated with an element x of the index set X. Furthermore, the $f(\mathbf{x})$ value is represented by the corresponding component of the random vector. For functions $f(\cdot)$, the prior distribution is often anticipated to be a zero-mean GP prior. A training set $\mathcal{L} = \{(\mathbf{x}_i, y_i)\}_{i=1}^{n}$ of i.i.d. samples is considered from an unknown distribution, where $\mathbf{x}_i \in \mathbb{R}^d$ and $y_i \in \mathbb{R}$. A response y_i is assumed by a GPR model to satisfy the following equation:

$$y_i = f(\mathbf{x}_i) + \epsilon_i \tag{34}$$

in which ϵ_i are i.i.d. noise variables, hence $\epsilon \sim \mathcal{N}(0, \sigma^2)$. A joint multivariate Gaussian distribution must be present in both the training and test points. As a result, the mean of a

posterior predictive distribution may be used to estimate any new value. In order to show the declining uncertainty in the model predictions, one needs to observe that the confidence interval size decreases as the quantity of training samples increases. In the present study, the BO-GPR approach is implemented with MATLAB 2023a.

7.8 Modelling Methodology

The above stated methods have been developed using the most recent version of MATLAB, 2023a. The models have been trained with data described in table 7.4. Dataset consists of input features such as Reynolds number Re, Richardson number Ri, eddy viscosity, ϵ. Since these data have been collected at two different positions of cavity - at top wall ($y = 1$) and at immediate downstream of cylinders ($x = 1$), binary values have been encoded to represent the cavity position as follows: $x = 1, y = 0$ in case of immediate downstream position, $x = 0, y = 1$ in case of top wall of cavity. In this manner, two additional input features x and y have been incorporated into our dataset. And as our target value, average Nusselt number $\overline{Nu}$ is incorporated. There are in total 91 observations in the dataset, elucidated in table 7.5 along with its statistical features such as mean, standard deviation, maximum and minimum value with range. During the implementation of both algorithms, the entire dataset has been randomly segregated into two parts- 70% for training and 30% for testing.

For a prediction model to be considered effective, it must meet more criteria than only the construction of the previously described models. It is predicated on the accuracy report of the model, for which a number of quantifiers are accessible in the literature. These include Mean Squared Error (MSE), Residuals (e) and Coefficient of Determination (R). The following parameter values, when used throughout model training, validation, and testing, will guarantee the accuracy of the $\overline{Nu}$ prediction.

$$e_i = Y^i_{ANN/GPR} - Y^i_{FEM} \tag{35}$$

$$MSE = \frac{1}{n}\sum \left(Y^i_{ANN/GPR} - Y^i_{FEM}\right)^2 \tag{36}$$

$$R = 1 - \frac{\Sigma\left(Y^i_{ANN/GPR} - Y^i_{FEM}\right)^2}{\Sigma\left(Y^i_{FEM}\right)^2} \tag{37}$$

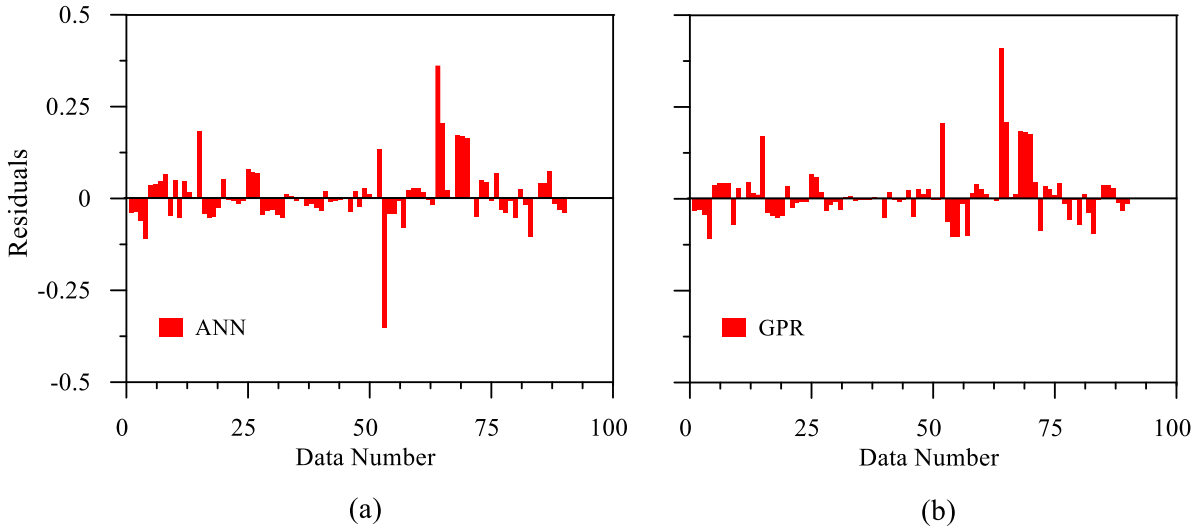

Figure 7.16. Residual plots in case of (a) ANN and (b) GPR models

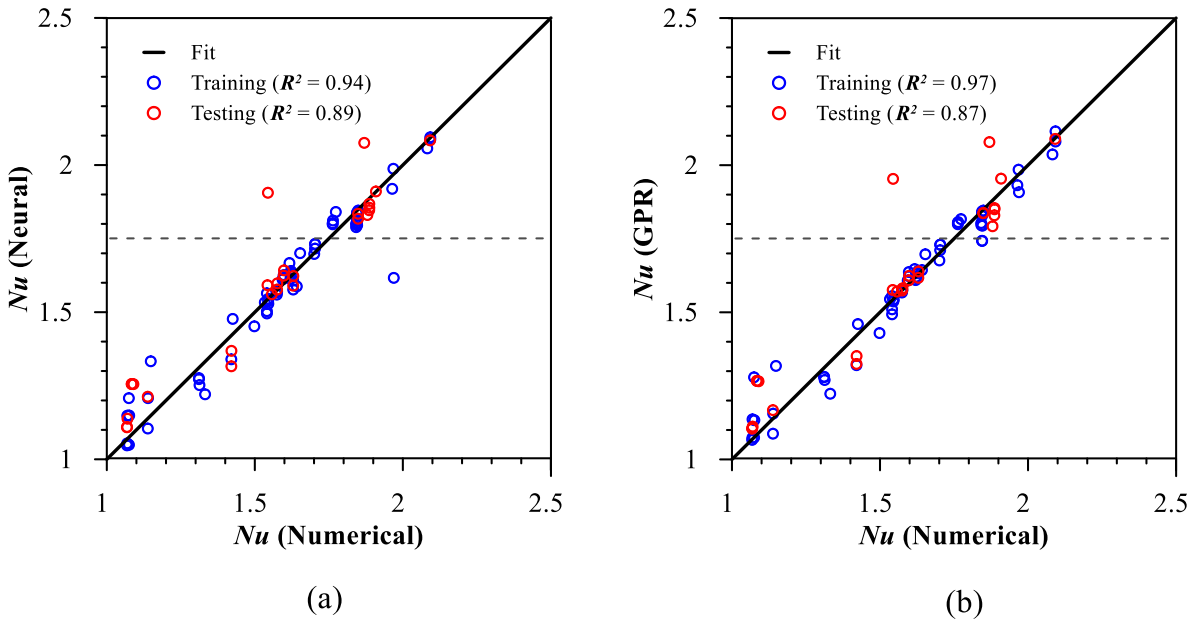

Figure 7.17. Crossplots of numerical and predicted $\overline{Nu}$ data during training and testing in case of (a) ANN and (b) GPR models

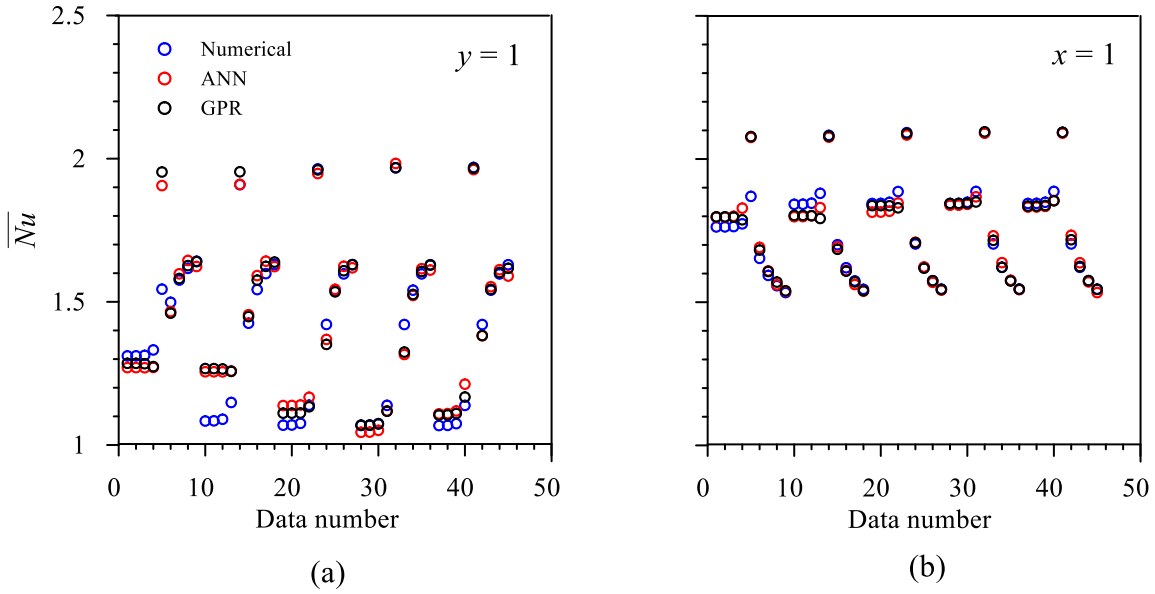

Figure 7.18. Comparison of numerical, ANN and GPR data at (a) $y = 1$ and (b) $x = 1$

7.9 Results and discussion - for predictive models

Analyzing the training performance graphs of the model is one of the data sources used to investigate the training and learning processes of the ML models. Figure 7.15 illustrates model performances through minimum MSE plots. In these plots, the algorithms are trained with certain hyperparameter values at each step or iteration and the corresponding MSE value obtained from that combination is reported, known as hyperparameter tuning. Bayesian optimization is used in all algorithms for hyperparameter tuning. During the training, the software attempts a different combination of hyperparameter settings with each iteration up to a pre-specified value, which is 30 in our case. It is seen from the graphs that although the errors appeared in the initial training of both algorithms are quite high, they gradually converges towards zero as iterations go forward; yielding bestpoint and minimum error hyperparameters - for which the models have performed the best so far. The bestpoints arrive at 9th and 13th iteration respectively in case of ANN and GPR, as in the subsequent iterations there are no improvements observed till 30th iteration. The hyperparameter values at the bestpoints are illustrated in figure 7.15, based on which final prediction models have been obtained. Both the models have been trained very well with our data, although it seems ANN is slightly more well

trained than GPR, as the minimum observed MSE values for ANN and GPR are found to be 0.0026018 and 0.0026428 respectively. However, there are other quantifiers that need to be verified.

An other technique for evaluating a model's training success is to look at the residual bars, which display the errors made throughout the training and testing periods. Figure 7.16 depicts the residual bars in case of ANN and GPR respectively, which, given their comparatively low findings, suggest appropriate training and good prediction. It has been noted that the residuals of both ANN and GPR models have less number of abrupt increases, with the majority of the bars being near to the zero error line. This indicates that both ANN and GPR models are reliable in predicting thermal distribution with rerspect to average Nusselt number.

At every stage, the degree to which the predicted data aligns with the actual data is determined using the coefficient of determination (R). In essence, a R that is closer to 1 denotes the assessed model's quality of fit. A ideal regression model has equal projected and true responses, therefore all points should lie on the $y = x$ line of agreement. The vertical distance from the line to the specified place is the estimation inaccuracy for that location. A well-fitted model has a few errors and predictions that are spread out near the line. Figure 7.17 elucidates crossplots of numerical and predicted $\overline{Nu}$ data during training and testing in case of ANN and GPR models. The R values obtained from training phase and testing phase are 0.94 and 0.89 respectively. These values effectively indicate that the ANN model possess a high efficacy of estimation. The GPR model illustrates a similar feature, with training and testing R values of 0.97 and 0.87. A machine learning model's ultimate objective is to perform well on unknown data, even when a high training accuracy indicates that the model has learned the training data well. Hence, due to a slightly higher testing accuracy, ANN is more preferred than GPR. Moreover, the model performs more robustly in the case of ANN, as evidenced by the smaller difference between training and testing accuracies $(0.94 - 0.89 < 0.97 - 0.87)$, which shows that the model generalizes to new data better.

Figure 7.18 depicts the prediction performance of ANN and GPR models in terms of comparing locationwise, at top wall of cavity ($y = 1$) and at immediate downstream position ($x = 1$). It is observed that in most cases the predicted data fall over the numerical data, except for a few cases mostly in $y = 1$. Due to the high dispersion of Nusselt number at top wall, modelling complexity is more severe there compared to the downstream position of cylinders.

7.10 Concluding Remarks

The investigation of turbulent mixed-convection in a driven square cavity with two internally heated cylindrical obstructions has been conducted numerically for various governing parameters. The RANS equations for turbulent flow have been remodelled and then solved using Galarkin finite element method. The Reynolds number, which is maintained in between 5-5000, eddy viscosity (0.1-0.5) and the Richardson number (0.01–100) are depictions of the flow parameters. Local and average Nusselt numbers at the top wall of cavity and behind the cylinders are computed and depicted, together with the streamline and isotherm lines inside the cavity for a few instances. Lastly, to predict the thermal distribution inside the cavity, ANN and GPR - two machine learning algorithms are implemented. The following key findings can be reported depending on the examination of the heat transport and fluid flow phenomena these studies showed:

- A whirling vortex moving in a clockwise fashion with its center slightly pushed towards the upper right corner is the basic flow tendency for the rightward lid motion alone. However, because there are two cylinders and the left wall is moving at a fixed speed, a vortex zone is forming downstream of the two cylindrical blocks.

- The isotherms for high Richardson values and low Reynolds numbers seem to be evenly distributed throughout the cavity, but in the following plots, they start to cluster more toward the cylindrical surfaces and bottom wall, directing the formation of weak boundary layers with prominent normal temperature gradients adjacent to these regions.

- The streamwise-velocity profiles show flow characteristics consistent with the configuration at the immediate downstream location; for example, a negative streamwise velocity is shown behind the wall-mounted cylinder, indicating a reversal of the flow. In the area of the cylindrical blockages, the streamwise velocities are all zero and negative, suggesting the presence of a channel flow characteristic.

- Local Nusselt number and Reynolds number Re are found to be positively correlated. In the case of laminar flow $Re = 5$, the Nusselt number peaks are not as high as those of transitional and turbulent flow i.e., $Re = 1000, 5000$.

- ANN outperforms GPR in testing accuracy, hence it is recommended for prediction task. Furthermore, the smaller gap between training and testing accuracies ($0.94 - 0.89 < 0.97 - 0.87$), which indicates that the model more effectively generalizes to new data, demonstrates the model's stronger prediction accuracy in the case of ANN.

Chapter 8

Summary and Conclusions

8.1 Turbulence in a wall-wake flow downstream of two horizontal cylinders

8.1.1 Summary

Experimental investigations of flow past two (one above other) horizontal cylinders have been presented in this paper. The experimental data captured over a rough-bed with double cylinders having three different diameters, were used for the analysis. Firstly, general characteristics such as streamwise velocity, Reynolds stress and turbulence intensity profiles have been elucidated at different downstream locations from cylinder position; then some advanced analysis such as length scales, turbulent kinetic energy (TKE) fluxes and budget have been investigated to exhibit their variations. Length scale profiles exhibit higher values in near bed; indicating comparatively larger eddies' downstream of both cylinders. TKE budget profiles indicate highly negative pressure diffusion rate together with a sufficient TKE production rate, stabilized by the amplified TKE diffusion and dissipation rates. To determine one of the most prime behaviors of turbulence characteristics, namely TKE dissipation rate more accurately, the concept of structure function has been employed. Primarily velocity gradient method elucidates TKE dissipation rate, then it has been verified by Kolmogorov's two-thirds law using second order structure function and Kolmogorov's -5/3 law using the method of power spectra.

8.1.2 Conclusions

The conclusions of the turbulence in a wall-wake flow downstream of two horizontal cylinders are summarized below:

- Due to the presence of two cylinders, recirculatory flow is observed in the near wake zone whereas no significant alteration is observed at the far wake zone.
- The stress and intensity profiles indicate a significant increase in values immediately downstream of both cylinders, which fall with both downstream position and vertical height.
- TKE dissipation rate profiles indicate higher amount of dissipation behind the suspended cylinder compared to wall-mounted cylinder in near-wake zone; but as we go far downstream it is observed that decaying of dissipation rate is more behind suspended cylinder. Length scale profiles show higher values in near bed; which indicates comparatively larger eddies' existence behind wall mounted cylinders within inertial subrange and dissipation range respectively.
- In near bed zone, positive streamwise flux and negative vertical flux are being observed, which directs streamwise and downward transportation of TKE fluxes respectively, whereas for the rest of the bed zones negative streamwise, positive vertical fluxes are visible suggesting an upward transport and retardation process with slow fluid motion.
- The TKE budget is prolonged, indicating that the wake flow is characterized by a significant negative pressure energy diffusion rate in conjunction with high TKE diffusion and dissipation rates, while the flow in gap is characterized by a small negative TKE diffusion rate peak and a very low positive pressure energy diffusion rate peak. To support these outcomes, three different experimental outcomes have been presented for each of the aforementioned characteristics, which show consistency of the graphs upon comparing at different downstream positions.

8.2 Turbulence anisotropy in a wall-wake flow downstream of two horizontal cylinders

8.2.1 Summary

In this research, experimental studies of flow behind two horizontal cylinders — one above the other are discussed. The research was conducted using experimental data collected on a rough-bed with double cylinders of three different sizes. First, fundamental features such as streamwise velocity, Reynolds shear stress (RSS), and turbulence intensity profiles have been explained at various downstream positions with respect to the cylinders; next, some advanced analysis such as correlation coefficient, stress anisotropy, and dissipation anisotropy have been presented and compared location-wise. To demonstrate anisotropy, stress, dissipation tensors along with anisotropic invariant map and function are plotted and thoroughly analyzed. Lastly, From Reynolds stress tensor, the eigenvalues have been computed to elucidate a newly developed graphical plot of turbulent anisotropy based on barycentric coordinates.

8.2.2 Conclusions

The major findings of the study are concluded below:

- Correlation values indicate a linear relationship between streamwise and vertical velocities in near bed and near surface zone, but having less / negative correlations behind the cylinders suggesting reverse flow due to opposite directions of streamwise and vertical fluctuations.
- Stress and dissipations tensor have been compared for different downstream positions which shows the near-bed flow produces lesser turbulence anisotropy in the streamwise direction in comparison with their upstream distributions. According to AIMs, the turbulence anisotropy in the wall-wake flow exhibits a behavior that converges towards a 2D (two-dimensional) isotropy close to the wall and gradually returns to a 1D (one-dimensional) isotropy beneath the mid flow depth zone because of the existence of two cylinders.
- Invariant function F indicates in near wake flow, data set are having values near zero in mid flow suggesting existence of strong turbulence anisotropy. Moreover, upon comparison,

stress F values are quite larger than dissipation F values, validating F (stress) = 1.85 F (dissipation), at near wake as well as far wake zone.

- To visualize anisotropy in a more convenient way, AIMs have been mapped into barycentric coordinates, which provide insights such as correspondence between the sudden falls in F with the loops formed inside the equilateral triangle. Three separate experimental results for some of the aforementioned features have been shown to corroborate these findings; these results demonstrate the consistency of the graphs when compared at various downstream points.

8.3 Turbulent bursting and higher-order moments in the wake flow behind two horizontal cylinders

8.3.1 Summary

Turbulent bursting in near- and far-wake flow zones past two horizontal cylinders was studied in the present article. The bursting events and associated time and frequency were first computed from the experimental data and then higher-order moments were evaluated to validate the experimental findings. From the stress ratio of Reynolds Shear Stress (RSS) plots, sweep was found to be the main contributing event that attains the maximum value up to 600% to the development of RSS in the near-wake flow region in the vicinity of the bed, causing a rush of accelerating fluid streaks. The average duration and interval of the bursting events indicate that in the near-wake flow zone, the bursting events are fundamentally shorter than their interval of occurrence. Furthermore, third order moments have been evaluated and utilized to validate the bursting events by comparing with the residual shear stress. The present study should enrich the knowledge of the bursting events in bluff-body hydrodynamics by adding new experimental findings in open-channel turbulence.

8.3.2 Conclusions

The observations of aforesaid research are concluded as below:

- From the stress ratio of RSS plot, sweep events have been found to contribute 600% ($S_{4,0} \approx 6$) to the production of RSS in the near-wake flow at $x/D = 1$ near the wall, causing a rush of accelerating fluid streaks. The Q_2 event describes the unaltered upstream flow far away from the bed ($z/D \approx 3.5$), indicating that it precedes a dominating, slower moving process.

- However, the contributions of the Q_1 and Q_3 events have remained very small, with the exception of the area just downstream of the cylinders, where the inward interaction Q_3 predominates over the outward interaction Q_1.

- The bursting events of the wall-wake flow are essentially more brief than their interval of occurrence, according to the average bursting durations and intervals. Additionally, the near-wake flow is specified by long-duration ejections and sweeps, as well as the intervals between them, particularly in the recirculation zone of two cylinders, where ejection predominates over sweeps. However, this dominance gradually wanes as downstream distance increases toward the far-wake zone.

- In most flow zones, particularly behind cylinders where $F_u >> 3$, the fourth-order moments have a leptokurtic nature, indicating substantial intermittencies in both directions for the near-wake zone. Subsequently, The amplitude of the M_{30} moment is much bigger than the other moments because of the considerable skewness of the streamwise fluctuation behind the cylinders.

- The interdependence of M_{30} with bursting is indeed validated by elucidating crossplots with residual shear stress, which shows well agreement when double cylinder disruptions are absent in the flow zone.

8.4 Machine learning algorithms on predicting the turbulent mixed convection flow in a driven-cavity with two horizontal cylinders

8.4.1 Summary

A finite element approach that utilizes the Galerkin method of weighted residuals is used to numerically investigate the turbulent mixed convective flow in a driven cavity with two circular cylinders positioned one above the other. Streamlines, isotherms, and both local and average Nusselt numbers are compared to illustrate how the Richardson number (*Ri*), Reynolds number (*Re*), and eddy viscosity (ε) influence the transport phenomena inside the cavity. The evaluation of the local and average Nusselt number reveals that strong convection at the top wall directs towards a progressive increase in the average Nusselt number with respect to *Ri* and ε., while steady or slightly varying profiles are seen with regard to *Re*. In order to predict the thermal distribution inside the cavity due to these hot cylinders, Artificial Neural Network (ANN) and Gaussian Process Regression (GPR) have been developed with these model parameters as input and average Nusselt Number as response or output values. Multiple plots have been portrayed to come to a conclusion that both models have been trained very effectively with the minimal observed Mean Square Error (MSE) values of 0.0026018 and 0.0026428 for ANN and GPR, respectively. In support to these findings, the coefficient of determination R^2 suggests that ANN (R^2 = 0.89) outperforms GPR (R^2 = 0.87) in testing accuracy, hence it is recommended for prediction task.

8.4.2 Conclusions

- The basic flow tendency for the rightward lid motion alone is a whirling vortex moving in a clockwise direction, with its center slightly displaced toward the upper right corner. However, with the presence of two cylinders and the left wall moving at a fixed speed, a vortex zone forms downstream of the two cylindrical blocks.

- The isotherms for high Richardson values and low Reynolds numbers seem to be evenly distributed throughout the cavity, but in the following plots, they start to cluster more toward the

cylindrical surfaces and bottom wall, directing the formation of weak boundary layers with prominent normal temperature gradients adjacent to these regions.

- Strong convection at the top wall causes the average Nusselt number to progressively rise with respect to Ri and ϵ, while steady or slightly varying profiles are seen with regard to Re, suggesting that flow being laminar or turbulent has little influence on total heat transfer. Due to the heated cylinder being located near the bottom wall, the average Nusselt number values in that zone are significantly higher than those observed at the other cold walls.
- ANN outperforms GPR in testing accuracy, hence it is recommended for prediction task. Furthermore, the smaller gap between training and testing accuracies ($0.94 - 0.89 < 0.97 - 0.87$), which indicates that the model more effectively generalizes to new data, demonstrates the model's stronger prediction accuracy in the case of ANN.
- In comparison with the downstream position of the cylinders, the modeling complexity is greater at the top wall due to the high dispersion of Nusselt number.

8.5 Future Scope of Studies

The experimental facility has a limitation due to the usage of ADV (Acoustic Doppler Velocimetry). The sample frequency has little impact on the time-averaged velocity for the ADV measurement, and there is a 1 cm sub-region of the total 3 cm profiling scope, past which turbulent characteristics cannot be accurately assessed. Therefore, great consideration must be given to the ADV measurements in open channel flow in order to accurately depict turbulent properties. This could be resolved if we had Particle Image Velocimetry (PIV) in our lab facility; which is capable of capturing both spatial-time data. Another alternative approach is the usage of numerical modelling and simulation. For instance, Baykal et al. (2015) investigated numerically scouring and flow behaviour around a vertical circular cylinder. They had implemented 3D numerical models dependent on RANS equations involving κ-ω turbulence closure, vortex shedding processes and sediment transport. Sidebottom et al. (2015) investigated turbulent characteristics behind a cylinder implementing Large Eddy Simulation (LES). Finite volume method was employed to undergo a parametric study, which showed inconsistency if the boundary layer near cylinder was not incorporated precisely in numerical model. In our scenario, it is possible to replicate the experimental facility into a model with proper boundary conditions,

preferably using a commercial software and solve it with the implementation of RANS equations together with κ-ω turbulence model; thus, generate data to analyse turbulence behaviour. Our future research will analyse other turbulent properties empirically and include the aforementioned numerical models into these experimental settings for verification.

Furthermore, Turbulence anisotropy, characterized by the directional dependence of turbulence properties, is integral to understanding and predicting atmospheric turbulence. Weather models, cloud dynamics, and aviation safety are all greatly impacted by anisotropic turbulence, which is caused by elements including wind shear, Earth's rotation, and thermal stratification. By incorporating the anisotropic nature of turbulence, models can more accurately predict phenomena like clear-air turbulence and boundary layer processes, ultimately enhancing weather forecasts, climate predictions, and aviation safety. The Long Short-Term Memory (LSTM) network is one particular machine learning approach that is frequently utilized in atmospheric turbulence study and prediction. Long-term relationship detection in sequential data is the focus of LSTMs, a category of recurrent neural network (RNN) that is ideally suitable for time-series forecasting problems. LSTMs are useful for accurately modeling the temporal dynamics of weather variables and turbulence features in atmospheric sciences, which enables the prediction of turbulence events. As a final observation, machine learning algorithms have applications in several fields of engineering, therefore, classification and regression models built in our study would significantly contribute in describing the nature of atmospheric turbulence and several hydrological phenomena, which will be our future scope of research.

References

1. Dey, S., Sarkar, S., Bose, S. K., Tait, S., & Castro-Orgaz, O. (2011). Wall-wake flows downstream of a sphere placed on a plane rough wall. *Journal of Hydraulic Engineering*, *137*(10), 1173-1189.
2. Dey, S., Lodh, R., & Sarkar, S. (2018). Turbulence characteristics in wall-wake flows downstream of wall-mounted and near-wall horizontal cylinders. *Environmental Fluid Mechanics*, *18*, 891-921.
3. Antonia, R. A., Djenidi, L., & Spalart, P. R. (1994). Anisotropy of the dissipation tensor in a turbulent boundary layer. *Physics of Fluids*, *6*(7), 2475-2479.
4. Rotta, J. C. (1951). Statistische theorie nichthomogener turbulenz. *Zeitschrift für Physik*, *129*, 547-572.
5. Lumley, J. L., & Newman, G. R. (1977). The return to isotropy of homogeneous turbulence. *Journal of Fluid Mechanics*, *82*(1), 161-178.
6. Banerjee, S., Krahl, R., Durst, F., & Zenger, C. (2007). Presentation of anisotropy properties of turbulence, invariants versus eigenvalue approaches. *Journal of Turbulence*, (8), N32.
7. Dey, S., Paul, P., Ali, S. Z., & Padhi, E. (2020). Reynolds stress anisotropy in flow over two-dimensional rigid dunes. *Proceedings of the Royal Society A*, *476*(2242), 20200638.
8. Longo, S., Clavero, M., Chiapponi, L., & Losada, M. A. (2017). Invariants of turbulence Reynolds stress and of dissipation tensors in regular breaking waves. *Water*, *9*(11), 893.
9. Dey, S., Paul, P., & Padhi, E. (2020). Conditional spatially averaged turbulence and dispersion characteristics in flow over two-dimensional dunes. *Physics of Fluids*, *32*(6).
10. Chang, F. J., Yang, H. C., Lu, J. Y., & Hong, J. H. (2008). Neural network modelling for mean velocity and turbulence intensities of steep channel flows. *Hydrological Processes: An International Journal*, *22*(2), 265-274.
11. Fang, R., Sondak, D., Protopapas, P., & Succi, S. (2020). Neural network models for the anisotropic Reynolds stress tensor in turbulent channel flow. *Journal of Turbulence*, *21*(9-10), 525-543.
12. Morita, Y., Rezaeiravesh, S., Tabatabaei, N., Vinuesa, R., Fukagata, K., & Schlatter, P. (2022). Applying Bayesian optimization with Gaussian process regression to computational fluid dynamics problems. *Journal of Computational Physics*, *449*, 110788.
13. Acikgoz, O., Çolak, A. B., Camci, M., Karakoyun, Y., & Dalkilic, A. S. (2022). Machine learning approach to predict the heat transfer coefficients pertaining to a radiant cooling system coupled with mixed and forced convection. *International Journal of Thermal Sciences*, *178*, 107624.
14. Kang, M., & Kwon, B. (2022). Deep learning of forced convection heat transfer. *Journal of Heat Transfer*, *144*(2), 021801.
15. Angrilli, F., S. Bergamaschi, and V. Cossalter. (1982). Investigation of Wall Induced Modifications to Vortex Shedding from a Circular Cylinder. *Journal of Fluids Engineering, 104* (4), 518–22.
16. Miyata, H., N. Shikazono, and M. Kanai. (1990). Forces on a Circular Cylinder Advancing Steadily beneath the Free-Surface. *Ocean Engineering, 17* (1-2), 81–104.
17. Fujisawa, N., Y. Kawaji, and K. Ikemoto. (2001). Feedback Control of Vortex Shedding from a Circular Cylinder by Rotational Oscillations. *Journal of Fluids and Structures, 15* (1), 23–37.

18. Norberg, C. (2003). Fluctuating lift on a circular cylinder: review and new measurements. *Journal of Fluids and Structures*, *17*(1), 57-96.
19. Reichl, P., Hourigan, K., & Thompson, M. (2003). The unsteady wake of a circular cylinder near a free surface. *Flow, Turbulence and Combustion*, *71*, 347-359.
20. Kumar, S., Laughlin, G., & Cantu, C. (2009). Near-wake structure behind two circular cylinders in a side-by-side configuration with heat release. *Physical Review E—Statistical, Nonlinear, and Soft Matter Physics*, *80*(6), 066307.
21. Zhou, Y., Zhang, H. J., & Yiu, M. W. (2002). The turbulent wake of two side-by-side circular cylinders. *Journal of Fluid Mechanics*, *458*, 303-332.
22. Xu, D., & Chen, J. (2013). Accurate estimate of turbulent dissipation rate using PIV data. *Experimental Thermal and Fluid Science*, *44*, 662-672.
23. Coscarella, F., Servidio, S., Ferraro, D., Carbone, V., & Gaudio, R. (2017). Turbulent energy dissipation rate in a tilting flume with a highly rough bed. *Physics of Fluids*, *29*(8).
24. Akilli, H., Akar, A., & Karakus, C. (2004). Flow characteristics of circular cylinders arranged side-by-side in shallow water. *Flow measurement and Instrumentation*, *15*(4), 187-197.
25. Sumner, D., Wong, S. S. T., Price, S. J., & Paidoussis, M. P. (1999). Fluid behaviour of side-by-side circular cylinders in steady cross-flow. *Journal of Fluids and Structures*, *13*(3), 309-338.
26. Dey, S., Lodh, R., & Sarkar, S. (2018). Turbulence characteristics in wall-wake flows downstream of wall-mounted and near-wall horizontal cylinders. *Environmental Fluid Mechanics*, *18*, 891-921.
27. Antonia, R. A., & Krogstad, P. Å. (2001). Turbulence structure in boundary layers over different types of surface roughness. *Fluid Dynamics Research*, *28*(2), 139-157.
28. He, J., Zhu, X., Verscharen, D., Duan, D., Zhao, J., & Wang, T. (2020). Spectra of diffusion, dispersion, and dissipation for kinetic Alfvénic and compressive turbulence: Comparison between kinetic theory and measurements from MMS. *The Astrophysical Journal*, *898*(1), 43.
29. Wan, M., Servidio, S., Oughton, S., & Matthaeus, W. H. (2010). The third-order law for magnetohydrodynamic turbulence with shear: Numerical investigation. *Physics of Plasmas*, *17*(5).
30. Dey, S., Swargiary, D., Sarkar, S., Fang, H., & Gaudio, R. (2018). Turbulence features in a wall-wake flow downstream of a wall-mounted vertical cylinder. *European Journal of Mechanics-B/Fluids*, *69*, 46-61.
31. Han, J., Arya, S. P., Shaohua, S., Lin, Y. L., & Proctor, F. H. (2000). *An estimation of turbulent kinetic energy and energy dissipation rate based on atmospheric boundary layer similarity theory* (No. NAS 1.26: 210298).
32. Frisch, U. (1995). *Turbulence: the legacy of AN Kolmogorov*. Cambridge university press.
33. Padhi, E., Penna, N., Dey, S., & Gaudio, R. (2019). Near-bed turbulence structures in water-worked and screeded gravel-bed flows. *Physics of Fluids*, *31*(4).
34. Ferraro, D., Servidio, S., Carbone, V., Dey, S., & Gaudio, R. (2016). Turbulence laws in natural bed flows. *Journal of Fluid Mechanics*, *798*, 540-571.
35. Vreman, A. W., & Kuerten, J. G. M. (2018). Turbulent channel flow past a moving array of spheres. *Journal of Fluid Mechanics*, *856*, 580-632.
36. Desikan, S. L. N., Saravanan, R., Subramanian, S., Sivararamakrishnan, A. E., & Pandian, S. (2015). Investigation of supersonic jet interaction with hypersonic cross flow. *Journal of Fluids Engineering*, *137*(10), 101101.

37. Chou, P. Y. (1945). On velocity correlations and the solutions of the equations of turbulent fluctuation. *Quarterly of applied mathematics*, *3*(1), 38-54.
38. Chang, C. K., Lu, J. Y., Lu, S. Y., Wang, Z. X., & Shih, D. S. (2020). Experimental and numerical investigations of turbulent open channel flow over a rough scour hole downstream of a groundsill. *Water*, *12*(5), 1488.
39. Wang, F., & Lam, K. M. (2021). Experimental and numerical investigation of turbulent wake flow around wall-mounted square cylinder of aspect ratio 2. *Experimental Thermal and Fluid Science*, *123*, 110325.
40. Deusebio, E., Augier, P., & Lindborg, E. (2014). Third-order structure functions in rotating and stratified turbulence: a comparison between numerical, analytical and observational results. *Journal of fluid mechanics*, *755*, 294-313.
41. Antonia, R. A., Zhou, T., & Romano, G. P. (1997). Second-and third-order longitudinal velocity structure functions in a fully developed turbulent channel flow. *Physics of Fluids*, *9*(11), 3465-3471.
42. Penna, N., Coscarella, F., & Gaudio, R. (2020). Turbulent flow field around horizontal cylinders with scour hole. *Water*, *12*(1), 143.
43. Dey, S. (2014). "Fluvial Hydrodynamics." *GeoPlanet: Earth and Planetary Sciences*. Springer Berlin, Heidelberg.
44. Krogstadt, P. Å., & Antonia, R. A. (1999). Surface roughness effects in turbulent boundary layers. *Experiments in fluids*, *27*(5), 450-460.
45. Irwin, H. P. A. (1973). Measurements in a self-preserving plane wall jet in a positive pressure gradient. *Journal of Fluid Mechanics*, *61*(1), 33-63.
46. Sarkar, M., Maurya, S. K., Gopmandal, P. P., & Sarkar, S. (2021). Hydrodynamics of flow through a degraded channel bed. *Journal of Turbulence*, *22*(12), 814-842.
47. Sarkar, M., & Sarkar, S. (2023). Structure functions of turbulence through a degraded channel bed. *European Journal of Mechanics-B/Fluids*, *98*, 292-318.
48. Ting, F. C., & Kirby, J. T. (1996). Dynamics of surf-zone turbulence in a spilling breaker. *Coastal Engineering*, *27*(3-4), 131-160.
49. Penna, N., Padhi, E., Dey, S., & Gaudio, R. (2020). Structure functions and invariants of the anisotropic Reynolds stress tensor in turbulent flows on water-worked gravel beds. *Physics of Fluids*, *32*(5).
50. Dey, S., Swargiary, D., Sarkar, S., Fang, H., & Gaudio, R. (2018). Turbulence features in a wall-wake flow downstream of a wall-mounted vertical cylinder. *European Journal of Mechanics-B/Fluids*, *69*, 46-61.
51. Grams, P. E., & Wilcock, P. R. (2007). Equilibrium entrainment of fine sediment over a coarse immobile bed. *Water Resources Research*, *43*(10).
52. Dey, S., Lodh, R., & Sarkar, S. (2018). Turbulence characteristics in wall-wake flows downstream of wall-mounted and near-wall horizontal cylinders. *Environmental Fluid Mechanics*, *18*, 891-921.
53. Schlichting, H., & Kestin, J. (1961). Boundary layer theory, Vol. 121. New York, US: McGraw-Hill.

54. Rao, S. K., Sumner, D., & Balachandar, R. (2004). A visualization study of fluid-structure interaction between a circular cylinder and a channel bed. *Journal of Visualization*, *7*, 187-199.
55. Smith, H. D., & Foster, D. L. (2007). Three-dimensional flow around a bottom-mounted short cylinder. *Journal of Hydraulic Engineering*, *133*(5), 534-544.
56. Verma, P. L., & Govardhan, M. (2011). Flow behind bluff bodies in side-by-side arrangement. *Journal of Engineering Science and Technology*, *6*(6), 745-768.
57. Wang, X. K., & Tan, S. K. (2008). Near-wake flow characteristics of a circular cylinder close to a wall. *Journal of Fluids and Structures*, *24*(5), 605-627.
58. Ozgoren, M. (2006). Flow structure in the downstream of square and circular cylinders. *Flow Measurement and Instrumentation*, *17*(4), 225-235.
59. Sadeque, M. A., Rajaratnam, N., & Loewen, M. R. (2008). Flow around cylinders in open channels. *Journal of engineering mechanics*, *134*(1), 60-71.
60. Wen, C. Y., & Lin, C. Y. (2001). Two-dimensional vortex shedding of a circular cylinder. *Physics of Fluids*, *13*(3), 557-560.
61. Kahraman, A., Özgören, M., & Şahin, B. (2012). Flow structure from a horizontal cylinder coincident with a free surface in shallow water flow. *Thermal Science*, *16*(1), 93-107.
62. Lacey, R. J., & Roy, A. G. (2007). A comparative study of the turbulent flow field with and without a pebble cluster in a gravel bed river. *Water Resources Research*, *43*(5).
63. Ozdil, N. F. T., & Akilli, H. (2015). Investigation of flow structure around a horizontal cylinder at different elevations in shallow water. *Ocean Engineering*, *96*, 56-67.
64. Zdravkovich, M. M. (1977). Review of flow interference between two circular cylinders in various arrangements. *Journal of Fluids Engineering*, *99*(4), 618-633.
65. Lumley, J. L., & Newman, G. R. (1977). The return to isotropy of homogeneous turbulence. *Journal of Fluid Mechanics*, *82*(1), 161-178.
66. Roussinova, V., Balachandar, R., & Biswas, N. (2009). Reynolds stress anisotropy in open-channel flow. *Journal of Hydraulic Engineering*, *135*(10), 812-824.
67. Coscarella, F., Penna, N., Servidio, S., & Gaudio, R. (2020). Turbulence anisotropy and intermittency in open-channel flows on rough beds. *Physics of Fluids*, *32*(11).
68. Dey, S., Paul, P., Ali, S. Z., & Padhi, E. (2020). Reynolds stress anisotropy in flow over two-dimensional rigid dunes. *Proceedings of the Royal Society A*, *476*(2242), 20200638.
69. Ali, N., Hamilton, N., Cortina, G., Calaf, M., & Cal, R. B. (2018). Anisotropy stress invariants of thermally stratified wind turbine array boundary layers using large eddy simulations. *Journal of Renewable and Sustainable Energy*, *10*(1), 013301.
70. Sarkar, S., & Dey, S. (2015). Turbulence anisotropy in flow at an entrainment threshold of sediment. *Journal of Hydraulic Engineering*, *141*(7), 06015007.
71. Sarkar, S., & Dey, S. (2015). Turbulent length scales and anisotropy downstream of a wall mounted sphere. *Journal of Hydraulic Research*, *53*(5), 649-658.
72. Longo, S., Clavero, M., Chiapponi, L., & Losada, M. A. (2017). Invariants of turbulence Reynolds stress and of dissipation tensors in regular breaking waves. *Water*, *9*(11), 893.
73. Sarkar, S., & Dey, S. (2020). Self-preserving characteristics in wall-wake flow downstream of an isolated bedform. *Environmental Fluid Mechanics*, *20*(4), 1119-1139.
74. Sarkar, M., & Sarkar, S. (2023). Structure functions of turbulence through a degraded channel bed. *European Journal of Mechanics-B/Fluids*, *98*, 292-318.

75. Hinze, J. O. (1960). Turbulence. *Journal of Applied Mechanics*, *27*(3), 601.
76. Schlichting, H. (1979). *Boundary-layer theory*. New York, US: McGraw-Hill.
77. Dey, S., & Nath, T. K. (2010). Turbulence characteristics in flows subjected to boundary injection and suction. *Journal of Engineering Mechanics*, *136*(7), 877-888.
78. Dey, S., & Raikar, R. V. (2007). Characteristics of loose rough boundary streams at near-threshold. *Journal of Hydraulic Engineering*, *133*(3), 288-304.
79. Sarkar, S., Papanicolaou, A. N., & Dey, S. (2016). Turbulence in a gravel-bed stream with an array of large gravel obstacles. *Journal of Hydraulic Engineering*, *142*(11), 04016052.
80. Pope, S. B., & Pope, S. B. (2000). Turbulent flows. Cambridge, England: Cambridge university press.
81. Smalley, R., Leonardi, S., Antonia, R., Djenidi, L., & Orlandi, P. (2002). Reynolds stress anisotropy of turbulent rough wall layers. *Experiments in fluids*, *33*(1), 31-37.
82. Rotta, J. C. (1951). Statistische Theorie nichthomogener Turbulenz. *Zeitschrift für Physik, 129*(6), 547–572.
83. Dey, S. (2014). *Fluvial hydrodynamics: Hydrodynamic and sediment transport phenomena*. Berlin, Germany: Springer-Verlag.
84. Hamilton, N. M., & Cal, R. B. (2014). Characteristic shapes of the normalized Reynolds stress anisotropy tensor in the wakes of wind turbines with counter-rotating rotors. *Proceedings of the 17th International Symposium on Applications of Laser Techniques to Fluid Mechanics,* 1–18.
85. Djenidi, L., & Tardu, S. F. (2012). On the anisotropy of a low-Reynolds-number grid turbulence. *Journal of Fluid Mechanics, 702,* 332–353.
86. Banerjee, S., Krahl, R., Durst, F., & Zenger, C. (2007). Presentation of anisotropy properties of turbulence: Invariants versus eigenvalue approaches. *Journal of Turbulence, 8,* N32.
87. Andersson, M., & Karlsson, M. (2021). Characterization of anisotropic turbulence behavior in pulsatile blood flow. *Biomechanics and Modeling in Mechanobiology, 20*(2), 491–506.
88. Ruonan, B., Liekai, C., Xingkui, W., & Li, D. (2016). Comparison of ADV and PIV measurements in open channel flows. *Procedia Engineering, 154,* 995–1001.
89. Baykal, C., Sumer, B. M., Fuhrman, D. R., Jacobsen, N. G., & Fredsøe, J. (2015). Numerical investigation of flow and scour around a vertical circular cylinder. *Philosophical Transactions of the Royal Society A: Mathematical, Physical and Engineering Sciences, 373*(2033), 20140104.
90. Sidebottom, W., Ooi, A., & Jones, D. (2015). A parametric study of turbulent flow past a circular cylinder using large eddy simulation. *Journal of Fluids Engineering - Transactions of the ASME, 137*(9), 091202.
91. Dey, S., Kishore, G. R., Castro-Orgaz, O., & Ali, S. Z. (2019). Turbulent length scales and anisotropy in submerged turbulent plane offset jets. *Journal of Hydraulic Engineering, 145*(2), 04018085.
92. Sharma, A., & Kumar, B. (2021). Anisotropy properties of turbulence in flow over seepage bed. *Journal of Fluids Engineering, 144*(2), 021501.
93. Sarkar, M., Maurya, S. K., Gopmandal, P. P., & Sarkar, S. (2021). Hydrodynamics of flow through a degraded channel bed. *Journal of Turbulence, 22*(12), 814–842.
94. Mahananda, M., Hanmaiahgari, P. R., Balachandar, R., & Roussinova, V. (2021). Effects of aspect ratio on higher-order moments, conditional statistics, TKE budget, and anisotropy in narrow open channel flow. *Canadian Journal of Civil Engineering, 48*(6), 702–715.

95. Sarkar, M., & Sarkar, S. (2022). Laws of turbulence and the estimation of turbulent kinetic energy budget for flow through a degraded channel-bed. *9th International Symposium on Hydraulic Structures*.
96. Chavan, R., Sharma, A., & Kumar, B. (2022). Turbulence anisotropy around bridge piers in seepage-affected sand bed channel. *Journal of Turbulence, 23*(1–2), 52–67.
97. Sarkar, M., Samanta, A., Sarkar, D., Das, R., & Sarkar, S. (2024). Turbulence in a wall-wake flow downstream of two horizontal cylinders. *Marine Georesources & Geotechnology*, *42*(7), 878-897.
98. Ali, S. Z., & Dey, S. (2021). Instability of large-scale riverbed patterns. *Physics of Fluids, 33*(1).
99. Ali, S. Z., & Dey, S. (2021). Interfacial instability of sand patterns induced by turbulent shear flow. *International Journal of Sediment Research, 36*(4), 449–456.
100. Ali, S. Z., & Dey, S. (2021). Linear stability of dunes and antidunes. *Physics of Fluids, 33*(9).
101. Ali, S. Z., & Dey, S. (2024). Generalized scaling law of equilibrium scour depth at a cylinder embedded in an erodible bed. *Physics of Fluids, 36*(6).
102. Ali, S. Z., Dey, S., & Mahato, R. K. (2021). Mega riverbed-patterns: Linear and weakly nonlinear perspectives. *Proceedings of the Royal Society A, 477*(2252), 20210331.
103. Bauri, K. P., & Sarkar, A. (2020). Turbulent bursting events within equilibrium scour holes around aligned submerged cylinders. *Journal of Turbulence, 21*(2), 53–83.
104. Ben Jebria, N., et al. (2023). Coupling 3D hydraulic simulation and fish telemetry data to characterize the behaviour of migrating smolts approaching a bypass. *Journal of Ecohydraulics, 8*(2), 144–157.
105. Corino, E. R., & Brodkey, R. S. (1969). A visual investigation of the wall region in turbulent flow. *Journal of Fluid Mechanics, 37*(1), 1–30.
106. Demare, S., Labraga, L., & Tournier, C. (1999). Comparison and scaling of the bursting period in rough and smooth wall channel flows. *Journal of Fluid Mechanics, 121*(4), 735–746.
107. Dey, S. (2014). *Fluvial hydrodynamics*. Heidelberg: Springer Berlin.
108. Dey, S., Lodh, R., & Sarkar, S. (2018). Turbulence characteristics in wall-wake flows downstream of wall-mounted and near-wall horizontal cylinders. *Environmental Fluid Mechanics, 18,* 891–921.
109. Dey, S., Mahato, R. K., & Ali, S. Z. (2022). Linear stability of sand waves sheared by a turbulent flow. *Environmental Fluid Mechanics,* 1–18.
110. Dey, S., & Nath, T. K. (2010). Turbulence characteristics in flows subjected to boundary injection and suction. *Journal of Engineering Mechanics, 136*(7), 877–888.
111. Dey, S., Paul, P., & Padhi, E. (2020). Conditional spatially averaged turbulence and dispersion characteristics in flow over two-dimensional dunes. *Physics of Fluids, 32*(6).
112. Dey, S., et al. (2011). Wall-wake flows downstream of a sphere placed on a plane rough wall. *Journal of Hydraulic Engineering, 137*(10), 1173–1189.
113. Dey, S., et al. (2018). Turbulence features in a wall-wake flow downstream of a wall-mounted vertical cylinder. *European Journal of Mechanics-B/Fluids, 69,* 46–61.
114. Dey, S., et al. (2020). Hydrodynamics of flow over two-dimensional dunes. *Physics of Fluids, 32,* 025106.
115. Farzadkhoo, M., et al. (2023). Flow hydrodynamics drive effective fish attraction behaviour into slotted fishway entrances. *Journal of Hydrodynamics, 35*(4), 782–802.
116. Ghasemi, A. (2016). Study of macroturbulence and bursting via the -1 spectral power law region of turbulent open channel flows over gravel beds.

117. Grams, P. E., & Wilcock, P. R. (2007). Equilibrium entrainment of fine sediment over a coarse immobile bed. *Water Resources Research, 43*(10).
118. Grass, A. J. (1971). Structural features of turbulent flow over smooth and rough boundaries. *Journal of Fluid Mechanics, 50*(2), 233–255.
119. Ikani, N., et al. (2023). Bursting phenomenon created by bridge piers group in open channel flow. *Environmental Fluid Mechanics, 23*(1), 125–140.
120. Keshavarzi, A., Melville, B., & Ball, J. (2014). Three-dimensional analysis of coherent turbulent flow structure around a single circular bridge pier. *Environmental Fluid Mechanics, 14,* 821–847.
121. Kline, S. J., et al. (1967). The structure of turbulent boundary layers. *Journal of Fluid Mechanics, 30*(4), 741–773.
122. Lu, S. S., & Willmarth, W. W. (1973). Measurements of the structure of the Reynolds stress in a turbulent boundary layer. *Journal of Fluid Mechanics, 60*(3), 481–511.
123. Madsen, J. D., et al. (2001). The interaction between water movement, sediment dynamics and submersed macrophytes. *Hydrobiologia, 444,* 71–84.
124. Mianaei, S. J., & Keshavarzi, A. R. (2010). Study of near bed stochastic turbulence and sediment entrainment over the ripples at the bed of open channel using image processing technique. *Stochastic Environmental Research and Risk Assessment, 24,* 591–598.
125. Mignot, E., Hurther, D., & Barthélemy, E. (2009). On the structure of shear stress and turbulent kinetic energy flux across the roughness layer of a gravel-bed channel flow. *Journal of Fluid Mechanics, 638,* 423–452.
126. Nakagawa, H., & Nezu, I. (1977). Prediction of the contributions to the Reynolds stress from bursting events in open-channel flows. *Journal of Fluid Mechanics, 80*(1), 99–128.
127. Padhi, E., et al. (2019). Near-bed turbulence structures in water-worked and screeded gravel-bed flows. *Physics of Fluids, 31*(4).
128. Raupach, M. R. (1981). Conditional statistics of Reynolds stress in rough-wall and smooth-wall turbulent boundary layers. *Journal of Fluid Mechanics, 108,* 363–382.
129. Raushan, P. K., Singh, S. K., & Debnath, K. (2018). Grid generated turbulence under the rigid boundary influence. *Journal of Wind Engineering and Industrial Aerodynamics, 182,* 252–261.
130. Sadeque, M. A., Rajaratnam, N., & Loewen, M. R. (2008). Flow around cylinders in open channels. *Journal of Engineering Mechanics, 134*(1), 60–71.
131. Samanta, A., et al. (2023). Turbulence anisotropy in a wall-wake flow downstream of two horizontal cylinders. *Flow Measurement and Instrumentation, 94*, 102456.
132. Sarkar, M., et al. (2023). Turbulence in a wall-wake flow downstream of two horizontal cylinders. *Marine Georesources & Geotechnology*, 1–20.
133. Sarkar, S. (2016). Measurement of turbulent flow in a narrow open channel. *Journal of Hydrology and Hydromechanics, 64*(3), 273–280.
134. Sarkar, S., & Dey, S. (2020). Self-preserving characteristics in wall-wake flow downstream of an isolated bedform. *Environmental Fluid Mechanics, 20*(4), 1119–1139.
135. Sarkar, S., Papanicolaou, A. N., & Dey, S. (2016). Turbulence in a gravel-bed stream with an array of large gravel obstacles. *Journal of Hydraulic Engineering, 142*(11), 04016052.
136. Schlichting, H., & Gersten, K. (1979). *Boundary-layer theory*. McGraw-Hill.
137. Wang, J., et al. (2022). Fluid–structure interaction in a flexible vegetation canopy in an open channel. *Journal of Fluid Mechanics, 951*, A41.

138. Wu, Y., et al. (2022). Modelling of flow-induced vibration of bluff bodies: A comprehensive survey and future prospects. *Energies, 15*(22), 8719.
139. Shankar, P., & Deshpande, M. (2000). Fluid mechanics in the driven cavity. *Annual Review of Fluid Mechanics, 32*(1), 93–136.
140. Wong, H., Ahmad, N., Siri, Z., & Noor, N. (2021). Viscous heating and cooling process in a mixed convection cavity with free-slip effect. *Case Studies in Thermal Engineering, 28*, 101349.
141. Ali, N., Nazeer, M., Javed, T., & Razzaq, M. (2019). Finite element analysis of biviscosity fluid enclosed in a triangular cavity under thermal and magnetic effects. *The European Physical Journal Plus, 134*(1), 2.
142. Ouertatani, N., Cheikh, N. B., Beya, B. B., Lili, T., & Campo, A. (2009). Mixed convection in a double lid-driven cubic cavity. *International Journal of Thermal Sciences, 48*(7), 1265–1272.
143. Waheed, M. (2009). Mixed convective heat transfer in rectangular enclosures driven by a continuously moving horizontal plate. *International Journal of Heat and Mass Transfer, 52*(21-22), 5055–5063.
144. Sivakumar, V., Sivasankaran, S., Prakash, P., & Lee, J. (2010). Effect of heating location and size on mixed convection in lid-driven cavities. *Computers & Mathematics with Applications, 59*(9), 3053–3065.
145. Dagtekin, I., & Oztop, H. (2002). Mixed convection in an enclosure with a vertical heated block located. In *Proceedings of ESDA2002: 6th Biennial Conference on Engineering Systems Design and Analysis* (pp. 1–8). Istanbul, Turkey.
146. Cheng, T. (2011). Characteristics of mixed convection heat transfer in a lid-driven square cavity with various Richardson and Prandtl numbers. *International Journal of Thermal Sciences, 50*(2), 197–205.
147. Islam, A. W., Sharif, M. A., & Carlson, E. S. (2012). Mixed convection in a lid-driven square cavity with an isothermally heated square blockage inside. *International Journal of Heat and Mass Transfer, 55*(19-20), 5244–5255.
148. Billah, M., Rahman, M., Sharif, U. M., Rahim, N., Saidur, R., & Hasanuzzaman, M. (2011). Numerical analysis of fluid flow due to mixed convection in a lid-driven cavity having a heated circular hollow cylinder. *International Communications in Heat and Mass Transfer, 38*(8), 1093–1103.
149. Rodrigues, P., Biserni, C., De Escobar, C., Rocha, L., Isoldi, L., & Dos Santos, E. (2020). Geometric optimization of a lid-driven cavity with two rectangular intrusions under mixed convection heat transfer: A numerical investigation motivated by constructal design. *International Communications in Heat and Mass Transfer, 117*, 104759.
150. Ismael, M. A., & Chamkha, A. J. (2015). Mixed convection in lid-driven trapezoidal cavities with an aiding or opposing side wall. *Numerical Heat Transfer, Part A: Applications, 68*(3), 312–335.
151. da Silveira Borahel, R., Zinani, F. S. F., Rocha, L. A. O., dos Santos, E. D., Isoldi, L. A., & Biserni, C. (2022). Geometric optimization of a rectangular isothermal block inside a lid-driven cavity by means of constructal design. *International Communications in Heat and Mass Transfer, 139*, 106499.

152. Ismael, M. A., Hussein, A. K., Mebarek-Oudina, F., & Kolsi, L. (2020). Effect of driven sidewalls on mixed convection in an open trapezoidal cavity with a channel. *Journal of Heat Transfer, 142*(8), 082601.
153. Subramanya, K. (2009). *Flow in open channels*. Tata McGraw-Hill.
154. Schmeling, D., Westhoff, A., Kühn, M., Bosbach, J., & Wagner, C. (2011). Large-scale flow structures and heat transport of turbulent forced and mixed convection in a closed rectangular cavity. *International Journal of Heat and Fluid Flow, 32*(5), 889–900.
155. Gladstone, C., & Woods, A. W. (2001). On buoyancy-driven natural ventilation of a room with a heated floor. *Journal of Fluid Mechanics, 441*, 293–314.
156. Fitzgerald, S. D., & Woods, A. W. (2007). Transient natural ventilation of a room with a distributed heat source. *Journal of Fluid Mechanics, 591*, 21–42.
157. Linden, P. F. (1999). The fluid mechanics of natural ventilation. *Annual Review of Fluid Mechanics, 31*(1), 201–238.
158. Bosbach, J., Pennecot, J., Wagner, C., Raffel, M., Lerche, T., & Repp, S. (2006). Experimental and numerical simulations of turbulent ventilation in aircraft cabins. *Energy, 31*(5), 694–705.
159. Costa, J., Oliveira, L., & Blay, D. (1999). Test of several versions for the k–ε type turbulence modelling of internal mixed convection flows. *International Journal of Heat and Mass Transfer, 42*(23), 4391–4409.
160. Blay, D. (1992). Confined turbulent mixed convection in the presence of horizontal buoyant wall jet. In *HTD Vol. 213: Fundamentals of Mixed Convection*.
161. Mehendale, S., Jacobi, A., & Shah, R. (2000). Fluid flow and heat transfer at micro- and meso-scales with application to heat exchanger design.
162. Walvekar, R., Siddiqui, M. K., Ong, S., & Ismail, A. F. (2016). Application of CNT nanofluids in a turbulent flow heat exchanger. *Journal of Experimental Nanoscience, 11*(1), 1–17.
163. Bhattacharya, S., Verma, M. K., & Bhattacharya, A. (2022). Predictions of Reynolds and Nusselt numbers in turbulent convection using machine-learning models. *Physics of Fluids, 34*(2).
164. Kocak, E., Aylı, E., & Turkoglu, H. (2022). A comparative study of multiple regression and machine learning techniques for prediction of nanofluid heat transfer. *Journal of Thermal Science and Engineering Applications, 14*(6), 061002.
165. Sanhueza, R. D., Akkerman, I., & Peeters, J. W. (2023). Machine learning for the prediction of the local skin friction factors and Nusselt numbers in turbulent flows past rough surfaces. *International Journal of Heat and Fluid Flow, 103*, 109204.
166. Pekmen Geridonmez, B. (2024). Modeling of average Nusselt number by machine learning and interpolation techniques. *ASME Journal of Heat and Mass Transfer, 146*(4).
167. Duan, Y., Cooling, C., Ahn, J. S., Jackson, C., Flint, A., Eaton, M. D., & Bluck, M. J. (2019). Using a Gaussian process regression inspired method to measure agreement between the experiment and CFD simulations. *International Journal of Heat and Fluid Flow, 80*, 108497.
168. Kumar, P. M., & Kavitha, R. (2021). Prediction of nanofluid viscosity using multi-layer perceptron and Gaussian process regression. *Journal of Thermal Analysis and Calorimetry, 144*(4), 1151–1160.
169. Morita, Y., Rezaeiravesh, S., Tabatabaei, N., Vinuesa, R., Fukagata, K., & Schlatter, P. (2022). Applying Bayesian optimization with Gaussian process regression to computational fluid dynamics problems. *Journal of Computational Physics*, *449*, 110788.

170. Schlatter, P. (2022). Applying Bayesian optimization with Gaussian process regression to computational fluid dynamics problems. *Journal of Computational Physics, 449*, 110788.
171. Said, Z., Sharma, P., Tiwari, A. K., Huang, Z., Bui, V. G., Hoang, A. T., et al. (2022). Application of novel framework based on ensemble boosted regression trees and Gaussian process regression in modelling thermal performance of small-scale organic Rankine cycle (ORC) using hybrid nanofluid. *Journal of Cleaner Production, 360*, 132194.
172. Asrari, S., Hakimzadeh, H., & Kardan, N. (2021). Investigation on the local scour beneath piggyback pipelines under clear-water conditions. *China Ocean Engineering, 35*, 422–431.
173. Sedahmed, G., & Nirdosh, I. (1995). Natural convection mass transfer at a vertical array of closely-spaced horizontal cylinders with special reference to electrochemical reactor design. *Industrial & Engineering Chemistry Research, 34*(6), 2133–2137.
174. Sarkar, M., Samanta, A., Sarkar, D., Das, R., & Sarkar, S. (2023). Turbulence in a wall-wake flow downstream of two horizontal cylinders. *Marine Georesources & Geotechnology*, 1–20.
175. Samanta, A., Sarkar, M., Mondal, H., Das, R., & Sarkar, S. (2023). Turbulence anisotropy in a wall-wake flow downstream of two horizontal cylinders. *Flow Measurement and Instrumentation, 94*, 102456.
176. Spiegel, E. A., & Veronis, G. (1960). On the Boussinesq approximation for a compressible fluid. *Astrophysical Journal, 131*, 442.
177. Rodi, W. (1997). Comparison of LES and RANS calculations of the flow around bluff bodies. *Journal of Wind Engineering and Industrial Aerodynamics, 69*, 55–75.
178. Samanta, A., & Mondal, H. (2023). Prediction model based on artificial neural network and bivariate spectral quasi-linearization method for compressible turbulent boundary-layer flow over a smooth flat surface. *Physics of Fluids, 35*(12).
179. Antonia, R., Djenidi, L., & Spalart, P. (1994). Anisotropy of the dissipation tensor in a turbulent boundary layer. *Physics of Fluids, 6*(7), 2475–2479.
180. Kafoussias, N., Karabis, A., & Xenos, M. (1999). Numerical study of two-dimensional laminar boundary layer compressible flow with pressure gradient and heat and mass transfer. *International Journal of Engineering Science, 37*(14), 1795–1812.
181. Fan, Y., Tanner, R. I., & Phan-Thien, N. (1999). Galerkin/least-square finite-element methods for steady viscoelastic flows. *Journal of Non-Newtonian Fluid Mechanics, 84*(2-3), 233–256.
182. Khanafer, K., & Aithal, S. (2013). Laminar mixed convection flow and heat transfer characteristics in a lid-driven cavity with a circular cylinder. *International Journal of Heat and Mass Transfer, 66*, 200–209.
183. Hilpert, R. (1933). Wärmeabgabe von geheizten drähten und rohren im luftstrom. *Forschung auf dem Gebiet des Ingenieurwesens A, 4*, 215–224.
184. Igarashi, T. (1985). Heat transfer from a square prism to an air stream. *International Journal of Heat and Mass Transfer, 28*(1), 175–181.
185. Feijó, B. C., Fragassa, C., Teixeira, F. B., Rocha, L. A. O., Isoldi, L. A., & dos Santos, E. D. (2022). Geometrical investigation of cooling channels with two alternated isothermal blocks under forced convective turbulent flow. *Continuum Mechanics and Thermodynamics, 34*(6), 1687–1709.
186. Morshed, K. N., Sharif, M. A., & Islam, A. W. (2015). Laminar mixed convection in a lid-driven square cavity with two isothermally heated square internal blockages. *Chemical Engineering Communications, 202*(9), 1176–1190.

187. Vraciu, C. V. (2020). An analytical model for thermal convection and convective rolls with a linear eddy viscosity. *Theoretical and Applied Climatology, 141*(3), 841–855.
188. Cho, H., Kim, Y., Lee, E., Choi, D., Lee, Y., & Rhee, W. (2020). Basic enhancement strategies when using Bayesian optimization for hyperparameter tuning of deep neural networks. *IEEE Access, 8*, 52588–52608.
189. Kopsiaftis, G., Protopapadakis, E., Voulodimos, A., Doulamis, N., & Mantoglou, A. (2019). Gaussian process regression tuned by Bayesian optimization for seawater intrusion prediction. *Computational Intelligence and Neuroscience, 2019*, 1–12.
190. Park, K., Kim, Y., Kim, M., Song, C., Park, J., & Ryu, S. (2022). Designing staggered platelet composite structure with Gaussian process regression-based Bayesian optimization. *Composites Science and Technology, 220*, 109254.